SPECTROSCOPIC STUDIES OF RV TAU AND RELATED OBJECTS

A THESIS SUBMITTED TO THE MANGALORE UNIVERSITY
FOR THE AWARD OF THE DEGREE OF

DOCTOR OF PHILOSOPHY IN PHYSICS

Submitted by

S. SUMANGALA RAO

Under the Supervision of
PROF. SUNETRA GIRIDHAR

INDIAN INSTITUTE OF ASTROPHYSICS
BANGALORE - 560 034, INDIA

APRIL 2013

To my beloved parents, grand-parents and Niranjan

”I gaze at the sky,
To the beauty of stars scattered in many,
The clouds do play funny,
Hiding firmament in dark, even on days sunny,
I, seek nature to reveal elements in stars so earnestly,
Am awake whole night with telescopic eye pointing to the sky,
Wonder if years rolled by ever slowly?
Am I an Astrophysicist to get flash of a spectacular new star?
Reflecting in drops of water from a lotus petal forever!
Here I’m collecting pearls of wisdom so carefully,
Stop not growing with Astrophysics infinitely!” .

DECLARATION

I hereby declare that the matter contained in the thesis entitled **"Spectroscopic Studies of RV Tau and Related Objects"** is the result of investigations carried out by me at the Indian Institute of Astrophysics under the supervision of Dr. Sunetra Giridhar. This thesis has not been submitted previously for the award of any degree, diploma, associateship, fellowship etc. of any University or Institute.

S. Sumangala Rao
(Candidate)

Indian Institute of Astrophysics
Bangalore-560034, India

CERTIFICATE

This is to certify that the matter contained in the thesis entitled "**Spectroscopic Studies of RV Tau and Related Objects**" submitted to Mangalore University by **Ms. S. Sumangala Rao** for the award of the degree of Doctor of Philosophy in the Faculty of Science, is based on the results of investigations carried out by her under my supervision and guidance, at the Indian Institute of Astrophysics. This thesis has not been submitted previously for the award of any degree, diploma, associateship, fellowship etc. of any University or Institute.

Dr. Sunetra Giridhar
(Supervisor)

Indian Institute of Astrophysics
Bangalore-560034, India

ACKNOWLEDGEMENTS

This dissertation would not have been possible without the guidance and the help of several individuals who in one way or another have contributed and extended their valuable assistance in the preparation and completion of this study.

First and foremost, I wish to pay obeisance to God Almighty for his blessings and for having given me this opportunity to pursue my childhood dream.

I would like to express my deepest gratitude to my Thesis Supervisor Prof. Sunetra Giridhar for her constant guidance, encouragement and support during my entire tenure at the Institute. I wish to thank her for having introduced me to the study of rare and evolved objects like RV Tau and Post-AGB stars. I wish to salute her for being a friend, mentor and a wonderful human-being. She has been a great source of inspiration to me. Despite the odds and challenges during the course of this work, it is her faith in me and my passion for this field which kept me going and has made this journey a scintillating and memorable experience.

I am eternally grateful to Prof. David L. Lambert for obtaining the high resolution spectra of my program stars at our request and for his valuable comments and suggestions throughout the course of my thesis work which immensely helped in enriching my knowledge and understanding of the subject.

I would like to specially thank Dr. Gajendra Pandey for introducing me to IRAF software during the initial stages of my thesis project and also for guiding me through the analysis and studies of the mildly hydrogen-deficient stars. The discussions I had with him during the course of this study were productive and fruitful.

I am thankful to all the members of the VBO observing support team: Mr. V. Moorthy, Mr. M. Appakutty, Mr. C. Velu and Mr. G. Selvakumar for obtaining the spectra of some of my program stars.

This research has extensively made use of NASA ADS literature archives, CDS (Simbad) database and vizier services. These services are acknowledged.

I would like to thank the Director of Indian Institute of Astrophysics, Prof. S. S. Hasan for giving me the opportunity to work in this Institute and providing all the support and facilities for completing my research work. I would like to acknowledge the support extended by Dr. B. A. Varghese, Dr. A. Subramaniam, Prof. K. N. Nagendra, Dr. Eswar Reddy, Dr. Aruna Goswami, the chairman and all the members of the BGS and the doctoral committee. I would also like to thank Ms. Christina Birdie and the the library staff for their help with the library facilities. I would also like to thank Mr. A. Narasimharaju and Mr. S. B. Ramesh in particular and all the other staff members of the administration

department.

I wish to thank my friends: Bharat Kumar Yerra, Sudhakara Reddy and Smitha Subramanian who have been helpful during my days at IIA.

I am indebted to Prof. K. M. Balakrishna (Chairman, Department of Physics), Dr. K. B. Vijaya Kumar (Department of Physics) of Mangalore University and Prof. T. K. Umesh (Department of Physics, Mysore University) for arranging and giving their valuable comments and suggestions during my Pre-Submission Colloquium at Mangalore University. I would also like to thank Ms. Anita (Administrative staff) of Mangalore University, for being extremely helpful and co-operative in all the formalities related to my Ph.D work.

I would like also like to acknowledge the contributions of my teachers in school and college, in particular Ms. Sheela, Prof. Pranesh and Mr. Johnson.

Finally, I would like to thank my parents, Ms. Sunita S. Rao and Mr. G. Sudhakar Rao, my grand-parents, Ms. Sujatha Kamath and Mr. Pundalik Kamath, my husband, Mr. Niranjan Ratnakar, my uncles, Mr. Narendra Kamath, Arvind Kamath and Mr. G. Umesh Rao and Mr. Muniyappa for their constant encouragement and unflinching faith in me.

I do not have enough words in my vocabulary to express my love, gratitude and appreciation for my parents for the unstinted support I have received from them through the ups and downs in my life so far. So with great humility, I dedicate this thesis to my beloved parents.

TABLE OF CONTENTS

ABSTRACT **v**

PUBLICATIONS **vii**

LIST OF FIGURES **ix**

LIST OF TABLES **xv**

1 INTRODUCTION **1**

1.1 CHARACTERISTICS OF RV TAURI VARIABLES 3

1.2 ALTERNATING BEHAVIOUR IN THE LIGHT CURVE OF RV TAURI STARS 4

1.3 PULSATING STARS AND THE INSTABILITY STRIP 8

1.3.1 THEORY OF STELLAR PULSATIONS 9

1.4 STELLAR EVOLUTION AFTER THE MAIN-SEQUENCE 11

1.5 AGB PHASE: 14

1.5.1 MASS LOSS 15

1.5.2 THE S-PROCESS: 16

1.6 POST-AGB PHASE: 18

1.6.1 DETECTIONS OF POST-AGB STARS 19

1.6.2 MASS RANGES IN POST-AGB STARS 22

1.7 PHOTOSPHERIC ABUNDANCE PATTERNS IN POST-AGB STARS: 22

1.7.1 DEPLETION: 23

1.7.2 S-PROCESS ENRICHMENT: 25

1.7.3 DUST GRAINS AND THE CIRCUMSTELLAR ENVIRONMENT . . . 27

1.8 Aim of the Thesis 33

2 OBSERVATIONS AND ANALYSIS **35**

2.1 OBSERVATIONS 35

2.1.1 INSTRUMENTS USED FOR OBTAINING THE STELLAR SPECTRA . 35

2.1.2 VARIOUS STEPS IN THE DATA REDUCTION OF THE RAW SPECTRA 37
2.2 DEFINITION OF ABUNDANCE AND EQUIVALENT WIDTH OF A SPECTRAL LINE . . . 38
2.2.1 MEASUREMENT OF EQUIVALENT WIDTHS . . . 39
2.2.2 CONCEPT OF CURVE OF GROWTH . . . 40
2.3 ANALYSIS . . . 42
2.3.1 ASSUMPTIONS FOR THE MODEL ATMOSPHERES USED . . . 42
2.3.2 ATMOSPHERIC MODELS . . . 44
2.3.3 COMPUTER CODES USED . . . 44
2.3.4 HYPER-FINE SPLITTING AND ISOTOPIC SHIFTS IN LINES . . . 46
2.3.5 ATOMIC DATA USED . . . 48
2.4 DETERMINATION OF ATMOSPHERIC PARAMETERS . . . 48
2.4.1 EFFECTIVE TEMPERATURE . . . 48
2.4.2 SURFACE GRAVITY . . . 49
2.4.3 MICROTURBULENT VELOCITY . . . 50
2.4.4 EFFECTS OF FE I NON-LTE CORRECTIONS ON THE STELLAR PARAMETER DETERMINATIONS: . . . 51
2.5 ERROR ANALYSIS . . . 52

3 CHEMICAL COMPOSITIONS OF RV TAURI STARS AND RELATED OBJECTS 55
3.1 ABSTRACT . . . 55
3.2 INTRODUCTION . . . 56
3.3 SELECTION OF THE SAMPLE . . . 58
3.4 OBSERVATIONS . . . 60
3.5 ABUNDANCE ANALYSIS . . . 61
3.5.1 THE ERRORS CAUSED BY ASSUMPTION OF LTE . . . 63
3.6 RESULTS . . . 66
3.6.1 IRAS 06165+3158 . . . 66
3.6.2 V820 Cen . . . 67
3.6.3 IRAS 06108+2743 (SU Gem) . . . 70
3.6.4 IRAS 22223+5556 (BT Lac) . . . 71
3.6.5 TX Per . . . 71
3.6.6 IRAS 19135+3937 . . . 71
3.6.7 IRAS 01427+4633 . . . 74
3.6.8 HD 52961 . . . 75

3.6.9 V453 Oph . . . 77
3.7 Evolutionary Context of RV Tauri stars . . . 77
3.8 Discussion . . . 82
3.8.1 Chemical Compositions of the RV Tauri sample . . . 82
3.8.2 Dust-gas winnowing . . . 83
3.8.3 RV Tauris with FIP effect . . . 93
3.8.4 The *s*-process rich RV Tauri stars . . . 93
3.8.5 RV Tauris with Normal Compositions . . . 99
3.9 Summary and Conclusions . . . 99

4 CHEMICAL COMPOSITIONS OF POST-AGB CANDIDATES 101
4.1 ABSTRACT . . . 101
4.2 INTRODUCTION . . . 102
4.3 SELECTION OF THE SAMPLE . . . 103
4.4 OBSERVATIONS . . . 105
4.5 Abundance analysis . . . 105
4.6 RESULTS . . . 109
4.6.1 IRAS 01259+6823 . . . 110
4.6.2 IRAS 04535+3747 (V409 Aur) . . . 111
4.6.3 IRAS 05208-2035 . . . 111
4.6.4 IRAS 07140-2321 . . . 113
4.6.5 IRAS 07331+0021 (AI CMi) . . . 114
4.6.6 IRAS 08187-1905 (V552 Pup) . . . 116
4.6.7 HD 107369 . . . 116
4.6.8 IRAS 12538-2611 . . . 117
4.6.9 IRAS 17279-1119 . . . 117
4.6.10 IRAS 22223+4327 . . . 119
4.6.11 BD+39^{o}4926 . . . 120
4.7 [Na/Fe] in sample stars . . . 121
4.8 α elements . . . 123
4.9 [Ca/Fe] . . . 123
4.10 DISCUSSION . . . 125
4.10.1 Post-AGB stars with s-process enhancements . . . 125
4.10.2 Post-AGB stars with depletion of refractory elements . . . 127
4.10.3 Post-AGB stars without significant s-process enhancement nor showing depletions . . . 132

4.11 Summary 135

5 Analysis of Two Mildly H-deficient Stars: SAO 40039 and HD 187885 **137**

5.1 Abstract 137
5.2 Introduction 138
5.3 Observations and data reduction 139
5.4 Abundance Analysis 140
5.4.1 Method for determining the stellar parameters . . . 141
5.4.2 The He/H ratio 144
5.5 Discussion and Results 147
5.6 Summary and Conclusions 151
5.7 Detailed Line Lists 154

6 Conclusions **169**

6.1 Future perspectives: 170

A Appendix **171**

A.1 Lines used for determining the stellar abundances 171

References **232**

ABSTRACT

Post-AGB stars represent a crucial phase in the evolution of low and intermediate mass stars (0.8-8$M_{\odot}$) where rapid change in the surface composition of the star and its circumstellar envelope takes place. A very small fraction of the known post-AGB objects show hard core post-AGB abundance pattern i.e. the C/O larger than 1 and enhancement of s-process elements. Many of them show chemical peculiarities not caused by the nucleosynthesis. From the spectroscopic studies of a number of RV Tauri and post-AGB objects it is found that many of these show abundance anomalies due to selective depletion of condensable elements. These abundance anomalies are found to be correlated with their condensation temperatures and this process is known as the Dust-Gas Winnowing. A large fraction of these stars are found to be binaries and this depletion is thought to be occurring in a dusty circumbinary disk. A few RV Tau stars show abundance anomalies correlated with the ionization potential of the neutral atoms. This process is known as the First Ionisation Potential (FIP) effect.

In our spectroscopic study of RV Tauri and post-AGB candidates, we try to find the signature of various processes that may affect the stellar composition during the course of its evolution like the initial composition of the Interstellar Medium (ISM), effect of First Dredge Up (FDU), effect of thermal pulses and Third Dredge Up (TDU), effects of dust-gas winnowing and FIP effect and also try to refine the boundary conditions (temperature, metallicity, binarity) for these processes to operate.

We have undertaken the study of unexplored (as well as the ones lacking comprehensive abundance analysis) RV Tau stars and post-AGB objects to understand the chemical changes taking place during the late stages of stellar evolution of low and intermediate mass stars. We have tried to enlarge the RV Tau and post-AGB sample and also present a critical compilation of all these objects studied till now to understand the importance of the stellar parameters and of the conditions such as binarity on post-AGB evolution. We have divided our compilations into several sub-groups such as those showing s-process enrichment, dust-gas winnowing, FIP effect and those having normal compositions. This compilation has enabled us to explore the evolutionary link between RV Tau and post-AGB stars; the latter appear to be in a more advanced stage of evolution. This finding has been further supported by their photometric behaviour. We also find that RV Tau stars generally do not exhibit s-process enhancement but they outnumber post-AGBs in dust-gas winnowing and exhibit different families of depletion curves. Starting with the depletion curve of R Sct with an almost precipice like fall at high condensation temper-

atures, the length and height of low and intermediate condensation temperature plateau show considerable variations. There are another set of RV Tau stars with depletion curve asymptoting at higher condensation temperatures at different [X/H] levels. An attempt has been made to explain the observed depletion curves taking into consideration conditions such as the temperature and composition of the circumstellar environment as well as the efficiency of mixing between the accreted clean gas with the atmosphere/envelope of the star.

In our exploration of post-AGB candidates we also discovered two mildly hydrogen-deficient stars: SAO 40039 and HD 187885 (with strong He I lines). The detections of these stars are very important as they provide an important evolutionary link between hydrogen-normal and hydrogen-deficient stars.

LIST OF PUBLICATIONS

REFEREED JOURNALS

S. Sumangala Rao., Pandey, G., Lambert, D. L., & Giridhar, S., *Is the Post-AGB Star SAO 40039 Mildly Hydrogen-Deficient*?, 2011, ApJ (Letters), 737, L7

S. Sumangala Rao., Giridhar, S., & Lambert, D. L., *Chemical Compositions of Post-AGB Candidates*, 2012, MNRAS, 419, 1254

S. Sumangala Rao., & Giridhar, S., *Chemical Compositions of RV Tauri Stars and Related Objects*, 2013, Submitted to Revista Méxicana de Astronomía y Astrofísica (RevMexxAA)

POSTER PRESENTATION

S. Sumangala Rao., Giridhar, S., & Lambert, D. L., *Elemental abundances for RV Tau and related stars*, 2011, 29^{th} Scientific Meeting of ASI, Eds. P. Khare & C. H. Ishwara-Chandra, ASI Conf. Ser. 3, 121

IN PREPARATION

S. Sumangala Rao., Pandey, G., & Lambert, D. L., *Analysis of Two Suspected He-rich Post-AGB Stars: HD 187885 and HD 331319*

LIST OF FIGURES

1.1 Position of RV Tauri variables in the H-R diagram. Courtesy: http://www.answers.com/topic/variable-star#Type_II_Cepheids 1

1.2 Typical V band light curve of a RV Tauri star (AC Her). Figure taken from Nook et al. (1990) 2

1.3 V band light curve of the RVa star UY CMa showing almost constant mean magnitude. Figure taken from Kiss et al. (2007) 2

1.4 V band light curve of the RVb star AR Pup showing conspicuous variation of mean magnitude from Kiss et al. (2007) 3

1.5 The C-M diagram for the globular cluster M5 (Buonanno et al. 1981) and positions of well known RV Tau stars as well as the evolutionary tracks for $0.605M_{\odot}$ and $0.546M_{\odot}$ post-AGB models by Schönberner (1993) are shown. The values of M_V for the RV Tauri stars were calculated by Gonzalez using the P-L relation for RV Tau stars described in Gonzalez (1994). The color excesses needed for calculating $(B-V)_O$ are taken from a number of sources that are listed in Gonzalez et al. (1997a). This figure has been taken from Giridhar (2000) 4

1.6 The form of characteristic RV Tauri light curve can be reproduced if $P_2=2P_1$ and the two modes of pulsation have a specific phase relationship from Pollard et al. (1996) 5

1.7 H-R diagram showing the Instability Strip. Courtesy:http://outreach.atnf.csiro.au/education/senior/astrophysics/variable_pulsating.html 9

1.8 Evolution of a $1M_{\odot}$ star in the H-R diagram from Lattanzio & Boothroyd (1997) 12

1.9 Evolution of a $5M_{\odot}$ star in the H-R diagram from Lattanzio & Boothroyd (1997) 13

1.10 Structure of an AGB star. Figure from Karakas (2010) 14

1.11 The s-process peaks. Courtesy:http://msowww.anu.edu.au/ akarakas/ Kodai _Lecture4.pdf 16

1.12 The main neutron sources in AGB stars. Courtesy:http://msowww.anu.edu.au/ akarakas/Kodai_Lecture4.pdf 17

1.13 H-R diagram of a complete $2M_{\odot}$ evolution track for solar metallicity from the main-sequence to the white dwarf evolution phase. In the cooler section of the post-AGB phase wiggles in the track are caused by numerical convergence difficulties. The blue track shows a born-again evolution of the same mass. The red and green stars mark the positions of the central stars of planetary nebulae. The number labels for each evolutionary phase indicates the log of the approximate duration for a $2M_{\odot}$ case. Larger or smaller mass cases would have smaller or larger evolutionary time scales respectively by Herwig (2005) 19
1.14 The spectral energy distribution of the optically bright post-AGB star HD 161796 from Hoogzaad et al. (2002) 20
1.15 Galactic latitude distribution of optically bright post-AGB stars (left) and of the new population of obscured post-AGB stars (right). Note the narrower distribution shown by the obscured sample which suggests a higher mass population from Suárez et al. (2006). 21
1.16 Sketch of the disk geometry around HR 4049. The double star is at the center of the disk. The inner surface of the disk is heated by the star and produces the blackbody radiation. The material behind the inner surface is shielded and cold, including the top, bottom and rear surfaces. The height of the disk is set by strong radiation forces which blow away the upper parts of the disk. The direction to the observer is such that we look through the edge of the disk from (Dominik et al. 2003). 23
1.17 Comparison between the spectra of the s-process enriched stars IRAS 14325-6428 and IRAS 08281-4850 with that of the A7Iab standard HD 81471 and the non-enriched post-AGB star HD 133656. Figure taken from Reyniers et al. (2007b) 25
1.18 Abundances of the LMC RV Tauri variable MACHO 47.2496.8 from Reyniers et al. (2007a) 27
1.19 Illustrative spectra of circumstellar environment of post-AGB stars; an O- rich (top, HD 161796); a C-rich (middle, HD 235858); and one with mixed chemistry (bottom HR 4049). In the top panel, the different crystalline dust composition signatures are indicated: fosterite, ensatite, and water ice. The bulk of the silicate dust is, however, in amorphous form Hoogzaad et al. (2002). The lower panel is a C-rich dust envelope, with plateau emission of CC and CH bonds of hydrocarbons (Kwok et al. 2001; Hony et al. 2003). At longer wavelengths, the 21 m band, which is attributed to TiC, and the 30 m emission feature attributed to MgS are apparent. The bottom panel shows the circumstellar spectrum of the enigmatic binary HR 4049. The continuum is well fitted with a pure, single-temperature black body, which constrains strongly the circumstellar physics (Dominik et al. 2003). The PAH features are strong, and in the inserts, the diamond (Geballe et al. 1989; Van Kerckhoven et al. 2002) and CO2 (Cami & Yamamura 2001) features are shown. Figure taken from Van Winckel (2003). 30

1.20 Spectral sequence followed by C-rich sources (left) and by O-rich sources (right) from García-Lario & Perea Calderón (2003) 32

2.1 Opto-mechanical layout of the spectrometer. F/5 beam emerging from the slit is fed into the collimator by a folding mirror. The collimated beam then passes through the cross disperser prism and gets pre-dispersed and illuminates the echelle grating. The dispersed beam from the grating passes through the prism a second time and finally comes to focus on the CCD plane where the spectrum is recorded. Figure taken from Rao et al. (2005). 36
2.2 Equivalent Width of a spectral line 40
2.3 Typical curve of growth for the K line of Ca II. Courtesy:http://cc.oulu.fi/jpoutane/teaching/TA07/TheorAstro11_handouts.pdf 41
2.4 Changes of the line profile with the increase in the number of absorbers: (a) for weak lines and (b) for strong lines. Figure taken from Böhm-Vitense (1989) 41

3.1 The IRAS color-color diagram showing the "RV Tauri" box. The figure contains our sample stars and all the well studied RV Tauri stars. The program stars are numbered according to the Table 3.1. 58
3.2 Sample spectra of our program stars presented in the descending order of temperature (top to bottom) in the 6100-6180Å region. 60
3.3 The agreement between synthesized and observed spectrum for IRAS 06165+3158 for selected regions containing the lines of s-process elements. 67
3.4 The agreement between synthesized and observed spectrum for V820 Cen for selected regions containing the lines of s-process elements. 68
3.5 Plot of [X/H] versus T_C for SU Gem 70
3.6 Plot of [X/H] versus T_C for HD 52961 76
3.7 Comparison between the spectrum of the heavily depleted star HD 52961 with that of γ Cyg a normal supergiant. In the spectrum of HD 52961, note the weakness of the metallic lines but the lines of C I and Zn I are clearly seen. 76
3.8 H-R diagram showing the location of the population II instability strip, lines of constant period and the theoretical evolutionary tracks for a 0.536 and 0.6$M_\odot$ star. The location of the well studied RV Tauri stars, W Vir variables and psot-AGB stars have been shown. 80
3.9 Plots of [X/H] versus T_C for the W Vir variables: CO Pup, V1711 Sgr and MZ Cyg. The values of [X/H] are from Maas et al. (2007) 85
3.10 Plots of [X/H] versus T_C for the RV variables: UY CMa, HP Lyr and DY Ori. The values of [X/H] are from Giridhar et al. (2005) 85
3.11 Plot of [X/H] versus T_C for the W Vir variable: CC Lyr. The values of [X/H] are from Maas et al. (2007) 86

3.12 Plot of [X/H] versus T_C for EP Lyr and AD Aql. The values of [X/H] for EP Lyr are from Gonzalez et al. (1997b) and for AD Aql from Giridhar et al. (1998) 87
3.13 Plot of [X/H] versus T_C for the RV variable: R Sct. The values of [X/H] are from Giridhar et al. (2000) 87
3.14 The solid curves denote the predicted stellar abundances [X/H] for the mixing fractions f=0.9, 0.99 and 0.999 for mixing between material having solar abundances with the material having the composition of the interstellar gas along the line of sight to ζOph. The open circles denote the observed interstellar abundances for different atomic species. 89
3.15 The observed data points are compared with Depletion predictions made using mixing fraction giving the best fitting curve for MZ Cyg and DY Ori. 90
3.16 The observed data points are compared with Depletion predictions made using mixing fraction giving the best fitting curve for EP Lyr and AD Aql. 90
3.17 Plot of [X/H] versus T_C and the first ionization potential χ_I for CE Vir - adapted from Rao & Reddy (2005). 98

4.1 The location of sample stars in IRAS color-color diagram containing the zones defined by van der Veen & Habing (1988) and area enclosed in the dashed line which according to Szczerba et al. (2007) is richly populated by post-AGB stars with colors like planetary nebulae. The sample stars are numbered as follows: 1- IRAS 01259+6823 2- IRAS 04535+3747 3- IRAS 05208-2035 4- IRAS 07140-2321 5- IRAS 07331+0021 6- IRAS 08187-1905 8- IRAS 12538-2611 9- IRAS 17279-1119 10- IRAS 22223+4327 104
4.2 Sample spectra of our stars presented in descending order of temperature (top to bottom) in the 6100-6180Å region. 105
4.3 Comparison of spectra of the stars: IRAS 17279-1119 and IRAS 22223+4327 showing s-process enrichment with IRAS 07140-2321, a normal star of similar temperature in the 4550-4590 Å region. The lines of s-process elements like Ba II, Ce II and Sm II are enhanced. 120
4.4 Plot of [X/H] vs [T_c] for the star BD+39^{o}4926. 121
4.5 Plot of [Ca/Fe] versus the effective temperature for all groups of post-AGBs including our Program Stars. 124

5.1 Equivalent widths for lines common between our spectra and Klochkova et al. (2007) for SAO 40039. 140
5.2 The upper panel shows the loci satisfying the ionization balance − see keys on the figure. The locus satisfying the H I Paschen lines is shown by dashed line. The solid line represents the excitation balance of both Fe I and Fe II. The cross shows the derived stellar parameters. Lower Panel shows the observed and synthesized profiles of Paschen lines of H I in the 8600Å region for $T_{\rm eff}$ = 8000K, He/H = 1.0 and log g = 0.5, 0.75 and 1.0 for the star SAO 40039. 142

5.3 The upper panel shows the loci satisfying the ionization balance − see keys on the figure. The locus satisfying the H I Paschen lines is shown by the green solid line. The red solid line represents the excitation balance of both Fe I and Fe II. The cross shows the derived stellar parameters. Lower Panel shows the observed and synthesized profiles of Paschen lines of H I in the 8600 region for $T_{\rm eff}$ = 8000K, He/H = 0.4 and log g = 0.5, 0.9 and 1.5 for the star HD 187885 143
5.4 The observed and synthesized He I profiles for the triplet lines at 5876, 4471 and 4713Å and for the singlet lines at 4922 and 5015Å for SAO 40039 using models with$T_{\rm eff}$ = 8000K, log g = 0.75 for He/H = 1.0, 0.4 and 0.1 − see keys on the figure. 144
5.5 The observed and synthesized He I profiles for the triplet lines at 5876, 4471 and 4713 and for the singlet lines at 4922 and 5015 for HD 187885 using models with$T_{\rm eff}$ = 8000K, log g = 0.9 for He/H = 1.0, 0.4 and 0.1 − see keys on the figure. 145
5.6 The [X] versus T_c plot for SAO 40039. 150

LIST OF TABLES

2.1 References for the log *gf* values 47

3.1 The Program Stars. 59
3.2 Stellar Parameters Derived from the Fe-line Analyses 62
3.3 Sensitivity of [X/Fe] to the uncertainties in the model parameters for a range of temperatures covering our sample stars 64
3.4 Elemental Abundances for IRAS 06165+3158 and V820 Cen 69
3.5 Elemental Abundances for IRAS 06108+2743 and IRAS 22223+5556 . . 72
3.6 Elemental Abundances for TX Per and IRAS 19135+3937 73
3.7 Elemental Abundances for IRAS 01427+4633, HD 52961 and V453 Oph 78
3.8 A compilation of RV Tauri, RV Tauri like and W Vir variables showing dust-gas winnowing and FIP effect 94
3.8 Contd.. 95
3.9 A compilation of RV Tauri and RV Tauri like variables showing s-process enrichment and normal compositions 96
3.9 Contd.. 97

4.1 The Program Stars. 104
4.2 Stellar Parameters Derived from the Fe-line Analyses 107
4.3 Sensitivity of [X/Fe] to the uncertainties in the model parameters for a range of temperatures covering our sample stars 108
4.4 Elemental Abundances for IRAS 01259+6823 and IRAS 04535+3747. . . 112
4.5 Elemental Abundances for IRAS 05208-2035, IRAS 07140-2321 and IRAS 07331+0021 115
4.6 Elemental Abundances for IRAS 08187-1905, HD 107369 and IRAS 12538-2611 118
4.7 Elemental Abundances for IRAS 17279-1119, IRAS 22223+4327 and BD +39 4926 122
4.8 A list of Post-AGB stars with enhancement of s-process elements 126
4.9 A list of Post-AGB stars showing depletion 128
4.9 Contd.. 129
4.10 A list of Post-AGB stars showing neither significant s-process enrichment nor depletion 133
4.10 Contd.. 134

5.1 Comparison between abundances estimated with MOOG using He/H=0.1 model and the abundances computed with SPECTRUM using the hydrogen deficient (He/H=1.0) model for SAO 40039 148
5.2 Comparision between abundances computed with SPECTRUM using the hydrogen-deficient He/H=0.4 model and our MOOG abundances using the He/H=0.1 model for HD 187885 149
5.3 Detailed line list for SAO 40039 154
5.4 Detailed line list for HD 187885 160

A.1 Line identification for the stars: 1 = IRAS 01427+4633, 2 = TX Per, 3 = IRAS 06108+2743, 4 = IRAS 06165+3158, 5 = HD 52961, 6 = V820 Cen, 7 = V453 Oph 172
A.2 Line identification for the stars: 8 = IRAS 19135+3937, 9 = IRAS 22223+5556, 10 = IRAS 01259+6823, 11 = IRAS 04535+3747, 12 = IRAS 05208-2035, 13 = IRAS 07140-2321, 14 = IRAS 07331+0021 191
A.3 Line identification for the stars: 15 = IRAS 08187-1905, 16 = HD 107369, 17 = IRAS 12538-2611, 18 = IRAS 17279-1119, 19 = IRAS 22223+4327, 20 = BD+39^o 4926 215

CHAPTER 1

INTRODUCTION

RV Tau stars represent a typical group of pulsating variables comprising of yellow/orange supergiant stars of spectral types F to K. The first variable to be placed in this group was R Sct, discovered by Pigott in 1795. The second one to be discovered was R Sge by Baxendell in 1859. However these stars could be classified as a special type of variable only after van der Bilt's analysis of the variable RV Tau (discovered by Tserasskaya).

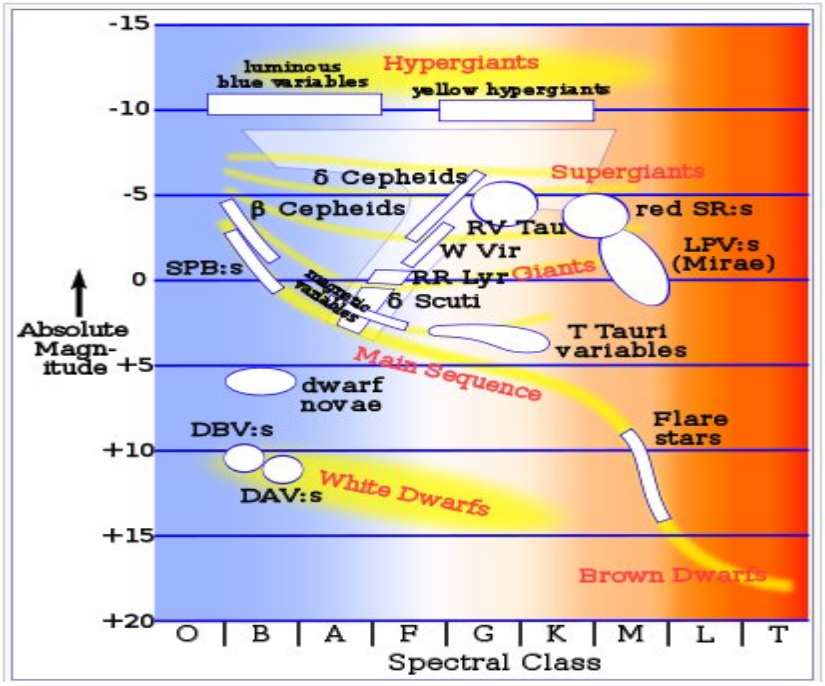

Figure 1.1: Position of RV Tauri variables in the H-R diagram. Courtesy: http://www.answers.com/topic/variable-star#Type_II_Cepheids

RV Tau stars are pulsating variables located in the instability strip along with the Cepheids but at relatively lower luminosities as can be seen in Figure 1.1. Their char-

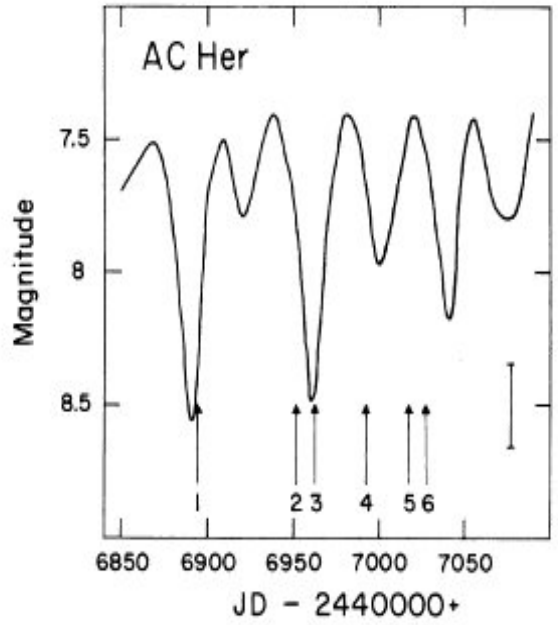

Figure 1.2: Typical V band light curve of a RV Tauri star (AC Her). Figure taken from Nook et al. (1990)

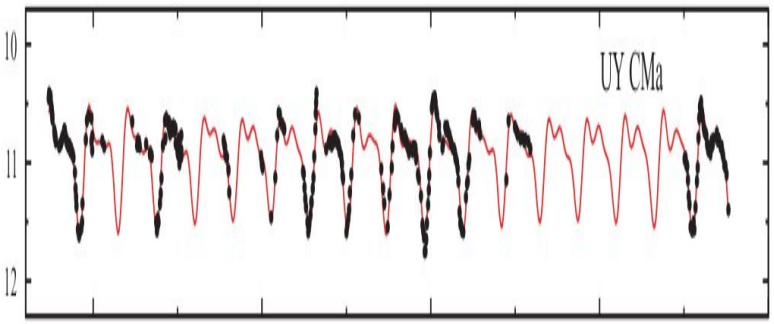

Figure 1.3: V band light curve of the RVa star UY CMa showing almost constant mean magnitude. Figure taken from Kiss et al. (2007)

acteristic light curve shows alternating deep and shallow minima with a formal period (time elapsed between two consecutive deep minima) of 30-150 days. Sometimes the light variations may become rather irregular, particularly for the stars having the longest periods and are also classified as semiregular variables. Figure 1.2 shows the typical light curve of the RV Tau star AC Her.

Because of intersection of evolutionary tracks with population II instability strip, Post-AGB (Post-Asymptotic Giant Branch) stars also contain variable stars such as RV Tauris,

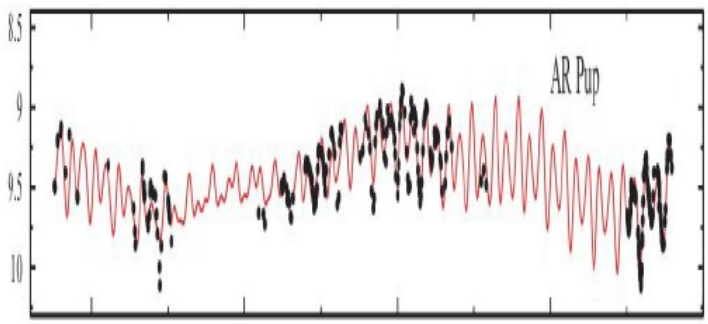

Figure 1.4: V band light curve of the RVb star AR Pup showing conspicuous variation of mean magnitude from Kiss et al. (2007)

W Virginis variables and some SRDs. Thus RV Tau stars are thought to be post-AGB objects evolving off the AGB after mass-loss has reduced the envelope mass to such an extent that the thermal flashes in the Helium-burning region cannot be sustained and they later end up as central stars of planetary nebulae.

1.1 CHARACTERISTICS OF RV TAURI VARIABLES

Photometric classification:

In the General Catalogue of Variable Stars (Kukarkin et al. 1958), RV Tauri stars were classified into two categories based on the appearance of their light curves.

RVa: These exhibit a constant mean magnitude. e.g. UY CMa (see Figure 1.3).

RVb: These have a variable mean magnitude and possess an additional long-term variation (600-1200 days) superimposed on the short-term pulsational variations. e.g. AR Pup (see Figure 1.4).

Spectroscopic classification:

The RV Tauri stars were divided into three spectroscopic classes by Preston et al. (1963).

RVA: These have spectral type G-K and TiO bands of abnormal strength are seen at light minimum. e.g. R Sge.

RVB: These have spectral type F and are weak-lined objects. Strong CN and CH bands are seen at light minimum. e.g. AR Pup

RVC: These are metal-poor objects commonly seen in globular clusters. The CN and CH bands are either very weak or absent at all phases. e.g. V453 Oph, V1 in ω Cen.

From the positions of the RV Tauri stars in the color-magnitude diagram (see Figure 1.5) it is clear that these are in the post-AGB phase of evolution.

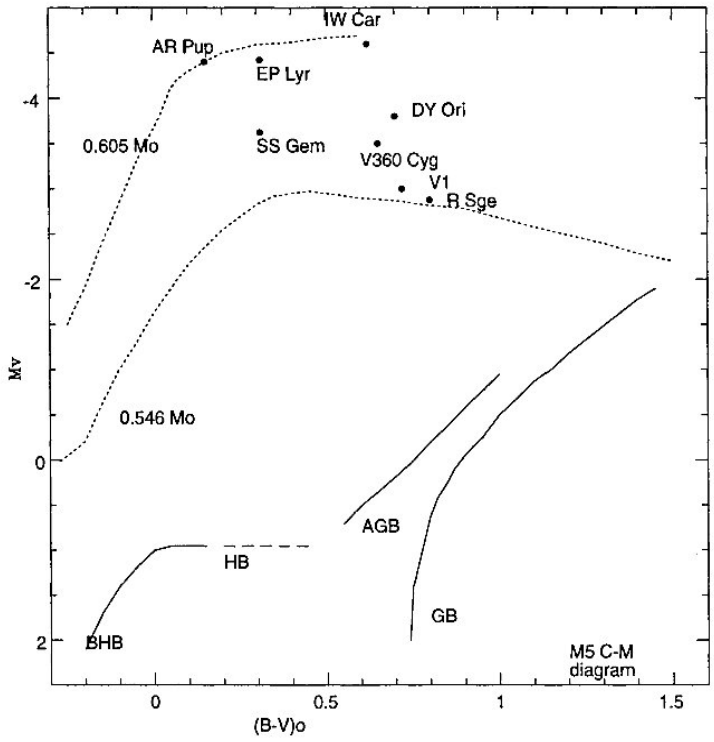

Figure 1.5: The C-M diagram for the globular cluster M5 (Buonanno et al. 1981) and positions of well known RV Tau stars as well as the evolutionary tracks for $0.605M_{\odot}$ and $0.546M_{\odot}$ post-AGB models by Schönberner (1993) are shown. The values of M_V for the RV Tauri stars were calculated by Gonzalez using the P-L relation for RV Tau stars described in Gonzalez (1994). The color excesses needed for calculating $(B-V)_O$ are taken from a number of sources that are listed in Gonzalez et al. (1997a). This figure has been taken from Giridhar (2000)

1.2 ALTERNATING BEHAVIOUR IN THE LIGHT CURVE OF RV TAURI STARS

Several theories were put forward to explain the alternating behaviour in the light curve of RV Tauri stars. Deupree & Hodson (1976) suggested that a coupling between the radial oscillations and the large amplitude convective motions can cause the observed alternation.

Aikawa & Bruegman (1987) came up with a theory of sub-harmonic resonance between the pulsation driving mode and a strongly damped mode of smaller frequency. This sub-harmonic resonance was thought to occur between the third overtone (driving mode) and the first overtone (strongly damped mode). Buchler & Kovács (1987); Kovács & Buchler (1988); Kolláth (1990) through their numerical hydrodynamical studies of W

Vir and RV Tau models found that from the steady regular pulsations they exhibit a series of period-doubling bifurcations and then to chaos as the effective temperature was decreased.

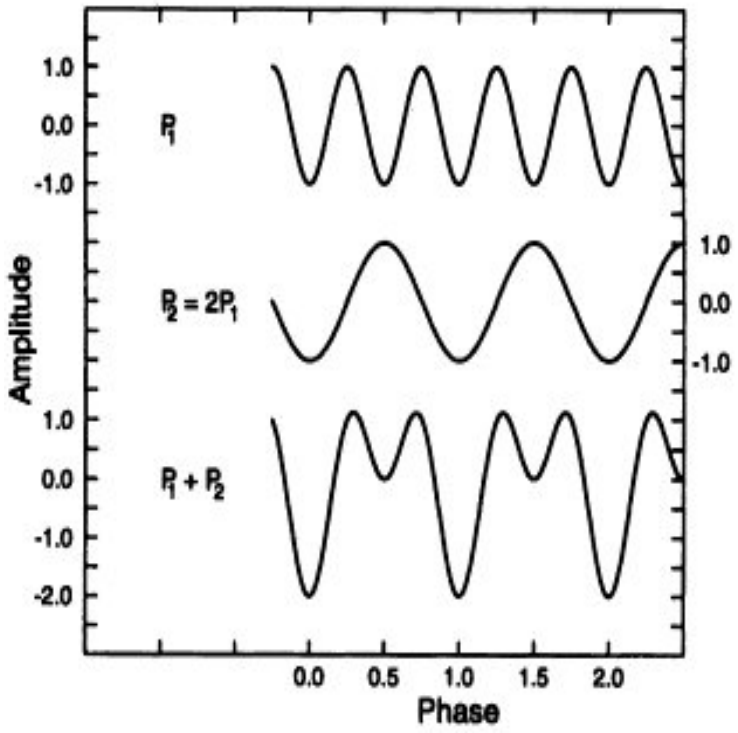

Figure 1.6: The form of characteristic RV Tauri light curve can be reproduced if P_2=2P_1 and the two modes of pulsation have a specific phase relationship from Pollard et al. (1996)

The resonance hypothesis (Takeuti & Petersen 1983) suggests that a 2:1 resonance exists between the fundamental mode and the first overtone. Evidence to support the resonance hypothesis was provided by Tuchman et al. (1993) through the linear non-adiabatic pulsation analysis of low-mass (0.5-0.8 $M_\odot$), high luminosity (10^3<$L/L_\odot$<10^4) models. This was also confirmed by Fokin (1994) through the theoretical studies of non-linear pulsations of luminous, low-mass (0.6$M_\odot$) RV Tauri models. These models were found to reproduce the observed periods and temperatures of the RV Tauri stars. Later Pollard et al. (1996) proposed that the alternating pattern in the light curve of RV Tauri stars can be reproduced by the addition of two sinusoidally varying functions as shown in Figure 1.6. This would correspond to simultaneous excitation of two pulsation modes in the star. If one mode has a period (P_2) almost twice than that of the other (P_1), then a simple resonance between these modes will result in the alternating deep and shallow

minima.

Insight gained through the multi-wavelength observations of RV Tauri stars:

While visual light curves of RV Tauri stars show characteristic deep and shallow minima; IR light curves of many RV Tauris observed by Gehrz (1971) show highly symmetrical light curves with both minima of equal depths. Gehrz suggested that it could be caused by non-radial oscillations, alternating between oblate and prolate spheroid at successive light minima.

The simultaneous optical-IR photometry had been conducted by Goldsmith et al. (1987) over a wavelength region 0.36 to 10 micron for a sample of RV Tauri stars. For those members exhibiting IR excess, by modelling the observed fluxes the optical depth of the circumstellar shell(s) could be calculated. By assuming an absorption law consistent with the chosen grains the circumstellar reddening and hence inner radius of the dust shell had been estimated. In the event of current mass loss the inner shell radii were equal to the condensation radius. In certain cases a large inner shell radius and/or evidence of two discrete shells suggesting a sporadic mass loss was obtained.

Multi-wavelength observations of RV Tauri stars have been conducted for AC Her (Shenton et al. 1992), R Sct (Shenton et al. 1994c), U Mon (Shenton et al. 1994b) and SX Cen (Shenton et al. 1994a) to determine not only the physical parameters of the dust shells(s), but also for understanding the observed light (visual and IR) and radial velocity curves in the framework of non-radial oscillations. They have deduced the time dependence of semi-major and semi-minor axes and effective temperature of star as it pulsates. The distinct signature of non-radial pulsations were obtained for AC Her, R Sct, U Mon while SX Cen exhibits radial pulsations.

AC Her:

IUE Spectrum shows Mg II h and k features at 2802 and 2795Å which almost close to secondary maximum (ϕ=0.75) appear like centrally reversed emission cores where red wings are absent. Such profiles are attributed to an outstreaming decelerating shock. These shocks have been postulated for RV Tauris for a long time. These Mg II emissions are absent at the phase ϕ=0.28 (close to primary maximum) which is surprising. However the model for stellar variations proposed by Shenton et al. (1992) requires the rapid expansion of the star at secondary minimum as a natural consequence of it undergoing strong non-radial oscillations; the expansion at primary minima is much more modest. It is therefore possible that, as a result of rapid expansion of the star during secondary maxima, a shock may always arise at this time however the situation at primary maxima is marginal, in that shock does not arise at all pulsations. The absorption components in the

Mg II h and k lines were found to comprise of three distinct systems: a) a system which was at rest relative to the star, b) a system implying an infall of 40 km s^{-1} relative to the star and c) a highly red-shifted component. The stationary component a) was speculated to be associated with the circumstellar environment and the other two components b) and c) were thought to represent infall of material blown out following the shocks associated with the primary and secondary minima.

The fitting of IR spectrum of AC Her required two shells; an inner shell comprised of SiC core/SiC mantle grains with an outer conducting grain shell thought to be the fossil of the AGB remnant.

U Mon:

The Mg II h and k features in U Mon comprised of a very broad photospheric absorption with centrally reversed emission cores. Unlike AC Her, the Mg II features were found to appear in emission at all phases which is in distinct contrast to that seen in pulsating stars displaying shock excited emission which is strongly correlated with the pulsational phase (Gillet et al. 1989). Thus the emission was thought to be arising in a permanent chromosphere.

The IUE observations further revealed the presence of three distinct components with velocities 0, -140 and -240 kms^{-1} respectively in the stellar reference frame. The blue shifted components arise in the stellar wind while the component at rest arises in circumstellar shell. The IR spectrum of U Mon is quite similar to AC Her with a strong broad emission feature at 10 micron indicating the presence of silicates in U Mon's circumstellar dust shell. The flux at 18 micron was found to be dominated by a smooth featureless dust continuum from a cool conducting grain shell. Similar to AC Her, U Mon comprises of warm inner shell rich in silicates and a cool outer shell composed of conducting grains. UV-IR data were not found to be consistent with binary interpretation of U Mon and the long term behaviour in the light curve was thought to be caused by some R CrB like ejection.

R Sct:

Although this object is similar to U Mon in spectral type and gravity (although a bit cooler) and changes in angular diameter with phase suggest non-radial pulsations but here Mg II h and K emission is associated with the shocks rather than chromospheric activities. The strongest emission occurs near deep minimum and weaker near shallow minima. The Mg II features have centrally reversed h and k lines with no emission in the red wing similar to AC Her attributed to outstreaming decelerating shock. The IR

spectrum shows that it has a warm inner shell of silicate grains and outer cool shell made of conducting material. The change in UV spectrum over the pulsation cycle is caused by variable circumstellar extinction in the form of Rayleigh scattering due to small grains.

SX Cen:

Although this star is similar to AC Her (RVB) the pulsational behaviour and the variation of atmospheric radius of SX Cen is totally different. By fitting the relevant Kurucz stellar atmospheric model to optical IR photometry and optical & UV spectroscopy, it is deduced that the star undergoes approximately sinusoidal variations in angular radius representing pure radial pulsations. The IR spectrum does not exhibit emission features of silicates as seen in other RV Tauris like AC Her. IR spectrum can be modelled with a dust atmosphere composed of some form of conducting material only: there are no emission features of silicate and SiC components. SX Cen appear to be less evolved than AC Her (from its position in the IRAS two-color diagram and the absence of period-doubling bifurcations in SX Cen) as it has not experienced onset of secondary mass-loss phase rich in silicates and SiC.
It is obvious that RV Tau objects are a mixed bag. However these multiwavelength observations allow a good comparison with theoretical predictions on the light curve modelling and post-AGB evolution.

1.3 PULSATING STARS AND THE INSTABILITY STRIP

Pulsating stars are the ones that undergo significant variations in their brightness. The star periodically swells and shrinks. The first pulsating star to be discovered was Omicron Ceti (Mira) in the 16^{th} century by David Fabricius. Miras are long period variables and are red supergiants with periods between 100-1000 days. They also have a large variability amplitude (upto the 10^{th} magnitude). About 200 years later, the star delta Cephei (prototype of classical Cepheids) was discovered to be variable by John Goodriche. In the early 1900's, Henrietta Leavitt discovered the Period-Luminosity (P-L) relation for the SMC (Small Magellanic Cloud) Cepheids. She found that Cepheids obey a well defined P-L relation and hence can be used as standard candles to determine distances to galaxies. In 1929 Hubble and Humason formulated the Hubble's law by combining Cepheid distances to several galaxies along with the speeds which they recede from us they discovered that the universe is expanding.

Cepheids populate the bright end of a zone in the H-R diagram known as the instability strip. The instability strip is a locus that covers a fairly small range of temperature, and

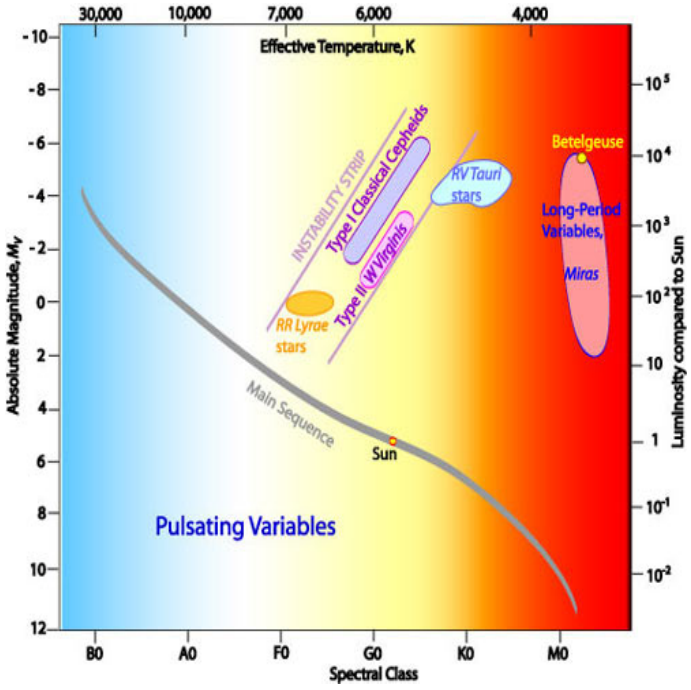

Figure 1.7: H-R diagram showing the Instability Strip. Courtesy:http://outreach.atnf.csiro. au/education/senior/astrophysics/variable_pulsating.html

the full range of luminosity from Supergiants to White Dwarfs. Figure 1.7 shows the instability strip with the location of RV Tauri variables and other pulsating stars in the H-R diagram.

By the 1920's, detailed observations of the periodic variation in magnitude, surface temperature, radius and radial velocity demonstrated that the variability of Cepheids must be due to their physical pulsation. The fact that a range in stellar types exhibit strong pulsation in one region of the H-R diagram (the instability strip) points out that there should be one underlying physical mechanism responsible for the pulsation.

1.3.1 THEORY OF STELLAR PULSATIONS

What causes the star to pulsate ? Sir Arthur Eddington in the 1920's and 30's came up with a theory to explain the pulsations. Eddington's key insight was to treat pulsation as a thermodynamic problem. In essence, to treat the star as a heat engine. This is called the Linear Adiabatic Theory of Stellar Pulsations and assumes that the pulsations are in the form of standing waves and also there is no transfer of energy between the parts of the star. With this the Period-Density relation was derived according to which the period of

pulsation is the largest when the mean density is the least. Thus the densest stars (White Dwarfs) have the shortest periods and the least dense stars like the supergiants have the longest periods. In order to drive pulsation modes in the envelope of a star, there must be a layer in which the opacity increases under compression. Normally, this does not hold in stellar envelopes. According to the Kramer's law of opacity:

$$\kappa \propto \rho/T^{3.5} \tag{1.1}$$

the opacity should actually decrease under compression as the temperature increases.

Later work by number of theorists like Zhevakin, Cox, Christy and others came up with the solution. The layers in a stellar envelope where hydrogen and helium change ionization states (partially ionized zones) can have the required thermodynamic behaviour of increasing opacity with increasing pressure. This is because compression of gas in these layers increases the relative ionization of the gas, rather than increasing the temperature. And decompression decreases the ionization thus releasing the heat and keeping the temperature stable. A partial ionization zone (PIZ) is a layer in which a phase transition is taking place in the stellar interior. The Hydrogen-PIZ occurs at a temperature of about 10,000K and the Helium-PIZ at about 40,000K. These layers occur in the interiors of all stars cooler than O spectral types and yet pulsation is a rare process, occurring in a fairly narrow band of stellar effective temperatures. Why? In stars hotter than 7500K, these PIZs occur close enough to the surface that the κ mechanism is unable to drive a sufficient amount of mass for significant pulsation to occur. In stars cooler than 5000K, the convective layer is sufficiently deep that it seems to disrupt the driving mechanisms for pulsation.

Detailed theoretical modelling indicated that Helium-PIZ is the dominant one for driving the stellar pulsation as it occurs much deeper and at higher densities in the stellar envelope than the Hydrogen-PIZ. Thus partial ionization of Helium is responsible for driving the pulsations in Cepheids. When the star contracts, the density and temperature of the He II layer increases and it ionizes to He III. The opacity increases and the energy flux from the interior of the star is effectively absorbed. The temperature of the layer increases and starts to expand. After expansion, the density and temperature decreases and the He III recombines to form He II. The outer layers contract and the cycle starts from the beginning. The restriction of Cepheid pulsations to stars in a limited temperature range follows from the requirement that the second Helium ionization zone lies near the transition from the nearly adiabatic interior where any driving is almost cancelled by an equal amount of damping to the non-adiabatic exterior where the thin outer layers lack

the heat capacity to modulate the outward flow of radiation. Thus pulsation is a property of the stellar envelope and is independent of the nuclear generating core.

1.4 STELLAR EVOLUTION AFTER THE MAIN-SEQUENCE

Once the hydrogen is exhausted in the core the star leaves the main-sequence. The helium rich core contracts and the hydrogen fusion starts in a shell surrounding the core, simultaneously the outer layers expand and becomes convective due to an increase in the opacity. The luminosity increases, surface temperature decreases and the star becomes a red giant for the first time.

During it's ascent on the Red Giant Branch (RGB), the convective envelope moves inward mixing the outer layers with the internal matter that has experienced partial hydrogen burning. This mixing event is called the FDU. The material processed by the CNO cycle of hydrogen fusion is carried to the star's surface. The result is increase in ^{4}He by 5%, ^{14}N by 30% and decrease in ^{12}C by 20%. During the ascent on the RGB, the He core continues to contract and becomes electron degenerate. The RGB life time terminates when the central temperature reaches 100 million degrees Kelvin which is sufficient to ignite He in the core. Now the 3-α reactions take place resulting in violent He ignition-core He flash. After the main He flash the He burning luminosity oscillates before settling to the quiescent core-He burning.

Following the core He flash the star moves to the Horizontal Branch (HB) where it burns He in a convective core and H in a shell which provides most of the luminosity. He burning in the core increases the fraction of ^{12}C and ^{16}O as can be seen in Figure 1.8. But in the case of more massive stars the He core remains non-degenerate and He burns quiescently without undergoing the core He shell flash as seen in Figure 1.9. The extent of blue loops seen in Figure 1.9 mainly arises due to the competition between the central helium burning and the hydrogen shell burning. It is during this blue-ward excursion across the HR-diagram that the star may cross the instability strip and is observed as a Cepheid variable. Following core helium exhaustion the strong expansion caused by the structural re-adjustment to helium-shell burning causes the hydrogen-shell to be extinguished as the star begins the ascent of the Asymptotic Giant Branch (AGB). It is during this ascent from the HB to the AGB that the products of hydrogen shell burning are dredged up to the surface by the convective envelope called the Second Dredge-Up (SDU). The results of SDU are very similar to FDU but are observed to be efficient only in massive stars with M>4.5M$_{\odot}$.

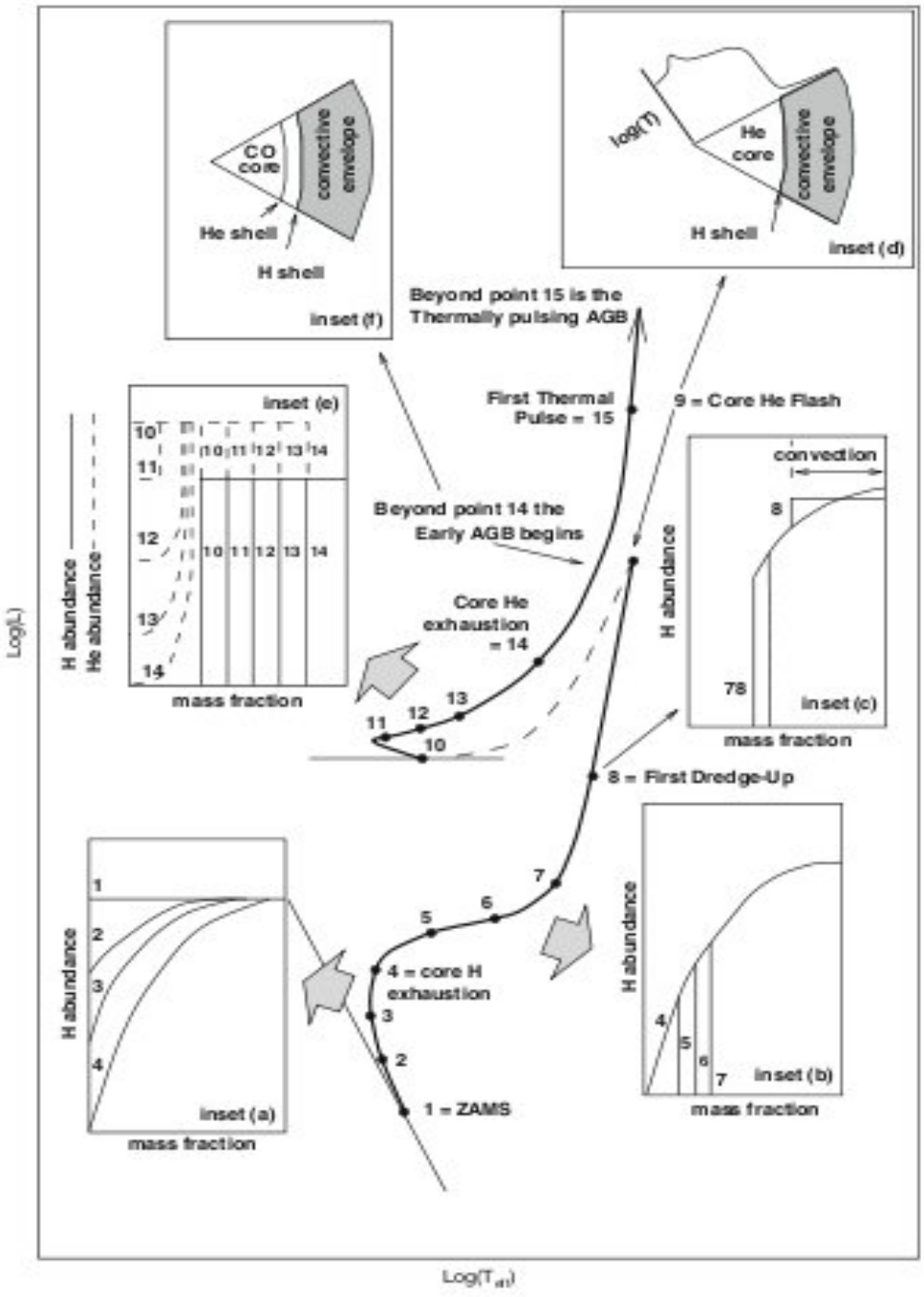

Figure 1.8: Evolution of a $1M_{\odot}$ star in the H-R diagram from Lattanzio & Boothroyd (1997)

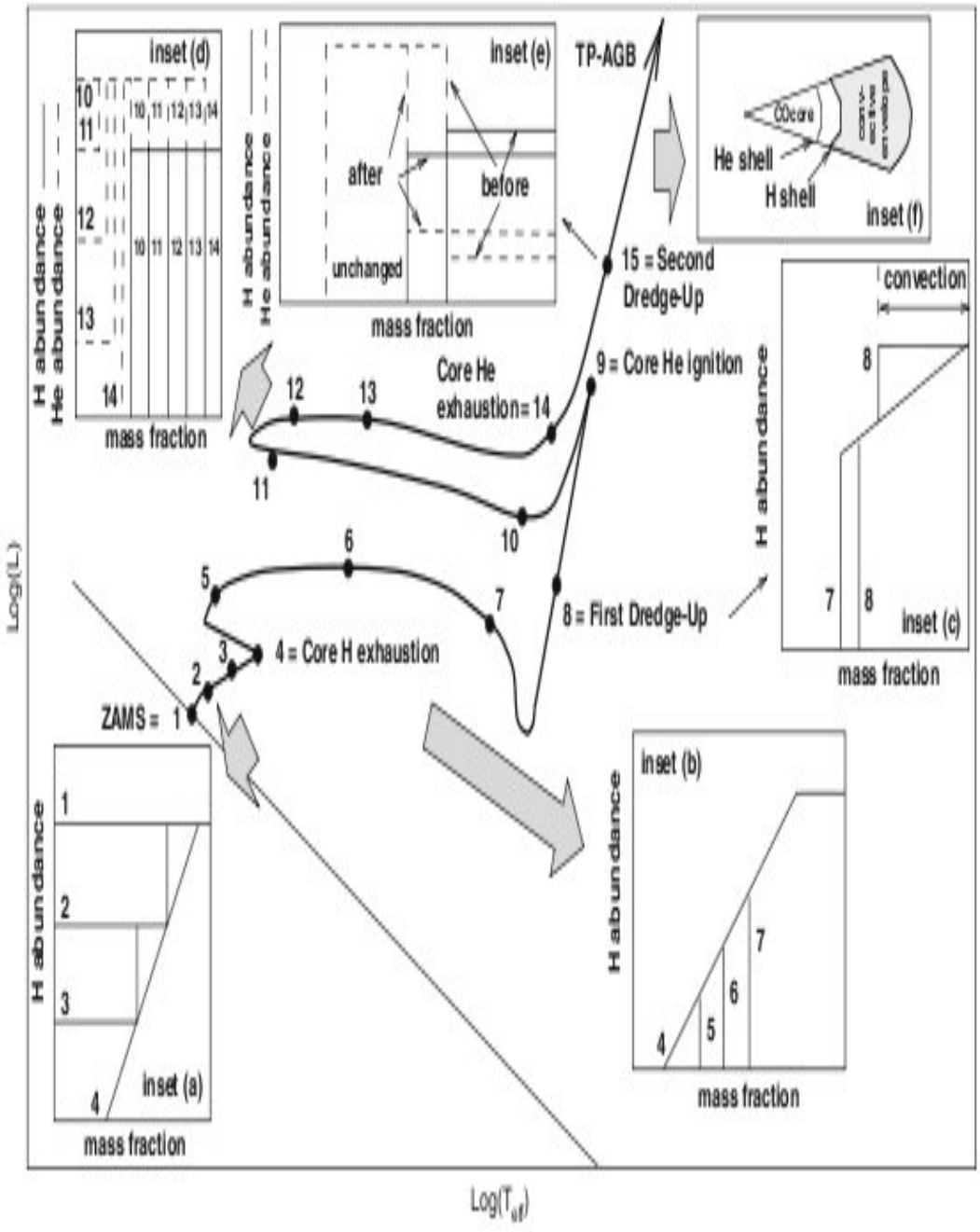

Figure 1.9: Evolution of a $5M_{\odot}$ star in the H-R diagram from Lattanzio & Boothroyd (1997)

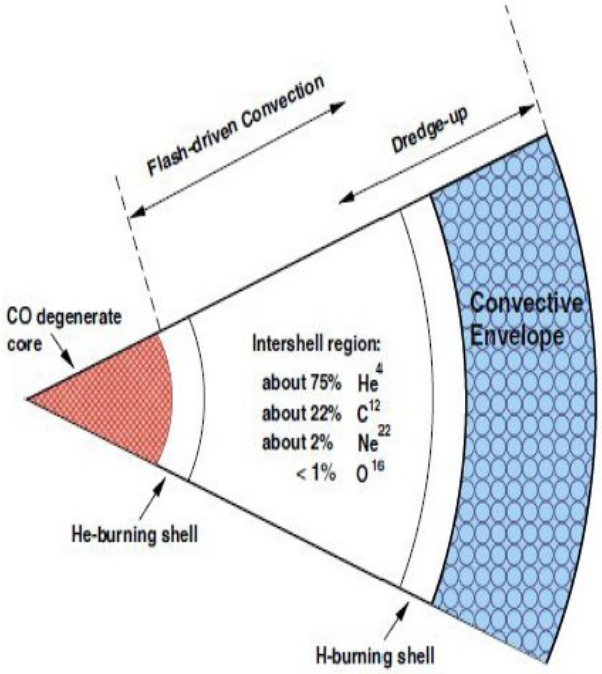

Figure 1.10: Structure of an AGB star. Figure from Karakas (2010)

1.5 AGB PHASE:

Once the star is in the AGB phase it comprises of a degenerate CO core, He fusing shell, H fusing shell and a H-rich convective envelope. Figure 1.10 shows the schematic structure of an AGB star.

The AGB is divided into two regimes: Early AGB phase (E-AGB): During this E-AGB phase which takes about 90% of the total AGB life-span, the AGB star burns He quiescently in a narrow shell surrounding the electron degenerate CO core.

Thermally Pulsing AGB phase (TP-AGB): When the helium burning is extinct, the energy production is taken over by episodes of quiescent hydrogen-shell burning also known as the interpulse phase interrupted by instabilities of the helium shell. The ashes of the hydrogen-shell increase the thickness of the hydrogen depleted region until the next thermal pulse occurs. During every thermal pulse or an instability also called the on-phase, the helium shell burns with luminosities upto $10^8 L_\odot$ for a few hundred years. This energy is utilised in driving a convective zone in the helium-intershell. When the helium shell finally dies down (power-down phase), the energy from the thermal pulse causes the expansion of the whole star and the hydrogen shell is pushed to cooler regions

and extinguished. At this time the convective envelope moves inwards and dredges up the products of hydrogen and helium shell burning to the surface in a process called the TDU which occurs periodically after each thermal pulse. This mechanism is responsible for producing the s-process elements as well as converting the photosphere from oxygen-rich to carbon-rich depending on the mass and metallicity of the star. After TDU, the whole star contracts and the helium shell is re-ignited and the cycle re-iterates.

1.5.1 MASS LOSS

A typical AGB star has a radius of about 430 $R_\odot$ or 2 AU, a luminosity of approximately 10^3 $L_\odot$ and an effective temperature of around 2500K and a mass between 0.6 and 6 $M_\odot$. The small mass and the large radius results in a very low surface gravity of about 10^{-1} cms^{-2}. The small escape velocity of about 40 kms^{-1} makes it easy for the outer layers to escape if there is an efficient driving mechanism. A combination of two processes results in the efficient driving of AGB winds: pulsation and radiation pressure on dust. Pulsation in an atmosphere of low gravity results in a large scale density height which facilitates the formation of dust. The radiation pressure on the dust grains and its interaction with the gas then results in a high mass-loss rates like the ones observed in Mira and OH/IR stars. Stars that show photometric variations with periods longer than 100 days and amplitudes greater than 2.5 magnitude are called Miras. If the mass-loss rates are too high then the dusty wind obscures the star and the stellar radiation is reprocessed by the dust and the star will become an IR source. The star is then an OH/IR star as the high mass-loss gives rise to strong OH maser lines. This phase of intense mass-loss is called the super-wind phase which can result in the complete loss of the envelope. The properties of AGB stars, their winds and circumstellar envelopes have been reviewed by Habing (1996). Mass-loss rates of AGB stars can be derived from IR spectral energy distributions (SEDs), from CO emission lines and also from the OH maser emission lines. Vassiliadis & Wood (1993) have derived an empirical relation for periods less than 600 days:

$$log(dM/dt) = -11.4 + 0.0123 \times P(days) \tag{1.2}$$

where the mass-loss rate is in terms of $M_\odot yr^{-1}$. Thus mass-loss rates for AGB stars increases exponentially with P until it reaches a very high value of $10^{-4} M_\odot yr^{-1}$ for the OH/IR stars. Vassiliadis & Wood (1993) propose the following relation for stars with $M > 2.5 M_\odot$:

$$log(dM/dt) = -11.4 + 0.0123 \times P(days) - 100(M_*/M_\odot - 2.5) \tag{1.3}$$

The typical terminal velocities of the AGB winds are small and are found to be of the order of 5 to 25 kms^{-1} (Loup et al. 1993).

1.5.2 THE S-PROCESS:

Heavy elements with atomic masses greater than 56 cannot be produced normally through thermo-nuclear reactions due to their large electrostatic repulsions. These heavy nuclei are formed in AGB stars through neutron capture by the Fe-seed nuclei already present in the stars. For this reason these processes are secondary.

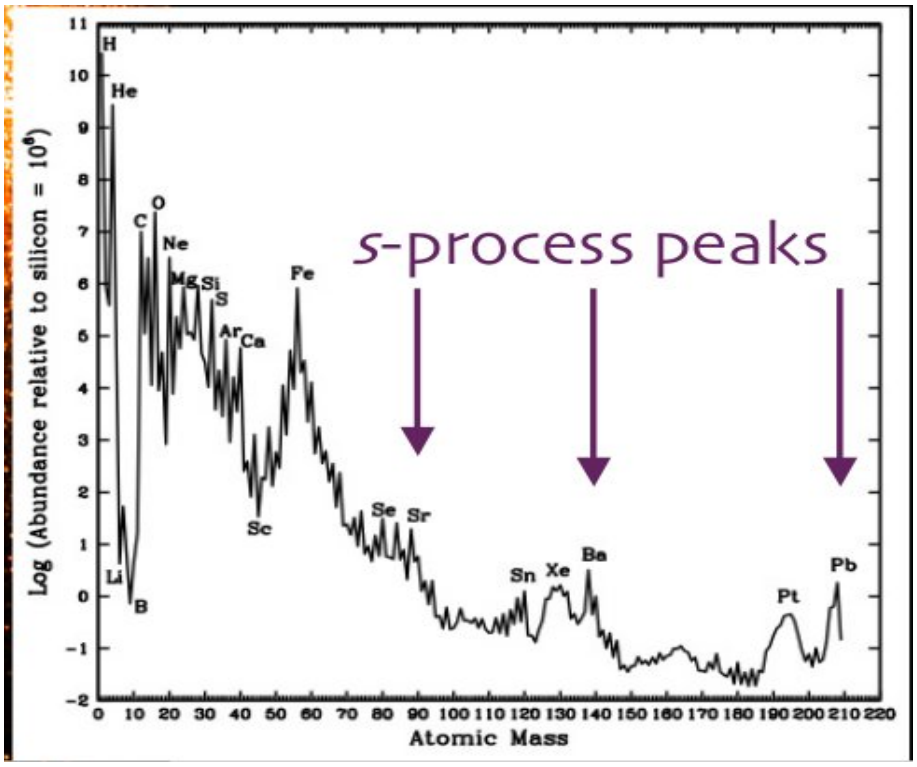

Figure 1.11: The s-process peaks. Courtesy:http://msowww.anu.edu.au/ akarakas/ Kodai _Lecture4.pdf

The s-process which is the slow neutron capture process is a nucleosynthesis process that occurs at relatively low neutron densities ($10^7/cm^3$) and intermediate temperature conditions in AGB stars. Under these conditions the rate of neutron capture by atomic nuclei is slower than the rate of radioactive β-decay. In the s-process, a stable isotope captures a neutron, but the radioactive isotope that results decays to its stable daughter before the next neutron is captured. This process produces stable isotopes by moving along the

valley of beta-decay stable isobars in the chart of isotopes. The s-process produces approximately half of the isotopes of the elements heavier than iron, and therefore plays an important role in the galactic chemical evolution. Examples of s-process elements include Sr, Y, Zr, Ba, Ce, Nd, La etc.

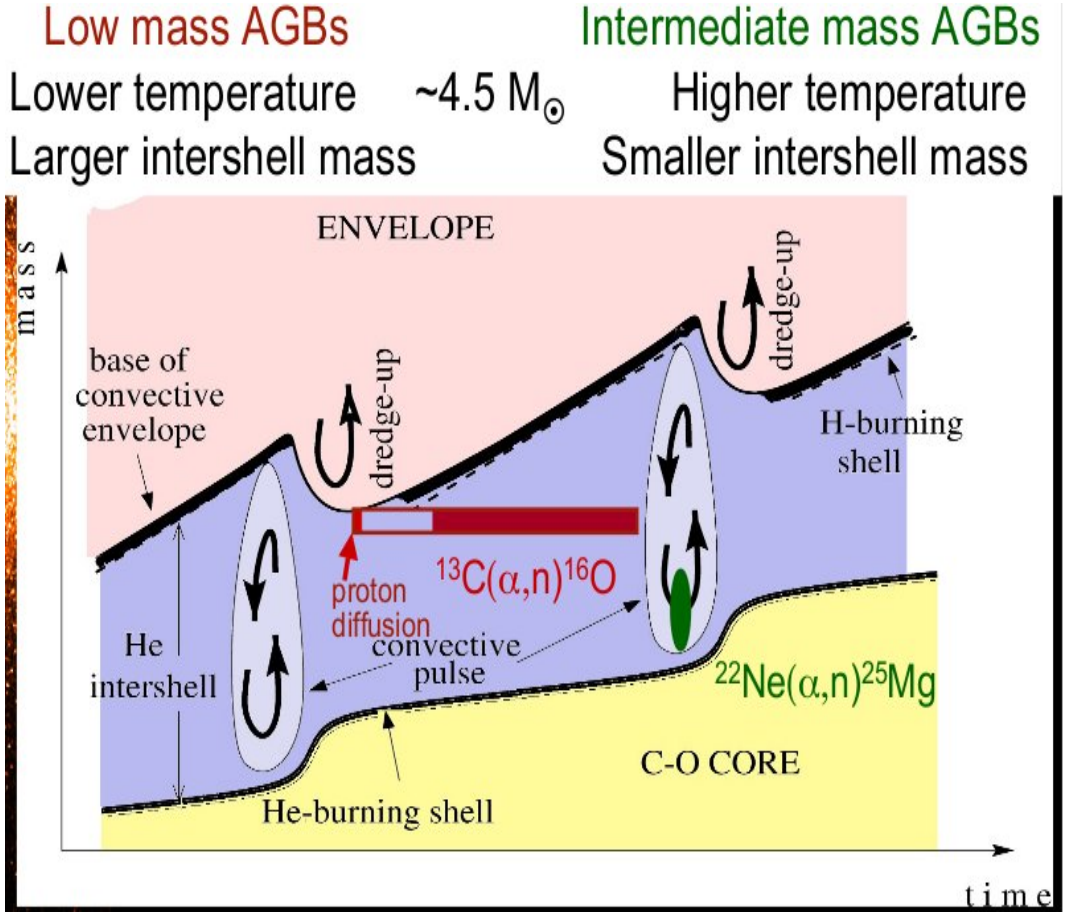

Figure 1.12: The main neutron sources in AGB stars. Courtesy:http://msowww.anu.edu.au/ akarakas/Kodai_Lecture4.pdf

Nuclei having magic number of neutrons are extremely stable against neutron capture and hence have low neutron capture cross sections. Thus they act as bottle necks and are seen as s-process peaks. For this reason nuclei having magic number of neutrons (n= 50, 82 and 126) show s-process peaks in the solar abundance distribution as can be seen in Figure 1.11. Efforts were made by Seeger et al. (1965) to explain the s-process abundance distribution in the solar system.

The neutron exposure τ is defined as the time averaged neutron flux and is given by

the equation:

$$\tau = \int n_n v_T dt \tag{1.4}$$

where n_n stands for the neutron density and v_T for the thermal velocity of the neutrons. The neutron flux is in units of mbarn^{-1}. Atleast three different distributions of exposures were necessary to account for the entire s-process abundance distribution in the solar system namely: The weak component (produced in massive AGB stars) which produces s nuclei with A≤90 from Fe to Sr and has τ of 0.06 mbarn^{-1}, main component (low mass AGB stars) which produces s nuclei with 90≤A≤204 from Sr to Pb with a τ of 0.3 mbarn^{-1} and finally the strong component (possibly produced by very metal poor low mass AGB stars) which is required to produce the Pb abundance with a τ of 7 mbarn^{-1}.

Neutron sources: Activation of the two neutron sources ^{13}C(α,n)^{16}O and ^{22}Ne(α,n) ^{25}Mg are responsible for the production of s-process elements in AGB stars (see Figure 1.12) (Smith & Lambert 1986; Busso et al. 1992; Gallino et al. 1998). The former is the dominant neutron source in low-mass (1-3$M_\odot$) AGB stars and occurs under radiative conditions at temperatures of 10^8K and neutron densities of N_n<10^7 cm^{-3} and requires the mixing of protons generated through H-shell burning in a He-burning region (Straniero et al. 1995). While the latter source operates during thermal pulses in massive stars (3-8$M_\odot$) at temperatures of 3×10^8K under convective conditions and also at much higher neutron densities (N_n>10^{10} cm^{-3}) (García-Hernández et al. 2006).

1.6 POST-AGB PHASE:

At the end of the AGB evolution, most of the outer envelope is lost and circumstellar shells are observed that are detectable at radio and IR wavelengths. When the mass of the H-rich convective envelope becomes smaller than 0.05$M_\odot$, the stellar effective temperature starts to increase and the mass loss rate decreases and the star begins its post-AGB phase as seen in Figure 1.13. Post-AGB stars are intermediate between AGB and planetary nebula. When the temperature of the central star exceeds 30,000K, this is sufficient to ionize the circumstellar material and a planetary nebula is formed. But for the stars having low mass progenitors, the longer transition times would result in the dissipation of the circumstellar envelope into the ISM and hence no planetary nebula is formed. e.g. BD+39^o 4926.

The post-AGB life time is very short 10^3 to 10^4 yrs and only about 326 very likely and 107 possible post-AGB candidates are listed in the Toruń catalogue of Galactic post-AGB and related objects. But post-AGB stars serve as excellent probes to study the AGB nucleosynthesis and mass-loss as they are optically brighter, have relatively stable

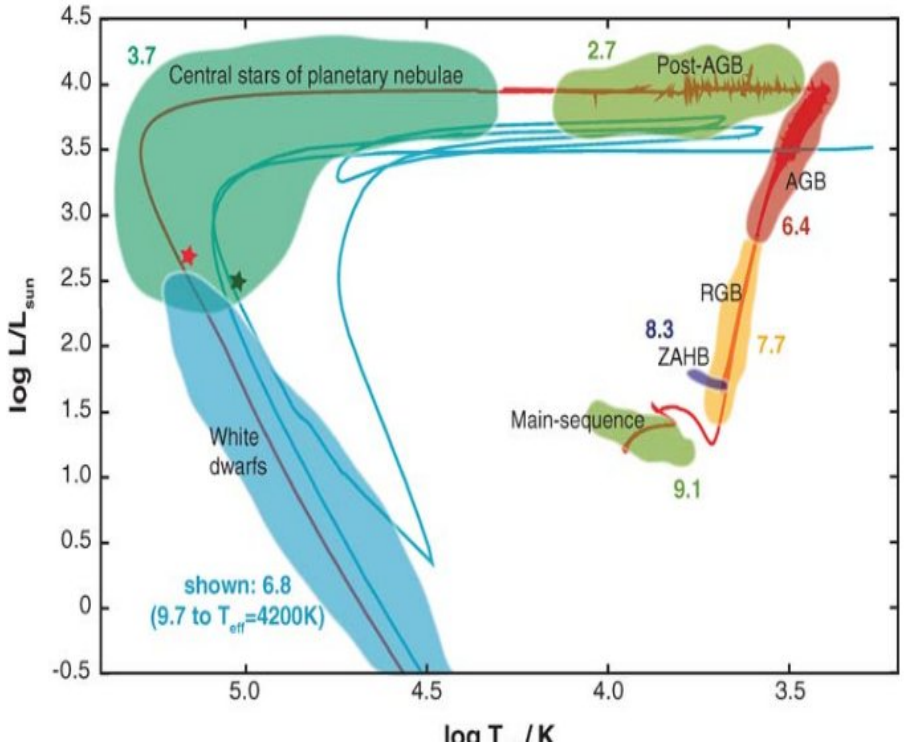

Figure 1.13: H-R diagram of a complete $2M_{\odot}$ evolution track for solar metallicity from the main-sequence to the white dwarf evolution phase. In the cooler section of the post-AGB phase wiggles in the track are caused by numerical convergence difficulties. The blue track shows a born-again evolution of the same mass. The red and green stars mark the positions of the central stars of planetary nebulae. The number labels for each evolutionary phase indicates the log of the approximate duration for a $2M_{\odot}$ case. Larger or smaller mass cases would have smaller or larger evolutionary time scales respectively by Herwig (2005)

atmospheres and being relatively warm their spectra permit comprehensive abundance analysis of a whole range of atomic species.

1.6.1 DETECTIONS OF POST-AGB STARS

Post-AGB stars have been identified based on either the properties of the central star (luminosities and the spectral type) and the properties of the circumstellar material (IR excess). Surveys such as IRAS, GLMP, ISO, Spitzer and AKARI have been very useful in detecting these objects. The Toruń catalogue of Galactic post-AGB and related objects (Szczerba et al. 2007) is also being regularly updated and the present version comprises of 326 very likely and 107 possible objects. Several classes of post-AGB objects are found

to exist.

• **IRAS sources:** Based on the IR colors and their position in the IRAS two-color diagram (van der Veen & Habing 1988; Garcia-Lario et al. 1997; Suárez et al. 2006) several objects with post-AGB and planetary nebula like colors were detected and were found to be faint at optical wavelengths.

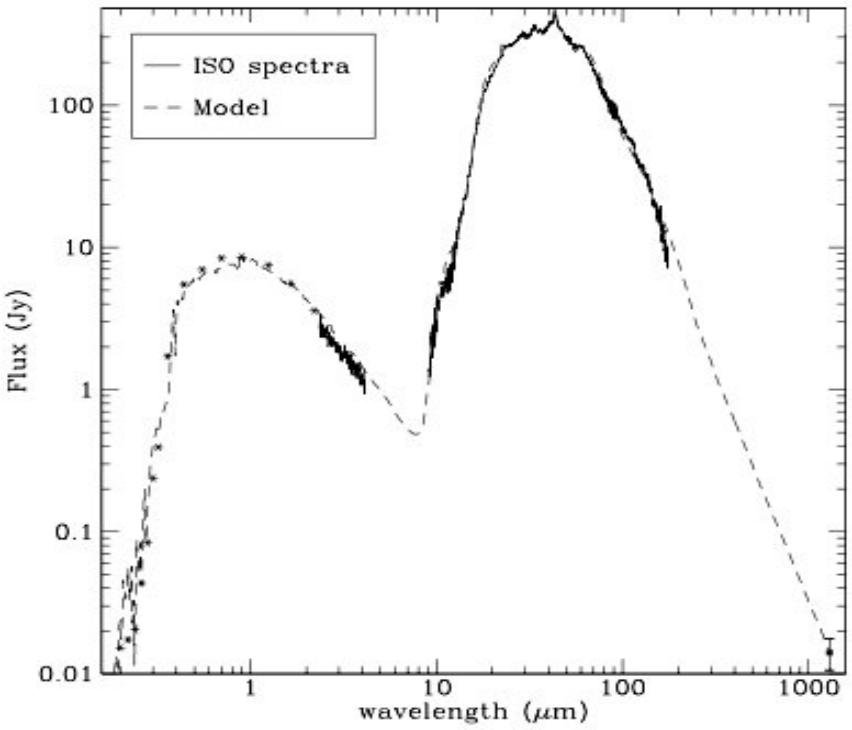

Figure 1.14: The spectral energy distribution of the optically bright post-AGB star HD 161796 from Hoogzaad et al. (2002)

• **High Galactic Latitude Supergiants:** Studies of the high galactic latitude supergiants like 89 Her, HD 161796 etc. by Luck et al. (1990) have also resulted in some detections. Many of these objects display a double-peaked SED the second peak arising due to the detached circumstellar dust shell ejected by the star when it was on the AGB as can be seen in Figure 1.14. Abundance analysis of these objects confirmed them to be population-II (metal-poor) objects with spectral types from A-F. Another small group of high galactic latitude supergiants characterised by small amplitude pulsations, high radial velocities and large IR excesses also contain a sizable fraction of post-AGB stars.

• **Hot Post-AGB objects:** These supergiants were discovered in the studies of the B-star population in the Galactic Halo (Conlon et al. 1991; McCausland et al. 1992). These

objects were found to be metal-poor and also underabundant in carbon indicating that they left the AGB before or at the beginning of the TP-AGB phase. Certain UV bright objects in globular clusters like Barnard 29 in M13 (Conlon et al. 1994) and also No. 1412 in M4 (Brown et al. 1990) also display chemical patterns similar to the halo B stars.

• **RV Tauri and Type-II Cepheids:** These variable stars also contain a noticeable fraction of post-AGB stars (Giridhar et al. 1994; Gonzalez & Wallerstein 1996; Maas et al. 2005; Giridhar et al. 2005; Maas et al. 2007). It is a consequence of the post-AGB evolutionary tracks intersecting the high luminosity end of the population II instability strip. The above detections were made on samples containing optically bright post-AGB stars and hence there is an observational bias towards the stars belonging to low mass progenitors. More recently color selected and flux selected samples have led to the detection of rapidly evolving heavily obscured post-AGB stars. These have central stars of spectral type B and possess circumstellar shells which are detectable in CO or OH at submillimeter/radio wavelengths. Most of these sources are found to be O-rich which may be attributed to Hot Bottom Burning (HBB). These objects included in the GLMP catalogue (Garcia-Lario 1992) do not show preference to F and G spectral type and high galactic latitude but have flatter distribution in spectral type and follow galactic distribution which corresponds to more massive population as can be seen in Figure 1.15 (García-Lario 2006).

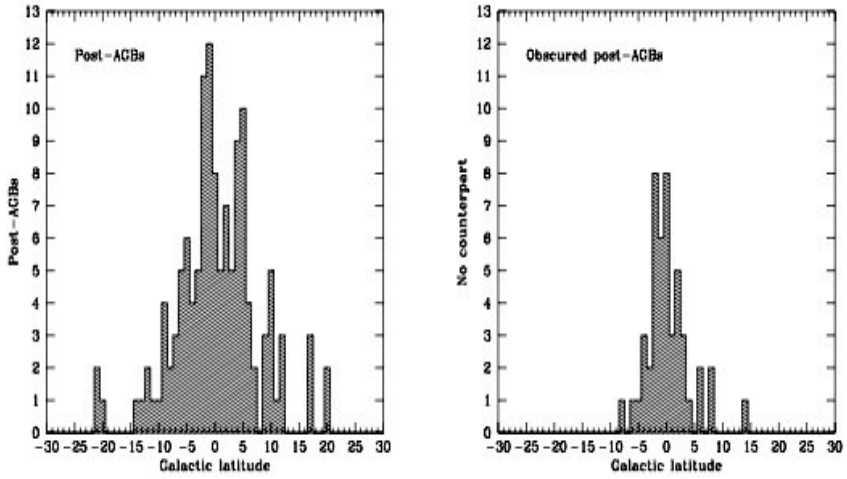

Figure 1.15: Galactic latitude distribution of optically bright post-AGB stars (left) and of the new population of obscured post-AGB stars (right). Note the narrower distribution shown by the obscured sample which suggests a higher mass population from Suárez et al. (2006).

1.6.2 MASS RANGES IN POST-AGB STARS

The AGB evolution is strongly affected by the mass and metallicity of the progenitors. From detailed AGB evolutionary model calculations Herwig (2005) suggested the following:

a) Low-mass stars (M<1.8$M_{\odot}$): may not undergo sufficient amount of thermal pulses at AGB and hence subsequent dredge-ups and remain O-rich (C/O<1). A large fraction of observed post-AGB stars are found to be O-rich.

b) Intermediate-mass stars (2-4$M_{\odot}$): would experience TDU where the products of helium-burning as well as s-process elements are transported to the outer envelope and they become carbon stars with C/O>1. The classical post-AGB stars like HD 56126 confirming these predictions are found in the thick disk of our Galaxy and they make a small fraction of the known post-AGB stars.

c) Massive stars (M>4$M_{\odot}$): In these stars the convective envelope penetrates the H-burning shell activating the process called HBB. HBB takes place when the temperatures at the base of the convective envelope is greater than 2×10^7K thereby converting all the dredged up ^{12}C to ^{13}C and ^{14}N through the CN cycle and remain O-rich. HBB models (Sackmann & Boothroyd 1992; Mazzitelli et al. 1999) predict the production of the short lived ^{7}Li isotope through the ^{7}Be Transport Mechanism (Cameron & Fowler 1971) which should be detectable at the stellar surface. The HBB activation in massive AGB stars is supported by Li overabundances in the luminous O-rich AGB stars of the Magellanic Clouds (Plez et al. 1993; Smith et al. 1995). A small group of stars showing the OH maser emission at 1612 MHz in our Galaxy has also been found to show Li abundances by García-Hernández et al. (2007).

1.7 PHOTOSPHERIC ABUNDANCE PATTERNS IN POST-AGB STARS:

Post-AGB stars represent a crucial phase in the evolution of low and intermediate mass stars (0.8-8$M_{\odot}$) where rapid change in the surface composition of the star and its circumstellar envelope takes place. The chemical composition of post-AGB stars exhibit larger diversity than the evolutionary predictions made for different mass ranges and at different metallicities.

1.7.1 DEPLETION:

The elemental abundances in the ultra-metal poor stars are thought to represent yields of the most metal-poor supernovae and therefore observationally constrain the earliest stages of chemical evolution in the universe. The most metal-poor galactic stars should reveal the earliest episodes of stellar nucleosynthesis in our galaxy. Earlier the most metal-poor stars known were the post-AGB stars HR 4049 and HD 52961 with [Fe/H]~-4.8 (Waelkens et al. 1991). These metal-poor post-AGB stars were found to exhibit chemical peculiarities not caused by stellar nucleosynthesis but instead showed under-abundances of elements having higher condensation temperatures like Fe, Ca, Ti, Sc, Al and also the s-process elements but showed almost normal abundances for elements with lower condensation temperatures like C, N, O, S, Zn etc. Their abundance patterns had a strong dependence on the predicted condensation temperatures for low pressure gas of

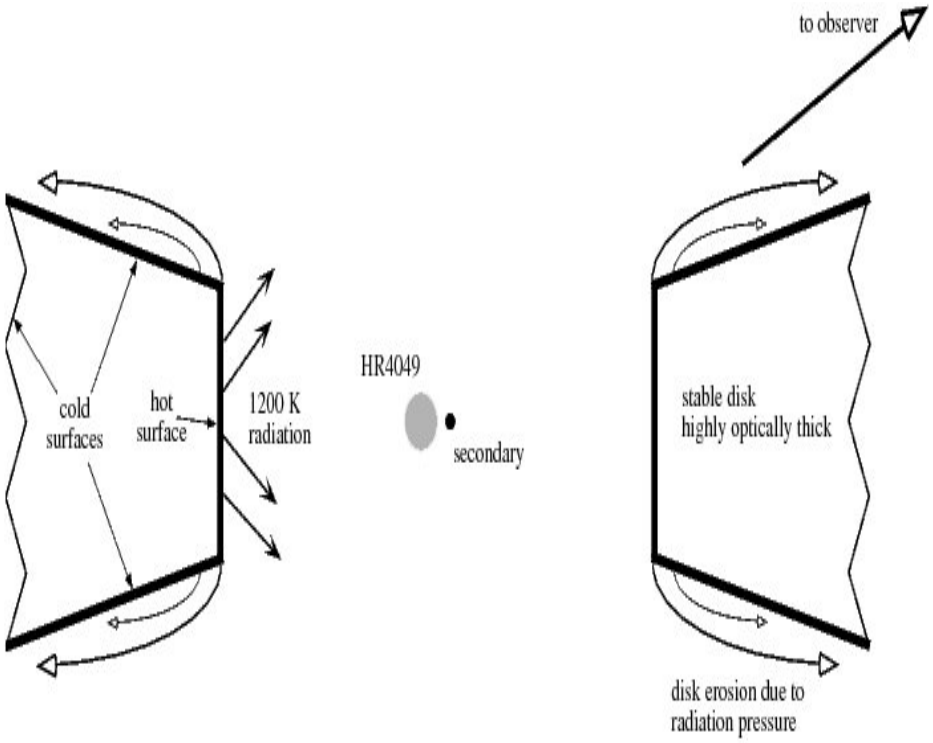

Figure 1.16: Sketch of the disk geometry around HR 4049. The double star is at the center of the disk. The inner surface of the disk is heated by the star and produces the blackbody radiation. The material behind the inner surface is shielded and cold, including the top, bottom and rear surfaces. The height of the disk is set by strong radiation forces which blow away the upper parts of the disk. The direction to the observer is such that we look through the edge of the disk from (Dominik et al. 2003).

solar composition thereby sharing a resemblance with the gas phase of the ISM. These stars were affected by a process known as depletion or dust-gas winnowing. Thus these metal-poor post-AGB stars were found to be irrelevant to study early stellar nucleosynthesis. Later ultra metal-poor stars were discovered which had -4.8<[Fe/H]<-5.3 (Christlieb et al. 2002; Frebel et al. 2005; Norris et al. 2007). Venn & Lambert (2008) found that there are actually similarities between the abundance ratios of the ultra-metal poor stars and the chemically peculiar stars like the post-AGBs, RV Taus and the Lambda-Bootis stars. Some of the abundance ratios of the ultra metal-poor stars were found to be uncharacteristic of metal-poor stars of higher Fe abundance. These stars were found to be C, N and O rich for their Fe abundance, a property shared with the most metal-poor post-AGB stars like HR 4049 and HD 52961. Thus Venn & Lambert (2008) concluded that ultra metal-poor stars are also chemically peculiar like HR 4049 and HD 52961 and are not truly metal-poor stars and thus may not be related to the first stars. They also stress upon finding an explanation in terms of stellar nucleosynthesis and the chemical evolution of the young Galaxy.

Extreme depletion patterns have also been observed for BD+39^{o}4926, HD 44179 (Kodaira et al. 1970; Van Winckel 1995) followed by several others (see Van Winckel (2003)). A similar effect for RV Tau star IW Car was reported by Giridhar et al. (1994) and was later seen in many RV Tau stars (Maas et al. 2005; Giridhar & Arellano Ferro 2005). More recently strong signature of dust-gas winnowing has been observed for the galactic binary post-AGB star: IRAS 11472-0800 ([Fe/H]=−2.7 and [Sc/H]=−4.2) with a pulsational period of 31 days very similar to that of population II Cepheids by Van Winckel et al. (2012). The depletion phenomenon has also been observed for the LMC (Large Megallanic Cloud) RV Tau variables (Reyniers & Van Winckel 2007; Gielen et al. 2009b). The explanation of the depletion phenomenon based upon the existence of circumbinary disk is gaining acceptance with increasing number of detected binaries among post-AGB and RV Tau stars (Van Winckel 2007). Figure 1.16 shows a geometry of the dusty disk around the heavily depleted post-AGB star HR 4049 (Dominik et al. 2003).

Observational evidence for stable circumbinary disks for a large number of post-AGB binary stars has been reported by De Ruyter et al. (2006), Van Winckel (2007) through their modelling of broad band SED characteristics of these objects. They found a dust excess starting near the sublimation temperature irrespective of the temperature of the central star. For this geometry to sustain at least part of the dust must be gravitationally bound since any typical AGB outflow velocity would bring the dust to cooler regions within years. Deroo et al. (2006); Deroo (2007) report very compact disks (radii about 50

AU in the N band) from the VLTI/MIDI interferometric studies of these objects. However, not all post-AGB binaries show this effect; notable exception is 89 Her which does not show depletion phenomenon despite being a member of the close binary system. BD $+39^{o}4926$ on the other hand is a member of the binary, known to be a depleted object but has no detected dust emission. A similar metal-poor, high galactic latitude star HD 105262 (without IRAS detection) studied recently by Giridhar et al. (2010) shows depletion phenomenon but also shows severe carbon deficiency. Hence a satisfactory set of boundary conditions to explain the above mentioned effect is yet to be evolved.

1.7.2 S-PROCESS ENRICHMENT:

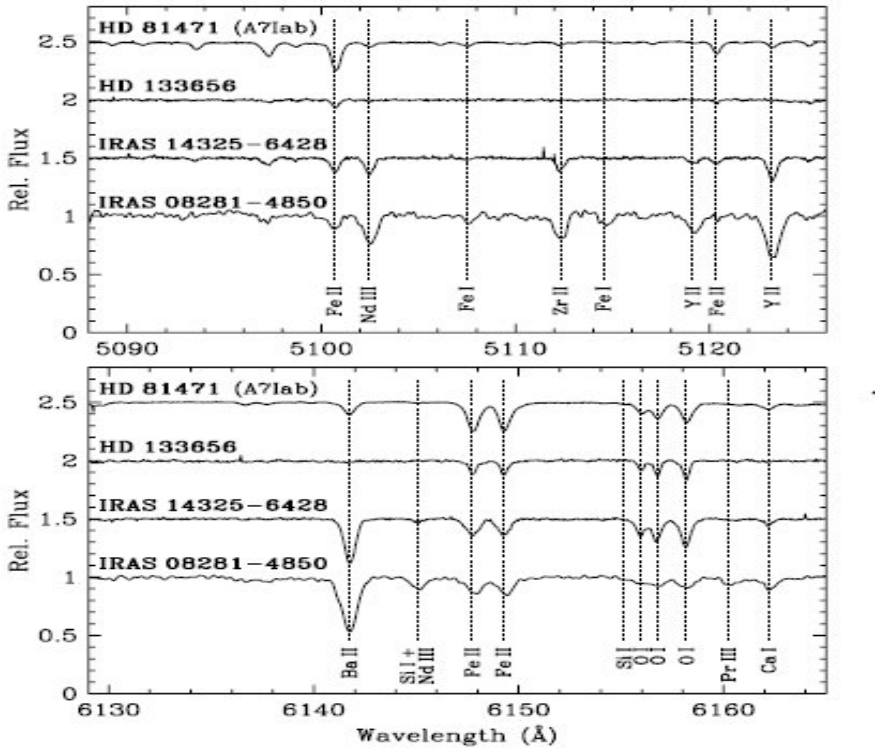

Figure 1.17: Comparison between the spectra of the s-process enriched stars IRAS 14325-6428 and IRAS 08281-4850 with that of the A7Iab standard HD 81471 and the non-enriched post-AGB star HD 133656. Figure taken from Reyniers et al. (2007b)

A very small fraction of the known post-AGB objects show hard core post-AGB abundance pattern i.e. the C/O larger than 1 and enhancement of s-process elements. Gonzalez & Wallerstein (1994) from their studies of the UV bright stars in the globular cluster ω Centauri found mild s-process enrichment with an integrated neutron flux of 0.6 mbarn^{-1}

for two of the most luminous stars V1 and ROA 24 accompanied with CNO enhancement. It is seen that till now among the field post-AGB candidates only the 21 micron sources show abundance patterns which are in agreement with the theoretical predictions of AGB nucleosynthesis. The 21 micron emission feature observed in the IR spectra of these objects was found to be originating from C-rich circumstellar material (Kwok et al. 1989).

Strong s-process enrichment in field post-AGB stars was first discovered by Klochkova (1995) in HD 56126 and later was seen in HD 187885 by Van Winckel et al. (1996). In Figure 1.17 a comparison is made between the spectra of the strongly s-processed objects: IRAS 08281-4850 and IRAS 14325-6428 with that of the A7Iab standard HD 81471 and the non-enriched post-AGB star HD 133656. Abundance analysis of these 21 micron objects (Reddy et al. 1999; Reyniers 2002) yielded C/O ratios in excess of unity indicating that these would have descended from carbon stars. Van Winckel & Reyniers (2000) measured the ratio of the heavy s-process elements (Ba-peak) to that of the lighter s-process elements (Sr-peak) and found a correlation between the neutron production and the s-process overabundances. A higher [hs/ls] ratio was found for all these objects implying a stronger neutron irradiation. This indicated that the dredge-up may be linked with the proton engulfment in the intershell region.

Two more spectacular objects with mild s-process enrichment accompanied by strong Li enhancements, low metallicities and carbon deficiency are known to exist: HD 172481, a double lined spectroscopic binary (Reyniers & Van Winckel 2001) having a Mira companion. A luminosity of $10^4 L_\odot$ was determined for this field post-AGB binary using the P-L relation for Mira variables thereby confirming its post-AGB status. Another being the population-II Cepheid HR 7671 (Luck et al. 1990) with no detected IR excess. The chemical compositions of these objects are not well understood.

Apart from our galaxy, strong s-process enrichment has also been observed in the LMC RV Tauri star MACHO47.2496.8 (Reyniers et al. 2007a) with a C/O of 2.0. A high Pb abundance as can be seen in Figure 1.18 was also determined indicating strong neutron irradiation and dredge-up efficiency in the low metallicity environment due to the leakage from the Ba-peak to the Pb-peak. Very Recently strong s-process enhancement has also been detected in the only known 21 micron post-AGB star in the SMC, J004441.04-732136.4 with a C/O ratio of 1.9 and [s/Fe] of around +2.4 by De Smedt et al. (2012).

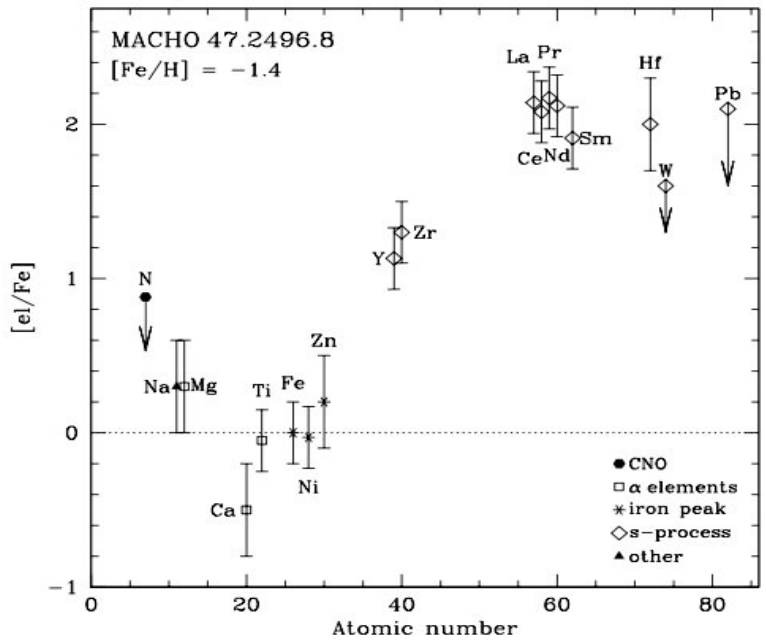

Figure 1.18: Abundances of the LMC RV Tauri variable MACHO 47.2496.8 from Reyniers et al. (2007a)

1.7.3 DUST GRAINS AND THE CIRCUMSTELLAR ENVIRONMENT

Dust grains play a crucial role in the formation and evolution history of stars and galaxies in the early universe. Dust grains absorb stellar light and reemit it as thermal radiation in the IR. Also the surface of dust grains is an efficient site for formation of H_2 molecules which act as an effective coolant at the time of formation of stars from IS clouds, enhance the star formation rate and affect the initial mass function in the metal-poor universe. Dust grains residing in IS space in the galaxies also cause obscuration and reddening of star light. How much dust grains absorb stellar light and re-emit it by thermal radiation depends on the chemical composition, size and abundance. Investigation of dust grains in the early universe is important to reveal the structure and evolution of the early universe (Nozawa et al. 2003).

In cosmic environments, dust grains form in a cooling gas outflowing from star to IS space such as in the stellar winds from AGB stars and in the ejecta of Supernovae. A major fraction of dust grains in our Galaxy are considered to be caused by AGB stars evolving from stars with initial masses $< 8\ M_{\odot}$. It has been estimated that 90% of the dust in the Galaxy today originated in the outflows of AGB stars but its percentage contribution to the early universe is not well understood (Sloan et al. 2008; Valiante et al. 2009). AGB

stars are important as they are major factories for production of elements in the universe. Knowledge of AGB evolution and nucleosynthesis is vital to obtain an estimate of the contribution of low and intermediate mass stars to the chemical evolution of galaxies. The AGB evolution is terminated through the development of strong dusty stellar winds called the super-wind phase during which a major portion of the stellar envelope is expelled to the ISM. Thus a study of post-AGB and RV Tau stars are useful in understanding the evolution driven by the dusty wind.

Most of the post-AGB objects are surrounded by circumstellar dust shells ejected by the star in its previous AGB phase. Dust grains in the circumstellar envelope absorb the radiation from the central star and re-radiate it in the IR which are observable as IR excess in the SEDs of these objects. Since the dust emission peaks in the IR, the dust features observed in the IR spectrum serve as important diagnostics of the chemical composition, size as well as the shape of the dust grains. Thus IR spectroscopy serves as an ideal tool to study the physiochemical characteristics of the circumstellar material since it samples the resonances of the most dominant dust species.

The type of grain formation mainly depends on the C/O ratio of the stellar photosphere. When the C/O<1, the photospheric gas is O-rich and the excess oxygen results in the formation of O-rich dust with broad resonances at 10 and 18 micron due to amorphous silicates. Narrower features due to crystalline silicates were also observed with the ISO at 11.3, 16.2, 19.7, 23.7, 28 and 33.6 micron (Molster et al. 1999). The KAO spectra of Frosty Leo revealed strong crystalline H_2O bands near 43 and 60 micron (Forveille et al. 1987).

A detailed study of the IR spectra and hence the spectral fitting of the various dust species in a large fraction of binary post-AGB and RV Tau stars both in our galaxy (33 sources) and LMC (24 sources) were performed by Gielen et al. (2007, 2008, 2009a,b, 2011a,b). All these sources show a broad IR excess indicating the presence of both hot (500-1300K) and cool (100-200K) dust components (van Winckel 1999; De Ruyter et al. 2006). To explain the presence of hot dust (Near IR excess) it was thought that dust must reside somewhere close to the star and the most likely geometry was postulated to be in a stable Keplarian disk. An outflow model as is the case for single stars cannot explain the near IR excess as it is expected to disappear within years after the cessation of the dusty mass-loss. Also the CO emission line measurements by Bujarrabal et al. (1988) for some of these objects showed Keplarian rotation velocities instead of outflows in the form of very narrow CO emission indicating that the gas is not freely expanding but is trapped in a stable Keplarian rotating disk. More support came from the studies of Deroo (2007)

who resolved the compact disks around several binary post-AGB and RV Tau stars and found N-band sizes of 30-50AU.

Gielen et al. have found that almost all of the stars studied by them were dominated by O-rich dust in their IR spectra (Mg-rich members of Amorphous and Crystalline Silicates). Their spectral fitting to the dust features showed that even though the dust was found to comprise of both hot and cold dust components they were found to have a similar composition indicating that the dust in the disk is well mixed. Crystallization requires high temperatures above 1000K. Thus crystalline dust must be confined to the hot inner regions of the disk. But since a homogeneous dust composition was seen throughout the disk shows that the mixing must be efficient in transporting the crystalline material to cooler regions which were initially dominated by amorphous material. Their spectral fitting also showed a high degree of crystallinity (Strong emission from Fosterite) ranging from 10-70% as the disks are the ideal environment for strong dust grain processing to occur both in grain growth and crystallinity. The dust was found to consist of irregularly shaped grains and the typical grain sizes ranged from 0.1-4 micron from the synthetic spectral fitting to the IR spectra. But larger grains with sizes greater than 2 micron were found to be dominant. This implies that very small grains either aggregate to form larger grains or are destroyed by the stellar radiation field. Submillimeter measurements indicated the presence of even cm sized grains in some of the circumstellar disks. A disk is an ideal environment for grain growth since it is a long-lived stable reservoir with relatively high densities consisting of small hot grains in the surface layer of the disk and a cooler mid plane of larger grains. Most of these disks being O-rich indicates that the primaries did not evolve to become carbon stars. The internal chemical evolution seems to have been cut short by binary interaction processes as some of these are detected binaries. Also in the Galactic sources higher degree of crystallinity was seen when compared to the LMC sources. This is due to the lower metallicity of the LMC resulting in a lower gas to dust ratio which will in turn reduce dust formation rate and hence grain growth (Gielen et al. 2011a).

Three of the binary post-AGB sources: HD 52961, HD 46703 and EP Lyr studied by Gielen et al. (2011) showed presence of PAH (Polycyclic Aromatic Hydrocarbon) features in their IR spectra despite the O-rich nature of the central star and its circumstellar environment. In fact in two of the stars: HD 52961 and HD 46703, Gielen et al. (2011b) have also detected for the first time the IR bands of C_{60} molecules in an O-rich environment. Gielen et al. have proposed that PAHs (Polycyclic Aromatic Hydrocarbons) may form in an O-rich environment through the Fischer-Tropsch Catalysis Mechanism which

is a chemical reaction process that can form hydrocarbons and H_2O out of CO and H_2. Also the C_{60} fullerenes could form from the destruction of PAHs due to the shock waves generated during strong stellar winds or pulsations in these post-AGB stars. Apart from the spectral fitting to the IR spectra, a detailed 2D-SED modelling of all these sources were conducted by Gielen et al. Through this the inner and outer radii of the dust shell were found to be in the range of 2-20AU and 100-500AU. Also the dust masses were found to be from 10^{-6} to $10^{-4}M_{\odot}$ using a gas to dust ratio of 100.

When the C/O>1, the photospheric gas is C-rich and the excess carbon results in the

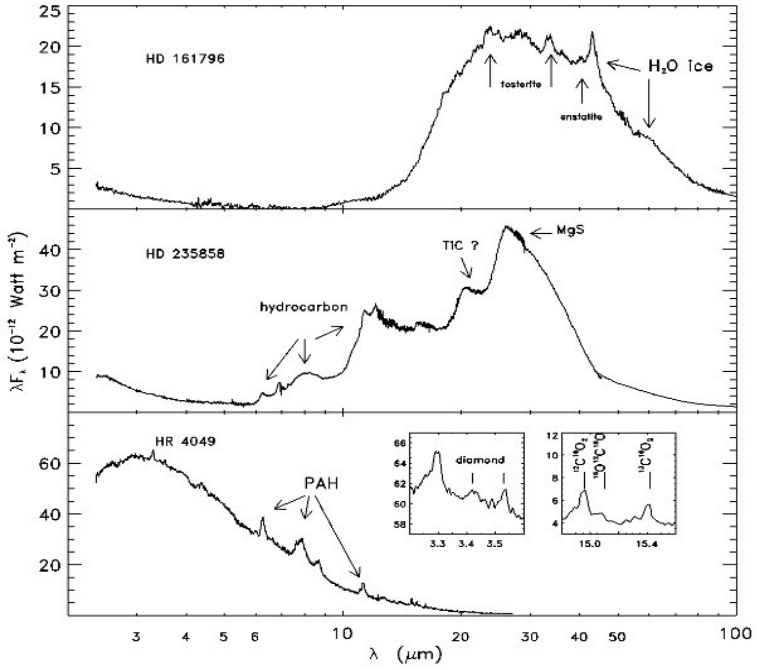

Figure 1.19: Illustrative spectra of circumstellar environment of post-AGB stars; an O-rich (top, HD 161796); a C-rich (middle, HD 235858); and one with mixed chemistry (bottom HR 4049). In the top panel, the different crystalline dust composition signatures are indicated: fosterite, ensatite, and water ice. The bulk of the silicate dust is, however, in amorphous form Hoogzaad et al. (2002). The lower panel is a C-rich dust envelope, with plateau emission of CC and CH bonds of hydrocarbons (Kwok et al. 2001; Hony et al. 2003). At longer wavelengths, the 21 m band, which is attributed to TiC, and the 30 m emission feature attributed to MgS are apparent. The bottom panel shows the circumstellar spectrum of the enigmatic binary HR 4049. The continuum is well fitted with a pure, single-temperature black body, which constrains strongly the circumstellar physics (Dominik et al. 2003). The PAH features are strong, and in the inserts, the diamond (Geballe et al. 1989; Van Kerckhoven et al. 2002) and CO2 (Cami & Yamamura 2001) features are shown. Figure taken from Van Winckel (2003).

formation of C-rich dust. Studies of the IR spectra of several C-rich post-AGB stars both in our Galaxy, LMC and SMC were conducted by Clube & Gledhill (2004); Hony et al. (2003); Hrivnak et al. (2009); Volk et al. (2011) and references therein. Almost all of these sources were found to have the 11.3 micron feature due to SiC, the unidentified 21 micron feature and the 30 micron feature thought to be due to MgS (Hony et al. 2002) and also several features (at 3.3, 6.2, 7.7, 8.6 and 11.3 micron) due to PAHs in their IR spectra. Since most of the Galactic (For example:Hrivnak et al. (2009) and Extra-Galactic (Volk et al. 2011) C-rich sources possess the 21 micron feature suggests that it is produced during the extreme mass-loss near the end of the AGB phase, is excited during the post-AGB phase and then subsequently destroyed during the PN phase due to the increasing strength of the radiation field from the central star (Hrivnak et al. 2009). The SED modelling of the C-rich post-AGB stars: HD 187885 (Clube & Gledhill 2004) and HD 56126 (Hony et al. 2003) were performed assuming spherical dust grains of amorphous carbon, SiC and MgS of sizes between 0.01-2 micron. Hrivnak et al. (2009) performed the 1D-SED modelling of these 21 micron sources where the continuum was assumed to be due to amorphous carbon grains with a typical grain size of 0.1 micron. The modelling indicated a dense cool (120-150K) shell of dust around the star and also a low-density hot (500-800K) dust closer to the star. From their modelling they found high mass-loss rates of 10^{-4} to $10^{-3}$$M_{\odot}$$yr^{-1}$ assuming a gas to dust ratio of 330. These resulted in shell masses of 0.2-1$M_{\odot}$ ejected over intervals of 160-820 years (duration of the intense mass-loss). The kinematical ages of the dust shell since the end of the high mass-loss was found to be of the order of 1000-3000 years from the modelling. Some sources also display a mixed chemistry like the famous post-AGB star HD 44179, the central star of the Red Rectangle Nebula where both O and C-rich features were detected in its IR spectra (Waters et al. 1998). They proposed that the formation of the O-rich disk preceded a more recent C-rich phase of the central object. Figure 1.19 depicts the circumstellar environment of post-AGB stars with ones having O-rich, C-rich and mixed chemistry.

García-Lario & Perea Calderón (2003) have proposed an evolutionary scheme to understand the evolution from the AGB to PN stage by studying the ISO spectra of a sample of transition objects. Figure 1.20 shows the evolutionary sequence for C and O-rich sources. The scheme takes into account the evolution of the gas-phase molecular bands seen in the AGB atmospheres as well as the solid state features in the circumstellar environment. When the star evolves along the AGB the thickness of the circumstellar shell keeps increasing and becomes optically thick during the super-wind phase. During this

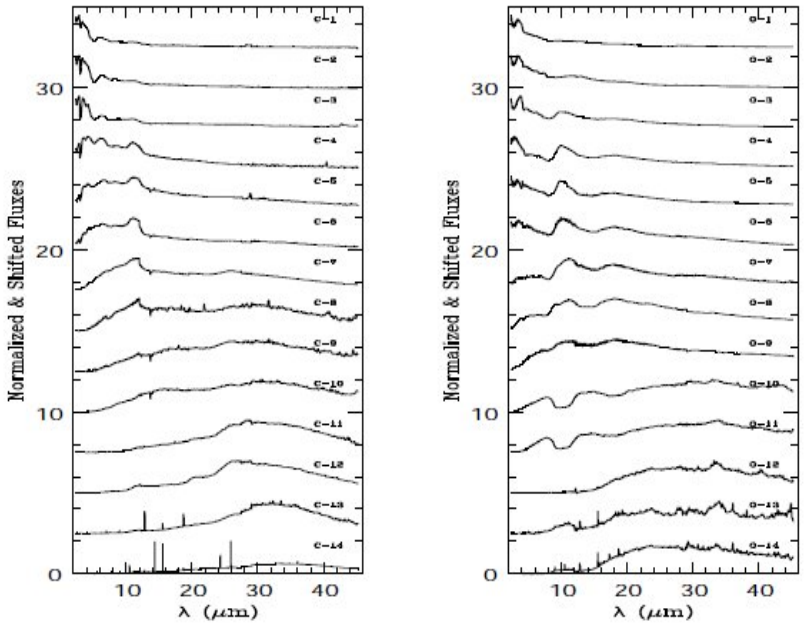

Figure 1.20: Spectral sequence followed by C-rich sources (left) and by O-rich sources (right) from García-Lario & Perea Calderón (2003)

stage the circumstellar features are seen in absorption. Once the AGB phase terminates the dust shell expands, cools and becomes optically thin and the features are seen in emission. Through this sequence one can follow in detail the condensation and growth of dust grains. Also the change in dust grain properties from amorphous to crystalline for O-rich chemistry and aliphatic to aromatic for C-rich chemistry is observed.

1.8 Aim of the Thesis

In this thesis, we have undertaken the study of unexplored (as well as the ones lacking comprehensive abundance analysis) RV Tau stars and post-AGB objects to understand the chemical changes taking place during the late stages of stellar evolution of low and intermediate mass stars. We have tried to enlarge the RV Tau and post-AGB sample and also present a critical compilation of all these objects studied till now to understand the importance of the stellar parameters and of the conditions such as binarity on post-AGB evolution. We have divided our compilations into several sub-groups such as those showing s-process enrichment, dust-gas winnowing, FIP effect and those having normal compositions. This compilation has enabled us to explore the evolutionary link between RV Tau and post-AGB stars; the latter appear to be in a more advanced stage of evolution. This finding has been further supported by their photometric behaviour.

We also find that RV Tau stars generally do not exhibit s-process enhancement but they outnumber post-AGBs in dust-gas winnowing and exhibit different families of depletion curves. Starting with the depletion curve of R Sct with an almost precipice like fall at high condensation temperatures, the length and height of low and intermediate condensation temperature plateau show considerable variations. There are another set of RV Tau stars with depletion curve asymptoting at higher condensation temperatures at different [X/H] levels. An attempt has been made to explain the observed depletion curves taking into consideration conditions such as the temperature and composition of the circumstellar environment as well as the efficiency of mixing between the accreted clean gas with the atmosphere/envelope of the star.

In our exploration of post-AGB candidates we also discovered two mildly hydrogen-deficient stars: SAO 40039 and HD 187885 (with strong He I lines). The detections of these stars are very important as they provide an important evolutionary link between hydrogen-normal and hydrogen-deficient stars.

CHAPTER 2

OBSERVATIONS AND ANALYSIS

2.1 OBSERVATIONS

The high resolution spectra of our program stars were obtained with the 2.34m Vainu Bappu Telescope at the Vainu Bappu Observatory (VBO) in Kavalur, India giving a resolution of 28,000 in the slitless mode (Rao et al. 2005). The high-resolution optical spectra of fainter stars in our sample were obtained at the W.J. McDonald Observatory with the 2.7m Harlan J. Smith reflector and the Tull coudé spectrograph (Tull et al. 1995) with a resolving power of 60,000. Spectral coverage in a single exposure from this cross-dispersed echelle spectrograph is complete up to 6000Å and extensive but incomplete at longer wavelengths. A S/N ratio of 80-100 over much of the spectral range was achieved.

2.1.1 INSTRUMENTS USED FOR OBTAINING THE STELLAR SPECTRA

• **The VBT Echelle spectrograph:**

The VBT Echelle spectrograph (see Figure 2.1) consists of a slit, collimator, grating, cross-disperser, camera and detector. The star light after falling on the primary mirror comes to a focus as an f/3.25 beam and is fed to a 100 micron core fiber located on the optical axis of the telescope. An image acquisition unit containing an intensified camera displays the stellar image and the fiber position on a monitor in the control room from where the guiding is done. The light from calibration lamps – ThAr for wavelength calibration and Xe-W lamps for flat fielding are also fed to the fiber through the same unit. The fiber output is collimated and converted to an f/5 converging beam that focuses onto the slit. The fiber output can also be used without the slit with a lower resolution for maximum throughput. The light beam emerging from the slit is fed into the collimator by

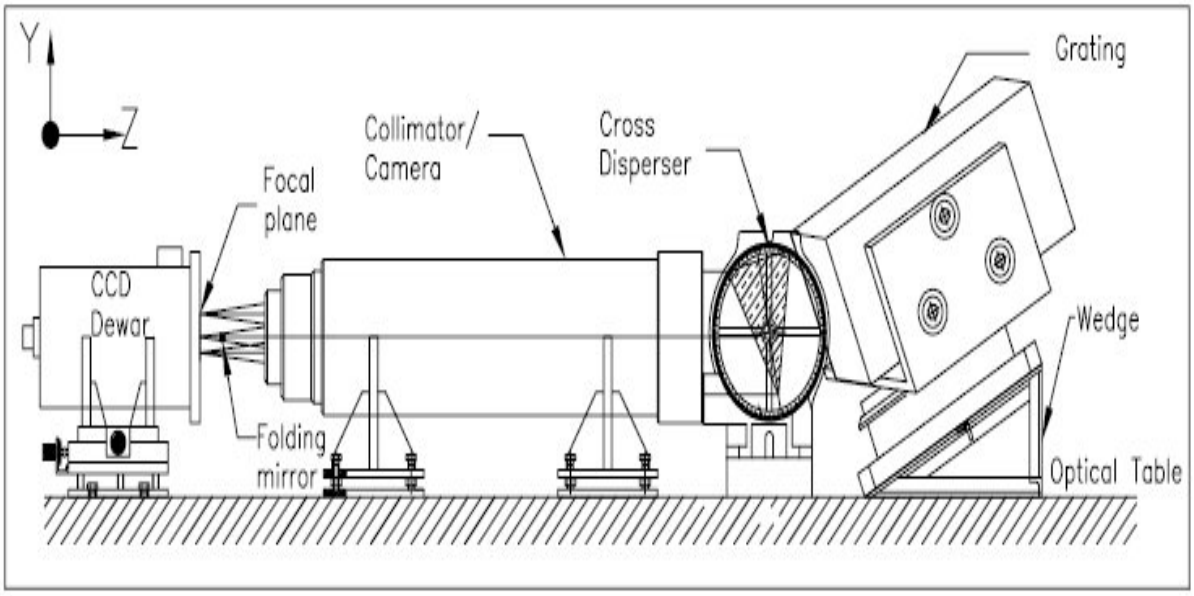

Figure 2.1: Opto-mechanical layout of the spectrometer. F/5 beam emerging from the slit is fed into the collimator by a folding mirror. The collimated beam then passes through the cross disperser prism and gets pre-dispersed and illuminates the echelle grating. The dispersed beam from the grating passes through the prism a second time and finally comes to focus on the CCD plane where the spectrum is recorded. Figure taken from Rao et al. (2005).

a 10mm folding mirror that sends the beam at an angle of 0.05^o to the optical axis of the spectrometer.

The collimator is a six element f/6 system designed for a beam size of 151 mm and has a focal length of 755 mm. The first element corrects for off-axis feeding of the beam. The system further contains a doublet and a triplet, all anti-reflection coated and chromatically corrected to a wavelength range of 4000Å to 1 micron. All the elements in the collimator are rigidly mounted in a single cylindrical tube with a provision to flush them with dry nitrogen. The collimated beam then passes through an LF5 prism of about 165mm height and an apex angle of 40^o which pre-disperses the light and sends it to the echelle grating. The echelle grating is illuminated by the incident beam fully. The grating has a size of 408×208mm. The dispersed beam retraces the same path and the prism cross-disperses for the second time thus ensuring enough order separation and enters the collimator for the second time. The collimator now acts as a camera and focuses the dispersed spectrum onto the CCD chip. The spectrum is finally recorded on a 2048×4096 pixels CCD camera. The CCD is a back illuminated, thinned Marconi chip with a pixel size of 15 micron

and is placed in a LN2 cooled dewar. The slit size of 60 micron covers about four pixels on the CCD. The CCD chip almost covers half of the area of the two dimensional spectrum format in the focal plane of the camera. The desired wavelength region is recorded either by adjusting the grating. All the optical components are mounted on a Milles Griot vibration free table of size 8×4 feet. The opto-mechanical layout of the spectrometer can be seen in Figure 2.1. The CCD dewar is mounted on a stage with a provision to move in X, Y and Z directions. The whole mechanical assembly is placed in an environmentally controlled dark room-Coude laboratory. The operations of the star acquisition, control of various lamp movements etc., are done from the telescope control room remotely through a PC. The grating and prism movements could also be accomplished remotely through PC commands.

•**The Tull Coudé Spectrograph:** This spectrograph is mounted at the focus of the 2.7m Harlan J. Smith Telescope at the McDonald observatory in the Davis Mountains of West Texas. The coudé focus is at F32.5. There are two science instruments available at coudé F32.5: (i) Tull spectrograph (TS1), which has two separate foci available for two cameras, 6-foot camera (TS11) and long focus camera (TS12), (ii) Cross-dispersed echelle spectrograph (TS2), which we have used for our observations is a high resolution spectrometer. This spectrometer is available with TK3, a thin, grade 1, Tektronix 2048×2048 CCD. Two-pixel resolving powers in its two modes of operation are 60,000 (TS23) and 240,000 (TS21). At R=60,000, data from the full bandwidth of 3,400-10,900Å are collected with the TK2048 CCD in as few as two exposures.

2.1.2 VARIOUS STEPS IN THE DATA REDUCTION OF THE RAW SPECTRA

We have used the IRAF (Image Reduction and Analysis Facility) package for reducing the spectra of our program stars. IRAF is developed and distributed by the National Optical Astronomy Observatory and operates under the UNIX environment. The raw data files comprises of the bias, flats, Th-Ar and the object images. When the final image is being processed by the CCD, the chip amplifier produces extra electrons resulting in the generation of noise. The noise can also be generated within the CCD chip when the charges are being transferred within the CCD. This noise can produce negative values when the final image is being created. To correct for this a small offset value is given to each pixel in the CCD called the bias. To correct for the pixel-pixel variations across the CCD the images from a uniformly illuminated source is taken. First the bias frames

taken on each night are averaged using the task ZEROCOMBINE. The master bias is then subtracted from the object and flat field frames using the task CCDPROC in the CCDRED package. The bias subtracted flat-fields are then combined using the median option in the task FLATCOMBINE. Before normalising the flats the spectral signature of the quartz lamp from the flats have to be removed. For this one needs to know the position of the different orders through the entire image. Since the flat field is more or less uniformly illuminated along the slit the centers of different orders cannot be traced properly. Thus using the task APALL in the ECHELLE package with a bright star the tracing of different orders are performed. The flats are then corrected for scattered light by using the task APSCATTER. The flat-fields are then normalised using the apnorm task in the SPECRED package. The pixel-pixel variations across the CCD chip are removed by dividing the object frames by flat field frame using the task CCDPROC. Extraction of the one-dimensional spectrum is carried out by the task APALL in the ECHELLE package. The result is a one-dimensional spectrum with counts versus the pixel number. The next step is the wavelength calibration of the object spectra. For this a comparison spectra which is extracted similarly for each slit is required. The comparison spectrum in our case is the emission line spectrum obtained from a Th-Ar arc. Several emission lines in the Th-Ar spectra are identified using the atlas of Th-Ar laboratory spectra by D'Odorico et al. (1987). The dispersion correction is determined from the arc spectrum by using the Legendre polynomial of the order 3-4 in the x-direction and order 2 in the y-direction. Generally a good value for an rms is 0.1-0.2 pixels (since the rms is given in Å one has to divide by the number of Ås per pixel in the spectra). The above procedure is carried out using the task ECIDENTIFY in the ECHELLE package. Finally each individual object spectrum is wavelength-calibrated using the task DISPCOR with the corresponding comparison spectrum as the reference. The resulting output is the spectrum in counts versus wavelength. The cosmic ray hits in the spectrum are removed and finally the spectrum is normalised to the continuum by fitting a slowly varying function such as a cubic spline. The continuum is estimated visually using the average of the highest points in the spectrum from regions free of emission and absorption features.

2.2 DEFINITION OF ABUNDANCE AND EQUIVALENT WIDTH OF A SPECTRAL LINE

Abundances are usually the logarithmic number densities on a standard scale in which log ϵ(H)=12. To obtain the abundances of elements in a cosmic object the standard practice

is to compare the element content in a cosmic object with the corresponding value for the Sun using the normal logarithmic abundance scale:

$$[X/H] = log(N_X/N_H)_* - log(N_X/N_H)_\odot = log\epsilon_{X,*} - log\epsilon_{X,\odot} \tag{2.1}$$

To derive abundances we need to measure the line strengths for a large number of lines for the species of interest. The line strength in abundance jargon is called the equivalent width. The equivalent width is the amount of energy which is subtracted from the neighbouring continuum due to the presence of line. It is measured as the area under the curve. It can be considered as a width of a black rectangle (Figure 2.2) which has the same area as the stellar line.

$$W_\lambda = \int (F_C - F_\lambda)/F_C d\lambda = \int R_\lambda d\lambda, \tag{2.2}$$

where F_C, F_λ and R_λ stand for flux in the continuum, line and the residual line strength respectively.

The relation between line strength and the number of absorbers and its dependence on other stellar parameters forms the basis of abundance determination methods.

2.2.1 MEASUREMENT OF EQUIVALENT WIDTHS

Equivalent widths of the absorption lines in the stellar spectrum of our program stars have been measured in two ways using the splot task in IRAF. One is by fitting a Gaussian to the absorption line and the other by measuring the total area under the line. We have measured mostly symmetric and unblended lines in our program stars. The accuracy of the equivalent width measurements depends on the spectral type of the star, the continuum fitting and also on the spectral resolution. For the program stars of spectral type A-F the equivalent widths could be measured with accuracy of 5-8% in the absence of line asymmetries . But for cooler stars the accuracy was about 8-10% due to the line blending and the difficulties involved with the continuum placement. This error corresponds to the basic precision that can be attained with the instrumental set-up. For example: a change in 200K at an effective temperature of 5500K causes a change in equivalent width of a moderate strength line by about 6%.

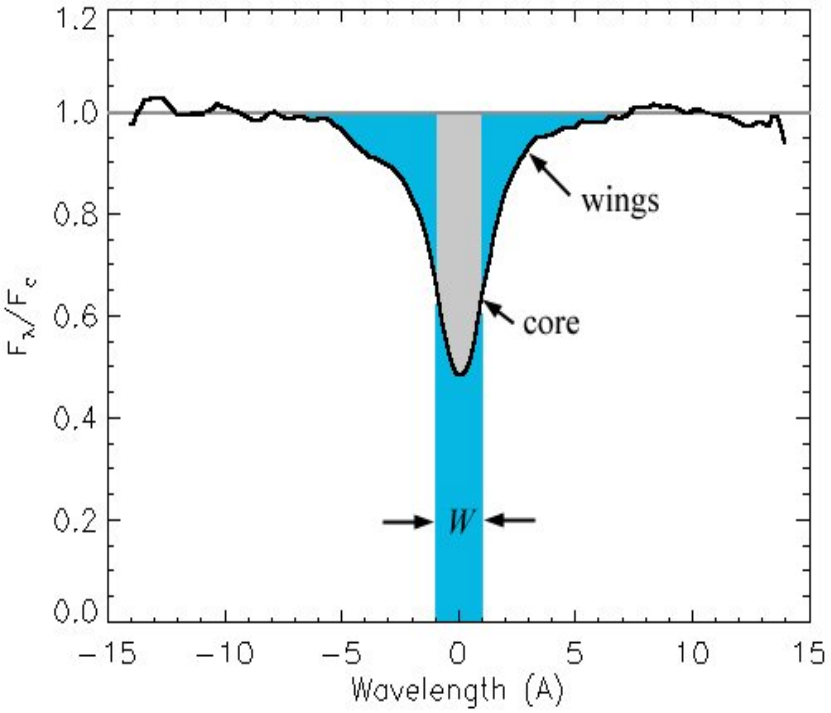

Figure 2.2: Equivalent Width of a spectral line

2.2.2 CONCEPT OF CURVE OF GROWTH

The curve of growth describes how the equivalent width depends on the number of absorbing atoms or ions. It also shows how the line strength and the profile grows as the abundance increases as can be seen in Figure 2.3.

a) For weak lines (see Figure 2.4), the line strength increases linearly with the abundance i.e. $W_\lambda \propto N$ and is called the linear part of the curve of growth. If there are very small number of absorbers, they will create a shallow optically thin spectral line. If the number of absorbers (abundance) is increased the line becomes deeper and stronger. Hence the first part of the curve is a linear relation (see also Figure 2.3). Here the line strength does not depend strongly on the atmospheric parameters. Hence weak lines are considered to be most suitable for abundance determinations.

b) As the abundance continues to increase, the Doppler core of the line becomes optically thick and saturates (see Figure 2.4). The wings of the line are optically thin and continue to deepen which occurs with little change in the line equivalent width and produces a plateau in the curve of growth and is called the flat part where $W_\lambda \propto (\ln N)^{1/2}$ (see also Figure 2.3).

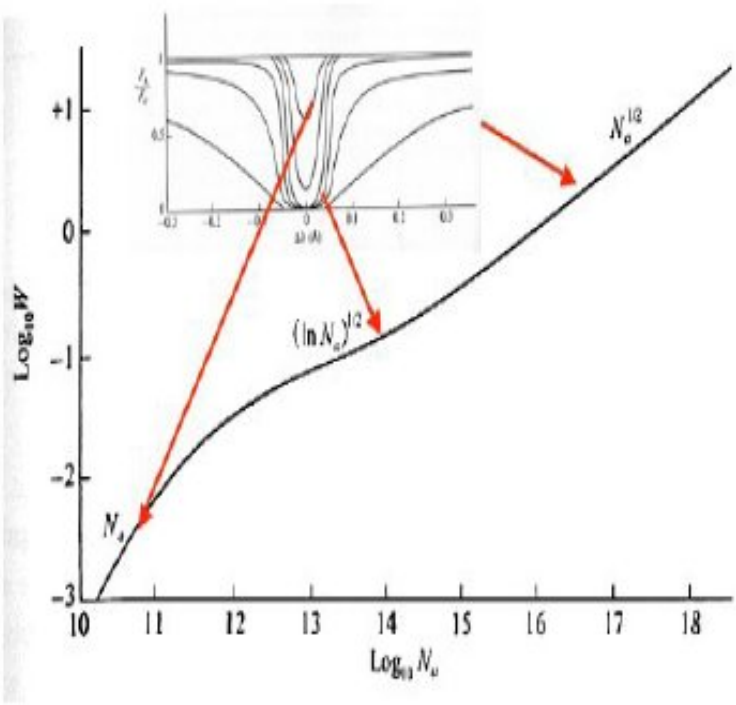

Figure 2.3: Typical curve of growth for the K line of Ca II. Courtesy:http://cc.oulu.fi/jpoutane/teaching/TA07/TheorAstro11_handouts.pdf

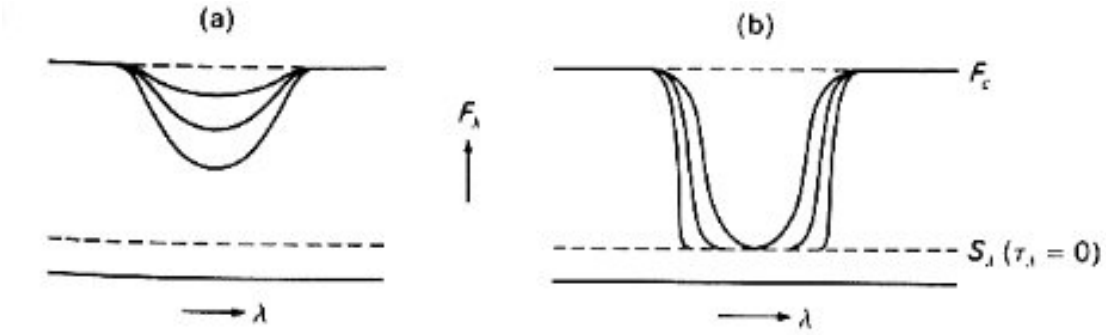

Figure 2.4: Changes of the line profile with the increase in the number of absorbers: (a) for weak lines and (b) for strong lines. Figure taken from Böhm-Vitense (1989)

c) As the abundance becomes very large the line becomes so strong that even the weak far out wings due to the damping become visible as can be seen in Figure 2.4 and is called the damping or the square root part and we have $W_\lambda \sim (N)^{1/2}$ (see also Figure 2.3).

2.3 ANALYSIS

2.3.1 ASSUMPTIONS FOR THE MODEL ATMOSPHERES USED

The general assumptions made for the model atmospheres used are:

a) The energy flux remains constant with depth of the atmosphere, since the energy source for the star lies far below the atmosphere and no energy comes into the atmosphere from above.

b) The atmosphere is plane-parallel i.e. the geometrical thickness of the atmosphere is small when compared to the radius of the star.

c) The atmosphere is in hydrostatic equilibrium i.e. there is no relative motion of the layers in the normal direction and no net acceleration of the atmosphere. Hence the pressure balances the gravitational attraction.

$$\rho d^2r/dt^2 = -\rho g + dP/dr = 0 \tag{2.3}$$

where ρ is the density and $g=GM_*/R_*^2$ is the gravitational acceleration, which is assumed constant as the atmosphere is thin. M_* and R_* are the mass and radius of the star respectively.

d) The atmosphere is in Local Thermodynamic Equilibrium (LTE). In LTE the assumption is that all transitions are only due to collisions between absorbers and that radiation is unimportant in determining the level populations. LTE is valid in the stellar interiors and also to some extent in the stellar photospheres where the densities are high and collisions dominate the level populations. Also in LTE, the distribution of kinetic energies are described by the Maxwell-Boltzmann equation, the level populations are given by the Boltzmann equation, the ionization ratios by the Saha's ionization equation and the material is assumed to radiate as a black body radiator (distribution of photon energies are given by the Planck's law of black body radiation) .

e) The atmosphere is homogeneous and that there are no spots, granules, magnetic fields etc.

Since we are dealing with pulsating variable stars in some cases with extended circumstellar shells we must also examine our basic assumptions of hydrostatic equilibrium

in a plane-parallel LTE atmosphere. Discussions of the validity of these assumptions for RV Tau variables have been given by Baird (1981) and Wahlgren (1986). They argue that standard model atmospheres can indeed be used as long as one avoids pulsational phases when the lines are doubled or when shock-wave passage is occurring as indicated by metallic line emission. Moreover in our study we have avoided lines formed high in the atmosphere by using only lines with line strengths < 200mÅ, where the non-LTE effects are known to be smaller and we have used only stable phases of the star for the analysis .

Also complete non-LTE model atmospheres that include detailed line blanketing are not available for A and F supergiants (Venn 1995a; Kubát & Korcáková 2004) since the lines of different ions form at very different depths and therefore there is a need for a huge amount of depth points to resolve all line formation regions sufficiently. Only LTE model atmospheres with non-LTE calculations of individual ions have been calculated. Most of the non-LTE model atmospheres that have been generated have included only H and He populations in the non-LTE calculations. Non-LTE model atmospheres have not been able to include a full treatment of line opacities (line blanketing) because of difficulties involved in calculating all atomic populations simultaneously with radiative transfer equations along with radiative and hydrostatic equilibrium (Venn 1995a). However for lower luminosity supergiants of type Ib, LTE is expected to be a reasonable assumption in calculating the model atmospheres (Venn 1993).

In the usual plane-parallel case, the radiative transfer is solved in only one depth variable neglecting the curvature of the atmosphere. For most stars this is justified as the extension of the atmosphere is negligible compared to the stellar radius. Extreme cases are cool giants and supergiants where the low surface gravities of supergiants results in their atmospheres having large geometric extensions and thus the geometry effects due to the thickness of the atmosphere has to be taken into account. F-K giants are commonly used to study abundances of stellar systems mainly due to their intrinsic brightness. With respect to atmosphere geometry they represent border line cases and are therefore usually analyzed using plane-parallel radiative transfer. In recent years grids of model atmospheres with spherical geometry have become available (Gustafsson et al. 2003; Hauschildt et al. 1999). But the line formation will be continued to be computed in plane-parallel geometry for abundance analysis procedures as geometry has a smaller effect on line formation than on model atmosphere. Thus it is more important to use a spherical model atmosphere.

Heiter & Eriksson (2006) recommend the use of spherical model atmospheres in abundance analyses for $log\ g < 2$ and 4000K$<T_{eff}<$6500K. With this one can avoid both sys-

tematic errors on abundances and differential effects which can lead to additional uncertainties in the stellar parameters. Also restricting the analysis to weak lines with line strengths < 100 mÅ will minimize the uncertainties on abundances caused by assuming a plane-parallel geometry. They found that when both the model atmosphere and line formation computations are done assuming a plane-parallel geometry called the p-p case the differences are upto +0.35 dex for minority species and -0.04 dex for majority species. These differences are based on Solar abundance models but the effects are expected to be similar in low metallicity models since the atmospheric extensions are similar. But in the s-p case i.e. with the use of a spherical model atmosphere but plane-parallel assumption for line formation, the differences were found to be -0.1 dex even in the worst case. These abundance differences due to sphericity effects can be used for error estimation in abundance studies relying on plane-parallel modelling.

2.3.2 ATMOSPHERIC MODELS

For the analysis of the RV Tau and post-AGB stars in our sample we have made use of the new grid of ATLAS09 model atmospheres available at the database of Kurucz*.

For the analysis of the mildly hydrogen-deficient post-AGB stars: SAO 40039 and HD 187885, the special models with different He/H ratios were computed by the code STERNE (Jeffery et al. 2001) and these grids were accessed by visiting Simon Jeffery's homepage†.

2.3.3 COMPUTER CODES USED

For all our program stars we have used the code MOOG (2009 version) developed by Sneden (1973) to determine the abundances and also for performing the spectral synthesis. In MOOG, we have used the subroutine **abfind** for abundance determinations and **synth** for synthesising the spectral lines in some cases.

First the the atomic lines in our stellar spectra are identified using The Multiplet Table by Moore (1972) and also The Solar Spectrum by Moore et al. (1966) and the equivalent widths of the lines are measured. For calculating the abundances for the various species, the subroutine **abfind** in MOOG requires the LTE model atmosphere and the line list of the star. The line list comprises of the central wavelength of the line, its lower excitation potential, oscillator strengths and the measured equivalent widths.

*http://kurucz.harvard.edu/grids.html
†http://www.arm.ac.uk/ csj/

The code evaluates the formal solution of the equation of radiative transfer for the spectral lines under the LTE assumptions and calculates the line depths over the profile and hence the equivalent widths for a given stellar model atmosphere for each line as a function of the abundance. For a chosen model, the code does numerous iterations and the abundance is modified until the computed equivalent widths matches with that of the observed equivalent widths. In the case of abundances calculated through equivalent width measurements, MOOG uses the least square fitting method by finding the best fitting curve to the data points by minimizing the sum of the squares (also called chi-squared) of the offsets/residuals of the points from the curve. To improve the fits further, the lines having the highest residuals are removed. Only lines having residuals of +/- 0.3 are retained. MOOG gives the slope and the correlation co-efficients of the least-square fits. The best fit usually as a slope close to zero and a high value of the correlation co-efficient. Hence the goodness of fit is usually examined from the slope and the correlation co-efficients calculated for the least-square fitting by MOOG. We have made use of only clean, unblended and symmetric lines for our abundance calculations.

In some cases when the element of interest only exhibits a few weak blended features or when the lines are affected by hyper-fine splittings (hfs) and isotopic shifts, the method of spectral synthesis has to be employed to derive the abundances. Spectral synthesis is a method of computing the emergent spectrum of a star by employing an appropriate stellar model atmosphere, atomic and molecular data and the numerical integration of the equation of radiative transfer at each point in the spectrum. The atomic and molecular data required for the synthesis are available at the database of Kurucz[‡].

For synthesising the spectral lines, we have used the subroutine **synth** in MOOG for deriving the abundances. **synth** is another standard MOOG running option which computes a set of trial synthetic spectra and matches these to an observed spectrum. Abundances can be deduced either by visual inspection of the plot or by mathematical minimization of the observed-computed spectrum difference. MOOG calculates the residuals by differencing the synthesized and observed spectra at each point in the range of interest in the observed spectrum. The standard deviation of the residuals in a fit gives the quantitative measures using which the best fit can be decided.

The inputs required for performing the synthesis are the stellar model atmosphere, the detailed line list for the region in the spectrum to be synthesized, starting and the end points of the wavelength region, step size which is sufficiently small for adequate sampling of the line profile in the spectrum and the width over which contributions from

[‡]http://www.cfa.harvard.edu/ampdata/databases.html

neighbouring lines are to be considered at each point in the spectrum. The synthesized spectrum has to be convolved with the instrumental profile as well as rotational broadening (if present) to match the observed spectrum. Given these as the inputs, the code calculates the continuum and line fluxes at each point separated by a step size. The code must be run several times with different trial values until the observed spectrum matches with the synthesized spectrum.

For the mildly hydrogen-deficient post-AGB stars: SAO 40039 and HD 187885, we have made use of the LTE code SPECTRUM (Jeffery et al. 2001) developed especially for hydrogen-deficient stars for deriving the abundances. The inputs to the code are the line list, an input file and the appropriate model atmosphere. The linelist comprises of the atomic number of the element describing the degree of ionization (either neutral or singly ionized), the central wavelength of the atomic line, *gf* value, the Stark, radiative and Van der Waal's broadening co-efficients taken from Kurucz[§] database and the input file consists of the atomic number of the element, the central wavelength of the line, the measured equivalent width of the spectral line and the microturbulent velocity.

2.3.4 HYPER-FINE SPLITTING AND ISOTOPIC SHIFTS IN LINES

Lines of certain elements like the ones having odd atomic numbers (Z) like Mn, Cu, Sc, Eu and also elements having even Z but odd number of neutrons like Ba are affected by hyper-fine splitting (hfs). Because of this the line appears broad and neglecting these hfs components in the line list during the spectral synthesis results in the over-estimation of the abundances. hfs arises due to the interaction of the electron spin with the nuclear spin thereby splitting the absorption lines of these elements into various components. For these elements the hfs components have typical splittings of upto a few tens of milliangstroms. In terms of stellar abundance studies, the hfs desaturates strong absorption lines resulting in features with larger equivalent widths than single lines with no hfs components. Thus if the splittings are ignored or underestimated, the computed abundances will be overestimated for strong lines as the size of the abundance overestimate increases with the line strength in the case of strong lines.

Hence to derive an abundance from a line affected by hfs, one must perform a spectrum synthesis with the linelist including the the hfs components thus the number of components, the wavelength splittings and the relative strengths must be known. The sources from which the hfs components for Sc, Mn, Cu, Ba and Eu taken have been mentioned in chapter 3 of the thesis.

[§]http://kurucz.harvard.edu

Table 2.1: References for the log *gf* values

Species	Accuracy[a]	Ref	Species	Accuracy[a]	Ref
C	B-C	1	Fe II	A-B	9
N	B-C	1	Co	B-C	10
O	B-C	2	Ni	B-D	10
Na	A	3	Cu	B-D	11
Mg	B-C	4	Zn	B-D	11
Al	B-D	5	Y	B-D	12
Si	B-D	6	Zr	B-D	13
S	D	22	Ba	B-D	21
Ca	C-D	23	La	B-D	14
Sc	D	7	Ce	B-D	15
Ti	B-D	7	Pr	B-D	16
V	B-D	7	Nd	B-D	17
Cr	B-C	20	Sm	B-D	18
Mn	B-C	7	Eu	B-D	19
Fe I	A-B	8	Dy	B-D	16

[a]Symbols indicating the accuracy of the *gf* values where A = ±3%, B = ±10%, C = ±25% and D = ±50%

[1]Wiese & Fuhr (2007), [2]Wiese et al. (1996), [3]Sansonetti (2008), [4]Kelleher & Podobedova (2008a)

[5]Kelleher & Podobedova (2008b), [6]Kelleher & Podobedova (2008c), [7]Martin et al. (1988), [8]Fuhr & Wiese (2006)

[9]Meléndez & Barbuy (2009), [10]Fuhr et al. (1988), [11]Fuhr & Wiese (2005), [12]Hannaford et al. (1982)

[13]Biémont et al. (1981), [14]Lawler et al. (2001a), [15] Lawler et al. (2009)

[16]Sneden et al. (2009), [17]Den Hartog et al. (2003), [18]Lawler et al. (2006), [19]Lawler et al. (2001b),

[20]Sobeck et al. (2007), [21]Curry (2004), [22]Podobedova et al. (2009), [23]Aldenius et al. (2009)

Certain elements like Eu (2 isotopes) and Ba (5 isotopes) are also affected by isotopic shifts. These are the shifts that arise between the spectral lines of different isotopes of the same atom. Isotopic shifts can arise due to a change in the reduced electronic mass as well as a change in the electric charge distribution of the nucleus and plays an important role especially for the heavy elements. Due to this all the isotopes of these elements

affected by isotopic shifts have to be taken into account during the spectral synthesis for determining accurate abundances. Even though these effects are small compared to the width of the line and instrumental profiles, they broaden and shift the lines and alter their shape leading to erroneous interpretations of spectra of astrophysical interest.

2.3.5 ATOMIC DATA USED

The atomic data are the *gf* values or the oscillator strengths which are the most important data in any abundance calculations. An atom or molecule can absorb light and undergo a transition from one quantum state to another. The oscillator strength is a dimensionless quantity which is used to express the strength of the atomic transition. The accuracy of the derived abundances to a great extent depend on the *gf* values. We have extensively used the NIST database[¶] as well as the Luck's (1993, Private communication) compilation of the *gf* values for the lines of some atomic species. The other sources of the *gf* values as well as the accuracy of the *gf* values for different atomic species are given in Table 2.1.

2.4 DETERMINATION OF ATMOSPHERIC PARAMETERS

2.4.1 EFFECTIVE TEMPERATURE

The equivalent width depends on the number of absorbers at a given excitation level. The distribution of atoms in the different excitation levels is controlled by the temperature. This can be understood through the Boltzmann equation which determines the relative numbers of atoms in different excitation states as a function of temperature. However it refers to only atoms in a certain ionization state but does not tell us about the number of atoms being ionized.

The star's effective temperature T_{eff} can be derived by using the Boltzmann's equation of excitation balance when LTE applies if the measured equivalent widths of the spectral lines are known:

$$N_n/N = g_n/U(T)10^{-\theta\chi_n} \tag{2.4}$$

where θ = 5040/T, U(T) refers to the partition function and χ_n stands for the excitation potential. For deriving the effective temperature *(T_{eff})* lines having a large range in their lower excitation potentials are used. If the temperature estimate is accurate, lines of all

[¶]http://physics.nist.gov/PhysRefData/ASD/lines_form.html

lower excitation potentials should give the same abundance. Usually lines of abundant species like Fe, Cr and Ti are used for this purpose. T_{eff} is estimated by forcing the condition that the derived abundances are independent of the lower excitation potentials. Balmer profiles of hydrogen are temperature sensitive and can also be used for temperature estimations but the Balmer profiles in our program stars were affected by emission and hence were unusable.

A rough estimate of T_{eff} can be made from the given spectral type and the calibration of Schmidt-Kaler (1982) given in Aller et al. (1982) for supergiants as a starting point. Also the (b-y) color in the Strömgren uvby system is sensitive to temperature. But the use of photometric calibrations in determining T_{eff} in the case of post-AGB and RV Tauri stars is rendered challenging as the temperature varies over the pulsation cycle so the phase of spectrometry must be properly matched with the photometric observations. Thus using the photometric method to determine T_{eff} for these objects may lead to high uncertainities. Also since these objects have dense circumstellar dust shells around them, they have circumstellar reddening which are difficult to determine.

2.4.2 SURFACE GRAVITY

It is known that the fraction of atoms in the ionized and neutral states are dependent on the pressure which in turn is related to the gravity through the equations:

$$P_g = C_1 X g^{1/3} \tag{2.5}$$

$$P_e = C_2 X g^{1/3} \tag{2.6}$$

Therefore pressure dependence can be translated into a gravity dependence. The surface gravity can be determined using the Saha's ionization equation which calculates the degree of ionization for the collision dominated gas:

$$log(N_1/N_0)P_e = 2.5log(T_{ion}) - 5040/T_{ion}I + log(U_1/U_0) - 0.1762 \tag{2.7}$$

where N_0 and N_1 are the abundances of a particular element in the neutral and the singly ionized state, U_0 and U_1 are the partition functions of corresponding states, T_{ion} and I are the ionization temperature and potential and P_e corresponds to the electron pressure which is proportional to the surface gravity. Once the effective temperature has been estimated accurately, the surface gravity *log g* is derived by iterating with model atmospheres with a range in gravities till the neutral and singly ionized species give the same abundances. For

this we have considered the ionization balance between Fe I/Fe II, Mg I/Mg II, Si I/Si II, Ti I/Ti II and Cr I/Cr II.

Another method of determining the surface gravity is by using the wings of H_γ and H_δ which are found to be very sensitive to both temperature and gravity especially in A Type stars (Venn 1995a). These in-turn provide locii of temperature-gravity pairs. But this method could not be used as all the Balmer profiles of hydrogen were distorted by the underlying emission in most of our program stars.

One can also determine the surface gravity using the Mass-Radius relation given by:

$$logg = log(M/M_\odot) - 10.62 - log(L/L_\odot) + 4log(T_{eff}) \tag{2.8}$$

But in most of the cases the masses and luminosities are quite uncertain for these stars. Another possibility is through photometry. The synthetic colors of UBV and uvby for different models of gravity and metallicity are computed by Relyea & Kurucz (1978). The c1-index Strömgren photometric system c1=(u-v)-(v-b) is very sensitive to changes in gravity for stars in the temperature range 5500-10,000K. But most of our program RV Tauri and post-AGB stars are surrounded by significant amounts of circumstellar dust and the parameters vary with the phase of the pulsation cycle.

2.4.3 MICROTURBULENT VELOCITY

The non-thermal motions in the photospheres of stars refers to turbulence. If the size of the photospheric gas element is small when compared to the photon mean-free path it refers to microturbulence. Here the elements of gas moving with different velocities absorb at different distances from the center of the line. Absorption can occur over a great range in wavelength because of the Doppler shifts introduced by the turbulence. When the line is particularly strong and saturated at the core, broadening introduced by the microturbulence desaturates the core and allows the equivalent width of the line to increase.

For determining the microturbulence (ξ_t) we have used lines having similar lower excitation potentials (to avoid the temperature dependence) but having a good range in equivalent widths. The ξ_t is estimated by requiring consistency between weak lines (nearly independent of ξ_t) and strong lines (affected by ξ_t). We have generally used Fe II lines for measuring the ξ_t for most of our program stars, since appreciable departures from LTE are known to occur for Fe I lines (Boyarchuk et al. 1985; Thévenin & Idiart 1999). However for coolest members, very few Fe II lines could be measured and hence

Fe I lines had to be used instead for fixing the microturbulence.

2.4.4 EFFECTS OF FE I NON-LTE CORRECTIONS ON THE STELLAR PARAMETER DETERMINATIONS:

The main non-LTE mechanism for Fe I is overionization of levels with excitation energy of 1.4-4.5 eV. This results in an underpopulation of neutral Fe where all the Fe I lines are weaker than their LTE strengths and leads to positive non-LTE corrections. Departures from non-LTE are significant for the derivation of Fe abundances from neutral lines at the level of < 0.1 dex in Solar metallicity stars and < 0.5 dex in metal-poor stars. Surface gravities obtained through ionization balance of neutral and singly ionized lines are affected by 2.5-3 times the typical non-LTE abundance correction in logarithmic units. Thus classical ionization equilibrium is far from being satisfied. Thus the surface gravities derived by LTE analysis are in error and should be corrected before final abundances are computed. This also solves the observed discrepancy between the spectroscopic gravities derived by LTE analysis and those derived from Hipparcos parallax. Whereas Fe II lines have higher ionization potentials and are formed much deeper in the photosphere and LTE is found to be a valid assumption (Thévenin & Idiart 1999; Collet et al. 2005; Mashonkina et al. 2011).

A detailed description of the effects of Fe I non-LTE corrections on the stellar parameters have been given by Lind et al. (2012). The summary is as follows:

Metallicity: The non-LTE effects on Fe I increase with decreasing metallicity as there will be no metals to block the uv radiation and thus results in more efficient overionization of Fe I.

Microturbulence: The non-LTE abundance corrections show a dependence on line strength beyond saturation (W>50mÅ) which will impact the determination of microturbulence from Fe I lines. Saturated (50<W<100mÅ) lines have an abundance correction that is larger than for unsaturated lines (factor of 5 less than non-LTE abundance correction). This leads to lower microturbulence in LTE compared to non-LTE. But the effect is found to be negligible for dwarfs and giant stars above [Fe/H]>-3. Extremely metal-poor stars are found to be more affected.

Effective Temperature: Since the non-LTE abundance corrections for Fe I are more positive for low excitation lines, the effective temperature derived through LTE analysis will be overestimated. For [Fe/H]=-3, dwarfs and red giants are found to be affected by less than 50 K. Thus excitation temperatures derived are not heavily influenced by non-LTE effects except for horizontal branch stars and extremely metal-poor stars.

Surface Gravity: Since Fe I lines are subject to significant non-LTE effects as mentioned above (since there is underpopulation of Fe I atoms in LTE), the LTE ionization balance is not always realistic and thus surface gravity will be underestimated. It has been found that for a non-LTE abundance correction of 0.1 dex for a dwarf at [Fe/H]=-2 and effective temperature of 6500K, LTE analysis underestimates the surface gravity by 0.25 dex. Due to this metal-poor stars will be misclassified as subgiants. Similarly for a red giant with [Fe/H]= -5 and effective temperature of 4500K and having a non-LTE abundance correction of 0.2 dex would underestimate the surface gravity by 0.6 dex in LTE.

In summary, the non-LTE abundance corrections are found to increase with decreasing metallicity, increasing effective temperatures and decreasing surface gravity.

2.5 ERROR ANALYSIS

The final abundances of each star are affected by random and systematic errors. Systematic errors may result from the faulty calibration of the equipment or bias on the part of the observer. This makes the measured value larger or smaller than the true value. They must be estimated from an analysis of the experimental conditions and techniques. Random or non-systematic errors are the fluctuations in observations that yield different results each time the experiment/observation is repeated and thus require repeated observations to yield precise results.

Systematic Errors: The systematic errors on the derived abundances are mainly due to uncertainties in the determination of atmospheric parameters, systematic errors in the *gf* values used and the presence of Non-LTE effects. Example calculations of systematic errors for our program stars arising due to the uncertainties in the determination of stellar atmospheric parameters covering a range of effective temperatures have been presented in Table 3.3 in Chapter 3 and Table 4.3 in Chapter 4 of the Thesis. The total systematic error (σ_{sys}) due to uncertainties in the stellar parameters is obtained by taking the square root of the sum of the squares of all the independent contributions i.e. the uncertainty in the effective temperature:$\Delta T_{\rm eff}$, uncertainty in the surface gravity:$\Delta \log g$ and the uncertainty in the microturbulence:$\Delta\xi$ and is given by $\sigma_{sys} = [(\Delta T_{\rm eff})^2 + (\Delta \log g)^2 + (\Delta\xi)^2]^{1/2}$.

However the uncertainties in the *gf* values have been presented in the footnote of Table 2.1 in the present chapter of the Thesis. In the case of Fe and Fe-peak elements large number of lines are measured and since the *gf* values are more accurate the abundances [X/H] are accurate within 0.10-0.25 dex. But for s-process elements the uncertainty in the

abundances [X/H] can be above 0.25 dex. But the errors in the abundances with respect to Fe i.e. [X/Fe] will be smaller as the effect of errors caused by the atmospheric parameters cancel to a certain extent. We have also investigated the possible systematic effects caused by the adopted *gf* values by measuring the Solar equivalent widths for our lines in the Solar flux atlas and have estimated the abundances using the model atmosphere appropriate for the Sun. We find that the agreement for most elements is within 0.04 to 0.09 dex although the line list is different for different stars.

Also the systematic errors caused due to the assumptions of LTE i.e. the Non-LTE corrections for several elements have been presented in Section 3.5.1 in Chapter 3 of the Thesis. To minimize the effects of Non-LTE we have used only those lines for which the equivalent widths < 200mÅ and we have considered only those phases where the atmosphere was more or less stable (Hydrostatic Equilibrium) i.e. we have avoided pulsation phases when the lines were doubled or when metallic line emissions were present indicating the passage of shock waves.

The systematic errors cancel to a first approximation when differential analysis is performed. In our case we have conducted a differential abundance analysis for our program stars with Sun as our reference star.

Non-Systematic or Random Errors: These errors include the photon shot noise, read out noise of the CCD (for which bias frames are taken), noise due to the non-uniformity in the pixel response to the light (for which flat frames are taken) etc. Read noise is produced in the camera electronics and during the readout process. The CCD read noise limits a camera's S/N ratio but as long as this noise exhibits a Gaussian or normal distribution its influence on the images can be reduced by combining frames and standard image processing techniques. Also the individual pixels have slightly different responses to light of same intensity introducing another source of error. To compensate for the effects outlined above bias and flat frames are taken.

Photon Shot Noise: which is caused by the random arrival of photons at the detector. Since each photon is an independent event, the arrival of any given photon cannot be precisely predicted. The probability of its arrival in a given time period is governed by a Poisson distribution. Shot noise can be reduced by collecting more photons either with a long exposure or by combining multiple frames. For our program stars, each object frame was of exposure time 30 mins and we have combined 3-4 frames to get a spectra with a good S/N.

Bias frames of CCD: A bias frame is an image exposed for zero seconds with a closed shutter. This contains information about the pixel to pixel variations in the read out noise

as well as any defects in the chip. The read out noise are random variations in the output signal each time the CCD is read out and arises during the conversion of the charge carriers into the voltage signal and subsequent processing and analog to digital conversion. This noise can be suppressed by combining a number of bias frames together and then subtracting the master bias frame from the object frames.

Flat frames: are images of a uniformly illuminated source which contains information about pixel to pixel variations in the quantum efficiency (i.e. response to light) and light variations due to the instrument configuration. Pixel non-uniformity can be reduced by calibrating an image with a flat field image. Thus dividing the object frames by the flats which have already been corrected for bias will remove these effects. All of the above processes mentioned above increase the overall noise level of the image. Thus by subtracting the object frames from bias and bias corrected flat frames one can compensate for this noise. Averaging many frames together then reduces their noise levels. As a result the amount of noise added by image calibration is minimized. As all these steps affect the S/N ratio of the spectra, the various steps in the data reduction process have to be executed well.

The S/N ratio of the spectra, spectral type of the star, instrumental resolution as well as the continuum placement affects our accuracy of the equivalent width measurements. For stars of spectral type A-F the equivalent widths could be measured with an accuracy of 5-8% in the absence of line asymmetries. But for cooler stars due to line blending and difficulty in the continuum placement, the line strengths could be measured only with accuracies of 8-10%. The line to line scatter which is the standard deviation of the mean given in our abundance tables was found to be around 0.15-0.2 dex and is mainly determined by the non-systematic errors in the equivalent width computation. Therefore the various steps involved in the raw data reduction process given in Section 2.1.2 in the present chapter of the Thesis have to be executed well to minimize these random errors. The random errors can be minimized by taking more measurements. For example: The line to line scatter in the abundance tables decreases with the increase in the number of lines measured.

Thus the total error is the cumulative effect of these systematic and non-systematic errors.

CHAPTER 3

CHEMICAL COMPOSITIONS OF RV TAURI STARS AND RELATED OBJECTS

3.1 ABSTRACT

We have undertaken a comprehensive abundance analysis for a sample of relatively unexplored RV Tauri and RV Tauri like stars to further our understanding of post-AGB evolution. An extensive abundance analysis has also been conducted for the well known RV Tauri star V453 Oph and the heavily depleted object HD 52961.

We have used high resolution spectra and grid of model atmospheres to conduct abundance analysis of our sample stars. Indications of mild s-processing (not common among RV Tauri objects) are found for V820 Cen and IRAS 06165+3158. V820 Cen bears close resemblance to another RVC object V453 Oph in high radial velocity, low metallicity and mild enhancement of s-process elements. On the other hand, SU Gem and BT Lac show mild effects of dust-gas winnowing, while the effect is not seen in IRAS 01427+4633 and IRAS 19135+3937 despite the favourable conditions like binarity and circumstellar matter indicated by their Infrared (IR) colors.

We have compiled the existing abundance data on RV Tau objects and find that a large fraction of them are afflicted by dust-gas winnowing and two RV Tauri stars show First Ionisation Potential (FIP) effect; and now added by the present work, we find a small group of three RV Tauris showing mild s-process enhancement in our Galaxy. With the two out of three reported s-process enhanced objects belonging to RV Tau spectroscopic class C; these intrinsically metal-poor objects appear to be promising candidates to analyse the possible s-processing in RV Tau stars.

The extended sample of RV Tauris showing dust-gas winnowing has resulted in iden-

tifying different kinds of slopes and structures in the depletion plots. We have attempted explaining these observed families of depletion plots in the framework of different star–circumstellar material geometries, the temperature and the composition of dust-gas reservoir, as well as the degree of mixing between the accreted clean gas with the atmosphere/envelope of the star.

3.2 INTRODUCTION

RV Tauri stars are pulsating variables located in the instability strip along with the Cepheids but at relatively lower luminosities. Their characteristic light curves show alternating deep and shallow minima with a formal period (time elapsed between two consecutive deep minima) of 30-150 days. Photometrically there are two types of RV Tauri stars, RVa and RVb (Kukarkin et al. 1958): RVa stars show a quasi-constant brightness of mean light whereas RVb stars exhibit a longer term variation in mean brightness with a period of about 600-1500 days. This variation is often ascribed to varying obscuration by dust as the star moves in a binary orbit (Pollard et al. 1996). It is also proposed that the viewing angle onto the disk can also determine the RV Tau photometric classification (De Ruyter et al. 2006; Gielen et al. 2011c). In this scenario the RVa objects are thought to be the ones with low inclination while RVbs are high inclination objects with the disk seen edge-on (Van Winckel et al. 1999). Preston et al. (1963) classified RV Tauri variables spectroscopically into RVA, RVB and RVC. RVA have spectral type G-K and near light minimum show TiO bands of abnormal strength. RVB are relatively warm weak-lined objects of spectral type F and exhibit strong CN and CH bands at light minimum. RVCs have weak metal lines in their spectra and have high radial velocities (Joy 1952). The CN and CH bands are weaker or absent at all phases. They are genuinely metal-poor objects.

As suggested by Wallerstein (2002) and Van Winckel (2003) in their reviews RV Tauri stars are post-AGB objects crossing the instability strip. With the detection of RV Tauri stars in the LMC (Large Magellanic Cloud) by Alcock et al. (1998), their location on the high luminosity end of the population II instability strip is confirmed. With the known distance modulus of the LMC, an absolute magnitude of -4.5 was estimated for RV Tauri variables with fundamental periods (time elapsed between a deep and a shallow minima) of about 50 days using the calibrated P-L-C (Period-Luminosity-Color) relation by Alcock et al. (1998) further supporting the above suggestion. The detection of IR fluxes (Jura 1986) and the high estimated luminosities (Alcock et al. 1998) supports the idea that these stars are in the post-AGB phase evolving towards the blue in the Hertzsprung-

Russell (H-R) diagram.

Studies of the chemical compositions of RV Tauri variables were undertaken initially in large part to glean information about their evolutionary status and in particular about the compositional changes wrought by internal nucleosynthesis and mixing processes (Dredge-ups). However, a considerable fraction of them exhibited a very different abundance peculiarity−a systematic depletion of refractory elements. A strong signature of this phenomenon has been observed in the post-AGB objects like HR 4049, HD 52961, BD+39^{o}4926, HD 44179 etc (see Van Winckel (2003) for a review). Through their study of λ Bootis stars showing similar depletions, Venn & Lambert (1990) noted the resemblance of the observed abundance pattern with that of the interstellar gas in which the metals are depleted through fractionation in the interstellar grains. Bond (1991) suggested that the extreme metal deficiency of HR 4049 like objects could be caused by the selective removal of metals through grain formation. A semi-quantitative model to explain this phenomenon observed in λ Bootis stars and HR 4049 like objects was developed by Mathis & Lamers (1992) . These authors proposed two scenarios: capture by the presently visible post-AGB star of the depleted gas from the binary companion or rapid termination of a vigorous stellar wind in a single star so that grains are blown outwards (and hence lost) resulting in a photosphere devoid of these grain forming elements. Waters et al. (1992) proposed an alternate scenario based upon slow accretion from the circumstellar or circum-system disk. This scheme provides favourable conditions for this effect to operate without any restriction on the nature of the binary companion. More observational support of this hypothesis such as large [Zn/Fe] for HD 52961 (Van Winckel et al. 1992) and strong correlation between stellar abundance for IW Car and depletions observed in the interstellar gas demonstrated by Giridhar et al. (1994) resulted in further detections of RV Tauri and post-AGB objects showing this effect commonly referred as 'dust-gas winnowing' or 'dust-gas separation' (Van Winckel 1995; Van Winckel et al. 1998; Gonzalez et al. 1997a,b; Klochkova & Panchuk 1998; Giridhar et al. 1998, 2000; Maas et al. 2002; Giridhar & Arellano Ferro 2005; Maas et al. 2005; Reyniers & Van Winckel 2007; Gielen et al. 2009b; Sumangala Rao et al. 2012; Van Winckel et al. 2012) and references therein. The condensation temperature (T_C)* being an important parameter measuring the propensity of a given element into grain formation, the dependence of the observed abundance on T_C can be used to identify these objects. For brevity, hereinafter we would refer to the 'dust-gas winnowing effect' as DG effect. Among RV Tauris, this effect is most prevalent in RVB objects while their cooler sibling RVA only show weak

*The condensation temperature T_C is the temperature at which half of a particular element in a gaseous environment condenses into dust grains.

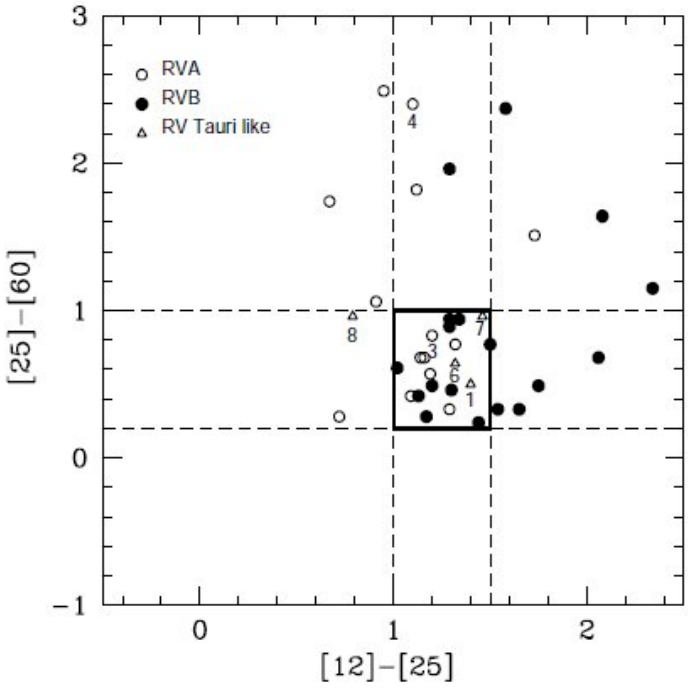

Figure 3.1: The IRAS color-color diagram showing the "RV Tauri" box. The figure contains our sample stars and all the well studied RV Tauri stars. The program stars are numbered according to the Table 3.1.

manifestations possibly due to the dilution caused by their deep convective envelopes. The genuinely metal-poor RVCs are unaffected by the dust-gas winnowing since their metal-poor environment are not conducive for grain formation (Giridhar et al. 2000).

In the present work we have enlarged the RV Tauri sample by studying seven unexplored RV Tauri stars and IRAS[†] objects located in or near the RV Tauri box in the IRAS two color diagram. We also present a more recent abundance analyses for the RVC star V453 Oph and the extremely depleted star HD 52961 which exhibits RVb like phenomenon in its light curve.

3.3 SELECTION OF THE SAMPLE

Our sample Table 3.1 comprises of unexplored RV Tau stars, stars having RV Tau like IR colors. We have also studied known RV Tauri object V453 Oph and heavily depleted

[†]Infrared Astronomical Satellite

Table 3.1: The Program Stars.

No.	IRAS	Other Names	Period (Days)	Var Type
1	06165+3158	...	...	...
2	...	V820 Cen, SAO 205326	150	RV Tauri
3	06108+2743	SU Gem, HD 42806	50	RV Tauri
4	22223+5556	BT Lac	41	RV Tauri
5	...	TX Per	78	RV Tauri
6	19135+3937	...	...	...
7	01427+4633	SAO 37487, BD+46^{o}442	...	...
8	07008+1050	HD 52961, PS Gem	71	SRD*
9	...	V453 Oph, BD-02^{o}4354	81	RV Tauri

* SRDs are semiregular variable giants and supergiants of spectral types F, G and K. Sometimes emission lines are seen in their spectra. They have pulsation periods in the range of 30-1100 days with an amplitude of variation upto the 4^{th} magnitude in their light curves.

object HD 52961 for which we provide a contemporary analysis covering more elements. The IR fluxes of known RV Tau stars have been investigated by Lloyd Evans (1985) and Raveendran (1989) who found that the RV Tau stars fall in a well-defined region of the IRAS two-color diagram. The study of SEDs of six RV Tau objects by De Ruyter et al. (2005) showed a large near IR excess but low line of sight extinction, this coupled with energy balance considerations suggested that likely distribution of the circumstellar dust is that of a dusty disk. Lloyd Evans (1999) suggested that RV Tauris are those stars with dusty disks which are currently located within the instability strip. Lloyd Evans (1999) hence proposed that this RV Tau box in the IRAS [12]−[25], [25]−[60] diagram enclosed by the limits [12]−[25]=1.0−1.5 and [25]−[60]=0.20−1.0 when supplemented by large near IR flux provides an alternative method of searching for RV Tauri stars among IRAS objects.

In fact, the photometric monitoring of IRAS sources following the above mentioned criteria did result in finding new samples of RV Tau objects studied by Maas et al. (2002) and Maas et al. (2005).

In Figure 3.1 we have plotted our program stars (only those having IR colors) which have been numbered according to Table 3.1. In the figure we have also plotted RV Tauri stars with known spectroscopic classification. Most of our program stars with the exception of BT Lac are located in or around the RV Tau box.

Although a large fraction of known RV Tau stars are found in RV Tauri Box, many well known RV Tau particularly RVB stars do not conform to these limits and have redder IRAS colors. The colors of RVB stars points to the existence of cooler dust shells

compared with the RVA members. Nevertheless this box provides a starting point for identifying RV Tau candidates among IRAS sources with no photometry. In what follows we will refer as "RV Tauri like" those objects with RV Tau like colors in IRAS two color diagram without photometric confirmation.

3.4 OBSERVATIONS

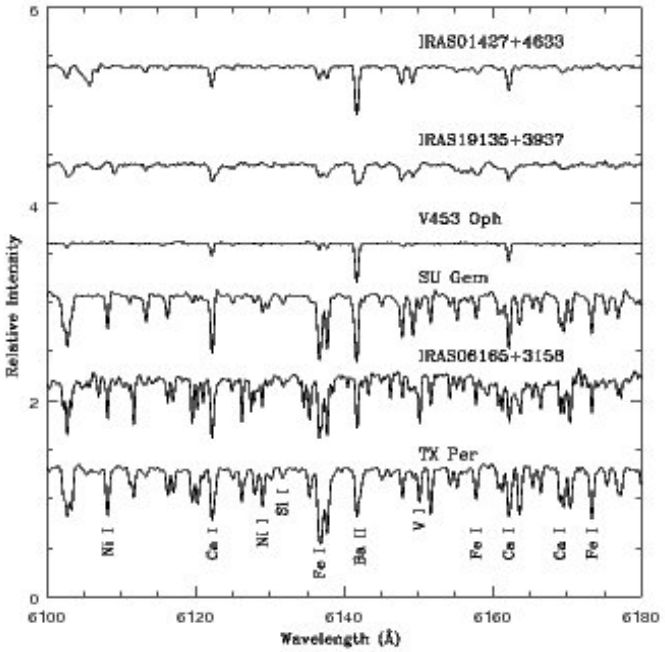

Figure 3.2: Sample spectra of our program stars presented in the descending order of temperature (top to bottom) in the 6100-6180Å region.

High-resolution optical spectra were obtained at the W.J. McDonald Observatory with the 2.7m Harlan J. Smith reflector and the Tull coudé spectrograph (Tull et al. 1995). This spectrometer gives a resolving power of about 60,000 and a broad spectral range was covered in a single exposure. A S/N ratio of 80-100 over much of the spectral range was achieved. Figure 3.2 illustrates the resolution and quality of sample spectra of our program stars in the wavelength region 6100-6180Å. The sample spectra have been arranged in the order of decreasing effective temperatures. Program stars IRAS 06165+3158 and TX Per have the same effective temperature.

The spectra of HD 52961 and V820 Cen were obtained with the echelle spectrometer of the 2.34m Vainu Bappu Telescope at the Vainu Bappu Observatory (VBO) in Kavalur, India giving a resolution of about 28,000 in the slitless mode (Rao et al. 2005).

3.5 ABUNDANCE ANALYSIS

We have made use of the new grid of ATLAS09 model atmospheres available at database of Kurucz[‡]. Spectrum synthesis code MOOG (2009 version) by Sneden (1973) has been used. The assumptions are standard, Local Thermodynamical Equilibrium (LTE), plane parallel atmosphere and hydrostatic equilibrium and flux conservation.

The hydrogen lines for most stars were affected by emission components hence could not be used for parametrization of stars. We have used Fe I and Fe II lines for deriving atmospheric parameters. Further, lines of Mg I, Mg II; Si I, Si II ; Ti I , Ti II and Cr I, Cr II were also used as additional constraints whenever possible. First, the microturbulence ξ_t is derived by requiring that the derived abundances are independent of line strengths. We have generally used Fe II lines for measuring ξ_t microturbulence for most of our sample stars, since appreciable departure from LTE are known to occur for Fe I lines (Boyarchuk et al. 1985; Thévenin & Idiart 1999). However for coolest members, TX Per and IRAS 06165+3158 very few Fe II lines could be measured and hence Fe I lines had to be used instead for fixing the microturbulence.

The temperature is estimated by requiring that derived abundances are independent of the Lower Excitation Potential (LEP). The gravity was derived by requiring Fe I and Fe II giving the same abundance. In addition, the ionization equilibrium of Mg I/ Mg II , Si I/Si II , Sc I/Sc II, Ti I/Ti II, Cr I/Cr II were used as additional constraints whenever possible.

The accuracy of equivalent width measurements depends on resolution, spectral type of the star and the continuum fitting. For stars of spectral type late A- F, the equivalent widths could be measured with an accuracy of $\sim$ 5 -8 % in absence of line asymmetries. With the above mentioned accuracy in measured equivalent widths, the microturbulence velocity could be measured with an accuracy of $\pm$0.25 km s^{-1}, temperature with $\pm$150K and *log g* of $\pm$0.25 cm s^{-2}.

But for cooler stars, line strengths could only be measured with accuracy of 8-10 %. The microturbulence velocity could be measured with an accuracy of $\pm$0.5 km s^{-1}, temperature with $\pm$250K and *log g* of $\pm$0.5 cm s^{-2}. The derived stellar parameters have been presented in Table 3.2.

The sensitivity of the derived abundances to the uncertainties of atmospheric parameters $T_{\rm eff}$, *log g*, and ξ are presented in Table 3.3. For three stars representing the full temperature range of our sample, we present changes in [X/Fe] caused by varying atmospheric parameters by 200K, 0.25 cm s^{-2} and 0.5 km s^{-1} (average accuracies of these parameters)

[‡]http://kurucz.harvard.edu/grids.html

Table 3.2: Stellar Parameters Derived from the Fe-line Analyses

Star	UT Date	V_r^a (km s^{-1})	T_{eff}, log g, [Fe/H]	ξ_t^b (km s^{-1})	Fe I^c		Fe II^c	
					log ϵ	n	log ϵ	n
IRAS 06165+3158	2007 Nov 5	−16.0	4250,1.50, −0.93	2.8	6.54 ± 0.15	55	6.49 ± 0.17	6
V820 Cen	2011 Mar 02	+259.0	4750, 1.5, −2.28	2.4	5.14 ± 0.16	67	5.21 ± 0.15	8
V820 Cen	2011 Mar 03	+266.0	4750, 1.5, −2.35	2.4	5.06 ± 0.17	39	5.15 ± 0.01	2
IRAS 06108+2743	2009 Dec 26	+8.9	5250, 1.00 ,−0.25	3.0	7.20 ± 0.10	31	7.19 ± 0.10	14
IRAS 22223+5556	2009 Oct 10	−70.0	5000, 2.00, −0.17	3.7	7.28 ± 0.13	36	7.27 ± 0.14	4
TX Per	2009 Dec 27	−17.0	4250,1.50, −0.58	3.1	6.81 ± 0.13	62	6.94 ± 0.13	7
IRAS 19135+3937	2007 Nov 3	−13.2	6000,0.50,−1.04	4.1	6.46 ± 0.15	26	6.36 ± 0.09	7
IRAS 01427+4633	2007 Dec 21	−98.2	6500,0.50,−0.79	3.5	6.71 ± 0.09	37	6.61 ± 0.11	8
HD 52961	2011 Jan 27	+4.2	6000, 0.5, −4.55	5.1	2.91 ± 0.00	1	2.89 ± 0.07	2
V453 Oph	2009 May 10	−125.9	5750,1.50, −2.26	3.7	5.19 ± 0.10	28	5.18 ± 0.11	7

$^a V_r$ is the radial velocity in km s^{-1}, $^b \xi_t$ is the microturbulence

$^c \log \epsilon$ is the mean abundance relative to H (with $\log \epsilon_H = 12.00$).
The standard deviations of the means as calculated from the line-to-line scatter are given. *n* is the number of considered lines.

with respect to the chosen model for each star. The total stellar parameter related error is estimated by taking the square root of the sum of the square of the systematic errors (individual errors associated with uncertainties in temperatures and gravities).

Having determined the atmospheric parameters, the abundances of different elements were derived using the available lines. The derived abundances relative to the solar abundances are presented in their respective tables. The solar photospheric abundances given by Asplund et al. (2005) have been used as reference values.

We have investigated possible systematic effects caused by the adopted *gf* values from different sources as follows. We have measured solar equivalent widths for our lines on Solar Flux Atlas by Kurucz et al. (1984) and estimated the abundances using model atmosphere appropriate for the Sun with $T_{\rm eff}$=5770K, *log g* of 4.4 and ξ_t of 0.9 kms^{-1}. The agreement for most elements is within 0.04 to 0.09 dex although the linelist is different for different stars. The lines of certain elements are affected by hfs. We have included the hfs components in our line list while synthesizing the spectral feature of these elements for deriving the abundances. For elements Sc and Mn, we have used hfs component list and their *log gf* given by (Prochaska & McWilliam 2000), for Cu (Allen & Porto de Mello 2011), for Eu (Mucciarelli et al. 2008) and for Ba (McWilliam 1998). The abundances of elements for all our program stars are presented in Table 3.4, Table 3.5, Table 3.6 and Table 3.7 respectively.

3.5.1 THE ERRORS CAUSED BY ASSUMPTION OF LTE

Non-LTE corrections for CNO elements show strong temperature dependence particularly for N see e.g. (Lyubimkov et al. 2011; Schiller & Pryzbilla 2008) and they also vary from multiplet to multiplet. Venn (1995b) have tabulated these corrections for C and N for a range of stellar temperatures for lines belonging to different multiplets. For B-F stars the correction for N varies from −0.3 dex to −1.0 dex while for C it is −0.1 to −0.5 dex. Takeda & Takada-Hidai (1998) have calculated non-LTE corrections for oxygen abundance using 6156-6158Å lines for A-F stars and correction varies between −0.1 to −0.4 dex. For the forbidden [O I] lines, the non-LTE corrections are found to be negligible and LTE is found to be a valid approximation for early K to late F type disk/halo stars of various evolutionary stages (Takeda 2003).

The neglect of departure from LTE also introduces errors in the estimated abundances of heavier elements. These errors for a given element vary with the stellar temperatures and also on metallicities. In very metal-poor stars the over-ionization and in some cases usage of resonance lines for abundance determination results in errors as large as +0.5

Table 3.3: Sensitivity of [X/Fe] to the uncertainties in the model parameters for a range of temperatures covering our sample stars .

	TX Per			IRAS 06108+2743			IRAS 01427+4633		
	(4250K)			(5250K)			(6500K)		
Species	$\Delta T_{\rm eff}$	$\Delta\log g$	$\Delta\xi$	$\Delta T_{\rm eff}$	$\Delta\log g$	$\Delta\xi$	$\Delta T_{\rm eff}$	$\Delta\log g$	$\Delta\xi$
	$-200K$	+0.25	+0.5	$-200K$	+0.25	+0.5	$-200K$	+0.25	+0.5
C I	...	...	...	−0.29	−0.07	−0.09	−0.08	−0.01	−0.05
N I	...	...	...	...	...	...	−0.13	−0.06	−0.04
O I	+0.24	−0.01	−0.10	+0.03	−0.06	−0.09	...	...	...
Na I	+0.41	+0.22	−0.08	+0.05	+0.06	−0.07	...	...	...
Mg I	+0.25	+0.15	−0.02	+0.02	+0.06	−0.04	+0.03	+0.05	−0.01
Al I	+0.37	+0.19	−0.11	+0.03	+0.05	−0.10	+0.00	+0.06	−0.05
Si I	−0.05	+0.05	−0.08	+0.02	+0.05	−0.10	+0.00	+0.06	−0.06
Si II	...	...	...	...	...	...	−0.10	−0.07	+0.06
S I	...	...	...	+0.24	−0.06	−0.09	−0.05	+0.03	−0.06
Ca I	+0.48	+0.23	−0.01	+0.09	+0.06	−0.01	+0.04	+0.07	+0.00
Sc II	...	...	...	−0.02	−0.06	−0.01	−0.01	−0.05	−0.04
Ti I	...	...	...	−0.18	+0.07	−0.08	+0.07	+0.06	−0.03
Ti II	+0.13	+0.00	+0.02	−0.03	−0.06	+0.14	+0.13	−0.06	+0.14
Cr I	+0.43	+0.18	−0.08	+0.18	+0.07	+0.08	−0.05	+0.06	+0.05
Cr II	−0.09	−0.04	−0.06	−0.13	−0.07	−0.05	−0.07	−0.05	−0.01
Mn I	+0.37	+0.21	−0.05	+0.12	+0.07	+0.00	+0.02	+0.07	−0.06
Ni I	+0.19	+0.08	+0.01	+0.11	+0.06	+0.01	+0.03	+0.06	−0.04
Zn I	−0.04	+0.03	−0.01	+0.03	+0.01	+0.05	+0.02	+0.06	−0.05
Y II	...	...	...	−0.02	−0.06	+0.02	−0.02	−0.05	−0.05
Ce II	+0.24	−0.01	−0.10	+0.04	−0.05	−0.07	+0.04	−0.03	−0.05
Nd II	...	...	...	+0.05	−0.06	−0.10	...	...	...
Sm II	...	...	...	+0.04	−0.05	−0.08	...	...	...

dex for elements like Na. We have only used subordinates lines for sodium, believed to be formed in deeper layers and for them non-LTE corrections of about −0.10 dex are reported (Lind et al. 2011; Gehren et al. 2004). Gehren et al have estimated non-LTE corrections for Mg and Al and for the lines used in our analysis for a sample of G stars covering a range in metallicities. For thick disk metallicities non-LTE corrections are +0.05 for [Mg/Fe] and +0.2 for [Al/Fe] is reported. For the resonance lines of Al: the non-LTE correction was found to be positive and in the range of 0.2-0.45 dex and the effect is found to be more pronounced with increasing effective temperatures and decreasing metallicities (Gehren et al. 2004).

The non-LTE corrections for S I lines have been estimated by Korotin (2009). For the S I lines used in our work (6042 − 6056, 6743 − 6758 Å), the effect is negligible. Wedemeyer (2001) has done non-LTE calculation for Si I lines and non-LTE correction in range −0.01 to −0.05 dex have been estimated for the Sun and Vega respectively. Mashonk-

ina et al. (2007) have studied departure from LTE over a range of stellar parameter and metallicities for a large number of Ca I and Ca II lines. At solar or moderately deficient metallicities the non-LTE correction is smaller than +0.1 dex for Ca I lines used in our analysis for deriving Ca abundance. Also the correction is negligible for very weak Ca I features. Scandium: With its relatively low ionization potential, Scandium is prone to overionization via non-LTE effects. For Sc I the non-LTE correction is +0.15 dex and for Sc II the correction is found to be very mild i.e. -0.01 dex in the case of Sun (Zhang et al. 2008). For supergiants the non-LTE corrections might be higher. Bergemann (2011) have computed non-LTE Ti I and Ti II for late type stars. At solar temperatures the non-LTE corrections between +0.05 to 0.10 dex are found for Ti I lines while the effect is negligible for Ti II lines. Bergemann suggests the use of only Ti II lines and [Ti/Fe] computed from Ti II and Fe II would be more robust. Non-LTE analysis of Cr I and Cr II by Bergemann & Cescutti (2010) for solar and metal-poor stars indicate an error of -0.1 dex at the solar metallicities which becomes larger +0.3 to 0.5 dex for very metal-poor stars. Non-LTE effects for Fe I and Fe II lines have been estimated by Mashonkina (2011) for A-F stars with more complete representation of model atom. It is found that LTE underestimates the abundance derived from Fe I lines by 0.02 to 0.1 dex depending upon the chosen line and stellar temperatures; the effect could be as large as 0.2 dex for giants. The non-LTE corrections are very small for Fe II lines. While deriving gravities from ionization equilibrium of Fe I & Fe II, relatively large non-LTE corrections for Fe I must be taken into consideration. Zinc: The non-LTE corrections for the Zn I lines at 4722, 4810 and 6362 Å lines tend to be positive and increase towards lower metallicity. The non-LTE corrections are usually small less than 0.1 dex for F, G and K dwarfs and supergiants (Takeda et al. 2005).

Resonance lines of Sr II: The non-LTE corrections for Sr II in the atmospheres of F and G stars with $T_{\rm eff}$ = 5500-6500K and *log g* = 1.0-4.5 and [Fe/H]=0 to -3 were studied by Belyakova & Mashonkina (1997). The correction is found to be positive and is of the order of 0.8-1.2 dex for supergiants. Velichko et al. (2010) have calculated non-LTE correction for Zr I and Zr II lines; both species become weak in LTE. The non-LTE correction for Zr II lines used and for our stellar parameters range does not exceed +0.1 dex. Our sample stars are F-K supergiants with metallicity range 0 to -1.2 dex. To disentangle the evolutionary effects (on abundances) from those inherent to the natal ISM we have compared the observed abundance pattern with those characterized for thin and thick disk by extensive studies like Bensby et al. (2005), Reddy et al. (2006) using extended samples of F-G dwarfs and subgiants and more recently by Takeda et al. (2008) using late G giants.

Between these samples the [X/Fe] vs [Fe/H] plots are remarkably similar for elements Si, Ca, Sc, Ti, V, Cr, Mn, Co, Ni and Cu and non-LTE effects for these elements are also generally very small. Hence it is possible to infer the population type of the sample stars from important abundance ratios such as [α/Fe] given for various disk components from the above mentioned studies. As explained above, the non-LTE effects for α elements are not large enough to mask the characteristic abundance differences.

3.6 RESULTS

There are several processes that affect the stellar composition during the course of its evolution such as a) the initial composition of the Interstellar Medium (ISM), b) the effect of nucleosynthesis and mixing processes such as dredge-ups , c) dust-gas winnowing that affects a large number of studied RV Tauri stars and post-AGBs, d) for a very small group of objects the abundances show dependences on their FIP. In the following subsections on individual stars, we discuss the derived abundances to infer the influence of these effects operating in our program stars.

3.6.1 IRAS 06165+3158

Miroshnichenko et al. (2007) gives the spectral type as K5Ib, remark that the star is 'probably metal deficient', and describe a strong IRAS infrared excess due to cold dust. No OH maser emission at 1612 MHz was detected for this star (Lewis et al. 1990). No photometric observations have been reported so the variable type and period are unknown. This star has been included in our analysis as it had RV Tauri like colors in the two-color diagram as can be seen in Figure 3.1.

Our abundance analysis confirms that this star is metal-deficient ([Fe/H] = -0.93). Mild enrichment of s-process elements (Y, Zr, La, Ce, Nd and Sm) and also that of Pr, an r-process element is seen with an average [*s*/Fe] of +0.4 dex - see Table 3.4. Due to the low temperature of the star and very poor S/N ratio in blue the number of clean s-process element lines (even for synthesis) are woefully small. Ba II feature at 6141.7Å has doubling in the core and the one at 5853.6Å has a distinct unresolved component hence could not be used. The estimated s-process abundances are supported by the synthesis of these features as can be seen in Figure 3.3. The O abundance has been determined from the forbidden line at 6300.3Å. But the C abundance is surprisingly low. The CH bands in the 4300Å region as well as the C_2 bands in the 5150-5165Å region appear weak and synthesis indicate [C/H] < -2.0.

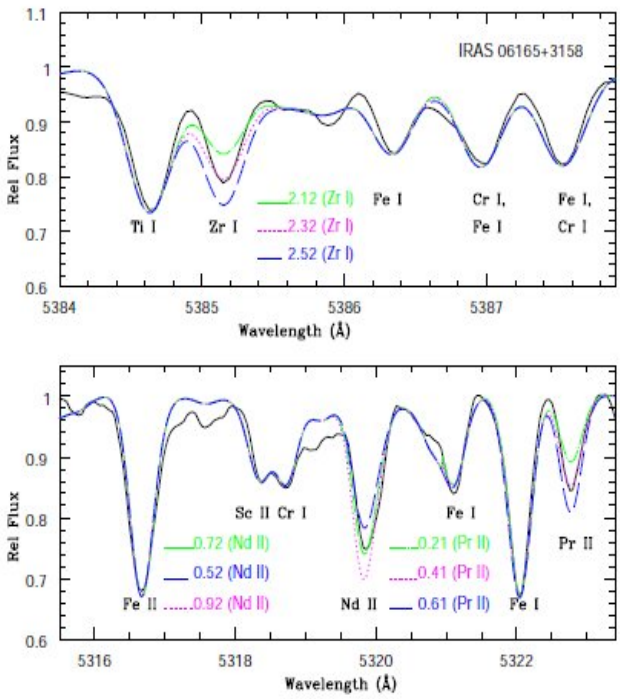

Figure 3.3: The agreement between synthesized and observed spectrum for IRAS 06165+3158 for selected regions containing the lines of s-process elements.

This is atypical star in the sense that at a metallicity of −0.93, the expected enrichment of α elements is not seen ([Ca/Fe]=−0.3, [Ti/Fe]=[Si/Fe]=[Mg/Fe]=0). Also the s-process enrichment is not accompanied by C-enrichment. A continuous photometric and spectrometric monitoring is required to detect the cause of s-process enhancement (binarity ?).

3.6.2 V820 Cen

V820 Cen is listed as an RV Tauri variable in the General Catalogue of Variable Stars (GCVS) with a period of 150 days but photometry (Eggen 1986; Pollard et al. 1996) shows considerable variations in the light curve with Pollard et al. finding three main periods (148, 94 and 80 days). It is assigned photometric type RVa and the spectroscopic type has not been given.

We had two spectra of this object observed on March 2 and 3, 2011. The echelle grating setting being different on these two nights, the coverage in each echelle order was different although some overlap existed. Hence we have conducted two independent

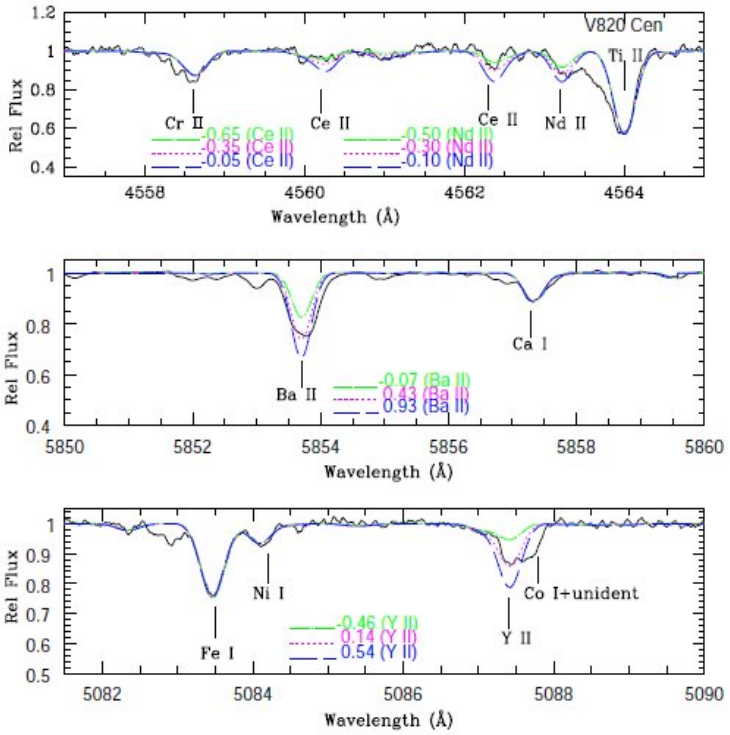

Figure 3.4: The agreement between synthesized and observed spectrum for V820 Cen for selected regions containing the lines of s-process elements.

abundance analyses for these two spectra. We found the same atmospheric parameters for these two epochs which is not surprising given the long period of the object. The abundance analysis (Table 3.4) shows the star to be very metal-poor ([Fe/H] = −2.3) and unaffected by dust-gas winnowing: the α-elements (Mg, Ca, Ti) have their expected [α/Fe] values and Sc is not underabundant. These abundances and the high radial velocity (+265 km s^{-1}) suggest halo membership. The C I lines are below the detection limit and the forbidden lines of O I indicate enhanced O abundance.

The most interesting feature was the detection of lines of several s-process elements present in both spectra. The metal-poor nature of this star was very helpful in detecting the features of these elements. In Figure 3.4 we have shown agreement between the synthesized and observed spectrum for several s-process elements. We do not find significant difference between the light and heavy s-process elements.

This object with RVC spectral characteristics however looks more or less like a twin of V453 Oph given the high radial velocities, low metallicity, C underabundance and mild s-process enrichment.

Table 3.4: Elemental Abundances for IRAS 06165+3158 and V820 Cen

		IRAS 06165+3158			V820 Cen[a]			V820 Cen[b]		
Species	$\log \epsilon_{\odot}$	[X/H]	N	[X/Fe]	[X/H]	N	[X/Fe]	[X/H]	N	[X/Fe]
O I	8.66	−0.49 ± 0.00	1	+0.44	−0.82 ± 0.00	1	+1.46	...		
Na I	6.17	−0.47 ± 0.05	3	+0.46	−1.86 ± 0.00	1	+0.42	...		
Mg I	7.53	−0.90 ± 0.06	2	+0.03	−1.95 ± 0.09	2	+0.33	−2.04 ± 0.00	1	+0.31
Mg II	7.53	...			...			−2.07 ± 0.00	1	+0.28
Si I	7.51	−0.86 ± 0.10	8	+0.07	−1.46 ± 0.11	4	+0.82	...		
Ca I	6.31	−1.22 ± 0.13	11	−0.29	−1.95 ± 0.12	9	+0.33	−2.03 ± 0.15	5	+0.32
Sc II	3.05	−0.95 ± 0.02	1s*	−0.03	−1.78 ± 0.16	3	+0.50	−1.83 ± 0.00	1	+0.52
Ti I	4.90	−0.96 ± 0.12	15	−0.03	−1.77 ± 0.06	2	+0.51	−1.76 ± 0.12	10	+0.59
Ti II	4.90	−1.10 ± 0.14	6	−0.17	−1.90 ± 0.14	11	+0.38	−1.83 ± 0.13	3	+0.52
Cr I	5.64	−0.66 ± 0.08	8	+0.27	−2.50 ± 0.08	6	−0.22	−2.45 ± 0.11	4	−0.10
Cr II	5.64	−0.79 ± 0.00	1	+0.14	−2.40 ± 0.00	1	−0.12	...		
Mn I	5.39	−1.22 ± 0.04	5	−0.29	−2.46 ± 0.01	2	−0.18	...		
Fe	7.45	−0.93			−2.28			−2.35		
Ni I	6.23	−0.69 ± 0.06	6	+0.24	−2.21 ± 0.15	11	+0.07	−2.08 ± 0.08	2	+0.27
Zn I	4.60	−0.99 ± 0.01	2	−0.06	−1.84 ± 0.20	2	+0.44	...		
Sr I	2.92	...			−1.77 ± 0.00	1	+0.51	−1.71 ± 0.00	1	+0.64
Y II	2.21	−0.55 ± 0.04	2	+0.38	−2.07 ± 0.13	1s*	+0.21	−1.98 ± 0.15	2	+0.37
Zr I	2.59	−0.27 ± 0.07	5	+0.66	...			...		
Zr I	2.59	−0.27 ± 0.04	1s*	+0.66	...			...		
Zr II	2.58	...			−1.80 ± 0.14	3	+0.48	−1.88 ± 0.00	1	+0.47
Ba II	2.17	...			−1.74 ± 0.01	1s*	+0.54	...		
La II	1.13	−0.67 ± 0.07	2	+0.26	−1.76 ± 0.17	2	+0.52	...		
Ce II	1.58	−0.63 ± 0.14	4	+0.30	−1.93 ± 0.12	3s*	+0.35	−2.07 ± 0.05	2	+0.28
Pr II	0.78	−0.37 ± 0.00	1s*	+0.56	...			...		
Nd II	1.45	−0.63 ± 0.01	2	+0.30	−1.98 ± 0.18	4	+0.30	−2.17 ± 0.02	2	+0.20
Nd II	1.45	−0.73 ± 0.03	1s*	+0.20	...			...		
Sm II	1.01	−0.67 ± 0.11	3	+0.26	−1.85 ± 0.12	4	+0.43	−1.79 ± 0.01	2	+0.56

* The number of features synthesized for each element has been indicated.

[a] The abundance measurements of V820 Cen for March 2, 2011.

[b] The abundance measurements of V820 Cen for March 3, 2011.

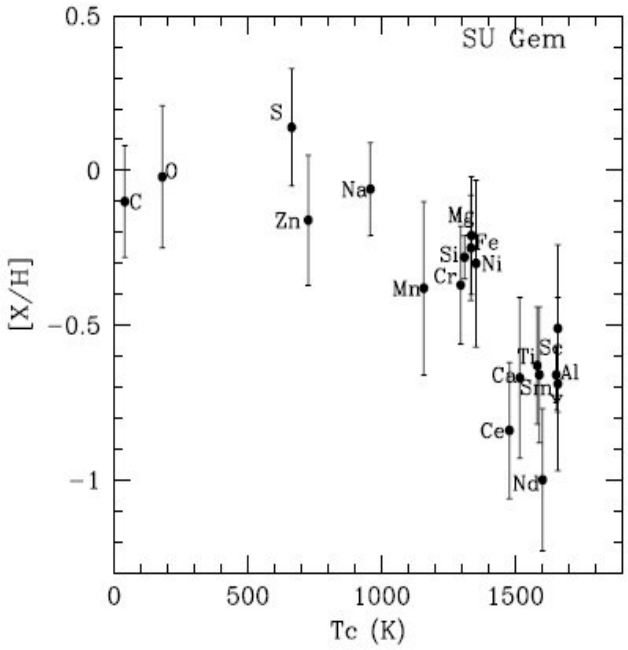

Figure 3.5: Plot of [X/H] versus T_C for SU Gem

3.6.3 IRAS 06108+2743 (SU Gem)

More popularly known as SU Gem, this star is a RVb variable with a pulsation period of 50 days and a long period of 690 days (Joy 1952). Preston et al. (1963) and Lloyd Evans (1985) assigned the spectroscopic type RVA. De Ruyter et al. (2005) constructed the SED for SU Gem and used an optically thin dust model to estimate the parameters of the dust shell and they suggested the possible dust distribution to be in a stable Keplerian disk. Detailed study of the IR spectra of SU Gem (Gielen et al. 2008) indicated the presence of amorphous and crystalline silicates pointing towards an O-rich disk.

The chosen model (Table 3.2) gives the abundances in Table 3.5. Ionization equilibrium is accounted with $\Delta = [X_{II}/H] - [X_I/H]$ is −0.01, +0.11 and +0.02 for Fe, Ti and Cr respectively. The C abundance was derived from the synthesis of the C I line at 6587Å and the O abundance from the 6300 and 6363 Å forbidden lines. It is evident from Figure 3.5 that depletion of elements with the highest T_Cs like Ca, Sc, Ti, Al as well as the s-process elements point to mild dust-gas winnowing.

3.6.4 IRAS 22223+5556 (BT Lac)

Also known as BT Lac, this star is a RV Tauri variable with a period of 40.5 days of the RVb class with a long period of 654 days (Tempesti 1955; Percy et al. 1997). The star was observed on the night of October 10, 2009 and has a V magnitude of 12.8 which is at the faint limit of the telescope. Hence the S/N ratio was only about 30-40 even after co-adding four exposures each of 30 min duration. The number of usable lines were much smaller than what one would expect for this temperature and gravity due to distorted profiles and suggestions of line doubling for several elements. Our analysis relies upon clean symmetrical lines. The metallicity of BT Lac is almost solar ([Fe/H]=−0.2). The O abundance has been determined from the forbidden line at 6300Å. The lines of C and S were distorted and appeared to be double and could not be used in our analysis. Mild dust-gas winnowing is suggested by almost solar Zn abundance and underabundances of Ca, Sc, Ti and the s-process elements Y, Zr, Ce and Sm − see Table 3.5.

3.6.5 TX Per

This star was classified as a RVa variable in the GCVS (see also Percy & Coffey (2005). Zsoldos (1995) gave a period of 78 days. TX Per does not have IRAS colors. Planesas et al. (1991) showed that TX Per had no detected OH maser emission and had weak CO emission pointing to a deficiency of molecules in its envelope.

The abundance analysis (see Table 3.6) shows that the star is mildly metal-poor ([Fe/H] = −0.58). The C and N abundances could not be determined due to the low temperature of the star. The O abundance has been determined using the forbidden lines at 6300 and 6363 Å. The high condensation temperature elements (T_C > 1500K) including α elements Ca, Ti and the s-process elements Zr and Ce again with T_C > 1500K are slightly under-abundant but no signature of dust-gas winnowing is seen as the low T_C element Zn is also underabundant.

3.6.6 IRAS 19135+3937

This is a relatively unexplored object, SIMBAD gives only IRAS fluxes and V magnitude. We list the star as RV-like based on its position in the IRAS two-color diagram− see Figure 3.1. A time-series monitoring of the high-resolution spectra for this star by Gorlova et al. (2012b), indicated radial-velocity variations of the order of 130-140 days. Also the Hα profile variations were found to correlate with the radial velocity phase indicating the possibility of a faint companion surrounded by an accretion disk with an outflow.

Table 3.5: Elemental Abundances for IRAS 06108+2743 and IRAS 22223+5556

		IRAS 06108+2743			IRAS 22223+5556		
Species	$\log \epsilon_{\odot}$	[X/H]	N	[X/Fe]	[X/H]	N	[X/Fe]
C I	8.39	−0.10 ± 0.01	1s*	+0.15	...		
O I	8.66	−0.02 ± 0.10	2	+0.23	+0.56 ± 0.00	1	+0.73
Na I	6.17	−0.06 ± 0.09	3	+0.19	+0.41 ± 0.01	2	+0.58
Mg I	7.53	−0.21 ± 0.02	2	+0.04	+0.02 ± 0.00	1	+0.19
Al I	6.37	−0.66 ± 0.08	4	−0.41	...		
Si I	7.51	−0.28 ± 0.09	9	−0.03	−0.11 ± 0.17	5	+0.06
S I	7.14	+0.14 ± 0.00	1	+0.39	...		
Ca I	6.31	−0.67 ± 0.07	8	−0.42	−0.56 ± 0.07	3	−0.39
Sc II	3.05	−0.51 ± 0.04	4	−0.26	−0.53 ± 0.02	2	−0.36
Ti I	4.90	−0.68 ± 0.05	4	−0.43	−0.57 ± 0.12	11	−0.40
Ti II	4.90	−0.57 ± 0.16	4	−0.32	−0.68 ± 0.01	2	−0.51
Cr I	5.64	−0.38 ± 0.10	4	−0.13	−0.14 ± 0.03	2	+0.03
Cr II	5.64	−0.36 ± 0.02	3	−0.11	−0.23 ± 0.00	1	−0.06
Mn I	5.39	−0.38 ± 0.04	3	−0.13	−0.40 ± 0.11	1s*	−0.23
Fe	7.45	−0.25			−0.17		
Ni I	6.23	−0.30 ± 0.17	6	−0.05	−0.22 ± 0.11	18	−0.05
Zn I	4.60	−0.16 ± 0.01	2	+0.09	−0.12 ± 0.05	2	+0.05
Y II	2.21	−0.69 ± 0.10	3	−0.44	−0.66 ± 0.09	2	−0.49
Zr II	2.59	...			−0.70 ± 0.00	1	−0.53
Ce II	1.58	−0.84 ± 0.13	3	−0.59	−0.36 ± 0.05	3	−0.19
Nd II	1.45	−1.00 ± 0.07	3	−0.75	...		
Sm II	1.01	−0.66 ± 0.05	3	−0.41	−0.50 ± 0.12	2	−0.33

* The number of features synthesized for each element has been indicated.

Table 3.6: Elemental Abundances for TX Per and IRAS 19135+3937

		TX Per			IRAS 19135+3937		
Species	$\log \epsilon_{\odot}$	[X/H]	N	[X/Fe]	[X/H]	N	[X/Fe]
C I	8.39	...			-0.23 ± 0.11	4	+0.81
O I	8.66	-0.11 ± 0.11	2	+0.47	-0.29 ± 0.00	1	+0.75
Na I	6.17	-0.68 ± 0.13	3	−0.10	-0.87 ± 0.00	1	+0.17
Mg I	7.53	-0.57 ± 0.08	2	+0.01	-0.75 ± 0.02	2	+0.29
Al I	6.37	-0.80 ± 0.00	1	−0.22	...		
Si I	7.51	-0.19 ± 0.07	6	+0.39	...		
S I	7.14	...			-0.74 ± 0.02	2	+0.30
Ca I	6.31	-1.12 ± 0.07	8	−0.54	-1.33 ± 0.17	4	−0.29
Ca II	6.31	...			-1.37 ± 0.00	1	−0.33
Sc II	3.05	...			-1.23 ± 0.01	3	−0.19
Ti I	4.90	-0.88 ± 0.09	9	−0.30	...		
Ti II	4.90	-0.79 ± 0.04	2	−0.21	-1.54 ± 0.10	4	−0.50
Cr I	5.64	-0.56 ± 0.05	4	+0.02	-1.20 ± 0.16	3	−0.16
Cr II	5.64	-0.66 ± 0.03	2	−0.08	-1.19 ± 0.13	7	−0.15
Mn I	5.39	-0.76 ± 0.12	6	−0.18	-1.05 ± 0.19	2	−0.01
Fe	7.45	−0.58			−1.04		
Ni I	6.23	-0.84 ± 0.10	10	−0.26	-0.86 ± 0.14	5	+0.18
Zn I	4.60	-0.86 ± 0.07	2	−0.28	-1.08 ± 0.01	2	−0.04
Y II	2.21	...			-1.33 ± 0.07	2	−0.29
Zr I	2.59	-1.40 ± 0.04	2	−0.82	...		
Zr II	2.59	...			-1.17 ± 0.12	2	−0.13
La II	1.13	...			-1.85 ± 0.00	1	−0.81
Ce II	1.58	-1.35 ± 0.04	3	−0.77	-1.63 ± 0.00	1	−0.59
Nd II	1.45	...			-1.28 ± 0.00	1	−0.24

Our spectrum is not ideal. All lines appear to have a red-shifted absorption component. We have measured a few reasonably clean lines. The lines of N and Si were heavily distorted indicating unresolved doubling and hence the abundances for these elements could not be determined. The star is metal poor with [Fe/H] of −1.0. The first α element sulfur yields [S/Fe] of +0.3 which is expected at this metallicity. The α elements Ca and Ti and the s-process elements have negative [X/H] values as can be seen in Table 3.6. The initial Fe abundance close to the observed [Fe/H] of −1.0 suggests halo or thick disk membership. But IRAS 19135+3937 despite being a possible member of a binary (Gorlova et al. 2012b) does not show signature of dust-gas winnowing as evident from the Zn abundance in Table 3.6. An overabundance of C I ([C/Fe]=+0.8 dex) is derived from the measurement of four reasonably clean (but asymmetric) lines. This star deserves further analysis with spectra at more stable phases.

3.6.7 IRAS 01427+4633

This was considered as a RV Tau like object based upon its location in two color IRAS diagram and no photometry is available. Recently Gorlova et al. (2012a) group conducted the radial velocity monitoring of this object for nearly three years starting 2009 and also conducted abundance analysis. Gorlova et al. found this object to be a spectroscopy binary with an orbital period of 140.8 ± 0.2 days and eccentricity e of 0.083 ±0.002 and asini of 0.31 AU.

The model parameters derived from our spectra are presented in Table 3.2. We estimate model atmospheric parameters $T_{\rm eff}$, $log\ g$, and ξ of (6500,0.5,3.5) while Gorlova et al. estimate (6250,1.5,4.0). Ionization equilibrium is satisfactorily accounted for in that $\Delta = [X_{II}/H] - [X_I/H]$ is −0.10, −0.06, +0.01 and +0.01 for Fe, Si, Ti and Cr respectively as can be seen in Table 3.7.

The star is metal poor with [Fe/H] of −0.79 and is enriched in the α elements Mg, Si, Ca and Ti with an average [α/Fe] of +0.34. The low metallicity and the α abundances point towards thick disk membership. Enrichment of the light elements C, N and O suggests that the star has evolved beyond the Red Giant Branch (RGB) but substantial exposure to thermal pulses on the AGB is unlikely to have occurred as the C/O ratio is around 0.5; the *s*-process elements are not overabundant.

The abundance analysis by Gorlova et al. (2012a) use solar *gf* values normalised to solar abundances of Grevesse et al. (1996) and model atmosphere by Kurucz (1992) while we use solar abundances from Asplund et al. (2005). We therefore chose to make comparison using logϵ derived from the two studies. We find difference between Gorlova et

al - Present work as follows; +0.27 for C, +0.07 for N, −0.11 for Mg, +0.10 for Si, −0.05 for S, −0.15 for Ca, −0.26 for Sc, −0.26 for Ti, +0.06 for Cr, +0.04 for Mn, −0.31 for Ni, −0.01 for Zn, −0.15 for Y and −0.13 for Ba. For majority of elements the agreement is within ±0.20 dex.

We did not find very convincing evidence for dust-gas winnowing. Although [S/Fe] is +0.37, it could be attributed to the fact that it is an α element. In fact other α elements like Si, Ti also show similar enrichment although [Ca/Fe] is relatively smaller. With [Zn/Fe] of −0.08 and positive [Sc/Fe], it very unlikely that dust-gas winnowing has affected this object. This star is similar to IRAS 07140-2321 studied in Sumangala Rao et al. (2012) in the sense that despite favourable conditions such as warm temperature, presence of binary companion and circumstellar material the effect of dust-gas winnowing is not seen thereby highlighting our inadequate understanding of this effect.

3.6.8 HD 52961

HD 52961 is a high Galactic latitude F type supergiant with a strong IR excess and is a semi-regular (SRD) variable with a pulsation period of 70 days (Waelkens et al. 1991). The light curve exhibits the long-term RVb like phenomenon in the mean magnitude (seen in RV Tau stars) thought to be caused due to the variable circumstellar extinction during orbital motion (Van Winckel et al. 1999). But the light curve does not exhibit alternate deep and shallow minima typically seen in RV Tau stars and has been labeled as RV Tau like object in Figure 3.1. Radial velocity monitoring was carried out by Van Winckel et al. (1999) who report the star to be a spectroscopic binary with an orbital period of 1310 days.

Deroo et al. (2006) who resolved the dusty disk of HD 52961 using N-band interferometry found that the dust emission at 8 micron originates from a compact region of diameter 50 AU. Gielen et al. (2009a) analyzed a high resolution IR spectrum and found that it was dominated by spectral features from both amorphous and crystalline silicates. The high crystallinity fraction and large sized grains show that the dust grains are strongly processed and that the disk is long-lived. Even though the analysis of HD 52961 showing significant depletion of refractory elements in its photosphere was conducted (Waelkens et al. 1991; Van Winckel 1995), an extensive abundance analysis with the most recent *gf* values was lacking.

Hence we have performed a detailed abundance analysis for HD 52961 (see Table 3.7) using our selection of *gf* values and Kurucz model atmospheres. We have compared our results with those of Van Winckel (1995) ; agreement is within ±0.2 dex for elements in

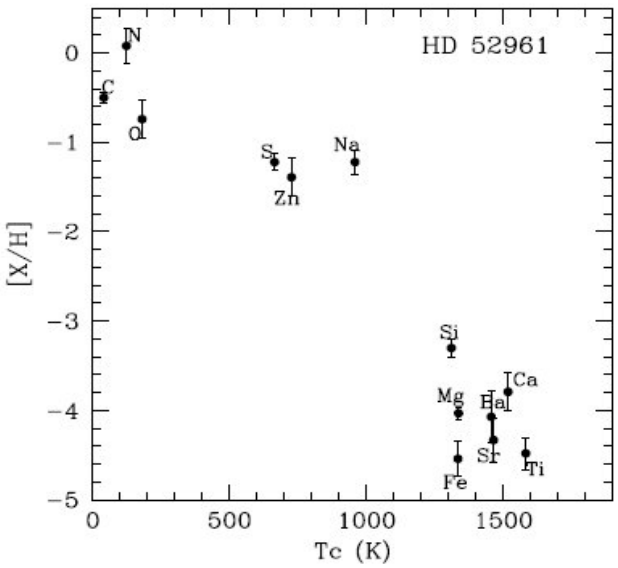

Figure 3.6: Plot of [X/H] versus T_C for HD 52961

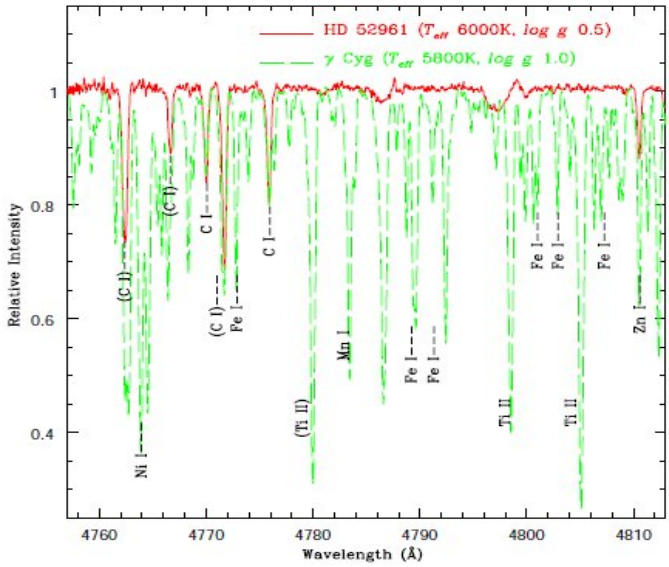

Figure 3.7: Comparison between the spectrum of the heavily depleted star HD 52961 with that of γ Cyg a normal supergiant. In the spectrum of HD 52961, note the weakness of the metallic lines but the lines of C I and Zn I are clearly seen.

common. We were able to determine for the first time the abundance of Na, Mg, Si, Ca and Ti as can be seen in Table 3.7. It has resulted in better definition of the depletion

curve. Figure 3.6 shows the plot of [X/H] versus T_C for HD 52961, a classic case of dust-gas winnowing. In 3.7 we compare the spectrum of HD 52961 with that of the normal F supergiant γ Cyg of similar temperature and gravity to demonstrate depletion.

3.6.9 V453 Oph

This is a RV Tauri variable of spectroscopic type RVC and photometric type RVa. A photometric period of 80 days was obtained by Pollard et al. (1996). The star does not have an IR excess (Deroo et al. 2005) .

Our spectrum gives model parameters ($T_{\rm eff}$ = 5750 K, log g =1.50, and $\xi_{\rm t}$ = 3.7 km s^{-1}) similar to those derived by Deroo et al. ($T_{\rm eff}$ = 6250 K, log g =1.50, and $\xi_{\rm t}$ = 3.0 km s^{-1}). The star is variable so exact agreement for atmospheric parameters is not expected. It would appear that we observed the star at a slightly cooler phase than Deroo et al. The abundances are in good agreement. We find δ [X/Fe] (present work − Deroo et al.) of +0.13 for C, −0.12 for O, +0.06 for Mg, +0.15 for Al, +0.18 for Si, −0.04 for Ca, −0.12 for Sc, +0.04 for Ti, −0.10 for Cr, +0.30 for Mn, −0.13 for Ni, +0.23 for Zn, +0.06 for Y, +0.07 for Zr, −0.06 for Ba, +0.23 for La, +0.19 for Ce, −0.02 for Nd, +0.32 for Eu and +0.15 for Dy. We could determine the additional elements Na and the s-process element Gd for this star. But the N abundance could not be determined as our spectrum was obtained at a cooler phase than that of Deroo et al. (2005).

The metal abundances and the high radial velocity (−126 kms^{-1}) suggest that V453 Oph is a member of the Galactic halo. There is no evidence that dust-gas winnowing has affected the star. An interesting feature is the clear *s*-process enrichment reported first by Deroo et al. The mean enrichment [*s*/Fe] is about +0.6 with possibly a larger enrichment for the heavy (Ba-Gd) than for the light (Y,Zr) elements as can be seen in Table 3.7. This enrichment is presumably the result of Third Dredge-Up (TDU) in the AGB progenitor but the lack of a C-enrichment, also reported by Deroo et al., is puzzling. (Our C abundance is obtained from CH lines at 4300-4320 Å. Deroo et al's C abundance was obtained from the synthesis of C lines around 9070Å.)

3.7 Evolutionary Context of RV Tauri stars

With the calibrated Period-Luminosity (P-L) relation for population II Cepheids and RV Tauri variables in the LMC by Alcock et al. (1998), it is possible to estimate the luminosities of RV Tauri stars so that they may be placed in the H-R diagram and compared

Table 3.7: Elemental Abundances for IRAS 01427+4633, HD 52961 and V453 Oph

		IRAS 01427+4633			HD 52961			V453 Oph		
Species	$\log \epsilon_{\odot}$	[X/H]	N	[X/Fe]	[X/H]	N	[X/Fe]	[X/H]	N	[X/Fe]
C I	8.39	−0.55 ± 0.11	5	+0.24	−0.15 ± 0.22	19	+4.39	−2.39 ± 0.01	CHs†	−0.13
N I	7.78	+0.02 ± 0.05	3	+0.81	+0.08 ± 0.00	1	+4.62	...		
O I	8.66	−0.50 ± 0.01	3s*	+0.29	−0.38 ± 0.03	2	+4.16	−1.39 ± 0.00	1	+0.87
Na I	6.17	...			−1.10 ± 0.01	2	+3.44	−1.91 ± 0.00	1	+0.35
Mg I	7.53	−0.50 ± 0.06	4	+0.29	−3.74 ± 0.02	2	+0.80	−1.95 ± 0.06	4	+0.31
Mg II	7.53	...			−3.68 ± 0.00	1	+0.86	...		
Al I	6.37	...			...			−2.68 ± 0.04	2	−0.44
Si I	7.51	−0.32 ± 0.09	3	+0.47	...			−1.61 ± 0.06	2	+0.65
Si II	7.51	−0.38 ± 0.00	1	+0.41	−3.08 ± 0.00	1	+1.46	−1.72 ± 0.02	2	+0.54
S I	7.14	−0.42 ± 0.05	2	+0.37	−0.92 ± 0.11	4	+3.62	...		
Ca I	6.31	−0.65 ± 0.04	5	+0.14	...			−2.12 ± 0.04	4	+0.14
Ca II	6.31	...			−3.61 ± 0.00	1	+0.90	...		
Sc II	3.05	−0.41 ± 0.07	4	+0.38	...			−2.10 ± 0.01	1s*	+0.16
Ti I	4.90	−0.31 ± 0.09	2	+0.48	...			...		
Ti II	4.90	−0.30 ± 0.02	2	+0.49	−4.27 ± 0.00	1	+0.27	−1.93 ± 0.11	10	+0.33
Cr I	5.64	−0.91 ± 0.12	2	−0.12	...			−2.49 ± 0.08	4	−0.23
Cr II	5.64	−0.90 ± 0.11	6	−0.11	...			−2.45 ± 0.07	2	−0.19
Mn I	5.39	−0.91 ± 0.07	2	−0.12	...			−2.59 ± 0.00	1s*	−0.33
Fe	7.45	−0.79			−4.54			−2.26		
Ni I	6.23	−0.55 ± 0.12	5	+0.24	...			−2.52 ± 0.10	4	−0.26
Zn I	4.60	−0.87 ± 0.07	2	−0.08	−1.27 ± 0.09	3	+3.27	−1.90 ± 0.11	2	+0.36
Sr II	2.92	...			−4.33 ± 0.00	1	+0.21	...		
Y II	2.21	−1.07 ± 0.00	1	−0.28	...			−1.93 ± 0.06	4	+0.33
Zr II	2.59	...			...			−1.58 ± 0.11	4	+0.68
Ba II	2.17	−0.64 ± 0.02	1s*	+0.15	−4.26 ± 0.00	1	+0.28	−1.91 ± 0.08	2	+0.35
La II	1.13	...			...			−1.54 ± 0.00	2	+0.72
Ce II	1.58	−0.98 ± 0.14	3	−0.19	...			−1.61 ± 0.08	4	+0.65
Nd II	1.45	...			...			−1.60 ± 0.12	4	+0.66
Eu II	0.52	...			....			−1.22 ± 0.00	1s*	+1.04
Gd II	1.14	...			...			−1.23 ± 0.00	1s*	+1.03
Dy II	1.14	...			...			−1.43 ± 0.07	2	+0.83

† refers to synthesis of CH bands.

* The number of features synthesized for each element has been indicated.

with evolutionary tracks for different progenitor masses. Figure 3.8 shows the H-R diagram adapted from Gingold (1985). The location of the population II instability strip are denoted by continuous lines. This strip was found to be three times wider and 3.5 magnitude fainter than the classical instability strip. The red edge of the population II strip was found to be redder than the classical instability strip possibly due to the variations in their metallicities (Demers & Harris 1974; Gingold 1985). The lines of constant period (dotted lines) are shown. The theoretical stellar evolutionary tracks for a $0.536M_{\odot}$ and a $0.6M_{\odot}$ star for Z = 0.001 (typical for population II Cepheids) and Y=0.3 are also shown starting from the blue horizontal branch. These tracks mainly depend on the mass of the stellar envelope and only weakly on the initial metallicity. The region of the thermal pulses and RV Tauri variables have been marked in the figure. The Period-Luminosity-Color (P-L-C) relation for the LMC RV Tauri and population II Cepheid variables (Alcock et al. 1998) uses the average (V-R) colors. The scatter in the P-L-C relation (σ=0.15) is smaller than for the P-L relation (σ=0.4). But the (V-R) colors are available only for a handful of RV Tauri stars (Goldsmith et al. 1987; Pollard et al. 1996). Also the T_{eff} calibration versus (V-R) colors for different metallicities are available only for dwarfs and giants (Alonso et al. 1999). Using the (V-R) colors from this calibration would produce incorrect luminosities for the RV Tauri variables as they are supergiants. Hence, we elect to use the P-L relation for determining the luminosities (M_V) and hence $\log(L/L_{\odot})$ for variables with periods available in the literature. The Bolometric corrections for determining the M_{bol} ($*$) for supergiants were taken from Schmidt-Kaler (1982) given in Aller et al. (1982). Finally the luminosities i.e. $\log(L/L_{\odot})$ in our Table 3.8 and Table 3.9 were calculated using the standard relation:

$$M_{bol}(*) - M_{bol}(\odot) = -2.5log(L*/L_{\odot}) \tag{3.1}$$

In addition to the uncertainty in the luminosity caused by the neglect of the color term, other uncertainties result due to the differences in metallicity between the stars in our galaxy and that of the LMC. To explore this, we have plotted a few LMC RV Tauri variables of almost similar periods (around 50 days) in Figure 3.8 and found that they are shifted systematically to higher luminosities by 0.2-0.3 magnitude. These error bars will have to be considered for the calculated luminosities in our Table 3.8 and Table 3.9.

For the post-AGBs plotted in the Figure 3.8 the sources of luminosities are as follows: HD 46703 (Luck & Bond 1984), HD 213985 (Waelkens et al. 1987), HD 56126 (Hony et al. 2003), HD 187885 (Clube & Gledhill 2004) and for HD 44179 (De Ruyter et al. 2006). In most of these post-AGBs the parallaxes/distance measurements are known

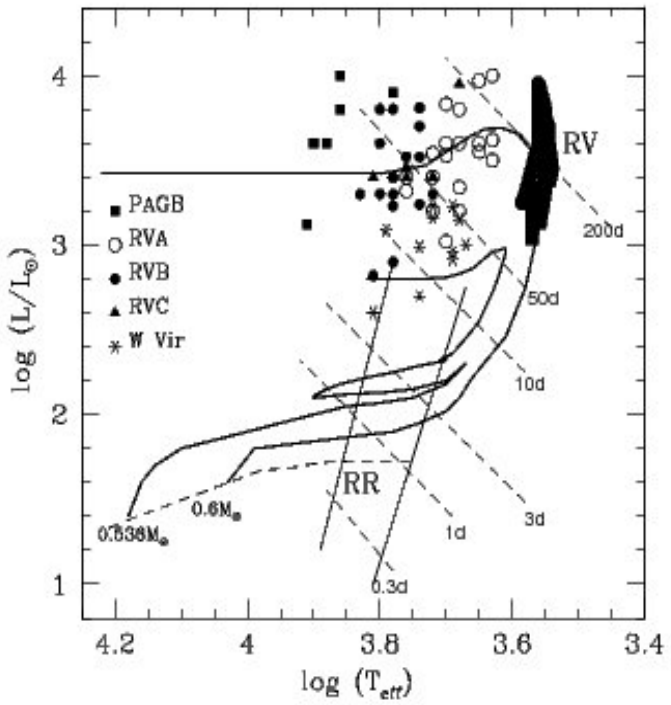

Figure 3.8: H-R diagram showing the location of the population II instability strip, lines of constant period and the theoretical evolutionary tracks for a 0.536 and 0.6$M_{\odot}$ star. The location of the well studied RV Tauri stars, W Vir variables and psot-AGB stars have been shown.

from the above mentioned sources. With the known distances we determined the absolute magnitudes through the distance-modulus formula and hence derived the luminosities from the above equation. For HD 172481 a post-AGB star having a Mira companion, a luminosity of $10^4 L_{\odot}$ was obtained using the P-L relation for Mira variables by Whitelock & Marang (2001).

Three categories of post-horizontal branch stars (BL Her, W Vir and RV Tauri variables) crossing the instability strip are known. BL Her variables are believed to be the low-luminosity analogs of the population II Cepheids having short periods in the range of 1-5 days. Following He exhaustion in their cores, they leave the horizontal branch and evolve towards the AGB by crossing the instability strip and define blueward noses due to structural re-adjustments between the hydrogen and helium burning shells. From the abundance analysis of several BL Her variables it was seen that excepting Na enrichment they show normal compositions (Maas et al. 2007). W Vir variables are the population-II Cepheids with periods greater than 10 days. They are believed to be undergoing blue-

ward loops from the AGB in response to the helium shell flashes and have more evolved double shell structure on the AGB. The W Vir variables are found to have smaller envelope masses when compared to RV Tauri variables. This is evident from the calculated luminosities for these variables presented in Table 3.8 and Table 3.9. Thus W Vir variables may finally evolve to become lesser luminous post-AGBs when compared to RV Tauris. RV Tauri stars on the other hand are at still higher luminosities (see Table 3.8 and Table 3.9) and are a longer period extension of the population II Cepheids which cross the instability strip to evolve towards higher temperatures (Gingold 1976, 1985). RV Tau variables may evolve off the AGB either before or during the era of thermal pulses. Evolution takes a star from the instability strip to the blue where it may be given the label of post-AGB star even though some post-AGB stars may not have experienced evolution along the population II instability strip and sufficient number of thermal pulses.

Even though there are some similarities between post-AGBs and RV Tauri variables with respect to luminosities and IR excesses certain differences exist. RV Tauri stars show large-amplitude variations due to radial pulsations in their envelopes and exhibit an almost regular light curve. They are thought to be still residing within the instability strip. Kiss et al. (2007) conducted the photometry for a sample of RV Tauri and post-AGB stars and reported the amplitude of light variation for RV Tauris in the range of 0.5-1.5 and 0.05-0.5 magnitude for post-AGBs. Thus post-AGBs can be thought to be more evolved than RV Tauris as some of them show small amplitude irregular pulsations possibly reminiscent of RV Tau variables. This is further substantiated by the position of the post-AGB and RV Tau variables in the H-R diagram (see Figure 3.8) notwithstanding the limited sample. From Figure 3.8 it appears that the RVB variables may be more evolved than RVAs which appear to be have just left past the AGB phase. But the post-AGBs which are to the left of all the RV Tau variables appear to be in a much more advanced stage of evolution. Thus it appears that all RV Tauri variables evolve finally to become post-AGB stars and atleast those post-AGBs that display the small amplitude pulsations might have passed through the instability strip briefly as a RV Tau variable. The proposed evolutionary status of RV Tau objects as post-AGBs evolving to the white dwarf stage is further supported by the photometric observations of Percy (1999) who found that 13 out of his sample of 16 RV Tau stars showed decreasing periods.

3.8 Discussion

3.8.1 Chemical Compositions of the RV Tauri sample

From the compilation of the existing data on the chemical compositions of RV Tau and RV Tau like objects it can be seen that they can be divided into roughly four groups. They either have a normal composition (elements of high T_C like Fe, Sc etc are unaffected), a composition affected by dust-gas winnowing, a clear enrichment of *s*-process products, or an otherwise abnormal composition like FIP effect (see Table 3.8 and Table 3.9). Footnotes being common for Table 3.8 and Table 3.9 are given at the end of Table 3.9. Within the different categories of stars in Table 3.8 and Table 3.9, the stars in each category have been arranged in the order of increasing temperatures first for stars with binary detections (Y) followed by non-detections (N). Stars with and without binary detections have been marked as Y and N. The explanation for Y and N have been provided in the footnote following Table 3.9. Only stars for which radial velocity monitoring have confirmed binary detections have been considered which has resulted in smaller fraction of binarity compared to other workers. This number may change when more detections are reported. Table 3.8 comprises only of stars showing dust-gas winnowing and FIP effect. Table 3.9 contains stars showing s-process enrichment and those having normal compositions.

The main signature of dust-gas winnowing is an observed dependence of depletion of condensable elements on the predicted T_C. Since Fe is also found to be depleted by this process, it cannot be the true indicator of intrinsic metallicity hence Zn and S which are least affected by this process (due to their low T_Cs) would serve as metallicity indicators. We have calculated the intrinsic metallicity: $[Fe/H]_o$ by taking the average of [S/H] and [Zn/H]. We consider the star to be well depleted when [Zn/Fe] is positive and [Sc/Fe] negative and denote them as DG in Table 3.8. Some stars have incomplete signature of dust-gas winnowing in the sense that [Sc/Fe] is negative while [Zn/Fe] is normal and are considered as stars for which the dust-gas winnowing is mild and are denoted as MDG in Table 3.8.

We have considered the high T_C elements Sc, Fe and the lower T_C elements Zn and S as a quantitative measure of DG and hence we have listed the abundances of these elements in stars affected by DG (see Table 3.8). To distinguish the DG effect from other effect related to ISM composition we have used the compilation of abundances for thin, thick disk and halo dwarfs and giants by Reddy et al. (2006).

In general, we adopt [Zn/Fe] $\geq +0.3$ and [Sc/Fe] ≤ -0.3 as potential and clean signatures of an abundance anomaly. In making a judgement about abundance anomalies,

we consider other elements from Na to Zn. We do not consider C, N and O in detail because they are surely affected by internal nucleosynthesis and dredge up and also present data on their abundances are sparse and uncertain. Elements heavier than Zn enter into the question of whether the star is enriched in *s*-process products. Where dust-gas winnowing is present, *s*-process enrichment is judged by comparing *s*-process elements with other (lighter) elements of similar T_C.

3.8.2 Dust-gas winnowing

Signatures of dust-gas winnowing are considered to be revealed by plotting elemental abundances versus the predicted T_C which, as noted above, are computed for a solar composition and equilibrium cooling at a low gas pressure. The higher the T_C the greater is the expected deficiency of that element in the residual gas. The pattern of abundance deficiency versus condensation temperature ([X/H] vs T_C) will depend on several factors such as the initial composition of the reservoir from which a star draws gas and the temperature (and pressure) distribution within the reservoir. Factors of particular concern appear to be the C/O and Mg/Si ratios (Bond et al. 2010a,b). As C/O crosses the boundary C/O=1, the predicted T_C for several elements decrease by several hundred degrees (e.g., Al 300K, Ca 300K, Mg 300K), some increase by several hundred degrees (e.g., C 800K, O 800K, Si 300K, Ti 200K) and others retain a similar T_C (e.g., Cr, Fe, Na, Ni, S). These estimates are drawn from Bond et al. (2010b)'s Table 9 where a restricted list of elements are given.[§]

In the entire sample of RV Tau and W Vir stars in Table 3.8, six of them (IW Car, RV Tau, TW Cam, V Vul, MZ Cyg and SZ Mon) have C/O ratios greater than 1. But the depletion plots of these stars with the Bond et al.'s T_C values for C/O>1 reduced the scatter only in the cases of the W Vir variables: SZ Mon and MZ Cyg.

The type of grain formation mainly depends on the C/O ratio in the stellar photosphere. When the C/O<1, the photospheric gas is O-rich and the excess oxygen will result in the formation of O-rich dust as in the form of amorphous silicates with broad features at 9.7 and 18 micron and narrower crystalline silicate features at 11.3, 16.2, 19.7, 23.7, 28 and 33.6 micron. When the C/O>1, the excess carbon results in the formation of C-rich dust which produces several features at 11.3 micron (SiC) , 21 micron (thought to be due to TiC nano crystals), 30 micron (MgS) and also several features at 3.3, 6.2, 7.7 and 8.7 micron arising due to PAHs are seen (Van Winckel 2003; García-Lario 2006).

[§]Bond et al. (2010a) show that their T_C agree very well with those given by Lodders (2003) for the same composition and pressure.

Gielen et al. (2007, 2008) have analyzed and modelled the IR spectra of a sample of RV Tauri and post-AGB stars. In most of the cases the circumstellar dust was found to be O-rich with varying degrees of amorphous and crystalline (Fosterite and Enstatite) features of silicates dominating the IR spectra. Large sized grains (larger than 2 micron) and high degree of crystallinity were found indicating that the disks were highly evolved. From the spectral fitting and modelling of RV Tauri stars with the dust-gas effect, they were found to have both cool (T=110-250K) and hot dust (T=230-900K) components. Only the RV Tauri star EP Lyr was found to have a mixed chemistry with both the PAH emission and silicate features present in its IR spectra (Gielen et al. 2009a).

Various abundance patterns ([X/H] vs T_c) attributed to dust-gas winnowing are seen among the RV Tau variables. To illustrate the variety of these patterns, we reproduce results for representative stars.

There are stars for which the signature is faint and the invocation of dust-gas winnowing perhaps questionable. These have been designated as 'Mild DG' in Table 3.8. These MDG RV Tauri stars (including MDG W Vir stars) have systematically lower temperatures in the range of 4250-5300K with the exception of RX Cap (5800K) when compared with the heavily depleted ones (DG). Out of the entire MDG RV sample, 33% have no IRAS detections (including RV Tau and W Vir stars but excluding RV Tau like stars denoted by MDG in Table 3.8). Since only a handful of these stars have orbital period determinations, we cannot comment on the correlation between the orbital period and depletion. Several such examples were found in the analysis of W Vir variables. Figure 3.9 shows the results for CO Pup, V1711 Sgr and MZ Cyg, three low luminosity variables where CO Pup and MZ Cyg do not have IRAS detections.

Abundances are adjusted to account for what were the presumed initial abundances based on the Zn abundance as the indicator of the initial Fe abundance, i.e., the α-elements Mg, Si, Ca and Ti were given initial abundances [α/Fe] = +0.3. At the high T_C, Al, Sc and Ti abundances are under-abundant relative to Zn, a low condensation monitor, and to Fe. For example, [Sc/Zn] is -0.5, -1.5 and -0.9 for CO Pup, V1711 Sgr and MZ Cyg respectively. It is not clear if this under-abundance can be attributed to dust-gas winnowing or to systematic errors in the abundance analysis, i.e., non-LTE effects having a more serious effect on Sc than Fe.

In contrast to Figure 3.9, Figure 3.10 shows results for UY CMa, HP Lyr and DY Ori where the [X/H] increases smoothly with decreasing T_C. Their [Sc/Zn] runs from -1.4 to < -2.9, that is Sc and other elements of high T_C are 3 dex deficient relative to the initial abundances for the star. The extreme case in our sample is CC Lyr where Fe is 3 dex

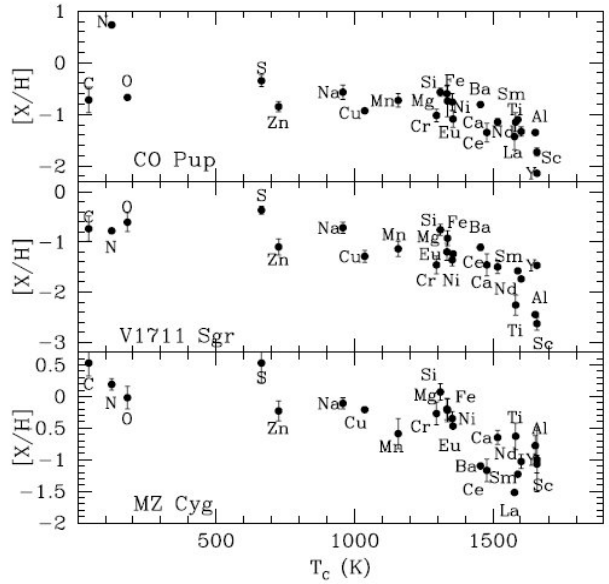

Figure 3.9: Plots of [X/H] versus T_C for the W Vir variables: CO Pup, V1711 Sgr and MZ Cyg. The values of [X/H] are from Maas et al. (2007)

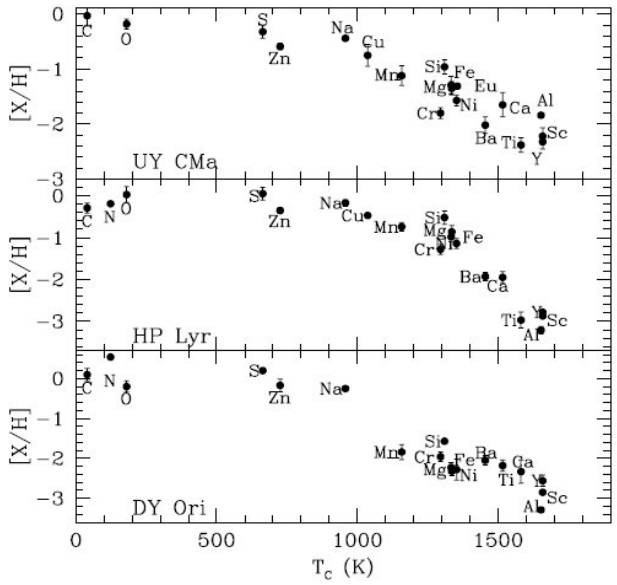

Figure 3.10: Plots of [X/H] versus T_C for the RV variables: UY CMa, HP Lyr and DY Ori. The values of [X/H] are from Giridhar et al. (2005)

deficient and Sc lines were not detectable − see Figure 3.11 for the depletion plot of CC Lyr. The shapes of the correlations at the highest T_C are different in these three cases. In

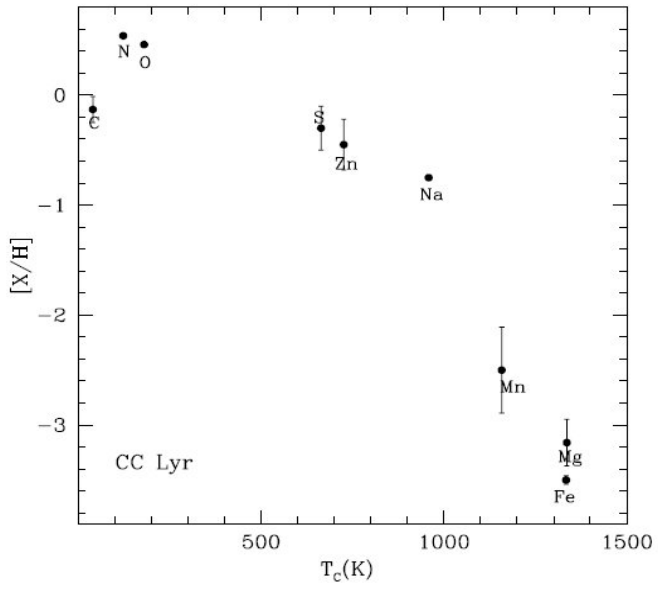

Figure 3.11: Plot of [X/H] versus T_C for the W Vir variable: CC Lyr. The values of [X/H] are from Maas et al. (2007)

particular, one notes the different slopes in [X/H] versus T_C above about 1000K. In some stars, the slope becomes almost a precipice, e.g., R Sct − see Figure 3.13, where [X/H] is −0.4 for Ti, −0.7 for Al but −1.4 for Sc (Giridhar et al. 2000) . This striking decline of the abundance [X/H] with increasing T_C from (say) Fe to Sc is shown by many of the affected stars.

For a few stars with large negative [X/H] for Fe to Sc, the impression given is that elements of the highest T_C (say, > 1400K) have similar deficiencies [X/H]. Figure 3.12 shows such results for EP Lyr and AD Aql. The observed abundances [X/H] for EP Lyr have been taken from Gonzalez et al. (1997b) and for AD Aql from Giridhar et al. (1998).

Whenever correlations with T_C are obvious there is scatter about a mean relation but often this is comparable to the measurement uncertainties. Inspection of the Figure 3.9, Figure 3.10 and Figure 3.12 illustrating dust-gas winnowing suggests the presence of several persistent outliers, for example, S and Zn have similar T_C but S is usually more abundant than Zn, Na tends to fall above the mean trend, and Si is almost always above the mean trend. Such outliers may be second-order clues to the working of the winnowing process.

The inferred initial metallicity $[Fe/H]_o$ of the dust-gas winnowed stars (considering both DG and MDG in Table 3.8) run from +0.2 for IW Car to −1.4 for the LMC RV Tauri: MACHO 81.8520.15.

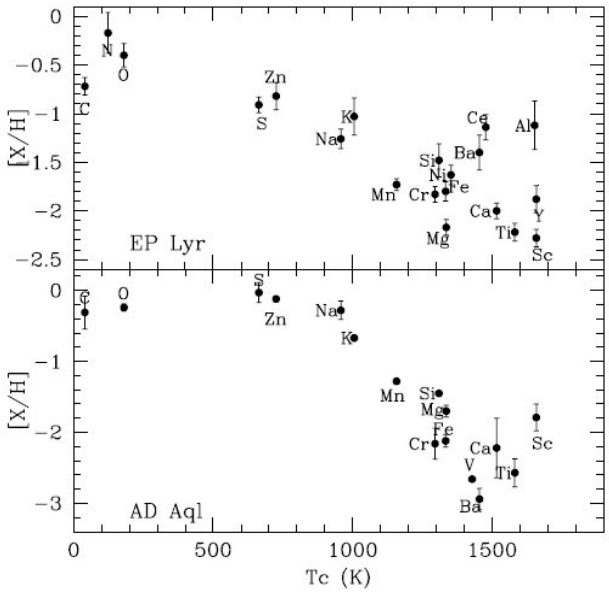

Figure 3.12: Plot of [X/H] versus T_C for EP Lyr and AD Aql. The values of [X/H] for EP Lyr are from Gonzalez et al. (1997b) and for AD Aql from Giridhar et al. (1998)

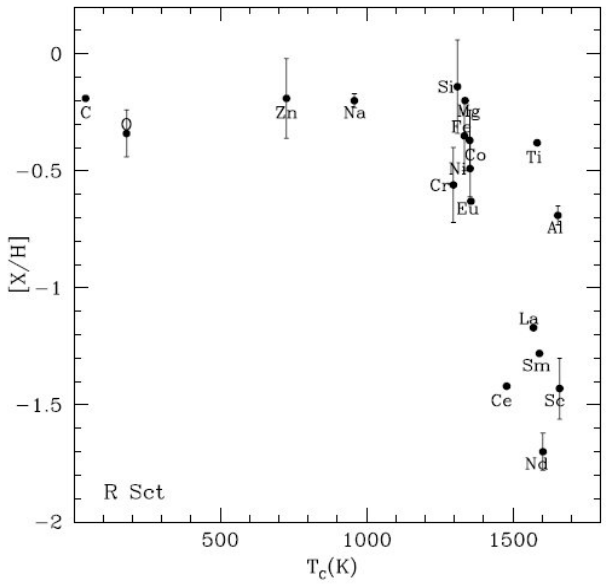

Figure 3.13: Plot of [X/H] versus T_C for the RV variable: R Sct. The values of [X/H] are from Giridhar et al. (2000)

The shape of the abundance−condensation temperature plot is expected to be dependent on several factors of which the following combination would seem to be important:

(i) the composition of the gas and dust in the environment from which material is accreted by the star; (ii) the gas to dust ratio of the accreted material; (iii) the rate and degree of mixing of the accreted material with the atmosphere/envelope of the star. Present consensus is that the dust-gas winnowing is most effective in RV Tauri variables that belong to a binary system with a circumbinary dusty disk providing the reservoir from which gas is accreted by the RV Tauri star (Maas et al. 2005; Van Winckel 2007).

A limiting case for accretion from the dusty reservoir is that gas but not dust is accreted. The stellar atmosphere attains a composition that is dependent on the rate of accretion and the speed with which the accreted gas is mixed with the existing envelope. If the mixing occurs very slowly with respect to the rate of accretion, there is the likely possibility that the atmosphere displays the composition of the accreted gas. If mixing is rapid, the atmosphere's composition depends on the mixing fraction and the differences between the abundance of an element in the accreted material and the envelope. If accretion occurs only over limited phases of the binary's orbit and the mixing timescale is less than the orbital period, there exists the possibility that the atmosphere's composition will vary appreciably around the orbit.

Perhaps, a guide to the pattern of abundance-condensation temperature in the dusty environment may be gleaned from the pattern measured for the cool diffuse interstellar clouds towards the bright star ζ Ophiuchi. Figure 3.14 shows this pattern as assembled from Savage & Sembach (1996), Cardelli (1994) and Jenkins (2009). Following the recipe outlined in Lambert (1996) his model can be expressed mathematically in the form:

$$[X/H] = log[f10^{D_{ISM}} + (1 - f)] \tag{3.2}$$

where D_{ISM} is the interstellar gas phase abundance in the cool diffuse clouds towards ζ Ophiuchi, f is a free parameter called the mixing fraction and [X/H] is the predicted stellar abundance after the mixing. When gas with the interstellar composition is mixed with normal (approximately solar) composition, the mixture assumes the compositions shown in Figure 3.14 for mixing fractions f = 0.9, 0.99, and 0.999 where the mixed composition asymptotes at high T_C to [X/H] = log(1 − f). In Figures 3.15 and 3.16, we show compositions for a value of f which is a rough fit to the abundances of MZ Cyg, DY Ori and for EP Lyr and AD Aql. Not surprisingly the fits are not very good. In particular, the RV Tauri [X/H] vs T_C relations do not show underabundances below about 1000 K at which point the interstellar underabundance is about [X/H] = −1.5. A simple interpretation of this difference is that the dusty regions from which the stars accrete gas are predominantly warm without cool gas (T < 1000 K). An extreme difference with the

interstellar case is presented by R Sct where only most of the high T_C elements show a steep decline in their abundances with [X/H] < -1 (see Figure 3.13) and presumably the dusty region is the warmest across our sample, say T $\geq$ 1600 K.

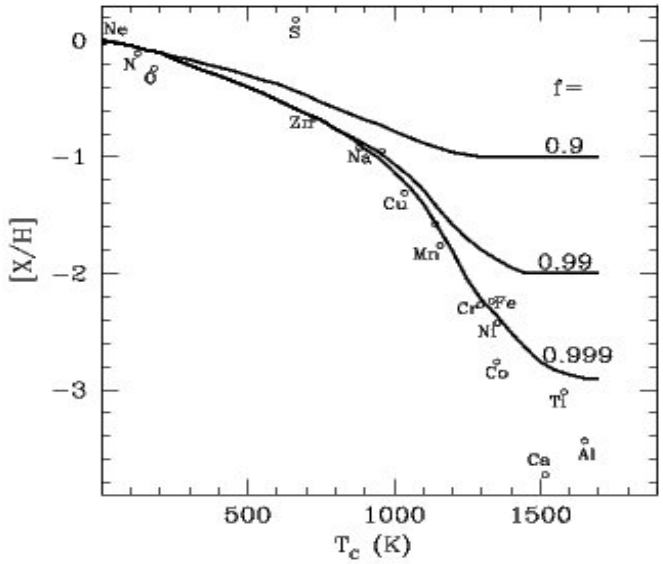

Figure 3.14: The solid curves denote the predicted stellar abundances [X/H] for the mixing fractions f=0.9, 0.99 and 0.999 for mixing between material having solar abundances with the material having the composition of the interstellar gas along the line of sight to ζOph. The open circles denote the observed interstellar abundances for different atomic species.

Scenarios to explain the observed depletion: Two sites were proposed by Giridhar et al. (2005) for the dust-gas separation to operate: in a stellar wind for single stars and a circumbinary disk in the case of binaries.

Circumbinary Disk:

The hypothesis of the dust-gas separation process taking place in a circumbinary disk is gaining wide acceptance through the studies of these objects by several groups. Photometric variations and radial velocity monitoring of several RV Tauri stars has enlarged the sample of known binaries and orbital periods in the range of 400-2000 days have been observed. The orbits of the binary RV Tau stars were found to lie within the dust condensation radius (De Ruyter et al. 2005, 2006; Gielen et al. 2011c) and hence the disks are likely to be circumbinary. The observed range in orbital parameter: asini (projection of semi-major axis) of these stars (0.33AU for HD 44179 to 2.4AU for EN TrA) is quite small, hence De Ruyter et al. (2005, 2006), Gielen et al. (2011c), proposed that they could

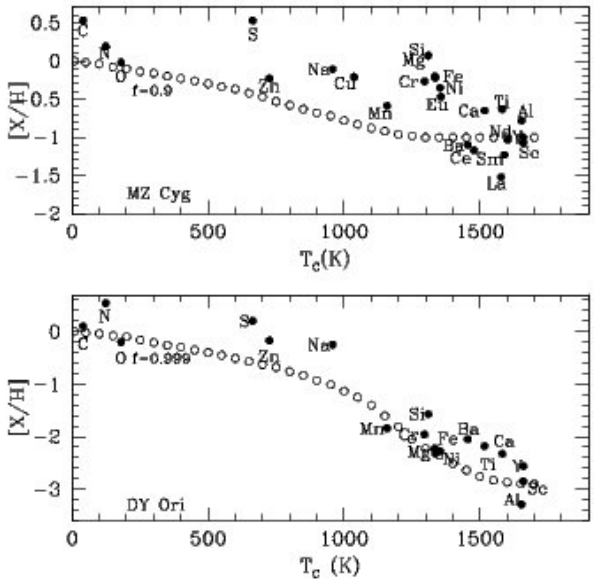

Figure 3.15: The observed data points are compared with Depletion predictions made using mixing fraction giving the best fitting curve for MZ Cyg and DY Ori.

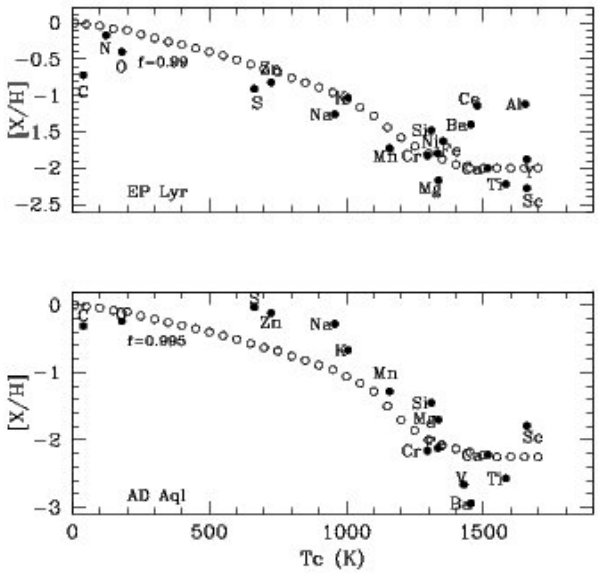

Figure 3.16: The observed data points are compared with Depletion predictions made using mixing fraction giving the best fitting curve for EP Lyr and AD Aql.

not have accommodated a fully grown AGB star (~200$R_\odot$) and the observed circumbinary disks would have formed during a poorly understood phase of severe binary interaction

when the star was at giant dimensions. This can also explain the lack of s-process enrichment seen in most of these stars as the star would have prematurely evolved from the AGB through mass-loss triggered by the companion. One cannot ignore the fact that the above hypothesis requires that s-process enhanced objects be more luminous than DG affected. With RV Tauris and post-AGB showing considerable range in luminosities and errors of luminosity estimates being large (particularly for post-AGBs) this effect is not discernible with our sample.

The CO interferometric measurements for AC Her by Bujarrabal et al. (1988) found evidence for a Keplerian rotating disk in terms of the very weak and narrow CO emission profile. This has been supported from the studies of the IR spectra of several RV Tauri stars by Gielen et al. (2008, 2009b) who found a high degree of processing and crystallinity fraction of the dust grains which is possible only when the dust geometry is in a disk rather than in an outflow. Disk geometry provides a stable environment for the growth of grains and the dust-gas separation to take place and also provides a slow accretion rate (Van Winckel 1995).

The SEDs of the confirmed binary RV Tauri and post-AGB stars were found to be much different when compared to single stars. Binary stars showed a broad IR excess with the dust excess starting at or near the sublimation temperature typical of disk structure (De Ruyter et al. 2006). These had a hot dust component with temperatures in the range of 500-1300K whereas single stars showed a double-peaked SED indicating a detached expanding cool dust shell typical of outflows with dust temperatures of 100-200K (van Winckel 1999).

Even though the formation and evolution of these disks still remain an open question, it is possible that at least some of the dust-gas affected RV Tauri stars might actually be undetected binaries. Also there are some known post-AGB and RV Tau stars which are on the hotter end where the observed dust-gas separation may not be happening in a stellar wind as their high effective temperatures may inhibit grain formation (Waters et al. 1992). Continued Time-series radial velocity campaign of these stars may resolve this issue.

Stellar Wind of single star:

Since RV Tauri stars are known to have large amplitude pulsations compared with the post-AGBs, it may be important to explore the role of pulsations in causing/aiding the dust-gas separation. It should be remembered that RV Tau pulsation do not require binarity. Modelling of the RV Tau atmospheres (Tuchman et al. 1993; Fokin 1994) showed that pulsations are driven by the partial ionization of the envelope and that pulsations are a property of the stellar envelope within the star. In addition to this if the stellar pulsa-

tions were indeed controlled by the companion it would have introduced scatter in the P-L relation. Thus the possibility of pulsations being controlled by a companion are remote.

As all stars may not necessarily belong to binary systems, the dust-gas separation may be taking place in a stellar wind fed by pulsations of the RV Tau star. Pulsations lift the matter above the photosphere where the density and the temperature conditions will be conducive for the grain growth. Radiation pressure on the dust grains provides the acceleration to drive it away from the star. After the dust-gas separation the dust free gas might fall back onto the photosphere during the next pulsation cycles. A dust driven wind can be initiated through the coupling of pulsations and the radiation pressure on the grains especially in metal-rich stars. But till now there has been no direct observational evidence to substantiate this. Also it is not clear whether pulsation driven wind would be strong enough to deposit sufficient amount of material from the photosphere to the proposed site (like in a stellar wind or a circumstellar shell) for the dust-gas separation process to operate. For long period variables like Mira variables it is proposed that pulsationally induced waves travel to outer layers where they steepen to become shocks and regions of high densities are formed a few stellar radii away from the star where the grains can form. This model has been explained in detail by Fleischer et al. (1992). As of now this scenario does not have much observational support. More theoretical work in modelling of the RV Tau atmospheres as well as optical-IR high resolution spectroscopy of these stars over their pulsation cycles may be required to explore the role of pulsations in aiding/causing the abundance anomalies.

Our present work on Dust-Gas Winnowing:

In the present work we have detected mild dust-gas winnowing effects in the additional RV Tau objects: SU Gem and BT Lac; mildness of DG effects may be ascribed to their low effective temperatures. However these stars do not have binary detections and hence radial velocity monitoring has to be carried out to confirm binarity.

The manifestation of the dust-gas winnowing effect is present in varying degrees in RV Tauri stars with and without binary detections (see Table 3.8). From the compilation of the RV Tau stars affected by dust-gas winnowing (Table 3.8) it is seen that some of these (9 out of 35) are confirmed binaries. From their positions in the H-R diagram using theoretical evolutionary tracks of different masses, Stasińska et al. (2006) estimate their masses to be around $0.56M_{\odot}$indicating that most of them have a low stellar mass. Van Winckel et al. (2009) suggest that the mass exchange induced by the binary companion might have reduced the mass of the primary RV Tauri star and would have caused it to prematurely evolve from the AGB phase. One wonders how far the dust-gas winnowing ef-

fect will be carried in their journey to Planetary Nebula (PN)? Periodic multi-wavelength monitoring of HR 4049 like objects over coming few years might spring a few surprises.

Although the binary scenario is supported by the increased detection of binarities especially in depleted post-AGBs (73%) and to some extent in RV Tau stars (26%); (this statistic may change if more detections result from long term monitoring of these objects. However we are aware of the fact that detection of binary companion is made difficult due to stellar pulsations; also the radial velocity measurements needs to be carried out over several pulsation cycles) the dust-gas winnowing process still remains poorly understood due to the existence of enigmatic objects like BD+39^o 4926 a post-AGB binary without IRAS detection showing strong depletion and on the contrary IRAS 19135+3937 and IRAS 01427+4633, two binaries with RV Tau like IR colors indicating the existence of circumstellar shells are not affected by dust-gas winnowing! We have not yet identified all operators and/or necessary conditions controlling this effect.

3.8.3 RV Tauris with FIP effect

While one generally encounters a normal composition, depletion of refractory elements, (not so common) mild s-process enrichment among RV Tauri stars, a couple (CE Vir and EQ Cas) exhibited very peculiar abundance distribution marked by Na deficiency (see Figure 3.17). Rao & Reddy (2005) showed that the observed abundances were related to the the first ionization potential or FIP (hence the name FIP effect). These authors proposed that the effect resulted from systematic removal of singly ionized species in the photospheres of these stars under the influence of outflowing magnetized columns of gas. The atoms with large FIP at these temperatures were in neutral state hence were unaffected while those with lower FIP were ionized and hence were moved away along with the outflow and hence systematically removed. We are not aware of any further addition to this group.

3.8.4 The *s*-process rich RV Tauri stars

The only known Galactic RV Tauri object showing s-process enrichment had been V453 Oph – an RVC object of long period (80 days). In this work, we report a mild s-process enhancement in yet another long period (150 days) RVC object V820 Cen. Both these objects exhibit large radial velocities, are metal-poor (expected for RVC), have no detected IR excess and also show the α enhancement seen in metal-poor stars.

Both V820 Cen and V453 Oph could be single stars as most classical post-AGBs

Table 3.8: A compilation of RV Tauri, RV Tauri like and W Vir variables showing dust-gas winnowing and FIP effect

IRAS	Other[a]	T_{eff}	V[b]	S[c]	[S/H]	[Zn/H]	[Sc/H]	[Fe/H]	$[Fe/H]_o$[d]	P[e]	L[f]	Pec[g]	Bin[h]	Ref
Depleted RV Tauri Stars														
19163+2745	EP Lyr	5750	b	B	−0.6	−0.7	−2.1	−1.8	−0.9	83	3.5	DG	Y	5
08011-3627	AR Pup	6000	b	B	+0.4	...	−2.2	−0.9	+0.4	75	3.4	DG	Y	5
18281+2149	AC Her	6000	a	B	−0.4	−0.9	−1.7	−1.4	−0.9	75	3.4	DG	Y	6
12067-4508	RU Cen	6000	a	B	−0.7	−1.0	−1.9	−1.9	−1.1	65	3.3	DG	Y	7
17243-4348	LR Sco	6250	a	B	+0.0	+0.2	−1.1	−0.0	+0.1	104	3.6	DG	Y	2
19199+3950	HP Lyr	6300	...	B	+0.0	−0.3	−2.8	−0.9	−0.2	141	3.8	DG	Y	2
12185-4856	SX Cen	6500	b	B	−0.1	−0.5	−1.9	−1.1	−0.3	33	2.8	DG	Y	7
...	UZ Oph	5000	a	A	−0.4	−0.7	−1.3	−0.7	−0.8	87	3.5	DG	N	2
06072+0953	CT Ori	5500	a	B	−0.5	−0.5	−2.5	−1.8	−0.5	136	3.8	DG	N	4
06160-1701	UY CMa	5500	a	B	−0.3	−0.6	−2.2	−1.3	−0.5	114	3.7	DG	N	2
06054+2237	SS Gem	5500	a	B	−0.4	+0.0	−1.9	−0.8	−0.2	89	3.5	DG	N	4
17250-5951	UY Ara	5500	a	B	+0.0	−0.3	−1.7	−1.0	−0.2	58	3.2	DG	N	1
20117+1634	R Sge	5750	b	A	+0.4	−0.2	−1.5	−0.5	+0.1	71	3.4	DG	N	5
...	79.5501.13†	5750	...	...	−0.6	−0.6	−3.0	−1.8	−0.6	97	3.6	DG	N	14
...	81.9728.14†	5750	...	...	...	−1.2	−2.0	−1.1	−1.2	94	3.6	DG	N	14
...	82.8405.15†	6000	...	...	−0.3	−0.3	−3.1	−2.5	−0.3	93	3.5	DG	N	13
06034+1354	DY Ori	6000	a	B	+0.2	−0.2	−2.9	−2.2	+0.0	60	3.2	DG	N	2
...	81.8520.15†	6250	...	...	...	−1.4	−1.9	−1.6	−1.4	84	3.5	DG	N	14
16230-3410	...	6250	...	A	−0.4	−0.4	−2.3	−0.7	−0.4	...	...	DG	N	8
18548-0552	BZ Sct	6250	...	B	+0.2	+0.0	−1.1	−0.8	+0.1	...	...	DG	N	2
17233-4330	...	6250	b	B	+0.1	−0.2	−1.6	−1.0	−0.1	...	...	DG	N	8
18564-0814	AD Aql	6300	a	B	−0.0	−0.1	−1.8	−2.1	−0.1	65	3.3	DG	N	6
09256-6324	IW Car	6700	b	B	+0.4	−0.0	−2.1	−1.0	+0.2	68	3.3	DG	N	9
17038-4815	...	4750	a	A	...	−1.2	−2.0	−1.5	−1.2	...	...	MDG	Y	8
07284-0940	U Mon	5000	b	A	−0.1	−0.7	−0.9	−0.8	−0.6	91	3.6	MDG	Y	1
19437-1104	DY Aql	4250	...	A	...	...	−2.1	−1.0	...	131	4.0	MDG	N	4
20343+2625	V Vul	4500	a	A	+0.6	−0.3	−0.7	−0.4	+0.1	76	3.6	MDG	N	2
18448-0545	R Sct	4500	a	A	...	−0.2	−1.4	−0.4	−0.2	147	4.0	MDG	N	1
...	AZ Sgr	4750	a	A	−0.3	...	−1.8	−1.6	−0.3	114	3.8	MDG	N	2

Table 3.8: Contd..

IRAS	Other[a]	T_{eff}	V[b]	S[c]	[S/H]	[Zn/H]	[Sc/H]	[Fe/H]	$[Fe/H]_o$[d]	P[e]	L[f]	Pec[g]	Bin[h]	Ref
...	TT Oph	4800	a	A	+0.0	−0.7	−1.1	−0.8	−0.8	61	3.3	MDG	N	1
F*17015+0503	TX Oph	5000	...	A	−0.6	−1.2	−1.8	−1.2	−1.1	135	3.8	MDG	N	2
22223+5556	BT Lac	5000	b	A	...	−0.1	−0.5	−0.2	−0.1	41	3.0	MDG	N	3
06108+2743	SU Gem	5250	b	A	+0.1	−0.1	−0.5	−0.2	+0.0	50	3.2	MDG	N	4
17530-3348	AI Sco	5300	b	A	−0.1	−0.6	−0.9	−0.7	−0.3	71	3.4	MDG	N	2
...	RX Cap	5800	...	A	−0.6	−0.6	−1.2	−0.8	−0.6	68	3.3	MDG	N	2
Depleted RV Tau like Stars														
11472-0800	AF Crt	5750	RV like	...	−0.5	−0.9	−4.2	−2.7	−0.9	32	...	DG	Y	15
07008+1050	HD 52961	6000	RV like	...	−0.9	−1.3	...	−4.5	−1.3	71	...	DG	Y	3
FIP affected RV Tauri Stars														
13467-0141	CE Vir	4250	...	A	...	−0.7	−2.5	−1.0	−0.7	67	3.5	FIP	N	10
..	EQ Cas	5300	a	B	−0.3	−0.3	−3.1	−0.8	−0.3	58	3.3	FIP	N	2
W Vir Variables														
F06472-3713	ST Pup	5500	CWA	...	−0.2	−0.1	−2.2	−1.5	−0.2	19	3.5	DG	Y	16
...	W Vir	5000	CWA	...	−0.3	−0.8	−2.0	−1.0	−0.8	17	2.6	DG	N	17
F19579-3039	V1711 Sgr	5000	CWA	...	−0.1	−0.9	−2.4	−1.2	−0.7	28	2.8	DG	N	17
...	RX Lib	5250	CWA	...	−0.6	−0.8	−2.2	−1.0	−0.9	25	2.7	DG	N	17
...	CC Lyr	6250	CWA	...	−0.5	−1.2	...	−3.4	−1.1	24	2.7	DG	N	17
06489-0118	SZ Mon	4700	CWA	...	+0.2	−0.4	−1.5	−0.4	−0.1	16	2.6	MDG	N	17
...	MZ Cyg	4750	CWA	...	+0.5	−0.2	−1.1	−0.2	+0.2	21	2.8	MDG	N	17
...	CO Pup	5000	CWA	...	−0.0	−0.7	−1.5	−0.6	−0.4	16	2.5	MDG	N	17

Table 3.9: A compilation of RV Tauri and RV Tauri like variables showing s-process enrichment and normal compositions

IRAS	Other[a]	T_{eff}	V[b]	S[c]	[S/H]	[Si/H]	[Ca/H]	[Fe/H]	[s/Fe][j]	P[e]	L[f]	Pec[g]	Bin[h]	Ref
s-process Enriched RV Tauri Stars														
...	V820 Cen	4750	a	C	...	...	−1.7	−1.9	+0.4	150	3.9	s-p	N	3
...	47.2496.8†	4900	...	...	...	...	−1.9	−1.5	+1.8	113	3.8	s-p	N	12
...	V453 Oph	5750	a	C	...	−1.7	−2.1	−2.2	+0.7	81	3.5	s-p	N	3
Normal Composition RV Tauri Stars														
14524-6838	EN TrA	6000	...	B	−0.6	−0.6	−1.0	−0.8	...	37	2.9	None	Y	11
09060-2807	BZ Pyx	6500	b	B	−0.7	−0.6	−0.5	−0.7	+0.2	...	...	None	Y	8
...	TX Per	4250	a	A	...	−0.2	−1.1	−0.6	−0.8	78	3.6	None	N	3
04440+2605	RV Tau	4500	b	A	...	−0.3	−0.5	−0.4	−0.4	79	3.6	None	N	1
19472+4254	DF Cyg	4800	a	A	...	+0.1	−0.2	−0.0	−0.7	50	3.2	None	N	2
04166+5719	TW Cam	4800	a	A	+0.0	−0.1	−0.7	−0.5	+0.1	87	3.6	None	N	1
...	V360 Cyg	5250	a	C	−0.9	−0.9	−1.3	−1.4	+0.0	70	3.4	None	N	6
...	AR Sgr	5300	a	A	−0.8	−0.8	−1.4	−1.5	−0.1	88	3.5	None	N	2
09538-7622	...	5500	b	A	−0.3	+0.0	−0.6	−0.6	−0.5	...	...	None	N	8
...	BT Lib	5800	...	C	−0.8	−0.7	−0.9	−1.2	+0.5?[k]	75	3.4	None	N	1
...	DS Aqr	6500	a	C	−0.8	−0.8	−1.0	−1.1	−0.1	77	3.4	None	N	1
RV Tauri Like Stars[i]														
06165+3158	...	4250	RV like	...	...	−0.9	−1.2	−0.9	+0.4	...	...	s-p	N	3
19135+3937	...	6000	RV like	...	−0.7	...	−1.3	−1.0	−0.4	...	...	None	Y	3
01427+4633	BD+46^{o}442	6500	RV like	...	−0.4	−0.4	−0.7	−0.7	−0.1	...	...	None	Y	3

†Refers to the RV Tau stars in the LMC discovered by Alcock et al. (1998) through the MACHO (Massive Compact Halo Object) project.

*F stands for Faint IRAS source

[a]Other refers to other names.

[b]Variability Type deduced from the behaviour of the light curves. a and b represent the RV Tauri photometric type which has been explained in the introduction part of this paper.

Table 3.9: Contd..

[c]Spectroscopic Type: A, B and C refer to the Preston's spectroscopic type for RV Tauri stars explained in detail in the introduction part of this paper.

[d]$[Fe/H]_o$ refers to the initial metallicity and is calculated by taking the average of [S/H] and [Zn/H].

[e]P refers to Pulsational Period in Days.

[f]L refers to $\log(L/L_\odot)$ and are the luminosities of the stars calculated from the P-L relation given by Alcock et al. (1998).

[g]Pec refer to the peculiarities (abundance anomalies) where DG refers to Dust-Gas separation, FIP to First Ionisation Potential effect, s-p to the signature of third dredge-up (s-process enrichment) and none refers to neither of the effects observed.

[h]Bin refers to binarity. The direct evidence for binarity comes from radial velocity monitoring (Y) while the other stars (N) do not have binary detections as of now.

[i]The RV Tauri like stars do not have published light curves and photometry. These have RV Tauri like IR colors in the two-color diagram and have been considered in this study.

[j][s/Fe] corresponds to the average of all the s-process elements

[k]Uncertain abundance as it is based on single line measurement of Ba II

[1]Giridhar et al. (2000), [2]Giridhar et al. (2005), [3]Present Work, [4]Gonzalez et al. (1997a)

[5]Gonzalez et al. (1997b), [6]Giridhar et al. (1998), [7]Maas et al. (2002), [8]Maas et al. (2005)

[9]Giridhar et al. (1994), [10]Rao & Reddy (2005), [11]Van Winckel (1997), [12]Reyniers et al. (2007a), [13]Reyniers & Van Winckel (2007)

[14]Gielen et al. (2009b), [15]Van Winckel et al. (2012), [16]Gonzalez & Wallerstein (1996), [17]Maas et al. (2007)

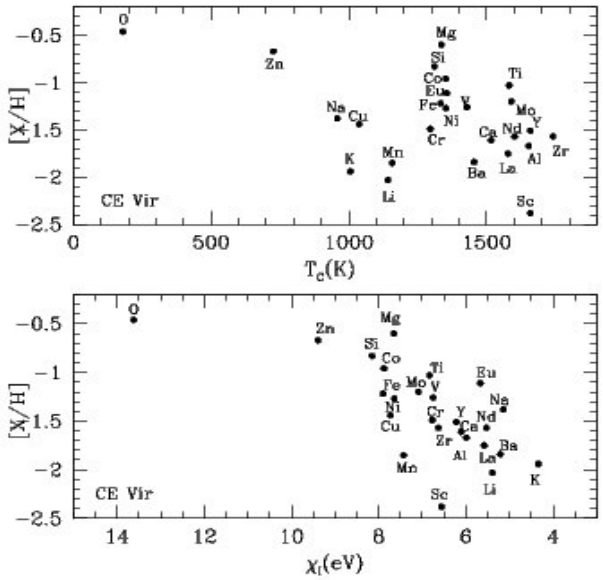

Figure 3.17: Plot of [X/H] versus T_C and the first ionization potential χ_I for CE Vir - adapted from Rao & Reddy (2005).

showing s-process enhancement are single stars (Sumangala Rao et al. 2012) . But to confirm the single/binary nature of these mildly s-process enriched RV Tau stars radial velocity monitoring over several pulsation cycles need to be carried out.

It appears that RV C objects are promising candidates to analyse s-processing in RV Tauris. The general paucity of s-process enhanced objects among RV Tauris could be ascribed to their relatively low mass and consequent early exit from AGB without sufficient number of thermal pulses at AGB. The models of AGB evolution predict that stars in mass range 1.8 to 4.0$M_\odot$ would experience TDU and show s-process enhancement (Herwig 2005) but at lower metallicity the TDU can take place even at lower masses (see Tables 2 and 3 of Karakas et al. (2002)). These authors have also pointed out the influence of mass-loss on AGB evolution in further lowering this mass limit.

Hence it is possible that the metal-poor environment of RVC might allow thermal pulses and efficient TDU even at the RV Tau like lower mass (0.8 to 1.0$M_\odot$ see Deroo et al. (2005) and Reyniers et al. (2007a)) for mass estimates. This suggestion is not unreasonable since the s-process enriched RV Tau star detected in the metal-poor environment of LMC : MACHO 47.2496.8 studied by Reyniers et al. (2007a) exhibits clear indication of s-process enhancement.

However there is a major difference; LMC RV Tauri has C/O greater than 1 and [s/Fe] is quite large +1.2 for lighter and +2.1 for heavier s-process elements. Galactic RV

Tauris exhibit very mild s-processing without carbon enrichment (see Table 3.9). Hence a scenario based upon nucleosynthesis could be an oversimplification.

The RVC stars V360 Cyg, DS Aqr have been studied by Giridhar et al. (1998) while BT Lib by Giridhar et al. (2000). DS Aqr with ([Fe/H]= −1.0) and BT Lib with ([Fe/H]=−1.2]) have measurement only for Ba with [Ba/Fe] of +0.9 and +0.5 respectively. These estimates are based upon very few lines. Surprisingly, V360 Cyg with [Fe/H] of −1.4 and high radial velocity of 250 kms^{-1} does not show s-process enhancement despite the analysis covering Y II and Ba II lines.

V453 Oph ([Fe/H]=−2.1]) and V820 Cen ([Fe/H]=−2.2) are more metal-poor than the three RVC stars mentioned above (see Table 3.9). One wonders if there is a metallicity limit below which RVC might show s-processing? We have reservations about considering IRAS 06165+3158 in this group for several reasons. It is a RV Tauri like object with no photometry, although it is metal-poor with moderate s-process enhancement, the α enrichment is not seen nor does it show high radial velocity expected of RVC objects.

3.8.5 RV Tauris with Normal Compositions

About 22% (with and without binary detections) of the RV Tauri stars exhibit normal composition i.e. they exhibit the signature of ISM for heavy elements while light elements may show the effect of CN processing (see Table 3.9). For significantly metal-poor stars the expected α enrichment is observed. Binarity is not very common although a small fraction have binary detections.

3.9 Summary and Conclusions

We have made a detailed abundance analysis using high resolution spectra of relatively unexplored RV Tauri stars and stars having RV Tauri like colors from its position in the IRAS two-color diagram. A more extensive abundance analysis for the stars V453 Oph and HD 52961 were also undertaken. With the study of additional elements, a better defined depletion curve for HD 52961 is obtained. Our findings are summarized below:

• A mild suggestion of dust-gas winnowing is seen in the RV Tau objects SU Gem and BT Lac. No abundance peculiarities are observed in IRAS 01427+4633 and IRAS 19135+3937 despite their binarity and the existence of circumstellar material surrounding them.

• The detection of small but significant s-processing in yet another RVC star: V820 Cen is very important as it makes them possible candidates to study nucleosynthesis near

the low mass end of AGB stars. However, it is difficult to account for lack of carbon enrichment in these objects. Mild s-processing is also detected in the star: IRAS 06165+3158 an object with RV Tauri like IRAS colors. Further photometric and spectroscopic monitoring is required to understand its variable nature.

• We also examine the evolutionary connection between RV Tauris and post-AGBs by estimating their luminosities to find their locations in HR diagram. It appears that following the AGB evolution the RV Tauris are presently residing in instability strip while most post-AGB has crossed it. This suggestion is supported by the photometry of RV Tauris and post-AGBs.

• Since a large number of RV Tauris (with or without binary detections) exhibit DG effect it provides us with an opportunity to study the diverse depletion patterns seen in RV Tauri stars. We propose a few possibilities to explain the families of the observed depletion plots.

• It is likely that the size of depletion depends on the extent of mixing between accreted gas and stellar photosphere; when the mixing fraction is nearly one the stellar photosphere develops almost the same composition as that of the interstellar gas. As the mixing fraction decreases, the severity of the depletion decreases as well as the depletion curves asymptotes at higher T_C. This model however can explain depletion plots for only few post-AGBs and RV Tauris with depletion plots that exhibit asymptotic behaviour for the high T_C elements. For example: AD Aql (f=0.995), EP Lyr (f=0.99), DY Ori (f=0.999) and MZ Cyg (f=0.9).

• The depletion plots are also affected by conditions of dust-gas reservoir. The extreme case of R Sct with almost a precipice like depletion plot is found to deviate from the ISM values possibly due to its warmest circumstellar dusty environment compared to other program RV Tauri stars.

• Optical-Infrared High-Resolution campaigns of selected RV Tauri stars over their pulsation periods may help in understanding various abundance patterns observed in these fascinating objects. Such a study may also unravel the possible role of pulsations/stellar wind in sustaining depletion. One cannot exaggerate the importance of photometric and radial velocity monitoring towards the increased detection of binary companions.

Till now only 67 RV Tauri stars have been studied in our Galaxy. But the GCVS lists 133 stars with the RV classification (in our Galaxy) and a large number of faint Galactic RV Tauri stars remain unexplored. The exploration of RV Tau stars in external galaxies could be very rewarding as exemplified by the detection of few depleted RV Tauri stars in the LMC and also the heavily s-process enriched RV Tauri star in the LMC.

CHAPTER 4

CHEMICAL COMPOSITIONS OF POST-AGB CANDIDATES

4.1 ABSTRACT

We have derived elemental abundances for a sample of nine IRAS sources with colors similar to those of post-AGB stars. For IRAS 01259+6823, IRAS 05208-2035, IRAS 04535+3747 and IRAS 08187-1905 this is the first detailed abundance analysis based upon high resolution spectra. Mild indication of s-processing for IRAS 01259+6823, IRAS 05208-2035 and IRAS 08187-1905 have been found. A more comprehensive study of s-process enhanced objects IRAS 17279-1119 and IRAS 22223+4327 have been carried out.

We have also made a contemporary abundance analysis of the high galactic latitude supergiants BD+39^o 4926 and HD 107369. The former is heavily depleted in refractories and estimated [Zn/H] of -0.7 dex most likely gives initial metallicity of the star. For HD 107369 the abundances of α and Fe-peak elements are similar to those of halo objects and moderate deficiency of s-process elements is seen. IRAS 07140-2321 despite being a short period binary with circumstellar shell does not exhibit selective depletion of refractory elements.

We have compiled the stellar parameters and abundances for post-AGB stars with s-process enhancement, those showing significant depletion of condensable elements and those showing neither. The compilation shows that the s-process enhanced group contains very small number of binaries, and observed [α/Fe] are generally similar to thick disk values. It is likely that they represent AGB evolution of single stars. The compilation of the stars showing depletion contains larger fraction of binaries and generally supports

the hypothesis of dusty disks surrounding binary post-AGB stars inferred via the shape of their SED and mid IR interferometry. IRAS 07140-2321 and BD+39^o 4926 are difficult to explain with this scenario and indicate the existence of additional parameter/condition needed to explain the depletion phenomenon. However the conditions for discernible depletion, minimum temperature of 5000K and initial metallicity larger than -1.0 dex found from our earlier work still serves as useful criteria.

4.2 INTRODUCTION

Considerable theoretical and observational interest has in recent years been focused on AGB stars but much remains mysterious about them. The AGB phase is enjoyed by low and intermediate mass stars (approximate mass range 0.8 to 8$M_\odot$). It is in this phase that a star experiences extensive internal nucleosynthesis whose fruits are dredged to the stellar surface (Herwig 2005). Furthermore, mass-loss ensures that the products of nucleosynthesis are dispersed into the circumstellar and subsequently the interstellar environment. Thus, AGB stars are likely major contributors of Li, C, N, F and *s*-process elements among others to Galactic chemical evolution (Romano et al. 2010).

Observational validation of theoretical investigations of how AGB stars achieve internal nucleosynthesis, dredge-up and mass-loss are generally hampered by the fact that the more evolved and more interesting of these stars have low temperature atmospheres and therefore spectra replete with dense and complex molecular lines. Although these spectra have been analysed by a few stellar spectroscopists, the abundance studies are generally limited to very few elements and isotopic ratios.

The AGB phase of stellar evolution concludes with a rapid phase of evolution to the tip of the white dwarf cooling track. This post-AGB phase takes a star in a few thousand years or so from a cool AGB star to a very hot central star of a planetary nebula and onto a white dwarf cooling track. Along this track, the star's spectrum is amenable to straightforward abundance analysis and thus offers apparently a way to infer the abundance changes brought by the post-AGB star's AGB progenitor. This inference is, of course, dependent on the assumption that the composition of an AGB star is exactly preserved by the post-AGB star. Observations of certain post-AGB stars show that this is a false assumption. For example, several post-AGB stars show abundance anomalies correlated with the condensation temperature (T_C)* for dust grains to condense out of gas of normal com-

*The condensation temperature T_C is the temperature at which half of a particular element in a gaseous environment condenses into dust grains. Condensable elements refer to the refractories like Ti, Ca, Sc and s-process elements which readily condense into dust grains because of their high T_C.

position (see Van Winckel (2003) for a review) – a process we refer to as 'dust-gas winnowing'. Other post-AGB candidate stars show abundance anomalies correlated with the ionization potential of the neutral atoms (Rao & Reddy 2005) – a process we refer to as 'the FIP effect'.

Given that the post-AGB phase is rapid, the number of identified post-AGB stars is relatively small and the number subjected to an abundance analysis is, of course, even smaller. In this paper, we report abundance analyses for 11 candidate post-AGB stars and have compiled abundance data of previously analysed post-AGB stars in an attempt to seek explanations for the diverse compositions of these objects.

4.3 SELECTION OF THE SAMPLE

Our sample stars are presented in Table 4.1 and displayed in the IRAS two color diagram Figure 4.1 which has proven to be a powerful tool for identifying candidate post-AGB stars (van der Veen & Habing 1988; Suárez et al. 2006; Szczerba et al. 2007). Nine of our eleven stars have measured IRAS fluxes and are identified in Figure 4.1; the stars, HD 107369 and BD $+39^{o}$ 4926 were not detected by IRAS.

It is known that zone 1 of IRAS two color diagram by van der Veen & Habing (1988) corresponds to fluxes from stellar photospheres warmer than 2000K. The IRAS colors of Zones II-III signify the emergence and evolution of circumstellar shell (CS) produced by increasing large mass-loss at AGB. Sources at Zone IV are at the super-wind phases or slightly beyond. Zone V contains objects with only signature of cold dust shell as the mass-loss has stopped hence warm dust is not being added. The objects with detached cold CS would be seen at region VIa, while objects in zone VIb contains objects with warm as well as cold CS. The Zone VII and dashed region is dominated by post-AGBs with PN like colors.

Our sample stars IRAS 05208-2035, IRAS 07140-2321, IRAS 12538-2611 and IRAS 01259+6823 belong to zone IIIa, IIIb and IV where signatures of CS formed by increased mass-loss at late AGB are evident. IRAS 17279-1119 (zone VIb) seems to possess the hot as well as cold dust shell while IRAS 07331+0021, IRAS 22223+4327, IRAS 08187-1905 have PN like colors.

Table 4.1: The Program Stars.

No.	IRAS	Other Names	Var Type	Colors
1	01259+6823	...	...	PN like
2	04535+3747	V409 Aur, HD 280138, BD+37^{o}996	SRD	...
3	05208-2035	BD-20^{o}1073	...	RV Tauri like
4	07140-2321	CD-23^{o}5180, SAO 173329	Irregular	RV Tauri like
5	07331+0021	AI CMi, BD+00^o 2006	Irregular	...
6	08187-1905	V552 Pup, HD 70379, BD-18^o 2290	SRD	...
7	...	HD107369, SAO 203367	...	...
8	12538-2611	HR 4912, HD 112374, BD-18^o 2290	SRD	RV Tauri like
9	17279-1119	HD 158616, BD-11^{o}4391, V340 Ser	RV Tauri	RV Tauri like
10	22223+4327	V448 Lac, BD +42^o 4388	SRD	PN like
11	...	BD+39^{o}4926, SAO 72704	..	...

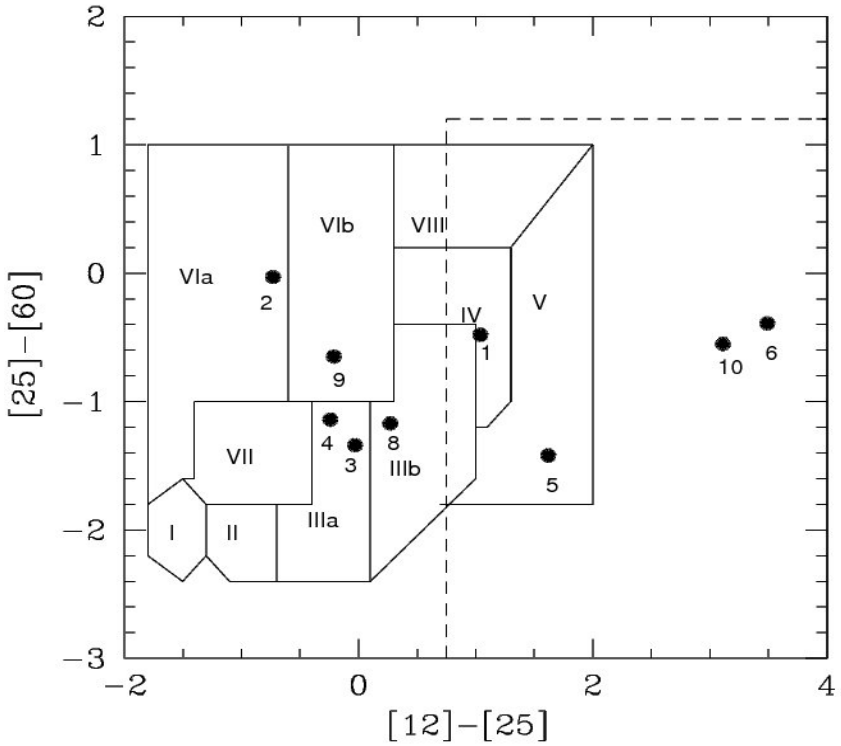

Figure 4.1: The location of sample stars in IRAS color-color diagram containing the zones defined by van der Veen & Habing (1988) and area enclosed in the dashed line which according to Szczerba et al. (2007) is richly populated by post-AGB stars with colors like planetary nebulae. The sample stars are numbered as follows: 1- IRAS 01259+6823 2- IRAS 04535+3747 3- IRAS 05208-2035 4- IRAS 07140-2321 5- IRAS 07331+0021 6- IRAS 08187-1905 8- IRAS 12538-2611 9- IRAS 17279-1119 10- IRAS 22223+4327

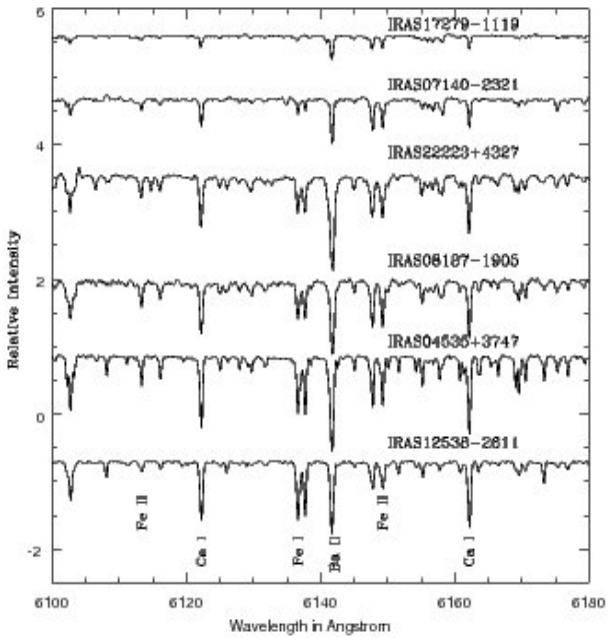

Figure 4.2: Sample spectra of our stars presented in descending order of temperature (top to bottom) in the 6100-6180Å region.

4.4 OBSERVATIONS

High-resolution optical spectra were obtained at the W.J. McDonald Observatory with the 2.7m Harlan J. Smith reflector and the Tull coudé spectrograph (Tull et al. 1995) with a resolving power of 60,000. Spectral coverage in a single exposure from this cross-dispersed echelle spectrograph is complete up to 6000Å and extensive but incomplete at longer wavelengths. A S/N ratio of 80-100 over much of the spectral range was achieved. Figure 4.2 contains a few representative spectra to illustrate the quality of typical spectra.

4.5 Abundance analysis

We have made use of the new grid of ATLAS09 model atmospheres available at database of Kurucz[†]. Spectrum synthesis code MOOG (2009 version) by Sneden (1973) has been used. The assumptions are standard, Local Thermodynamical Equilibrium (LTE), plane parallel atmosphere and hydrostatic equilibrium and flux conservation.

The hydrogen lines for most stars were affected by emission components hence could

[†]http://kurucz.harvard.edu/grids.html

not be used for parametrization of stars. We have used Fe I and Fe II lines for deriving atmospheric parameters. Further, lines of Mg I, Mg II; Si I, Si II ; Ti I , Ti II and Cr I, Cr II were also used as additional constraints whenever possible.

Our sample stars were generally hotter than 5000K with the exception of IRAS 07331+0021 and IRAS 05208-2035, which fortunately turned out to be metal-poor by -1.2 dex and -0.65 dex. Hence adequate number of unsaturated clean lines could be measured for number of elements for them.

First, the microturbulence ξ_t is derived by requiring that the derived abundances are independent of line strengths. We have generally used Fe II lines for measuring ξ_t microturbulence for most of our sample stars, since appreciable departure from LTE are known to occur for Fe I lines (Boyarchuk et al. 1985; Thévenin & Idiart 1999). However for coolest members, IRAS 05208-2035 and IRAS 07331+0021 very few Fe II lines could be measured and hence Fe I lines had to be used instead for fixing the microturbulence.

The temperature is estimated by requiring that derived abundances are independent of the Lower Excitation Potential (LEP). IRAS 07140-2321, HD 107369 and BD+39^{o}4926 had large number of usable Fe II lines. In fact, for HD 107369 Fe II lines cover good LEP range to estimate the temperature. For IRAS 07140-2321 and BD+39^{o}4926 the LEP covered by Fe II lines was lesser than those by Fe I hence both species were employed although we did not find any difference between the temperatures estimated from them. For cool stars the observed Fe II did not have a good range in LEP hence Fe I lines were employed. The gravity was derived by requiring Fe I and Fe II giving the same abundance. In addition, the ionization equilibrium of Mg I/ Mg II , Si I/Si II , Sc I/Sc II, Ti I/Ti II, Cr I/Cr II were used as additional constraints whenever possible.

The accuracy of equivalent width measurements depends on resolution, spectral type of the star and the continuum fitting. For stars of spectral type late A- F, the equivalent widths could be measured with an accuracy of $\sim$ 5 -8 % in absence of line asymmetries. With the above mentioned accuracy in measured equivalent widths, the microturbulence velocity could be measured with an accuracy of $\pm$0.25 km s^{-1}, temperature with $\pm$150K and *log g* of $\pm$0.25 cm s^{-2}.

But for cooler stars, line strengths could only be measured with accuracy of 8-10 %. The microturbulence velocity could be measured with an accuracy of $\pm$0.5 km s^{-1}, temperature with $\pm$250K and *log g* of $\pm$0.5 cm s^{-2}.

The derived atmospheric parameters and heliocentric radial velocities for the epoch of observations for the program stars are presented in Table 4.2 .

The sensitivity of the derived abundances to the uncertainties of atmospheric param

Table 4.2: Stellar Parameters Derived from the Fe-line Analyses

Star	UT Date	V_r^a (km s^{-1})	T_{eff}, log g, [Fe/H]	ξ_t^b (km s^{-1})	Fe I^c		Fe II^c	
					log ϵ	n	log ϵ	n
IRAS01259+6823	2007 Nov 5	−49.1	5000,1.50,−0.60	3.3	6.82 ± 0.10	60	6.88 ± 0.11	11
IRAS04535+3747	2008 Feb29	−37.4	6000,1.25,−0.48	3.6	6.96 ± 0.19	97	6.99 ± 0.10	12
IRAS05208-2035	2007 Nov 3	+50.3	4250, 0.75, −0.65	1.6	6.80 ± 0.20	49	6.81 ± 0.11	7
IRAS07140-2321	2007 Nov 2	+68.0	7000,1.00, −0.92	3.6	6.55 ± 0.14	75	6.52 ± 0.11	19
IRAS07331+0021	2008 Apr 19	+47.9	4500, 1.00 ,−1.16	5.2	6.27 ± 0.16	26	6.32 ± 0.10	4
IRAS08187-1905	2008 Feb 26	+ 61.5	6250,0.50, −0.59	3.8	6.90 ± 0.15	33	6.82 ± 0.13	11
HD107369	2008 Apr 20	−39.0	7500, 1.50, −1.33	1.3	6.09 ± 0.13	19	6.15 ± 0.12	30
IRAS12538-2611	2009 May 10	−31.3	5250,1.00, −1.12	4.6	6.34 ± 0.11	59	6.33 ± 0.11	12
IRAS17279-1119	2008 Aug 10	+68.7	7250, 2.25, −0.43	4.7	7.02 ± 0.21	21	7.01 ± 0.16	12
IRAS22223+4327	2009 Dec 27	−41.3	6500, 1.00, −0.33	4.3	7.14 ± 0.08	20	7.11 ± 0.10	16
BD +39^o 4926	2007 Nov 19	−36.3	7750, 1.00, −2.37	3.0	5.02 ± 0.15	9	5.15 ± 0.13	21

[a] V_r is the radial velocity in km s^{-1}

[b] ξ_t is the microturbulence

[c] log ϵ is the mean abundance relative to H (with log ϵ_H = 12.00).
The standard deviations of the means as calculated from the line-to-line scatter are given. *n* is the number of considered lines.

Table 4.3: Sensitivity of [X/Fe] to the uncertainties in the model parameters for a range of temperatures covering our sample stars .

	IRAS 05208-2035			IRAS 12538-2611			IRAS 22223+4327			BD +39^{o}4926		
	(4250K)			(5250K)			(6500K)			(7750K)		
Species	$\Delta T_{\rm eff}$	$\Delta\log g$	$\Delta\xi$	$\Delta T_{\rm eff}$	$\Delta\log g$	$\Delta\xi$	$\Delta T_{\rm eff}$	$\Delta\log g$	$\Delta\xi$	$\Delta T_{\rm eff}$	$\Delta\log g$	$\Delta\xi$
	$-200K$	+0.25	+0.5	$-200K$	+0.25	+0.5	$-200K$	+0.25	+0.5	$-200K$	+0.25	+0.5
C I	...	...	...	−0.31	−0.07	−0.02	+0.10	+0.01	−0.03	−0.03	+0.06	+0.06
N I	...	...	...	...	...	...	+0.19	−0.04	−0.02	−0.27	−0.09	+0.04
O I	+0.30	−0.03	−0.13	+0.03	−0.06	−0.03	+0.22	−0.05	−0.03	−0.24	−0.08	+0.01
Na I	+0.21	+0.09	−0.01	+0.04	+0.07	−0.03	−0.03	+0.10	−0.03	+0.02	+0.13	+0.01
Mg I	+0.18	+0.09	+0.06	+0.06	+0.06	−0.03	−0.08	+0.10	+0.06	+0.09	+0.12	+0.00
Al I	+0.22	+0.07	−0.09	+0.02	+0.07	−0.05	−0.04	+0.12	−0.05	+0.07	+0.13	−0.01
Si I	−0.03	+0.02	−0.10	+0.01	+0.06	−0.04	−0.03	+0.10	−0.03	...	...	...
Si II	...	...	...	...	...	...	+0.17	−0.07	+0.09	−0.32	−0.11	+0.01
S I	...	...	...	−0.23	−0.02	−0.04	+0.03	+0.05	−0.03	+0.00	+0.10	−0.01
Ca I	+0.24	+0.08	+0.03	+0.07	+0.06	−0.02	−0.07	+0.11	+0.01	...	...	...
Ca II	...	...	...	...	...	...	+0.13	−0.04	−0.04	...	...	...
Sc II	...	...	...	−0.44	−0.06	−0.01	−0.01	−0.09	−0.02	−0.01	−0.08	−0.01
Ti I	+0.35	+0.06	+0.00	+0.28	−0.07	+0.01	...	...	...	...	...	...
Ti II	+0.14	−0.01	+0.01	−0.06	−0.19	+0.05	+0.00	−0.10	+0.07	−0.04	−0.10	+0.00
Cr I	+0.25	+0.07	+0.36	+0.20	+0.08	−0.02	...	...	...	...	...	...
Cr II	−0.08	+0.00	−0.04	−0.16	+0.03	−0.01	+0.06	−0.08	+0.00	−0.08	−0.10	+0.00
Mn I	...	...	...	+0.19	+0.03	−0.01	−0.07	+0.09	−0.02	...	...	...
Co I	+0.00	+0.00	+0.10	...	...	...	...	...	...	...	...	...
Ni I	+0.13	+0.02	+0.11	+0.13	+0.06	−0.04	−0.07	+0.10	−0.03	...	...	...
Cu I	...	...	...	+0.15	+0.06	−0.04	...	...	...	...	...	...
Zn I	...	...	...	+0.06	+0.02	+0.02	−0.07	+0.10	−0.02	+0.06	+0.12	−0.01
Y II	+0.18	−0.01	+0.00	−0.04	−0.04	−0.01	−0.02	−0.09	+0.01	...	...	...
Zr I	+0.43	+0.01	+0.03	...	...	...	...	...	...	...	...	...
Zr II	...	...	...	...	...	...	+0.00	−0.08	+0.01	...	...	...
Mo I	+0.40	+0.04	−0.09	...	...	...	...	...	...	...	...	...
Ba II	...	...	...	+0.04	−0.08	+0.04	...	...	...	...	...	...
La II	+0.29	−0.02	−0.08	...	...	...	−0.05	−0.05	−0.02	...	...	...
Ce II	+0.24	−0.02	−0.12	...	...	...	−0.06	−0.06	+0.01	...	...	...
Pr II	+0.31	−0.02	−0.11	...	...	...	−0.18	−0.02	−0.04	...	...	...
Nd II	+0.26	−0.02	−0.08	...	...	...	−0.12	−0.03	−0.01	...	...	...
Sm II	+0.29	−0.01	−0.02	...	...	...	−0.03	−0.05	−0.02	...	...	...

eters $T_{\rm eff}$, *log g*, and ξ are summarized in Table 4.3. For four stars representing the full temperature range of our sample, we present changes in [X/Fe] caused by varying atmospheric parameters by 200K, 0.25 cm s^{-2} and 0.5 km s^{-1} (average accuracies of these parameters) with respect to the chosen model for each star.

The total stellar parameter related error is estimated by taking the square root of the sum of the square of the systematic errors (individual errors associated with uncertainties in temperatures and gravities) and bars in the abundance plot correspond to the systematic error.

Having determined the atmospheric parameters, the abundances of different elements were derived using the available lines. The derived abundances relative to the solar abundances are presented in their respective tables. The solar photospheric abundances given by Asplund et al. (2005) have been used as reference values.

We have investigated possible systematic effects caused by the adopted *gf* values from different sources as follows. We have measured solar equivalent widths for our lines on Solar Flux Atlas by Kurucz et al. (1984) and estimated the abundances using model atmosphere appropriate for the Sun with $T_{\rm eff}$=5770K, *log g* of 4.4 and ξ_t of 0.9 $\rm kms^{-1}$. The agreement for most elements is within 0.04 to 0.09 dex although the linelist is different for different stars.

The lines of certain elements are affected by hfs. We have included the hfs components in our line list while synthesizing the spectral feature of these elements for deriving the abundances. For elements Sc and Mn, we have used hfs component list and their *log gf* given by (Prochaska & McWilliam 2000), for Cu (Allen & Porto de Mello 2011), for Eu (Mucciarelli et al. 2008) and for Ba (McWilliam 1998). The effect of isotopic components were considered for Eu II (2 isotopes) and Ba II (5 isotopes) lines. The errors caused due to the neglect of non-LTE has been discussed in detail in Chapter 3.

4.6 RESULTS

Results of our abundance analyses are presented in this section. If the candidate post-AGB star has preserved the composition of its AGB progenitor, the C, N, O (and Li) abundances betray information about the abundance changes brought by the first and second dredge-ups in the giant prior to the AGB and changes brought about by the TDU on the AGB. We also look for the signature of HBB which can operate if the star had a massive progenitor ($M>4M_{\odot}$) (Ventura & D'Antona 2009) and its manifestation can produce enrichments of Li, N, Na, Mg and Al (Blöcker & Schönberner 1991). Abundances of

elements from Si through the iron group are expected to be unchanged as a star evolves from the main sequence to the AGB phase. These abundances may, in principle, be used to assign a stellar population to the star, e.g., thin disk, thick disk or halo. Beyond the iron group, abundances of *s*-process nuclides are predicted to be enriched in AGB stars that experienced the TDU. Such nuclides dominate elements such as Y, Zr and Ba.

If the post-AGB star has been subject to dust-gas winnowing or to selective diffusion of elements according to the FIP effect, abundance anomalies will be present that are unrelated to those arising from nucleosynthesis.

In this section, we present an abundance analysis for each star and comment briefly on the abundance anomalies, if any. The primary initial goal is to draw attention to the observational clues, if any, to the prior action of the TDU on the AGB and, thus, to the C, N and O abundances as well as the indicators of *s*-process contamination. Another goal is to scan the anomalies for dust-gas winnowing and/or the FIP effect.

We postpone to Sections 4.8 a discussion of abundances, especially the [X/Fe] values, which might betray the stellar population from which the post-AGB is drawn. One potential indicator of population is the abundance of α elements Mg, Si, S, Ca and Ti which have a higher ratio in thick disk stars than in the thin disk at the same [Fe/H]. This postponement arises in large part from the fact that in essentially every star the [α/Fe] ratios do not consistently point to a thick or a thin disk origin. The α-elements are sending a mixed message whose interpretation is best discussed for the whole sample.

4.6.1 IRAS 01259+6823

Our analysis appears to be the first detailed abundance analysis for this star with our final abundances presented in Table 4.4. A low resolution spectrum presented by Suárez et al. (2006) shows an absorption spectrum with emission limited to Hα. Stellar lines are sharp (FWHM about 0.26Å corresponding to 14 kms^{-1}) and symmetric at our resolution.

Atmospheric parameters (Table 4.2) estimated from Fe I and Fe II lines were found to give satisfactory ionization equilibrium for Si, Ti, Cr and Fe: Δ = [X_{II}/H] − [X_I/H] is +0.21, −0.03, +0.22 and +0.06 respectively. The question of thick vs thin disk is discussed for the sample as whole in Section 4.8.

Of the elements anticipated to be affected by internal nucleosynthesis and dredge-up by the termination of the AGB phase, C with [C/Fe] = +0.2 appears enriched slightly by the TDU in an AGB star; C is lowered by the FDU with [C/Fe] $\simeq -0.2$. The C/O ratio of 0.4 by number shows that the star in not C-rich and, hence, the TDU was mild. A mild *s*-process enrichment is seen in the light s-process elements: Y and Zr, with a slightly

higher enrichment for the so-called heavy s-process elements (e.g., Ba) with an average [s/Fe] of +0.3 dex. Inspection of the abundances shows no sign for operation of dust-gas winnowing or the FIP effect. In short, IRAS 01259+6823 evolved at an early phase off the AGB before dredge-up from the He-shell began in earnest.

4.6.2 IRAS 04535+3747 (V409 Aur)

This is the first abundance analysis for this SRD variable which with an effective temperature of 6000K has presumably evolved from the AGB or possibly the horizontal branch. The star occupies the box VIa in the IRAS two color diagram (Figure 4.1). This position is occupied by objects having detached cold CS dust shells.

Strong absorption lines have a weak asymmetry in their blue wings. This asymmetry has been ignored in the measurement of the equivalent width. We assume that a classical atmosphere may be used for the abundance analysis. Model atmosphere parameters are given in Table 4.2 and the final abundances have been presented in Table 4.4.

The star is mildly metal-poor ([Fe/H] = −0.48). Ionization equilibrium is adequately achieved not only for Fe but also for Si, Ti and Cr: $\Delta = [X_{II}/H] - [X_I/H]$ is −0.04, −0.14, +0.01 and +0.03 respectively. This star has not evolved from an AGB star in which the TDU has enriched the atmosphere in C and the *s*-process. The C/O ratio of 0.3 by number is that expected for a star at the beginning of the AGB and the *s*-process has not enriched the heavy elements. To within the uncertainties about the initial C, N and O abundances, their alterations by the FDU and the errors of the abundance analysis, the C, N and O abundances are those anticipated for a star beginning the AGB following either a stay on the horizontal branch or may execute blue loops given the present uncertainties in the masses of SRDs.

4.6.3 IRAS 05208-2035

The infrared excess is typical of RV Tauri variables (De Ruyter et al. 2006). De Ruyter et al. complain lack of a published spectrum and of estimates for the stellar parameters. This lack we correct here. An orbital period of 236 days has been reported in Gielen et al. (2008). The chosen model (Table 4.2) gives the abundances as presented in Table 4.5.

Ionization equilibrium is satisfactorily accounted for in that $\Delta = [X_{II}/H] - [X_I/H]$ is +0.01, −0.02, and +0.05 for Fe, Ti and Cr respectively. In terms of the evolutionary history, the most significant aspect of the star's composition is an enhancement of the heavy elements. In particular, those elements (e.g., Y, Zr and Ba) dominated by an *s*-

Table 4.4: Elemental Abundances for IRAS 01259+6823 and IRAS 04535+3747.

		IRAS 01259+6823			IRAS 04535+3747		
Species	$\log \epsilon_{\odot}$	[X/H]	N	[X/Fe]	[X/H]	N	[X/Fe]
C I	8.39	−0.42 ± 0.08	2	+0.18	−0.43 ± 0.10	5	+0.05
N I	7.78	...			+0.24 ± 0.08	5	+0.72
O I	8.66	−0.29 ± 0.08	2	+0.31	−0.17 ± 0.11	3	+0.31
Na I	6.17	−0.25 ± 0.05	3	+0.35	+0.05 ± 0.04	3	+0.53
Mg I	7.53	−0.52 ± 0.10	2	+0.08	−0.46 ± 0.14	4	+0.02
Al I	6.37	−0.68 ± 0.14	3	−0.08	−0.42 ± 0.19	3	+0.06
Si I	7.51	−0.40 ± 0.09	10	+0.20	−0.27 ± 0.14	16	+0.21
Si II	7.51	−0.19 ± 0.03	2	+0.41	−0.31 ± 0.17	2	+0.17
S I	7.14	−0.43	synth	+0.17	−0.16 ± 0.15	2	+0.32
Ca I	6.31	−0.79 ± 0.09	11	−0.19	−0.59 ± 0.19	13	−0.11
Sc II	3.05	−0.80 ± 0.02	synth	−0.20	−0.75 ± 0.00	synth	−0.27
Ti I	4.90	−0.67 ± 0.11	11	−0.07	−0.56 ± 0.13	13	−0.08
Ti II	4.90	−0.70 ± 0.08	3	−0.10	−0.70 ± 0.08	5	−0.22
V I	4.00	−0.80 ± 0.11	11	−0.20	...		
Cr I	5.64	−0.74 ± 0.07	4	−0.14	−0.58 ± 0.12	8	−0.10
Cr II	5.64	−0.52 ± 0.04	4	+0.08	−0.57 ± 0.09	5	−0.09
Mn I	5.39	−0.72 ± 0.08	7	−0.12	−0.62 ± 0.14	7	−0.14
Fe	7.45	−0.60			−0.48		
Co I	4.91	−0.75 ± 0.11	3	−0.15	...		
Ni I	6.23	−0.79 ± 0.15	21	−0.19	−0.53 ± 0.14	23	−0.05
Zn I	4.60	−0.69 ± 0.10	3	−0.09	−0.53 ± 0.13	3	−0.05
Sr I	2.92	−0.30 ± 0.00	1	+0.30	...		
Y II	2.21	−0.53 ± 0.11	5	+0.07	−0.40 ± 0.20	13	+0.08
Zr II	2.58	−0.48 ± 0.02	2	+0.12	−0.49 ± 0.17	5	−0.01
Ba II	2.17	−0.04 ± 0.00	synth	+0.56	...		
La II	1.13	−0.19 ± 0.10	3	+0.41	−0.33 ± 0.23	2	+0.15
Ce II	1.58	−0.36 ± 0.05	8	+0.24	−0.42 ± 0.13	18	+0.06
Pr II	0.78	−0.48 ± 0.06	3	+0.12	−0.31 ± 0.23	3	+0.17
Nd II	1.46	−0.38 ± 0.07	10	+0.22	−0.42 ± 0.08	5	+0.06
Sm II	0.95	−0.30 ± 0.10	5	+0.30	−0.44 ± 0.05	3	+0.04
Eu II	0.52	−0.31 ± 0.01	synth	+0.29	...		
Dy II	1.14	...			−0.65 ± 0.00	2	−0.17

process contribution are overabundant relative to Fe by about 0.3 dex. The *r*-process dominated elements (e.g., Eu) are also overabundant but this is as expected for a star of [Fe/H] = −0.6. Although the star is a spectroscopic binary and thus a candidate for dust-gas winnowing, this effect is absent but this is not surprising given the extensive convective envelope of such a cool star.

4.6.4 IRAS 07140-2321

IRAS 07140-2321 (also known as SAO 173329) is a post-AGB star belonging to a spectroscopic binary with a dusty circumbinary disk (Van Winckel et al. 2000; De Ruyter et al. 2006; Gielen et al. 2008). The orbital period is 116 days (De Ruyter et al. 2006). Photometrically, the star is an irregular small amplitude variable for which Kiss et al. (2007) suggests variations with periods of about 24 and 60 days. Here, we are responding to a call by Van Winckel (1997) who published the only previously reported abundance analysis and wrote 'SAO 173329 is a metal-deficient object for which more data are needed'. Specifically, Van Winckel noted the lack of an oxygen abundance determination and the need for 'more good Fe II lines'. The lack of abundance data for heavy or *s*-process elements was also a notable omission. Results from our analysis summarized in Table 4.5 are based on the model atmosphere summarized in Table 4.2. The star is metal-poor: [Fe/H] = −0.9. The C/O ratio of 0.4 and the limited data on heavy element abundances show that this star did not evolve from a thermally pulsing AGB star. The N abundance shows evidence of N enrichment by the FDU. The observed [N/Fe] after Non-LTE correction of −0.4 dex (Lyubimkov et al. 2011) is +0.3 dex which is similar to FDU prediction of +0.5 dex as given in Schaller et al. (1992). Heavy elements – Y, Zr and Ba are not enriched relative to Fe. For elements in common, our abundances are in fair agreement with those reported by Van Winckel (1997) who used solar *gf*-values and a different grid of model atmospheres. Abundance differences between those in Table 4.5 and those reported by Van Winckel for a 7000 K model atmosphere are small (except for S I and Cr I): δ [X/Fe] (present work − VW97) is −0.20 dex for C I, +0.11 dex for N I, +0.43 dex for S I, −0.22 for Ca I, −0.22 for Ti II, −0.37 for Cr I, +0.14 for Mn I, +0.13 for Ni I and −0.03 for Zn I.

The inspection of the estimated abundances shows that the observed [S/Fe] is +0.6; the possible α enrichment of +0.3 dex expected at [Fe/H] of −0.9 may indicate actual [S/Fe] of +0.3 dex. But nearly zero [Zn/Fe] and lack of depletion for high T_C elements Ca and Sc shows that the star is not affected by dust-gas winnowing. It is surprising given the fact that the star is a spectroscopic binary with an orbital period of only 115.9 days (Van Winckel et al. 2000) and has detected circumstellar material. It appears that

conditions for effective dust-gas winnowing are far from understood.

4.6.5 IRAS 07331+0021 (AI CMi)

This cool variable exhibits TiO bands in its spectrum at its coolest phases (Klochkova & Panchuk 1996) which necessarily impair a full abundance analysis at such phases. Luck & Bond (1989) undertook an analysis of an image-tube spectrum obtained in 1981 and found the star was metal-poor ([Fe/H]= −1.0) with a larger under-abundance of *s*-process elements. Noting that all of the elements deficient with respect to iron had second ionization potentials less than the ionization potential of hydrogen, they speculated that Lyman continuum emission from shock waves in the atmosphere over-ionized these elements and therefore they appear under-abundant when a standard analysis with a classical atmosphere is performed. Klochkova & Panchuk (1996) and Klochkova & Panchuk (1998) reported abundance analyses from CCD spectra of AI CMi taken at three different epochs. Results for the separate phases are given in their 1996 paper and average results with the addition of O and Zn are provided in the 1998 paper. Inspection of the 1996 tabulation of abundances shows that results for several species vary from spectrum to spectrum: for example, the [Sc/Fe] ratio is variously given as −0.63, −0.22, and −0.05. Luck & Bond's shocking hypothesis might allow for this kind of variation. From their comparison with Luck & Bond's results, Klochkova & Panchuk (1996) conclude that the two analyses are in good agreement. They further write 'We come to the conclusion that from 1981 to 1995 abundances of elements heavier than oxygen remained the same in the AI CMi atmosphere, i.e., no transfers of matter processed in the inner layers of the star to the star's atmosphere is observed.'

Our spectrum taken on April 19, 2008 exhibits strong bands of CN, CH, MgH and TiO. Strong lines exhibit blue-shifted components. The atmospheric parameters (Table 4.2) fall within the range reported by Klochkova & Panchuk (1998). We estimate [Fe/H] of −1.16 while KP1998 derive −1.14. For the most elements the abundances derived by us agree with KP1998.

Our analysis covers additional elements C, Co and Sm (see Table 4.5). Of note is that our analysis and that of KP1998 do not confirm the under-abundance of heavy elements reported by Luck & Bond. Heavy elements have a normal abundance for a star with [Fe/H] = −1.16. The C and especially the O abundance are unusually high. C abundance has been measured from 5380.3Å line and O from [O I] lines. A fair conclusion may be that the star like others in our sample has not experienced the full effect of the TDU on the AGB branch.

Table 4.5: Elemental Abundances for IRAS 05208-2035, IRAS 07140-2321 and IRAS 07331+0021

		IRAS 05208-2035			IRAS 07140-2321			IRAS 07331+0021		
Species	$\log \epsilon_{\odot}$	[X/H]	N	[X/Fe]	[X/H]	N	[X/Fe]	[X/H]	N	[X/Fe]
C I	8.39	....			−0.61 ± 0.10	12	+0.31	−0.44 ± 0.03	2	+0.72
N I	7.78	....			−0.15 ± 0.16	4	+0.77	...		
O I	8.66	−0.25 ± 0.27	2	+0.40	−0.54 ± 0.00	1	+0.38	+0.04 ± 0.09	2	+1.20
Na I	6.17	−0.22 ± 0.09	5	+0.43	−0.40 ± 0.16	4	+0.52	...		
Mg I	7.53	−0.52 ± 0.14	2	+0.13	−0.61 ± 0.14	3	+0.31	−0.68 ± 0.00	1	+0.48
Mg II	7.53	...			−0.74 ± 0.00	1	+0.18	...		
Al I	6.37	−0.45 ± 0.05	4	+0.20	−1.18 ± 0.00	1	−0.26	....		
Si I	7.51	−0.56 ± 0.19	8	+0.09	−0.56 ± 0.12	5	+0.36	−0.89 ± 0.24	5	+0.27
Si II	7.51	...			−0.74 ± 0.00	1	+0.18	...		
S I	7.14	...			−0.32 ± 0.04	3	+0.60	...		
Ca I	6.31	−0.79 ± 0.13	6	−0.14	−0.97 ± 0.19	15	−0.05	−1.25 ± 0.09	3	−0.09
Sc II	3.05	...			−0.92 ± 0.13	9	+0.00	−1.35 ± 0.15	2	−0.19
Ti I	4.90	−0.52 ± 0.24	15	+0.13	....			...		
Ti II	4.90	−0.54 ± 0.26	4	+0.11	−0.73 ± 0.14	8	+0.19	−0.89 ± 0.05	5	+0.27
Cr I	5.64	−0.64 ± 0.12	6	+0.01	−0.71 ± 0.10	4	+0.21	−0.98 ± 0.16	2	+0.18
Cr II	5.64	−0.59 ± 0.00	2	+0.06	−0.74 ± 0.05	5	+0.18	−0.97 ± 0.10	2	+0.19
Mn I	5.39	...			−1.00 ± 0.01	synth	−0.08	−1.35 ± 0.08	3	−0.19
Fe	7.45	−0.65			−0.92			−1.16		
Co I	4.92	−0.53 ± 0.08	2	+0.12	....			−0.97 ± 0.11	6	+0.19
Ni I	6.23	−0.44 ± 0.17	13	+0.21	−0.85 ± 0.07	7	+0.07	−1.19 ± 0.10	10	−0.03
Cu I	4.21	...			...			−1.30 ± 0.08	synth	−0.14
Zn I	4.60	...			−0.87 ± 0.16	2	+0.05	...		
Y II	2.21	−0.41 ± 0.16	4	+0.24	−1.10 ± 0.13	5	−0.18	−1.15 ± 0.00	1	+0.01
Zr I	2.59	−0.30 ± 0.10	4	+0.35	....			...		
Mo I	1.92	−0.16 ± 0.12	2	+0.49	...			...		
Ba II	2.17	−0.34 ± 0.00	synth	+0.31	−0.64 ± 0.00	synth	+0.28	...		
La II	1.13	−0.31 ± 0.15	3	+0.34	...			−0.89 ± 0.11	3	+0.27
Ce II	1.58	−0.29 ± 0.05	2	+0.36	...			−1.22 ± 0.00	1	−0.06
Pr II	0.71	−0.40 ± 0.00	1	+0.25	...			−1.02 ± 0.00	1	+0.14
Nd II	1.45	−0.31 ± 0.11	6	+0.34	...			−1.36 ± 0.22	2	−0.20
Sm II	1.01	−0.39 ± 0.18	3	+0.26	...			−1.02 ± 0.13	5	+0.14
Eu II	0.52	−0.51 ± 0.03	synth	+0.14	...			....		

4.6.6 IRAS 08187-1905 (V552 Pup)

High-resolution optical spectra have not been previously reported. Low resolution spectroscopy and photometry was obtained by Reddy & Parthasarathy (1996). Our abundance analysis (Table 4.6) with the model atmosphere in Table 4.2 suggests that the star is slightly metal-poor ([Fe/H] = −0.6) and is C-rich. The O abundance is as expected for a [Fe/H]= −0.6 star but the C enrichment suggests addition of C to the original material. Formally, C/O by number of atoms slightly exceeds unity. The light-*s* elements Y and Zr as well as the heavy *s* element Ba point to a mild *s*-process enrichment. One is led to suggest that the star, after a FDU which decreased the C and increased the N abundance, experienced the TDU which increased the C abundance and thus the C/O ratio and also mildly enriched the *s*-process content of the atmosphere.

4.6.7 HD 107369

This high-galactic latitude F supergiant is not an IRAS source. Van Winckel (1997) who undertook an abundance analysis using high-resolution spectra of selected wavelength intervals found the star to be metal-poor ([Fe/H] = −1.3). Our abundance analysis with the model in Table 4.2 is reported in Table 4.6. We estimate a temperature of 7500K and log *g* of 1.5 using the Fe I and Fe II lines. However, the estimated gravity is also supported by ionization equilibrium of Mg I & Mg II, Ca I & Ca II, Cr I & Cr II. Our abundances are in good agreement with Van Winckel's results. To make comparison easy we have used his line strengths with new set of *gf* values and models. The scanty Fe line data supports the temperature and gravity estimated by us. Adopting our model (7500,1.5,2.2) we find following δ (present work − VW1997) +0.34 dex for N I, +0.13 dex for O I, +0.18 for Si II, +0.24 for S I, −0.09 for Ca I, +0.26 for Ti II, −0.03 for Cr II, +0.06 for Fe I, +0.12 for Fe II and +0.04 for Ba II respectively. Our analysis covers additional elements Mg, Ni, Sr and Y. The star does not provide the expected abundance signature of a typical AGB star such as C/O greater than one and a strong *s*-process enrichment. Nor do we see any indication of dust-gas winnowing. The lines of Zn were not detectable.

The elements with higher condensation temperature such as Ca, Sc did not exhibit expected depletion. The N abundance appears very high at [N/Fe] = +1.15 and in excess of the value expected by the FDU. However, Non-LTE corrections for the N I lines are −0.5 dex from Lyubimkov et al. (2011) is indicated. After applying this correction we get [N/Fe] of +0.7 dex which is marginally larger than prediction of FDU. Van Winckel reported [C/Fe] of −0.2 dex from a single line. There is no compelling evidence for HBB

in the form of very large [N/Fe] nor do we see Li I feature. Being a high galactic latitude metal-poor object it does not seem to have evolved from a massive progenitor since M > $4M_{\odot}$ is required for HBB (Ventura & D'Antona 2009). With low C/O ratio, high galactic latitude and low metallicity it appears to have evolved from a low mass progenitor.

4.6.8 IRAS 12538-2611

Also known as HR 4912, this variable star was studied spectroscopically by Luck et al. (1983) (LLB83) who found it metal-poor ([Fe/H]=−1.2). With its high luminosity it is quite likely to be a post-AGB object. An abundance analysis was also performed by (Giridhar et al. 1997) (GAFP97). Our spectra have better resolution and spectral coverage than earlier studies. There is fair agreement between our abundances and those by LLB83 and GAFP97. The run of C and O abundances offer no evidence that the star evolved from a thermally pulsing AGB star: the C/O ratio is 0.06 by number of atoms (see Table 4.6). There is no evidence for *s*-process enrichment.

4.6.9 IRAS 17279-1119

This post-AGB star has been the subject of two previous abundance analyses. In introducing IRAS 17279-1119, Van Winckel (1997) hereinafter VW97 noted that optical photometry shows that it has some RV Tauri-like characteristics with possible periods of 61 and 93 days (Bogaert 1994) but additional photometry is needed; inspection of SIMBAD shows that photometry has not been reported recently. Van Winckel's abundance analysis for a model atmosphere with $T_{\rm eff}$= 7400K and *log g*=0.5 showed the star to be metal-poor ([Fe/H] = −0.7) with a C/O close to unity and possibly exceeding unity and *s*-process enriched, both markers of prior TDU on the AGB. His discussion of the star concluded with the observation that "this as yet poorly studied star deserves further research'. An appreciated limitation of Van Winckel's analysis was the limited wavelength coverage of his spectroscopic snapshots. Arellano Ferro et al. (2001) hereinafter AGM2001 acquired new spectra with complete coverage from 3900-6800 Å which enabled them to determine he abundances of all elements considered by VW97 (except for N) and add Na, Mg, Mn, La and Ce to the list. The star was again shown to be metal-poor ([Fe/H]−0.6) and *s*-process enriched. Unusual aspects of the composition are found from these analyses. Most striking perhaps, AGM2001 found [Na/Fe] =+0.6 and from both analyses a high Sc abundance was reported, [Sc/Fe]=+0.9 (VW97 from one Sc II line) and +0.6 (AGM2001 from eight Sc II lines).

Table 4.6: Elemental Abundances for IRAS 08187-1905, HD 107369 and IRAS 12538-2611

		IRAS 08187-1905			HD 107369			IRAS 12538-2611		
Species	$\log \epsilon_{\odot}$	[X/H]	N	[X/Fe]	[X/H]	N	[X/Fe]	[X/H]	N	[X/Fe]
C I	8.39	+0.03 ± 0.25	9	+0.62	...			−1.09 ± 0.13	3	+0.03
N I	7.78	−0.10 ± 0.23	4	+0.49	−0.18 ± 0.25	5	+1.15	...		
O I	8.66	−0.33 ± 0.24	3	+0.26	−0.68 ± 0.09	4	+0.65	−0.17 ± 0.01	2	+0.95
Na I	6.17	+0.03 ± 0.19	3	+0.62	...			−0.61 ± 0.05	3	+0.51
Mg I	7.53	−0.46 ± 0.19	3	+0.13	−0.95 ± 0.04	2	+0.38	−0.80 ± 0.00	1	+0.32
Mg II	7.53	...			−0.77 ± 0.04	2	+0.56	...		
Al I	6.37	...			...			−1.38 ± 0.11	2	−0.26
Si I	7.51	−0.11 ± 0.15	5	+0.48	...			−0.89 ± 0.19	6	+0.23
Si II	7.51	...			−0.80 ± 0.24	4	+0.53	...		
S I	7.14	+0.05 ± 0.06	3	+0.64	−0.84	synth	+0.49	−0.69 ± 0.01	2	+0.43
Ca I	6.31	−0.63 ± 0.17	8	−0.05	−1.28 ± 0.09	3	+0.05	−1.34 ± 0.14	10	−0.22
Ca II	6.31	....			−1.43 ± 0.00	1	−0.10	...		
Sc II	3.05	−0.75 ± 0.00	synth	−0.16	−1.45	synth	−0.12	−1.55 ± 0.03	synth	−0.43
Ti I	4.90	....			.....			−0.81 ± 0.00	1	+0.31
Ti II	4.90	−0.99 ± 0.10	2	−0.40	−1.09 ± 0.10	18	+0.24	−0.89 ± 0.19	6	+0.23
Cr I	5.64	−0.52 ± 0.15	3	+0.07	−1.52 ± 0.05	2	−0.19	−1.50 ± 0.02	2	−0.38
Cr II	5.64	−0.66 ± 0.14	7	−0.08	−1.43 ± 0.10	7	−0.10	−1.49 ± 0.05	4	−0.37
Mn I	5.39	...			...			−1.52 ± 0.06	2	−0.40
Fe	7.45	−0.59			−1.33			−1.12		
Ni I	6.23	−0.60 ± 0.11	7	−0.01	−1.05 ± 0.04	2	+0.28	−1.13 ± 0.18	11	−0.01
Zn I	4.60	−0.58 ± 0.16	3	+0.01	...			−1.04 ± 0.06	2	+0.08
Sr II	2.92	...			−1.85 ± 0.00	1	−0.52	...		
Y II	2.21	−0.19 ± 0.20	4	+0.40	−1.81 ± 0.07	2	−0.48	−1.28 ± 0.09	2	−0.16
Zr II	2.59	−0.33 ± 0.14	2	+0.25	...			...		
Ba II	2.17	−0.34 ± 0.00	synth	+0.25	−1.80 ± 0.12	2	−0.47	−1.34 ± 0.00	1	−0.22
La II	1.13	...			...			−1.37 ± 0.05	2	−0.25
Ce II	1.58	...			...			−1.45 ± 0.07	3	−0.33
Nd II	1.45	...			...			−1.51 ± 0.07	3	−0.39

Since the solar abundances used by AGM2001 and VW97 are different from our work we have transformed these abundances to the abundance scale of Asplund et al. (2005) for comparison. The present analysis covers additional elements Sr, Zr, Pr and Nd (see Table 4.7). In general, the results of the present analysis agree well with those of prior analyses. An exception is that we do not confirm the anomalously high Sc abundance reported by VW97 and AGM2001. The progenitor of IRAS 17279-1119 was likely a thermally pulsing AGB star. This suggestion accounts for the C/O of unity and the modest *s*-process enrichment.

4.6.10 IRAS 22223+4327

This star has been classified as a proto-planetary nebula and, therefore, a post-AGB star (Hrivnak 1995; Kwok 1993). Even on a low resolution spectrum, Hrivnak (1995) could see the enhancement of lines of s-process elements. From the UBV photometry, Arkhipova et al. (2003) found this star to be pulsating variable with a period of ~ 90 days.

Long term monitoring of this star using high resolution spectra has been carried out by Klochkova et al. (2010) with following interesting findings. The strong absorption lines such as low excitation line of Ba II at 6141 Å not only show asymmetries in the profile with short wavelength side of the profile showing extended wing than the red wing; these strong lines also show large amplitude profile variations (with time) caused by variations in blue wing while red wing remained unchanged. The spectrum contains C_2 lines most likely formed in the circumstellar shell. At the epoch of largest asymmetry in strong Ba II line the C_2 (0;1) band head at λ 5635 is seen in emission. The cores of hydrogen lines show larger variations in radial velocities ($\sim$ 8 kms^{-1}) while weak metallic lines show smaller amplitude variations in radial velocities ($\sim$ 1 kms^{-1}). Molecular C_2 lines remain stationary with time; the shift in circumstellar features relative to systemic velocity gives an expansion velocity V_{exp} of 15.0 kms^{-1}. Our spectrum taken on Dec 27, 2009 also exhibits the features mentioned in Klochkova et al. (2010). This star was analysed by Van Winckel & Reyniers (2000) (hereinafter WR2000) who found it moderately metal-poor [Fe/H] of -0.3 dex and showing enhancement of s-process elements. The present analysis covers additional elements Na, Mg and Zn and uses larger number of lines for many species (see Table 4.7). Since the solar abundances used in WR2000 are different from our work, we have transformed these abundances to solar abundances of Asplund et al. (2005) to facilitate comparison. All elements agree within ± 0.15 dex.

IRAS 22223+4327's progenitor was most probably a thermally pulsing AGB star. This is indicated by the C/O ratio of unity and the about one dex enrichment of the *s*-

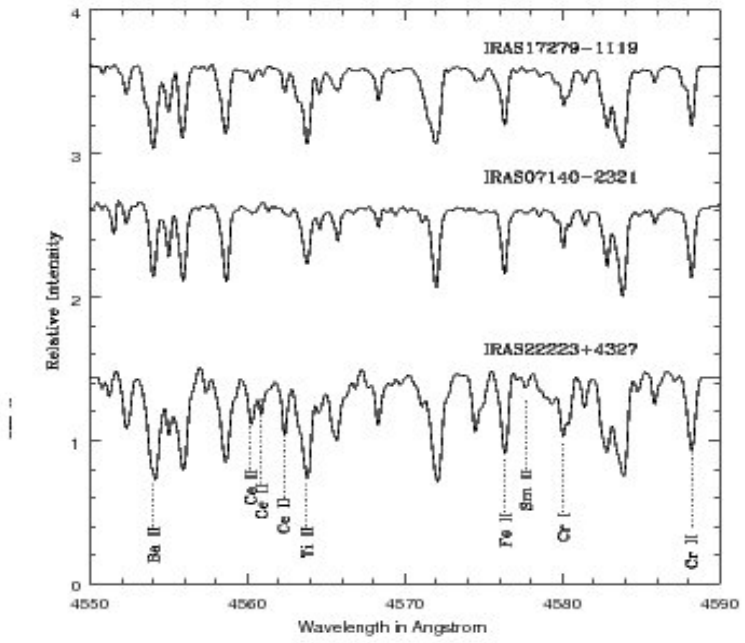

Figure 4.3: Comparison of spectra of the stars: IRAS 17279-1119 and IRAS 22223+4327 showing s-process enrichment with IRAS 07140-2321, a normal star of similar temperature in the 4550-4590 Å region. The lines of s-process elements like Ba II, Ce II and Sm II are enhanced.

process elements. Two of our program stars IRAS 17279-1119 and IRAS 22223+4327 show significant s-process enhancement. We have compared the spectra of these two objects with IRAS 07140-2321 with similar temperature but without s-process enhancement in Figure 4.3.

4.6.11 BD+39^{o}4926

Although this object has been mentioned in several papers on post-AGB stars, a contemporary abundance analysis using high-quality digital spectra, modern model atmospheres and refined atomic data has not been undertaken. Abundance data from Kodaira et al. (1970) show strong effects of dust-gas winnowing. Yet, this star unlike other stars exhibiting severe dust-gas winnowing does not have an infrared excess. However, the star is a spectroscopic binary, as are many or even all other stars exhibiting severe dust-gas winnowing. For these reasons, we chose to include this object in our sample.

Our spectral coverage (particularly in red region) has been more extensive and we could make a more detailed analysis employing more number of lines per species and

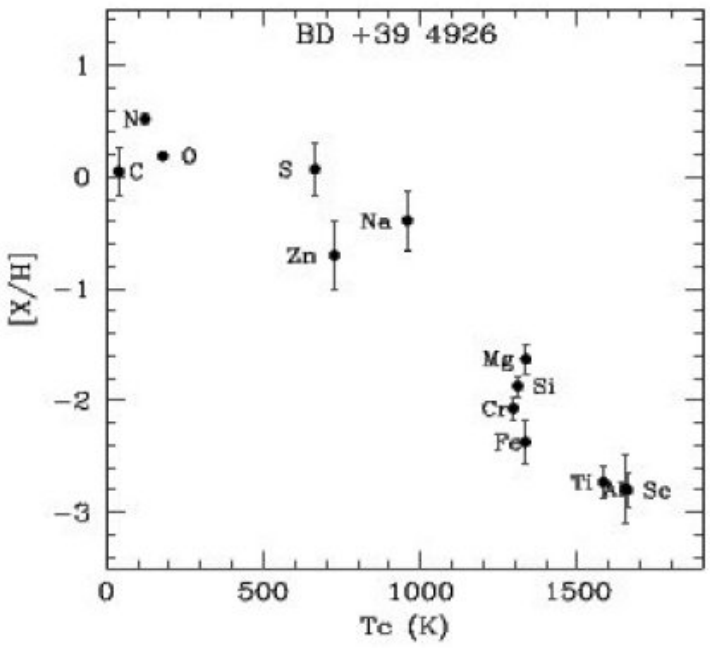

Figure 4.4: Plot of [X/H] vs [T_c] for the star BD+39^{o}4926.

also including the important element Zn. The star's final abundances are presented in Table 4.7. Figure 4.4 shows the plot of [X/H] vs [T_C] for this star. This star shows a clear indication of the dust-gas separation without possessing IR indications of circumstellar envelope. From this plot, we infer that the initial metallicity of the star is −0.7 dex. (Another such star showing selective depletion of refractory elements without IR excess is HD 105262 (Giridhar et al. 2010) which has the temperature of 8000K and [Fe/H] of −1.8 dex.)

4.7 [Na/Fe] in sample stars

The relative enrichment of Na has been observed in most of our program stars. The Na abundance has been measured using weak subordinate lines for which the estimated non-LTE correction does not exceed −0.1 dex (Lind et al. 2011; Gehren et al. 2004). The Na enrichment is believed to be caused by products of Ne-Na cycle involving proton capture on ^{22}Ne in H burning region which are mixed to the surface following FDU. The verification of expected dependence of [Na/Fe] on stellar mass remains illusive. All our program stars give [Na/Fe] in excess of FDU predictions (e.g. El Eid & Champagne (1995) predict [Na/Fe] of +0.18 dex for 5 $M_\odot$ model). A further increase in surface

Table 4.7: Elemental Abundances for IRAS 17279-1119, IRAS 22223+4327 and BD +39 4926

		IRAS 17279-1119			IRAS 22223+4327			BD +39 4926		
Species	$\log \epsilon_{\odot}$	[X/H]	N	[X/Fe]	[X/H]	N	[X/Fe]	[X/H]	N	[X/Fe]
C I	8.39	−0.08 ± 0.17	11	+0.35	+0.27 ± 0.14	20	+0.60	+0.05 ± 0.12	17	+2.42
N I	7.78	+0.20 ± 0.12	4	+0.63	+0.33 ± 0.01	2	+0.66	+0.52 ± 0.26	9	+2.89
O I	8.66	−0.31 ± 0.00	1	+0.12	+0.07 ± 0.05	2	+0.40	+0.19 ± 0.09	10	+2.56
Na I	6.17	−0.04 ± 0.12	2	+0.39	+0.10 ± 0.06	2	+0.43	−0.39 ± 0.17	2	+1.98
Mg I	7.53	−0.42 ± 0.10	3	+0.01	+0.07 ± 0.09	2	+0.40	−1.91 ± 0.15	4	+0.46
Al I	6.37	...			+0.15 ± 0.01	2	+0.48	−2.79 ± 0.00	1	−0.42
Si I	7.51	−0.19 ± 0.22	4	+0.24	+0.09 ± 0.07	4	+0.42	..		
Si II	7.51	−0.24 ± 0.09	2	+0.19	+0.06 ± 0.00	1	+0.39	−1.87 ± 0.25	6	+0.50
S I	7.14	+0.03 ± 0.12	4	+0.46	+0.25 ± 0.10	2	+0.58	+0.07 ± 0.17	4	+2.44
Ca I	6.31	−0.54 ± 0.19	7	−0.11	−0.20 ± 0.09	8	+0.13	..		
Ca II	6.31	...			−0.22 ± 0.08	2	+0.11	...		
Sc II	3.05	−0.43 ± 0.03	synth	+0.00	−0.38 ± 0.05	2	−0.05	−2.80 ± 0.08	2	−0.43
Ti II	4.90	+0.04 ± 0.22	6	+0.47	−0.17 ± 0.08	6	+0.16	−2.73 ± 0.14	10	−0.36
Cr II	5.64	−0.53 ± 0.02	3	−0.09	−0.41 ± 0.15	8	−0.08	−2.07 ± 0.15	5	+0.30
Mn I	5.39	−0.62 ± 0.27	2	−0.19	−0.46 ± 0.05	2	−0.13	...		
Fe	7.45	−0.43			−0.33			−2.37		
Ni I	6.23	−0.60 ± 0.43	2	−0.17	−0.22 ± 0.11	11	+0.11	...		
Zn I	4.60	−0.28 ± 0.11	2	+0.15	−0.45 ± 0.00	1	−0.12	−0.70 ± 0.08	2	+1.67
Sr I	2.92	−0.20 ± 0.00	1	+0.23	...			...		
Y II	2.21	+0.50 ± 0.22	5	+0.93	+1.15 ± 0.15	3	+1.48	...		
Zr II	2.58	+0.52 ± 0.07	2	+0.95	+0.82 ± 0.16	5	+1.15	..		
Ba II	2.17	+0.16 ± 0.00	synth	+0.59	+1.16 ± 0.00	synth	+1.49	..		
La II	1.13	+0.18 ± 0.17	2	+0.61	+0.97 ± 0.14	16	+1.30	...		
Ce II	1.58	+0.43 ± 0.11	7	+0.86	+0.48 ± 0.13	11	+0.81	..		
Pr II	0.78	+0.00 ± 0.00	1	+0.43	+0.70 ± 0.09	5	+1.03	..		
Nd II	1.45	+0.26 ± 0.06	2	+0.69	+0.60 ± 0.10	14	+0.93	..		
Sm II	0.95	...			+0.50 ± 0.07	5	+0.83	...		
Eu II	0.52	...			+0.10 ± 0.01	synth	+0.43	...		

abundance of Na during AGB evolution is predicted by Mowlavi (1999) but the lack of correlation between the observed [Na/Fe] with s-process enhancement cautions against a simplistic interpretation of observed [Na/Fe].

4.8 α elements

Our analysis covers whole range of elements including α elements which are important diagnostics of stellar population. Although abundances are estimated for all α elements Mg, Si, S, Ca and Ti, we chose to use only Mg, Si and S to compute [α/Fe]. The Ca and Ti abundances derived from Ca I and Ti I lines could be affected by non-LTE effects. For dwarfs and subgiants the corrections are estimated to be about +0.1 dex as described in section 3.5.1 in our chapter 3, but can become larger for supergiants. More importantly they are prone to depletion via grain condensation due to their large condensation temperatures (T_C for Ca and Ti are 1517 and 1582K respectively.) As explained in section 3.5.1, the non-LTE correction for Mg I lines used by us is about +0.05 dex and for S I and Si I lines it is negligible.

The mean [α/Fe] values of +0.15 for IRAS 01259+6823 is indicative of thin disk population, a similar value +0.18 for [α/Fe] is exhibited by IRAS 04535+3747 and +0.13 for IRAS 05208-2035 and +0.21 is seen for IRAS 17279-1119. The [α/Fe] of +0.45 for IRAS 07140-2321 is indicative of thick disk population; it also shows [Fe/H] of -0.9, IRAS 07331+0021 does not have good representation of α elements. The [α/Fe] of +0.36 for IRAS 08187-1905 and its [Fe/H] of -0.6 supports its thick disk candidature. HD 107369 also exhibits [α/Fe] of +0.41 while it is +0.37 for IRAS 12538-2611 with [Fe/H] of -1.2. Like other s-process enhanced post-AGBs IRAS 22223+4327 exhibits [α/Fe] value of +0.46 not withstanding its [Fe/H] of -0.3. Hence our sample stars are a mixed lot.

4.9 [Ca/Fe]

For most of our sample stars as well as for a large fraction of RV Tau stars and post-AGB stars we find [Ca/Fe] and [Ti/Fe] much lower than those expected even for thin disk stars. Although Fe abundance can be estimated with better precision using Fe II lines, for Ca, the abundance is estimated using Ca I lines hence non-LTE corrections for supergiants need to be investigated (for dwarfs and subgiants a correction of +0.1 dex is estimated but could be larger for lower gravity post-AGB stars). Although the non-LTE correction for supergiant gravities are not available, it is comforting to note that there is no perceptible

difference between [Ca/Fe] for a sample of giants used by Takeda et al. (2008) and those of dwarfs and subgiants (Bensby et al. 2005; Reddy et al. 2006). Hence we do not expect very large reduction in [Ca/Fe] caused by non-LTE effect (a likely non-LTE correction would be in +0.1 to 0.2 dex range).

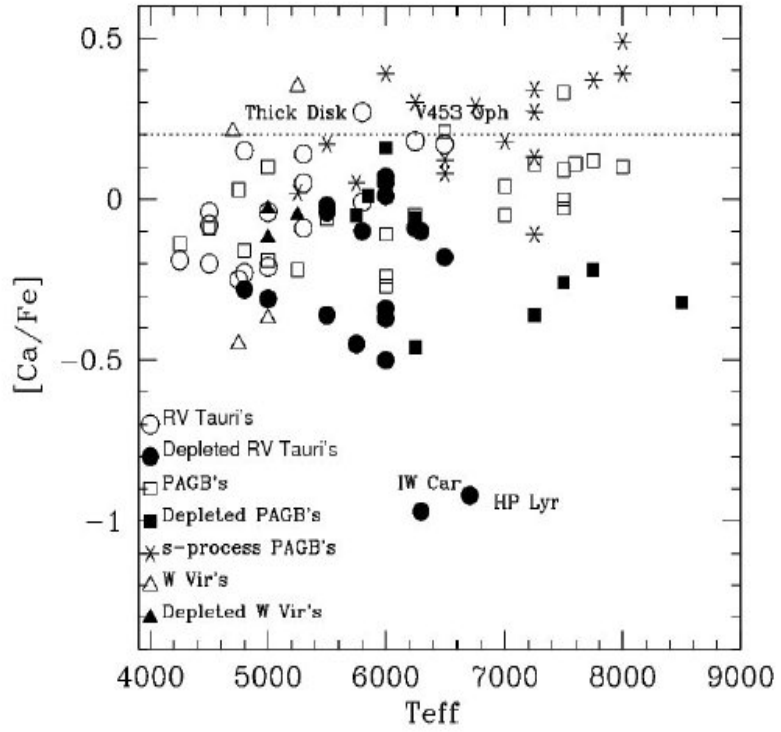

Figure 4.5: Plot of [Ca/Fe] versus the effective temperature for all groups of post-AGBs including our Program Stars.

Mild to severe reduction in [Ca/Fe] can be caused by the fact that the T_C for Ca and Fe are 1517K and 1334 respectively, hence Ca is relatively more susceptible to depletion via condensation onto the grains.

To understand [Ca/Fe] variations seen in post-AGBs and RV Tau stars a plot of [Ca/Fe] as function of temperature could be instructive notwithstanding the fact that some of the heavily depleted objects do not have Ca measurements and non-LTE correction could result in at least +0.1 dex vertical shift to all data points. Figure 4.5 shows thick disk [Ca/Fe] value of +0.21 by dotted horizontal line. The post-AGB stars with s-process enhancement generally have [Ca/Fe] > 0. For these objects, α elements including [Ca/Fe] are consistently positive. A few post-AGB stars with very mild or no s-process enrichment also show [Ca/Fe] of +0.1 to 0.0. RV Tauris such as V453 Oph showing mild s-process

enhancement also show similar [Ca/Fe] values. Depleted post-AGBs and RV Tauris understandably show negative [Ca/Fe]. IW Car and HP Lyr are well known depleted objects with very small scatter in their T_C vs [X/H] plots. Even objects with no established indication of dust-gas separation have small negative [Ca/Fe] in excess of what can be ascribed to non-LTE effects. A large fraction of them have temperatures lower than 5000K, hence the signature of depletion may be muffled for them.

4.10 DISCUSSION

From the study of extended samples of post-AGB stars it has become obvious that they exhibit an enormous chemical variety. However, hardcore post-AGB stars showing the predicted outcome of TDU (increased C/O ratio and s-process enhancements) make a much smaller fraction of known post-AGB stars. We have compiled the abundance data for post-AGB stars and present them in three tables. We have tabulated separately the post-AGB stars showing very distinct s-process enhancement ([s/Fe] > 0.5 dex), those showing very distinct depletion of condensable elements (Depletion Index (DI) > 1.0) and those exhibiting neither distinct s-process enhancement nor depletion in an attempt to statistically infer the influence of factors such as binarity, IR fluxes etc.

4.10.1 Post-AGB stars with s-process enhancements

Our compilation of data for post-AGB stars with significant s-process enhancements is presented in Table 4.8. A few stars have more than one analysis. Most analyses employ resolution around 40,000. More recent analyses employ more accurate oscillator strengths. It should be noted that a majority of them belong to thick disk population with [Fe/H] in range −0.3 to −0.8 dex. Early discoveries of this class with large [s/Fe] led to phrase "have" meaning members with [s/Fe] in range +1.5 to +2.3 and "have not" with [s/Fe] ∼ 0.

However, recent studies (including the present work) have found the objects with moderate s-process enhancements and C/O not exceeding one. Heavily enriched objects seem to favour a temperature range of 6000K to 7500K. They all have [α/Fe] in similar to those of thick disk stars. A large fraction of them show 21 micron feature. The SED generally contains well resolved IR component of strength comparable to photospheric component. Three objects from Table 4.8 IRAS 08143-4406, IRAS 22223+4327 and IRAS 23104+6147 have nebulae of SOLE class (generally of 2 arcsec size) detected by Siódmiak et al. (2008). Another interesting feature of this class of s-process enhanced

Table 4.8: A list of Post-AGB stars with enhancement of s-process elements

IRAS	Other names	T_{eff}	[Fe/H]	[α/Fe]	[s/Fe]	[ls/Fe]	[hs/Fe]	[hs/ls]	Ref	Binarity
08281-4850	...	7750	−0.33	+0.25	+1.24	+1.23	+1.25	+0.02	8	No
22223+4327	BD+42^{o}4388, V448 Lac	6500	−0.33	+0.25	+0.92	+1.31	+1.18	−0.13	1	No
...	...	6750	−0.30	+0.24	+1.08	+1.36	+0.94	−0.42	9	No
08143-4406	...	7250	−0.39	+0.24	+1.51	+1.53	+1.50	−0.02	2	No
06530-0213	...	7250	−0.46	+0.20	+2.06	+1.83	+2.18	+0.35	2	No
17279-1119	HD 158616, V340 Ser	7250	−0.43	+0.25	+0.64	+0.70	+0.62	−0.08	1	No
...	...	7300	−0.60	+0.44	+0.69	+0.95	+0.60	−0.35	5	No
...	...	7400	−0.68	+0.78	+0.50	+0.50	..	−0.50	6	No
Z02229+6208	...	5500	−0.50	+0.17	+1.37	+2.08	+1.13	−0.95	4	No
07430+1115	...	6000	−0.50	+0.09	+1.60	+2.09	+1.44	−0.65	4	No
14325-6428	...	8000	−0.55	+0.30	+1.25	+1.23	+1.29	+0.06	8	No
18384-2800	HD 172481, V4728 Sgr	7250	−0.62	+0.46	+0.48	+0.58	+0.44	−0.14	5	Yes
...	...	7250	−0.55	+0.37	+0.48	+0.49	+0.47	−0.02	9	Yes
04296+3429	...	7000	−0.65	+0.38	+1.55	+1.66	+1.49	−0.17	9	No
19500-1709	HD 187885, V5112 Sgr	8000	−0.66	+0.30	+1.15	+1.40	+1.03	−0.37	9	No
...	...	8000	−0.44	+0.54	+1.31	+1.29	+1.35	+0.06	7	No
05341+0852	...	6500	−0.72	+0.29	+2.22	+2.01	+2.32	+0.32	9	No
05113+1347	...	5250	−0.75	+0.18	+2.00	+1.61	+2.16	+0.55	3	No
23304+6147	...	6750	−0.81	+0.32	+1.60	+1.55	+1.63	+0.09	9	No
22272+5435	HD 235858, V354 Lac	5750	−0.82	+0.17	+1.99	+1.56	+2.17	+0.61	3	No
07134+1005	HD 56126, CY CMi	7250	−1.03	+0.08	+1.51	+1.56	+1.49	−0.06	9	No

[1]Sumangala Rao et al. (2012), [2] Reyniers et al. (2004), [3]Reddy et al. (2002),
[4]Reddy et al. (1999)

[5]Arellano Ferro et al. (2001), [6]Van Winckel (1997), [7]Van Winckel et al. (1996)

[8]Reyniers et al. (2007b), [9]Reyniers (2002)

post-AGB stars is that very few of them are known binaries. They appear to represent single star evolution of moderately metal-poor thick disk stars.

4.10.2 Post-AGB stars with depletion of refractory elements

Although a working hypothesis of dust-gas separation in circumbinary disk causing selective depletion of refractory elements has been proposed, the actual mechanism of disk formation and its evolution is far from understood.

We have compiled the existing data for all known post-AGB stars and RV Tau stars and chosen very stringent selection criteria to define the group of post-AGB stars showing depletion due to selective removal of condensable elements. The guideline being [S/Fe] and [Zn/Fe] > 0 and [Ca/Fe], [Sc/Fe], [Ti/Fe] < 0.0. We present our compilation in Table 4.9. It is possible that adherence to this criteria would result in non- inclusion of some post-AGB stars considered mildly depleted in other studies.

Quantifying the depletion process is a very difficult task. S and Zn are good representatives of non-depleted elements due to their low condensation temperatures :704 and 726K respectively. CNO inspite their lower T_C are not useful since they are affected by nuclear processing and dredge-ups. However Zn I lines are strongest at around 4700K and remain strong at even lower temperatures but the spectrum gets too crowded to measure them. At higher temperatures like 7000K and above they become weak and are weaker than 10 mÅ at 8000K. The lines of S I are at the strongest near 6700K but weaken drastically at cooler as well as hotter temperatures. Hence the abundance errors are highly temperature dependent. We have taken mean of heavily depleted elements Ca, Sc and Ti (with similar condensation temperatures 1517, 1582 and 1659K respectively) and subtracted it from [S/H] to define depletion index given in Table 4.9. Ideally [Al/H] should have been included in the calculations, but Al abundances were not available for many stars. For a few stars only two of these three elements are measured; then the mean is taken of the elements for which data is available. For heavily depleted stars [Zn/H] is a better metallicity indicator; hence the objects with [Zn/H] < -0.5 dex could belong to thick disk and halo population.

We have studied T_C vs [X/H] curves for all stars of Table 4.9 and have indicated by $*$ those that exhibit very smooth curves like HP Lyr in the column for DI (Depletion Index). The DI basically defines the degree/strength of depletion. Higher the depletion index greater is the degree of depletion suffered by the star. The depletion index has been calculated using the formula: DI = [S/H]-([Ca/H]+[Sc/H]+[Ti/H])/3. In the absence of other elements the DI has been calculated from S and Fe as in the case of heavily

Table 4.9: A list of Post-AGB stars showing depletion

IRAS	Other[a]	T_{eff}	[12]-[25]	[25]-[60]	[S/H]	[Zn/H]	[Ca/H]	[Sc/H]	[Ti/H]	[Fe/H]	DI[b]	Ref	Bin[c]
...	TT Oph	4800	..	..	+0.01	−0.71	−1.13	−1.09	−0.82	−0.85	1.02	2	N
...	UZ Oph	5000	..	..	−0.38	−0.74	−1.10	−1.26	−1.00	−0.79	1.50	4	N
...	W Vir	5000	..	..	−0.26	−0.84	−1.03	−2.03	−1.08	−1.00	1.12	12	N
...	V1711 Sgr	5000	..	..	−0.07	−0.98	−1.32	−2.46	−2.05	−1.20	1.87	12	N
...	RX Lib	5250	..	..	−0.58	−0.80	−1.05	−2.22	−1.14	−1.00	0.89	12	N
17250-5951	UY Ara	5500	+0.27	−0.95	+0.01	−0.29	−1.06	−1.74	..	−1.02	1.41*	2	N
06054+2237	SS Gem	5500	−0.28	+0.08	−0.42	+0.02	−1.05	−1.92	−2.00	−0.87	1.24	3	N
06072+0953	CT Ori	5500	−0.11	−1.63	−0.53	−0.58	−1.80	−2.58	−2.51	−1.87	1.65*	3	Y
06160-1701	UY CMa	5500	−0.38	−1.59	−0.32	−0.59	−1.65	−2.22	−2.38	−1.29	1.65*	4	Y
20117+1634	R Sge	5750	−0.37	−1.38	+0.37	−0.19	−0.95	−1.48	−1.34	−0.50	1.63	5	Y
19163+2745	EP Lyr	5750	+0.52	−0.24	−0.61	−0.70	−1.82	−2.11	−2.01	−1.80	1.26*	5	Y
09144-4933	..	5750	−0.25	−1.57	−0.01	...	−0.37	−1.65	−1.28	−0.31	1.09	14	N
20056+1834	QY Sge	5850	+0.03	−1.31	+0.14	−0.14	−0.28	−0.70	−1.15	−0.29	0.85	13	Y
07008+1050	HD 52961	6000	−0.77	−0.92	−1.00	−1.40	..	..	..	−4.80	3.80†	8	Y
06338+5333	HD 46703	6000	−0.21	+0.05	−0.40	−1.40	−1.60	..	−1.79	−1.60	1.00*	11	Y
18281+2149	AC Her	6000	+0.50	−1.21	−0.37	−0.93	−1.50	−1.70	−1.64	−1.40	1.13*	6	Y
08011-3627	AR Pup	6000	−0.36	−1.39	+0.44	..	−1.37	−2.16	..	−0.87	2.20	5	Y

Table 4.9: Contd..

IRAS	Other[a]	T_{eff}	[12]-[25]	[25]-[60]	[S/H]	[Zn/H]	[Ca/H]	[Sc/H]	[Ti/H]	[Fe/H]	DI[b]	Ref	Bin[c]
06034+1354	DY Ori	6000	+0.19	−1.38	+0.16	+0.21	−1.70	..	−2.33	−2.30	2.65*	4	Y
12067-4508	RU Cen,	6000	+0.78	−0.72	−0.68	−1.00	−1.89	−1.88	−1.96	−1.90	1.11	7	Y
18548-0552	BZ Sct	6250	+0.05	+0.49	+0.18	+0.04	−0.91	−1.13	−1.22	−0.82	1.27	4	N
...	CC Lyr	6250	..	..	−0.50	−1.20	..	..	..	−3.40	2.90†	12	N
16230-3410	...	6250	−0.27	−1.52	−0.36	−0.42	−0.74	−2.28	−1.45	−0.68	1.13	14	Y
17233-4330	...	6250	−0.26	−1.40	+0.14	−0.21	−1.39	−1.60	−1.62	−0.98	1.68	14	Y
17243-4348	LR Sco	6250	−0.22	−0.94	+0.04	+0.22	−0.17	−1.11	−0.61	−0.05	1.07	4	Y
18564-0814	AD Aql	6300	+0.09	−1.55	−0.03	−0.12	−2.22	−1.79	−2.57	−2.12	2.16*	6	Y
19199+3950	HP Lyr	6300	−0.02	−1.56	+0.05	−0.35	−1.95	−2.87	−2.97	−0.98	2.83*	4	N
12185-4856	SX Cen	6500	−0.54	−1.28	−0.08	−0.54	−1.52	−1.96	−1.97	−1.15	1.62	7	Y
09256-6324	IW Car,	6700	−0.05	−1.11	+0.36	−0.04	−1.97	−2.13	..	−1.0	2.41*	10	Y
08544-4431	V390 Vel	7250	−0.14	−1.13	+0.12	+0.09	−0.36	−0.87	−0.85	−0.50	0.81*	15	Y
15469-5311	..	7500	−0.16	−1.08	+0.51	+0.25	−0.46	−1.56	−1.57	+0.04	1.70	14	Y
10158-2844	HR 4049	7500	−1.76	−1.83	−0.40	−1.30	−5.30	..	..	−4.80	4.90*	8	Y
06176-1036	HD 44179	7500	+0.09	−1.05	−0.30	−0.60	−3.11	..	..	−3.30	2.69*	8	Y
19125+0343	BD+03^{o}3950	7750	−0.09	−1.32	+0.48	+0.13	−0.51	..	−2.15	−0.35	1.75*	14	Y
...	BD+39^{o}4926	7750	..	..	+0.07	−0.70	..	−2.80	−2.73	−2.37	2.72*	1	Y
22327-1731	HM Aqr	8200	−0.19	−0.86	+0.36	..	..	−1.31	−1.49	−0.90	1.76	8	Y
...	HD 105262	8500	..	..	−0.50	..	−2.10	−2.07	−1.58	−1.90	1.42*	9	Y

[a]Other refers to other names. ,[b]DI refers to Depletion Index. † refers to D.I measured from S and Fe in absence of other elements. ∗ indicate that the depletion plots of these stars had less scatter. ,[c]Bin refers to Binarity. ,[1]Sumangala Rao et al. (2012), [2]Giridhar et al. (2000), [3]Gonzalez et al. (1997a), [4]Giridhar et al. (2005), [5]Gonzalez et al. (1997b), [6]Giridhar et al. (1998), [7]Maas et al. (2002), [8]Van Winckel (1995), [9]Giridhar et al. (2010), [10]Giridhar et al. (1994), [11]Hrivnak et al. (2008), [12]Maas et al. (2007), [13]Rao et al. (2002), [14]Maas et al. (2005), [15]Maas et al. (2003)

depleted stars.

A range of depletion indices is observed in these stars (see Table 4.9). This can be due to the orbital properties of the binary system. But the orbital parameters are known accurately only for a handful of post-AGB and RV Tau stars. The range in depletion indices can also be due to its dependence on several other factors like the initial composition of the gas and dust in the reservoir from which a star accretes gas and the temperature distribution within the reservoir, the gas to dust ratio of the accreted material, rate and degree of the mixing of the accreted material with the atmosphere/envelope of the star.

The compilation brings about intriguing statistics; out of 36 depleted post-AGB stars 25 are known binaries, 28 have IRAS detections seven are without (which is about 19%).

Hence it is obvious that binarity plays very important role. Non-detection of IRAS fluxes could be caused by weakening and cooling of the disk hence surveys at longer wavelengths and with increased sensitivities are required to resolve this issue.

But the dust-gas winnowing process still remains poorly understood due to the existence of enigmatic objects like IRAS 07140-2321, BZ Pyx, IRAS 01427+4633, IRAS 19135+3937 etc (see Table 4.10 and Table 3.9). All these objects have favorable conditions for dust-gas separation process to operate like presence of strong IR excess, conducive effective temperatures and binarity, still these objects do not show the effects of dust-gas winnowing! The absence of abundance anomalies (no observed DG effect) in these objects might be due to two reasons. Firstly these above mentioned objects are all short period binaries having orbital periods in the range of 116-140 days (The orbital period range for depleted objects are usually in the range of 300-1500 days). Secondly objects like IRAS 07140-2321, IRAS 01427+4633 and IRAS 19135+3937 show a strong P-Cygni Hα profile in their spectra which is evidence for ongoing mass-loss in these stars (Van Winckel et al. 2000; Gorlova et al. 2012a,b). Maas et al. (2005) suggest that the ongoing mass-loss induced by the companion may be responsible for no depletions observed in these stars.

In our study of extended sample for RV Tau stars (Giridhar et al. 2005) we had proposed two scenarios (based upon the single star and binary configuration) and also discussed the parameters strongly affecting the depletion caused by dust-gas separation.

The surface temperature: The first important requirement was that the star must be hotter than $\sim$ 5000K. The cooler RV Tau stars (RVA) did not show the abundance anomalies, possibly their massive convective envelopes diluted the effect of accreted gas which was cleaned of refractory elements. The masses of convective envelopes for post-AGB stars increases with decreased temperature (see Frankowski (2003) for more details)

varies from 0.016 $M_\odot$ at 4000K to 0.0001 $M_\odot$ at 6000K. At 6000K the mass of convective envelope is about 1000 times that of observable photosphere. At hot temperatures the abundance deficiency of readily condensable elements (those with high T_c) may approach a thousandfold and in such cases the surface and convective envelope would be composed of almost undiluted accreted gas. At lower temperatures, in addition to larger convective mass the stronger stellar wind may oppose the accretion of the clean gas.

The metallicity: The dust-gas separation process has not been seen in stars with intrinsic metallicity lower than ~ -1.0 irrespective of their temperatures. It is likely consequence of the inability of radiation pressure on dust grains to force a separation of dust from gas when the mass fraction of the dust is very low as seen in metal-poor environments. A dust-gas reservoir with metallicity in excess of -1.0 is mandatory for efficient separation of dust from the gas. These conditions can be easily realized in binary scenario with circumbinary disk since it may contain gas from either binary companion or the main star before the onset of accretion.

Although a revised minimum temperature 4800K for discernible depletion has been identified, but stars in temperature range 6000K to 7500K tend to show larger depletions. At hotter side $T_{eff}>$ 8500K DI is smaller; a shift in ionization structure causing the observable features to become too scarce for S and Zn may be responsible.

Many stars such as CC Lyr, HR 4049, BD+39^{o}4926 show large differences between S and Zn despite these elements having nearly the same T_C. For thick disk and halo stars relative enrichment of S by +0.3 dex can be anticipated since the S is an α element but for larger differences found in the above mentioned objects there is no ready explanation.

Another intriguing observation is that DI are not correlated with IRAS colors nor do they show any correlation with IR flux at a given wavelength.

Since the SED characteristics can be used to develop a model for circumstellar material, De Ruyter et al. (2006) have done optical photometry and have also used the IR and sub-millimeter data for a large sample of known binary post-AGB stars and other objects (like RV Tau stars) of similar IR characteristics. Using the optically thin dust model they found the dust at or near sublimation temperature (1200K) and also very close to the star ($\sim$ 10 AU from the central source) irrespective of the effective temperature of the star. These authors argued that at least a part of the dust must be gravitationally bound since any typical AGB outflow velocity would bring the dust to cooler region within years. Although their sample of known post-AGB binary and RV Tau stars of similar characteristics had a large range in the size of IR excess, but the shape of IR excess indicated that CS was not freely expanding but was stored in the system. A study of orbital pa-

rameters for the well-studied objects point to orbits which are too compact for sizes of post-AGB stars. These authors further suggest that it is highly improbable that these stars have evolved as single stars; a strong interaction phase while the star was in giant stage is required to explain the present configuration.

The high spatial resolution interferometry in mid IR has been used to resolve compact dusty disks around the depleted binary post-AGB stars. For Red Rectangle, HR 4049 and recently for HD 52961 the dusty disks have been resolved (Deroo 2007). It is comforting to see the additional information provided by high spatial resolution interferometry towards better understanding of these systems but the accuracies of disk dimensions are constrained by the radiative transfer models.

4.10.3 Post-AGB stars without significant s-process enhancement nor showing depletions

A good number of post-AGB candidates displaying basic post-AGB characteristics like IRAS colors, high luminosity, small amplitude light and radial velocity variations do not belong to the above mentioned classes.

Regarding s-process enhancements, the earlier samples of post-AGB belonged to only two classes ”have” and ”have not”; the ”have” showing strong s-process enhancements ([s/Fe] > 1] while many of the ”have nots” had subsolar [s/Fe] ratios. With increased sample the moderately enhanced members are making an appearance. IRAS 17279-1119 has been known for some time but IRAS 01259+6823, IRAS 05208-2035 and IRAS 08187-1905 are new additions.

Then there are other post-AGB stars including RV Tauris without significant s-process enhancement nor showing depletions. We have tabulated 42 such objects (more than half are RV Tauris and Semi-regular variable of type D SRDs) in Table 4.10. A large fraction of them (30) are IRAS sources, one fourth (13) are binaries all showing IRAS fluxes. In terms of temperature range and IRAS colors they are indistinguishable from those in Table 4.9. Post-AGB with s-process enhancements (Table 4.8) appear to be systematically warmer. It should be noted that larger DI post-AGB also seem to favour the same temperature range. Then it would appear that condition of low surface temperature are not conducive for the survival of abundance peculiarities although unglamorous objects are found even among objects in temperatures range of 6000K to 7500K.

Table 4.10: A list of Post-AGB stars showing neither significant s-process enrichment nor depletion

IRAS	Other[a]	T_{eff}	[12]-[25]	[25]-[60]	[S/H]	[Zn/H]	[Ca/H]	[Sc/H]	[Ti/H]	[Fe/H]	Ref	Bin[b]
02008+4205	HD 12533	4250	−1.55	−2.05	..	−0.05	−0.20	−0.08	−0.21	−0.06	8	N
19437-1104	DY Aql	4250	+0.17	−0.37	..	..	−1.22	−2.13	..	−1.03	3	N
20343+2625	V Vul	4500	−0.84	−1.60	+0.57	−0.27	−0.47	−0.69	−0.18	−0.39	1	Y
18448-0545	R Sct	4500	−0.89	−0.14	..	−0.19	..	−1.43	−0.38	−0.35	2	N
04440+2605	RV Tau	4500	−0.24	−1.11	..	+0.02	−0.48	−0.35	−0.53	−0.40	2	Y
07331+0021	AI CMi	4500	+1.62	−1.42	..	..	−1.25	−1.35	−0.89	−1.16	11	N
06489-0118	SZ Mon	4700	−0.54	−1.38	+0.24	−0.43	−0.19	−1.46	−1.25	−0.40	10	N
...	MZ Cyg	4750	..	..	+0.53	−0.23	−0.65	−1.07	−0.63	−0.20	10	N
...	AZ Sgr	4750	..	..	−0.34	..	−1.80	−1.78	−1.57	−1.55	1	N
17038-4815	..	4750	+0.19	−0.84	..	−1.20	−1.47	−2.00	−1.40	−1.50	6	Y
17193+8439	HD 159251	4800	−1.27	+0.99	..	−0.14	−0.21	−0.03	−0.10	−0.05	8	N
19472+4254	DF Cyg	4800	−0.65	−0.82	..	−0.62	−0.23	−0.96	−0.04	+0.00	1	N
04166+5719	TW Cam	4800	−0.42	−1.20	−0.05	−0.34	−0.65	−0.43	−0.64	−0.50	2	Y
07284-0940	U Mon	5000	−0.37	−1.31	−0.15	−0.71	−0.96	−0.97	−0.70	−0.79	2	Y
F17015+0503	TX Oph	5000	..	..	−0.63	−1.23	−1.43	−1.79	−1.18	−1.22	1	N
01369+4124	HD 10132	5000	−0.62	+0.02	+0.15	−0.14	+0.05	+0.36	−0.02	−0.05	8	N
...	CO Pup	5000	..	..	−0.05	−0.73	−0.97	−1.56	−0.94	−0.60	10	N
...	TW Cap	5250	..	..	−1.40	−1.52	−1.45	−1.61	−1.42	−1.80	10	N
...	V360 Cyg	5250	..	..	−0.88	−1.36	−1.26	..	−1.28	−1.40	4	N
17530-3348	AI Sco	5300	−0.47	−1.46	−0.08	−0.61	−0.64	−0.96	−0.89	−0.69	1	Y
...	AR Sgr	5300	..	..	−0.82	−1.20	−1.44	−1.41	−1.21	−1.33	1	N
09538-7622	...	5500	−0.40	−1.20	−0.30	−0.60	−0.66	−0.90	−0.70	−0.60	6	Y

Table 4.10: Contd..

IRAS	Other[a]	T_{eff}	[12]-[25]	[25]-[60]	[S/H]	[Zn/H]	[Ca/H]	[Sc/H]	[Ti/H]	[Fe/H]	Ref	Bin[b]
...	RX Cap	5800	..	..	−0.57	−0.63	−0.79	−1.20	−0.62	−0.78	1	N
...	BT Lib	5800	..	..	−0.76	−1.06	−0.91	−0.71	−0.96	−1.18	2	N
04535+3747	V409 Aur	6000	−0.73	−0.03	−0.16	−0.53	−0.59	−0.75	−0.63	−0.48	11	N
13110-5425	HD 114855	6000	+2.08	+1.39	+0.34	−0.26	−0.35	−0.34	−0.41	−0.11	5	N
14524-6838	EN TrA	6000	−0.28	−0.99	−0.61	−0.56	−1.03	..	−1.11	−0.76	7	Y
08187-1905	V552 Pup	6250	+ 3.49	−0.39	+0.05	−0.58	−0.63	−0.75	−0.99	−0.59	11	N
09060-2807	BZ Pyx	6500	−0.43	−1.46	−0.70	−0.50	−0.49	−0.80	−0.70	−0.70	6	Y
...	DS Aqr	6500	..	..	−0.82	−1.07	−0.97	−1.17	..	−1.14	2	N
12222-4652	HD 108015	7000	+0.03	−1.55	−0.15	−0.16	−0.05	−0.80	−0.26	−0.09	7	Y
IRAS 07140-2321	SAO 173329	7000	−0.24	−1.14	−0.32	−0.87	−0.97	−0.92	−0.73	−0.92	11	Y
04002+5901	HD 25291	7250	−1.46	−0.02	+0.08	..	−0.22	+0.01	−0.30	−0.33	8	N
07018-0513	HD 53300	7500	−0.97	+0.30	−0.04	−0.71	−0.62	−0.96	−0.83	−0.62	5	N
18439-1010	HD 173638	7500	−1.38	+0.59	..	−0.06	+0.01	+0.16	−0.05	−0.08	9	N
12175-5338	SAO 239853	7500	+3.25	−1.08	−0.40	−0.73	−0.48	−1.11	−0.54	−0.81	7	N
04175+3827	HD 27381	7500	−0.99	+0.24	−0.30	..	−0.59	−0.39	−0.57	−0.67	8	N
...	HD 107369	7500	..	..	−0.84	..	−1.36	−1.45	−1.09	−1.33	11	N
11000-6153	HD 95767	7600	−0.37	−0.39	+0.01	−0.12	+0.24	..	−0.11	+0.13	7	Y
19157-0247	...	7750	−0.23	−1.17	+0.20	..	..	−0.40	−0.20	+0.10	6	Y
...	HD 10285	7750	..	..	+0.04	−0.36	−0.19	−0.07	−0.30	−0.31	8	N
...	HD 218753	8000	..	..	+0.17	+0.18	−0.09	+0.00	−0.26	−0.19	9	N

[a]Other refers to other names, [b]Bin refers to Binarity. [1]Giridhar et al. (2005), [2]Giridhar et al. (2000), [3]Gonzalez et al. (1997a), [4]Giridhar et al. (1998) ,[5]Giridhar et al. (2010), [6]Maas et al. (2005), [7]Van Winckel (1997), [8]Giridhar & Arellano Ferro (2005) ,[9]Arellano Ferro et al. (2001), [10]Maas et al. (2007), [11]Sumangala Rao et al. (2012)

4.11 Summary

In our exploration of post-AGB candidates we find mild enhancements of s-process elements in IRAS 01259+6823, IRAS 05208-2035 and IRAS 08187-1905, while significant enhancement is found for IRAS 17279-1119 and IRAS 22223+4327. Mild s-process enhancement and low temperatures of IRAS 05208-2035 and IRAS 01259+6823 are not of common occurrence in post-AGB stars although the theory does not prohibit such objects since the degree of s-process enhancement gradually builds with number of thermal pulses. However further evidence like intrinsic luminosity estimates are awaited.

A survey of well established s-process enhanced post-AGB stars shows majority of this group to be most likely thick disk objects of intermediate temperatures. It does not appear that their evolution is strongly affected by the presence of binary companion. Most of these heavily s-processed objects have temperatures between 6000K to 7500K, although a spread in [s/Fe] for similar atmospheric parameters is seen indicating the influence of additional processes on third dredge-up efficiency.

A contemporary analysis of BD+39^o 4926 has been conducted and initial metallicity of -0.7 dex has been estimated. HD 107369 appear to be a metal-poor, high galactic latitude supergiant with strong influence of CN processing. The observed N enhancement is in excess of that predicted by the FDU but cannot be ascribed to large rotation at main sequence as the stellar lines are very sharp and narrow – not much broader than the instrumental profile.

Our compilation of the post-AGB stars showing the abundance peculiarities caused by selective depletion of refractory elements reiterates the temperature and metallicity limits observed earlier for their detection. The observed SED with dust excess of these objects have been interpreted by De Ruyter et al. (2006) via a circumstellar dust shell contained in Keplerian rotating disks. But the actual resolution of dusty disks and measurement of their sizes has been possible only for heavily depleted objects like HR 4049, Red Rectangle and more recently HD 52961 although HD 52961 does not exhibit large IR excess. Search of such depleted objects and their follow-up using high spatial resolution mid IR interferometry and IR spectrometry can provide valuable insight into the circumstellar geometries of these objects.

Our compilation of post-AGB stars showing neither of these two peculiarities (those having normal compositions) are indistinguishable from the ones showing s-process enhancements and those affected by dust-gas winnowing in terms of basic stellar parameters. Hence the cause separating these subgroups among post-AGB stars is not understood.

The extension of abundance analysis to post-AGB candidates located in uniform stellar system such as globular clusters, or in neighbouring galaxies would help since each system would have small range in mass and metallicity. The poorly known distances and hence luminosities and masses of the limited sample of Galactic post-AGB stars hamper our interpretation of the variety of abundances in the theoretical context of stellar evolution. By observing post-AGB stars in different clusters we can measure post-AGB chemical composition as a function of both mass and metallicity. Globular cluster observations will provide a template that will allow accurate identification of field post-AGB stars and their initial metallicites. Finally since the distances and hence the absolute luminosities of globular cluster stars can be estimated it should be possible to determine the distances and hence the luminosities of field post-AGB objects.

Studying post-AGB stars in neighboring galaxies like LMC and SMC covering a wide range in luminosities and metallicites with well constrained distances will help in the better understanding of AGB nucleosynthesis like TDU and its dependence on mass and metallicity.

CHAPTER 5

ANALYSIS OF TWO MILDLY H-DEFICIENT STARS: SAO 40039 AND HD 187885

5.1 ABSTRACT

We have conducted an LTE abundance analysis for SAO 40039 and HD 187885, two warm post-AGB stars whose spectra are known to show surprisingly strong He I lines for their effective temperatures and have been suspected of being H-deficient and He-rich. High-resolution optical spectra are analyzed using a family of model atmospheres with different He/H ratios. Atmospheric parameters are estimated from the ionization equilibrium set by neutral and singly ionized species of Fe, Mg and Cr, the excitation balance of Fe I and Fe II lines, and the wings of the Paschen lines. On the assumption that the He I lines are of photospheric and not chromospheric origin, a He/H ratio of approximately unity is found for SAO 40039 and He/H of 0.4 for HD 187885 by imposing the condition that the adopted He/H ratio of the model atmosphere must equal the ratio derived from the observed He I triplet lines at 5876, 4471 and 4713Å, and singlet lines at 4922 and 5015Å. Using the model with the best-fitting atmospheric parameters for this He/H ratio, SAO 40039 is confirmed to exhibit mild dust-gas depletion, i.e., the star has an atmosphere deficient in elements of high condensation temperature. This star appears to be moderately metal-deficient with [Fe/H]=−0.4 dex. But the star's intrinsic metallicty as estimated from Na, S and Zn, elements of a low condensation temperature, is $[Fe/H]_o$[*] $\simeq -0.2$. The star is enriched in N and perhaps O too, changes reflecting the

[*] $[Fe/H]_o$ refers to the star's intrinsic metallicity

star's AGB past and the event that led to He enrichment. HD 187885 on the other hand, is known to exhibit strong s-process enhancement with [s/Fe] of +1.3 dex and also an enrichment of C, N and O pointing towards the operation of efficient TDU and thermal pulses and the abundances are found to be in agreement with the AGB nucleosynthesis predictions. Using the appropriate H-deficient model with He/H=0.4 we report the [Fe/H] of −0.9 dex for this star.

5.2 INTRODUCTION

SAO 40039: also known as IRAS 05040+4820 and BD +48°1220, is judged by several criteria to be a post-AGB star: its spectral type (A4Ia), its position in the IRAS color-color diagram and the double-peaked SED indicating a detached youthful cold dust shell around the central star. Using VBRIJHK photometry and adopting a simple dust shell model, Fujii et al. (2002) find a dynamical age of 2460 years for the dust shell with dust at 97K, and estimate the star to have a core mass of $0.55 M_{\odot}$ indicating a low-mass progenitor for this post-AGB star. Klochkova et al. (2007) have presented an abundance analysis of SAO 40039 based on high-resolution spectra with a wavelength coverage of 4500-6760Å. They have also discussed the star's radial velocity changes spanning over three years and also time-dependent differential velocity shifts between different classes of absorption lines. Their spectra showed a variable Hα line with two emission components. Variable emission was also reported in Hβ and in some lines of Si II, Fe I and Fe II. The photospheric absorption lines were found to vary between -7 to -15 kms s^{-1}. The error in the radial velocity determination being 1 km s^{-1}. Since large amplitude radial velocity variations were seen it is likely that SAO 40039 is a binary but Klochkova et al. (2007) stress upon the need for additional radial velocity measurements to confirm binarity in this star.

But, in particular, these authors pointed out the abnormal strength of the He I 5876Å absorption feature in this star with the 'low' effective temperature of about 8000 K. Their abundance analyses conducted with model atmospheres computed for a normal He/H ratio (=0.1) gave the He/H ratio of 0.7.

HD 187885: is a high-galactic latitude F-supergiant with strong far-IR colors (Parthasarathy & Pottasch 1986) attributed to cool dust shells/envelopes around the central star and is thought to be the remnant of the previous AGB phase of evolution. This object also known as IRAS 19500-1709 shows a weak 21 micron feature (Justtanont et al. 1996) as well as the broad 30 micron feature (Hony et al. 2002) in its IR spectra which is

typical signature of carbon-rich objects. Clube & Gledhill (2004) presented the mid-IR imaging and suggested the presence of optically thin detached axisymmetric dust shell. Their SED modelling of the dust shell around HD 187885 yielded dust temperatures in the range 50-170K and the best fit to the SED was obtained by considering grains like SiC, MgS and amorphous carbon with grain sizes of about 0.01 micron. A distance estimate of 4kpc was obtained from a radiative transfer model.

The abundance analysis of HD 187885 was first conducted by Van Winckel et al. (1996) based on a high-resolution spectra. Subsequently a more detailed analysis with a broader spectral coverage and a higher S/N spectra was done by Van Winckel & Reyniers (2000) covering more number of atomic species. These analyses showed the star to be super-rich in He, C and s-process elements pointing towards efficient TDU and in accordance with theoretical predictions of AGB nucleosynthesis.

The He I 5876 and 4471 lines in absorption were detected in their spectra. Abundance analyses with a solar (He/H=0.1) model yielded a He/H ratio of 1.0.

Detection of He I lines in A and F-type supergiants suggest either a He enrichment, if the lines are of photospheric origin, or a contribution from a thick hot chromosphere of presumably a normal He abundance. The above studies adopt the assumption of a photospheric origin and report the photosphere to be moderately H-poor and He-rich. However, these analyses use model atmospheres computed for a normal He/H ratio and do not iterate on the construction of the model atmosphere and the abundance analysis to obtain agreement between the input and output He/H ratio.

Our goal in making a fresh analysis of SAO 40039 and HD 187885 is to iterate to find the self-consistent He/H ratio. In undertaking the analysis, we also adopt the assumption that the He I lines originate in a He-rich photosphere and are not chromospheric in origin.

5.3 OBSERVATIONS AND DATA REDUCTION

Spectra of SAO 40039 were obtained on the nights of 2007 November 5 and 2011 February 21 and that of HD 187885 on the nights of 2011 May 14 and 15 at the W.J. McDonald Observatory with the 2.7m Harlan J. Smith telescope and the Tull coudé spectrograph (Tull et al. 1995). The spectra taken at these epochs were found to be similar. The spectra correspond to a resolving power of 60,000 (5 kms s^{-1}). Reduction of the raw data was performed with the Image Reduction and Analysis Facility (IRAF[†]) software package.

[†]The IRAF software is distributed by the National Optical Astronomy Observatories under contract with the National Science Foundation

An additional spectrum of SAO 40039 was obtained on 2011 January 28 using the echelle spectrometer at Vainu Bappu Observatory in Kavalur, India giving a resolution of about 28,000 (10 kms s^{-1}) in slitless mode (Rao et al. 2005). Additional spectra of HD 187885 were acquired on 2001 July 19 and on 2002 July 25 with the 2.1m Struve reflector with the CCD-equipped Sandiford Cassegrain echelle spectrograph (McCarthy et al. 1993) and a spectral resolving power of 50,000 (6 kms s^{-1}).

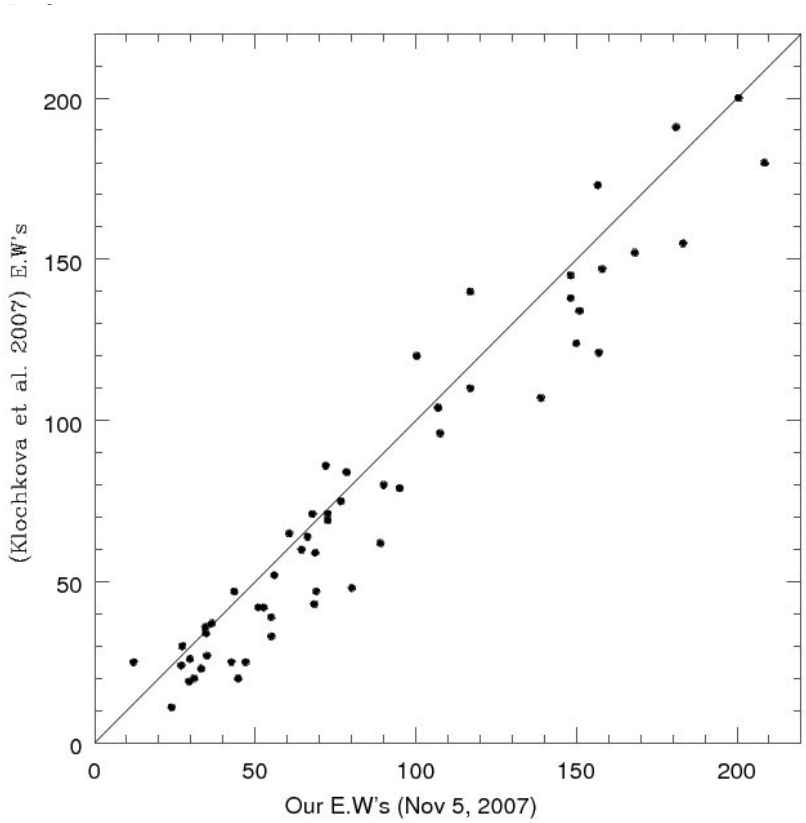

Figure 5.1: Equivalent widths for lines common between our spectra and Klochkova et al. (2007) for SAO 40039.

Our spectra of SAO 40039 resemble closely those described by Klochkova et al. (2007) with regards to emission in Balmer lines, the complex structure of the Na D lines and variable profiles of the metallic lines, and the equivalent widths of lines unaffected by obvious emission. For our analysis we have used only clean, unblended and symmetric absorption lines.

We have compared the equivalent widths of lines common between our spectra and those of Klochkova et al. (2007) as can be seen in the Fig 5.1. A small systematic difference possibly caused by differences in resolution is discernible, but it appears that there

were no major variations in the atmospheric parameters at these epochs. This is also supported by the fact that the average radial velocity of lines in our spectra (-12 kms s^{-1}) lies within the range as reported by Klochkova et al. (2007) in their spectra (-7 to -15 kms s^{-1}). Also no major differences in the heliocentric radial velocities are seen in the case of HD 187885 for spectra taken at different epochs.

Abundance analysis was done first on the assumption that the atmosphere has a normal He/H ratio. Model atmospheres for normal He/H ratio (He/H=0.1) were taken from the Kurucz database[‡]. Atmospheres of different He/H ratios were computed by the code STERNE (Jeffery et al. 2001). The LTE spectrum synthesis code MOOG (2009 version) by Sneden (1973) was used with the grid of model atmospheres taken from the Kurucz database as mentioned above. The LTE code SPECTRUM (Jeffery et al. 2001) was used with the STERNE models.[§]

The procedure begins with the determination of the atmospheric parameters from the spectrum, continues with the abundance analysis for He and other elements and ends when the model of a certain He/H ratio reproduces the observed He I lines.

5.4.1 METHOD FOR DETERMINING THE STELLAR PARAMETERS

SAO 40039: First, we estimated the microturbulent velocity (ξ_t) using Fe II lines with small range in lower excitation potentials (LEP)(2.6−3.2 eV) as these lines have a good range in their equivalent widths thereby reducing any temperature dependence of the estimated ξ_t. The ξ_t is found from the standard requirement that the abundance be independent of the measured equivalent width. The effective temperature ($T_{\rm eff}$) was estimated by the requirement that the abundance of a given species be independent of a line's LEP. This step was conducted independently for Fe I and Fe II lines as they are both well represented in the spectrum and show a range in their LEPs. Finally, the surface gravity ($\log g$) was estimated by the condition that there be ionization balance between the neutral and the singly ionized Fe lines. This condition defines a locus in the ($T_{\rm eff}$, $\log g$) plane and the $T_{\rm eff}$ derived from Fe I and Fe II breaks the degeneracy. This exercise is repeated for grids of model atmospheres with He:H ratios of 10:90, 30:70 and 50:50.

A microturbulence $\xi_t = 4.8 \pm 1.0$ km s^{-1} is found for all models with acceptable effective temperature and surface gravity and the value is insensitive to the He/H ratio of the models. The effective temperature $T_{\rm eff}$ is found to be 8000±300K from 26 Fe I and

[‡]http://kurucz.harvard.edu/grids.html

[§]Note that the stellar parameters and the abundances derived by adopting the Kurucz models and the code MOOG for He/H = 0.1 are in excellent agreement with results from the STERNE models and the LTE code SPECTRUM, also for He/H = 0.1.

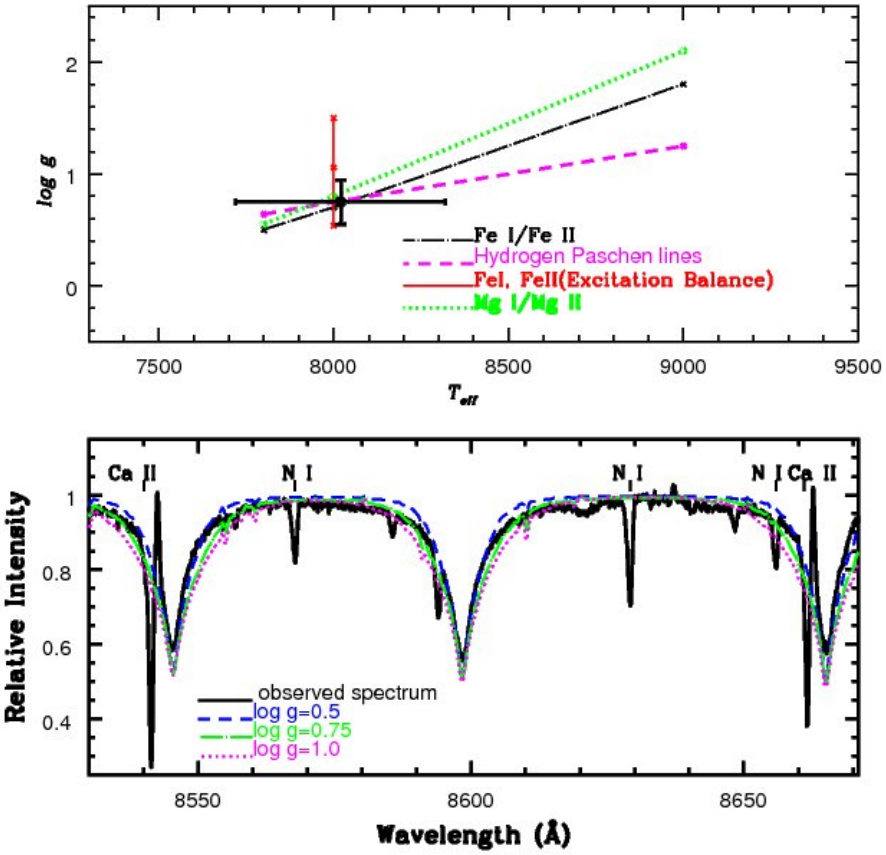

Figure 5.2: The upper panel shows the loci satisfying the ionization balance – see keys on the figure. The locus satisfying the H I Paschen lines is shown by dashed line. The solid line represents the excitation balance of both Fe I and Fe II. The cross shows the derived stellar parameters. Lower Panel shows the observed and synthesized profiles of Paschen lines of H I in the 8600Å region for $T_{\rm eff}$ = 8000K, He/H = 1.0 and $\log g$ = 0.5, 0.75 and 1.0 for the star SAO 40039.

20 Fe II lines. Within the 300K uncertainty, the temperature is independent of surface gravity over a considerable range and is not sensitive to the He/H ratio of the model atmosphere. The $T_{\rm eff}$, $\log g$ locus found from the ionization balance for Fe is illustrated in Fig 5.2 for the model atmosphere grid with He:H = 50:50. With $T_{\rm eff}$ = 8000±300 K from the excitation of Fe I and Fe II, the $\log g$=0.75±0.25 cgs is found. The surface gravity changes slightly with He:H running from 0.94 for He:H=10:90 through 0.83 for He:H=30:70 to the above result for He:H=50:50. A second locus is provided by Mg I and Mg II lines – see upper panel of Fig 5.2. The Mg and Fe loci are in good agreement. A third locus is offered by the Paschen lines (see below).

HD 187885: An average microturbulent velocity ξ_t = 5.0 ± 1.0 kms s^{-1} for HD

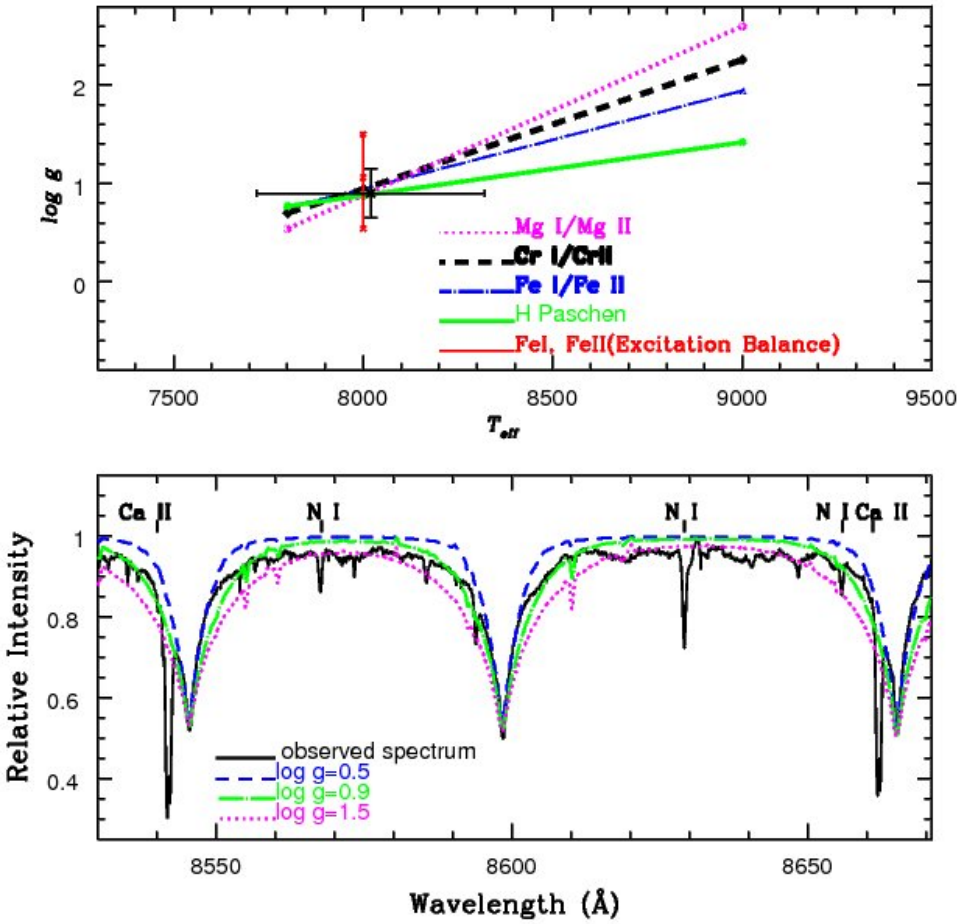

Figure 5.3: The upper panel shows the loci satisfying the ionization balance – see keys on the figure. The locus satisfying the H I Paschen lines is shown by the green solid line. The red solid line represents the excitation balance of both Fe I and Fe II. The cross shows the derived stellar parameters. Lower Panel shows the observed and synthesized profiles of Paschen lines of H I in the 8600 region for $T_{\rm eff}$ = 8000K, He/H = 0.4 and $\log g$ = 0.5, 0.9 and 1.5 for the star HD 187885 .

187885 has been determined from Fe II (2.8-3.3 eV), Ti II (1.1-1.6 eV) and Cr II (3.7-4.2 eV) lines having similar lower excitation potentials. An effective temperature $T_{\rm eff}$ of 8000±300K is found from 28 Fe I and 59 Fe II lines having a good range in their lower excitation potentials. The surface gravity $\log g$ for HD 187885 has been determined by considering ionization balance between neutral and singly ionized species of Fe, Mg and Cr. An estimate of $\log g$ has also been obtained from the wings of the H I Paschen lines in the 8600 region. Figure 5.3 depicts the $T_{\rm eff}$ $\log g$ locus found from the ionization balance for Fe, Mg and Cr and also from the wings of the H I Paschen lines (see bottom panel of Fig 5.3) for the model atmosphere with a He/H=30/70. A $\log g$ of 0.9±0.25 cgs is found.

5.4.2 THE HE/H RATIO

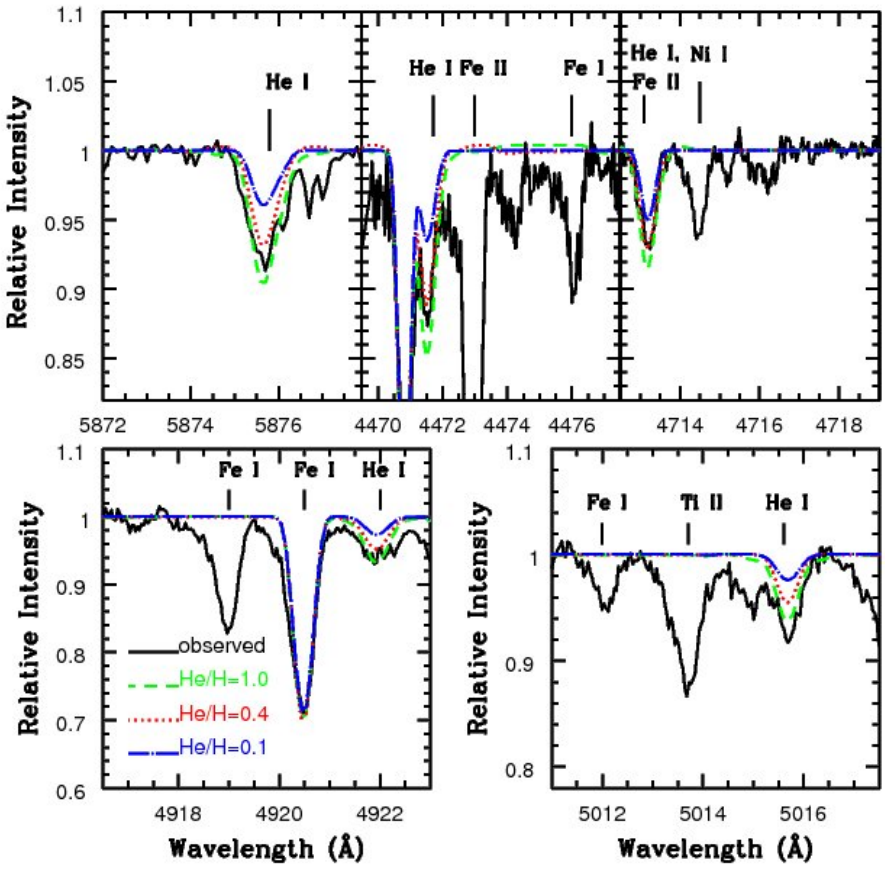

Figure 5.4: The observed and synthesized He I profiles for the triplet lines at 5876, 4471 and 4713Å and for the singlet lines at 4922 and 5015Å for SAO 40039 using models with$T_{\rm eff}$ = 8000K, log g = 0.75 for He/H = 1.0, 0.4 and 0.1 − see keys on the figure.

Our spectra of SAO 40039 confirm the presence of the D3 5876Å He I line with an equivalent width very similar to that reported by Klochkova et al. (2007). The strength of this line suggests that several other lines should be present unless the excitation of the D3 line is highly peculiar. Our search also provided the additional triplets (4471 and 4713Å) and two singlet lines (4921 and 5015Å). Since the He I at 4713Å is blended with the Fe II line, its contribution has been included while synthesizing the He I profile at 4713Å as shown in the Figure 5.4, we get a consistent He/H ratio of approximately unity for SAO 40039. Other possible He I lines are predicted to be below the detection limit, or blended with other lines or inaccessible due to inter-order gaps. The presence of these triplets and singlets mentioned above have also been detected in the case of HD 187885.

The He I lines were computed for model atmospheres with ($T_{\rm eff}$, log g, ξ_t)=(8000, 0.75,

4.8) for SAO 40039 and with the the appropriate model for the He/H ratios: 0.1 (normal; solar abundance), 0.4 (30/70), and 1.0 (50/50). The synthesized profiles are convolved with the instrumental and the stellar rotation profiles, before matching with the observed spectrum as described in Pandey (2006). The data for computing the He I profiles were taken from Jeffery et al. (2001). A projected rotational velocity of about 13−16 km s^{-1} is estimated by using unblended moderately strong lines. As shown in Fig 5.4, the best fits to the observed He I profiles at 5875, 4471, 4713, 4922 and 5015Å were obtained for He/H ratio of 1.0 (50/50) with an uncertainty of approximately ±0.2. Similarly Fig 5.5 shows the best fits to the He I profiles for HD 187885 for He/H ratio of 0.4 (30/70) for the model atmospheres with ($T_{\rm eff}$, log g, ξ_t)=(8000, 0.9, 5.0).

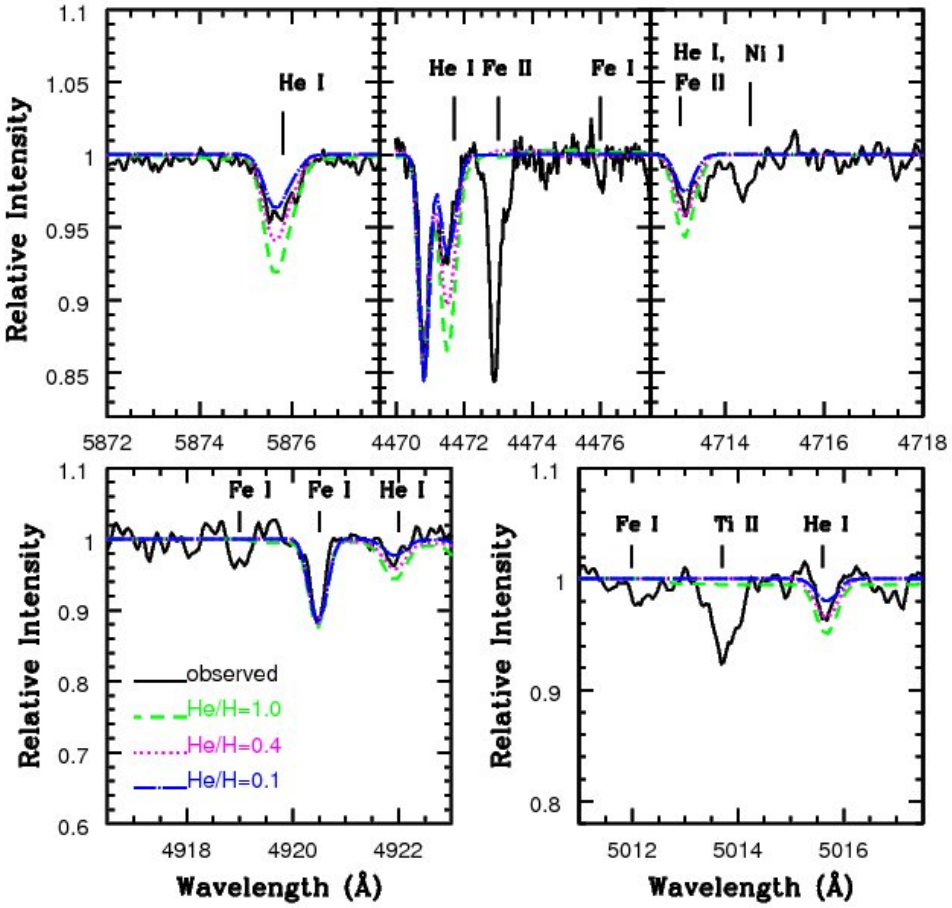

Figure 5.5: The observed and synthesized He I profiles for the triplet lines at 5876, 4471 and 4713 and for the singlet lines at 4922 and 5015 for HD 187885 using models with$T_{\rm eff}$ = 8000K, log g = 0.9 for He/H = 1.0, 0.4 and 0.1 − see keys on the figure.

To verify the model atmosphere parameters, we explore fits to the Paschen lines. The Balmer lines are affected by emission and blends with other lines for their line profiles

to be useful as monitors of the atmospheric parameters but the Paschen lines appear free of emission and blends. The Stark broadening tables for the Paschen lines of hydrogen are taken from Lemke (1997). In the lower panel of the Fig 5.2, we show observed and synthesized Paschen profiles near 8600Å for SAO 40039 for the model with He/H=1.0 and $T_{\rm eff}$ = 8000K and for surface gravities $\log g$ = 0.5, 0.75 and 1.0. The best fitting profile is for $\log g$ of 0.75 for SAO 40039. Similarly the best fitting profile for HD 187885 is for $\log g$ of 0.9 (see bottom panel of Figure 5.3). We also synthesized the Paschen lines in the 8400Å region for the above mentioned temperature and gravities and we get consistent results. These profiles are also sensitive to the adopted effective temperature with a 1000K increase approximately mimicking a 0.5 dex increase in surface gravity. The Paschen lines give the locus shown in the upper panel of Fig 5.2. As the Paschen limit is approached, the Paschen lines overlap and depress the local continuum. In addition, the location of the continuum is rendered more challenging because of the echelle's blaze function. Yet, the synthesized profiles closer to the limit are able to reproduce the observed profiles quite well – see lower panel of Fig 5.2.

Our demonstration that SAO 40039 and HD 187885 are H-deficient and He-rich rests on the assumption that the He I absorption lines originate in the stellar photosphere and are not a product of a stellar chromosphere. (A second assumption is that the real stellar photosphere approximates the model atmospheres computed by classical procedures). A chromospheric origin is not trivially dismissed. One recalls that the D3 line appears in absorption in spectra of F dwarfs with active chromospheres (Wolff & Heasley 1984; Danks & Lambert 1985); the correlation between D3 equivalent width and X-ray luminosity points strongly to a chromospheric origin. A chromospheric origin for He absorption is required to account for the presence of He I 10830 Å in spectra of warm-cool giants and supergiants where it may appear in absorption and/or emission (O'Brien & Lambert 1986) and cannot be of photospheric origin.

The possibility of the photospheric origin of the He I lines in our spectra are supported by several facts. Firstly, the lines have the photospheric velocity. Secondly and more importantly, the equivalent widths of all He I lines – singlets and triplets – are reproduced by a photospheric model. If the lines originated in the chromosphere, one would expect a difference between singlets and triplets, as previously noted by Klochkova et al. (2002) in their discussion of the He I absorption lines found in HD 331319, a star similar to SAO 40039 and HD 187885. While our analysis do not preclude a chromospheric origin, we agree with Klochkova et al. who remark 'the hypothesis of a photospheric origin for the He I lines in HD 331319 is not rejected'. Certainly, there must be a suspicion that SAO

40039 and HD 187885's atmosphere are mildly H-deficient such that the corresponding ratios He/H=1 and He/H=0.4, indicating appreciable loss of H and enrichment of He since the star was a main sequence star with He/H $\simeq$ 0.1.

5.5 DISCUSSION AND RESULTS

Using the adopted model parameters ($T_{\rm eff}$, $\log g$, ξ_t)=(8000, 0.75, 4.8) with He/H of 1.0 for SAO 40039 and using the model parameters ($T_{\rm eff}$, $\log g$, ξ_t)=(8000, 0.9, 5.0) with He/H of 0.4 for HD 187885, the measured equivalent widths of different species were used to derive the abundances. In Table 5.1 we present the abundances derived with the SPECTRUM code using the He/H=1.0 model and the abundances generated with the code MOOG using the He/H=0.1 model for SAO 40039.

A detailed line list has been presented in Table 5.3 and Table 5.4 which lists the lines of SAO 40039 and HD 187885 used in our analysis. The line list provides the lower excitation potential (χ) for each line , the $\log gf$ value, the measured equivalent widths (W_λ) in mÅ and the abundance ($\log \epsilon$) derived from each line for the adopted model atmosphere. The sources of $\log gf$ values used have been listed in great detail in Table 2.1 of our Chapter 2. The solar abundances for all the elements have been taken from Asplund et al. (2009).

SAO 40039 seems to be mildly iron-poor. Klochkova et al.'s analysis assuming He/H= 0.1 gave a solar Fe abundance, a value essentially confirmed by our analysis for the model atmosphere also with He/H = 0.1. A principal effect of the higher He abundance is to reduce the continuous opacity per gram and so demand a lower iron abundance to match the same observed line strength. Inspection of the [X/Fe] entries in Table 5.1 points to several anomalies when the composition of an unevolved disk star is taken as the reference. The two most extreme anomalies are nitrogen which is very overabundant ([N/Fe] = +1.1), and aluminium which is markedly under-abundant ([Al/Fe] = −0.7). Closer study shows that sodium may be overabundant ([Na/Fe] = +0.3) and a suite of elements are mildly under-abundant: Ca, Sc, Ti, Zr and Ba with [El/Fe] $\simeq$ −0.35.

This abundance pattern is largely reminiscent of the pattern exhibited by stars affected by dust-gas separation, i.e., the photosphere is dominated by accretion of gas but not dust from a cool envelope, possibly a circumbinary dusty disk. Dust-gas separation is most remarkably exhibited by post-AGB binaries such as HR 4049 (Van Winckel 2003). In such cases, the abundance anomalies are correlated with the condensation temperature (T_c): elements with high T_c are most under-abundant. In Fig 5.6, we plot [X] (where [X]

Table 5.1: Comparison between abundances estimated with MOOG using He/H=0.1 model and the abundances computed with SPECTRUM using the hydrogen deficient (He/H=1.0) model for SAO 40039

		MOOG[a]			SPECTRUM[b]				SPECTRUM[c]	
Species	$\log\epsilon_\odot$	$\log\epsilon$	[X/Fe]	n	$\log\epsilon$	[X/Fe]	n	$\triangle^d$	[X/Fe]	n
H I	12.00	12.00	...	...	11.45	...	...	...	...	...
He I	10.98	10.98	...	...	11.45	...	...	0.2	...	...
Li I	3.26	4.03	<+0.68±0.00	1	3.50	<+0.67±0.00	1	...	...	
C I	8.43	8.78	+0.26±0.16	21	8.24	+0.24±0.16	21	0.3	+0.27±0.18	9
N I	7.83	9.05	+1.13±0.25	9	8.48	+1.08±0.20	9	0.1	+1.32±0.04	2
O I	8.69	9.47	+0.69±0.15	8	8.93	+0.67±0.14	8	0.1	+0.76±0.14	2
Na I	6.24	6.58	+0.25±0.10	2	6.08	+0.27±0.07	2	0.3	...	...
Mg I	7.60	7.76	+0.07±0.31	4	7.13	−0.04±0.18	4	0.4	−0.26±0.11	2
Mg II	7.60	7.78	+0.09±0.15	4	7.12	−0.05±0.15	4	0.1	−0.10±0.03	3
Al I	6.45	5.95	−0.59±0.01	2	5.32	−0.70±0.03	2	0.4	...	...
Si II	7.51	7.90	+0.30±0.16	3	7.37	+0.29±0.13	3	0.2	+0.31±0.00	1
S I	7.12	7.53	+0.32±0.01	2	7.01	+0.32±0.02	2	0.3	...	...
Ca I	6.34	6.18	−0.25±0.12	2	5.55	−0.36±0.16	2	...	...	...
Ca II	6.34	6.21	−0.22±0.00	1	5.64	−0.27±0.00	1	0.4	−0.36±0.00	1
Sc II	3.15	2.89	−0.35±0.17	5	2.42	−0.30±0.15	5	0.3	−0.05±0.16	2
Ti II	4.95	4.83	−0.21±0.23	20	4.32	−0.20±0.20	20	0.3	−0.24±0.16	12
V II	3.93	4.21	+0.19±0.04	2	3.74	+0.24±0.03	2	0.2	...	...
Cr I	5.64	5.62	−0.11±0.13	3	5.11	−0.10±0.10	3	0.4	−0.06±0.23	2
Cr II	5.64	5.83	+0.10±0.11	9	5.33	+0.12±0.10	9	0.2	+0.09±0.06	4
Mn II	5.43	5.73	+0.21±0.00	1	5.24	+0.24±0.00	1	...	...	
Fe I	7.50	7.54	−0.05±0.18	26	7.02	−0.05±0.17	26	0.4	−0.01±0.19	7
Fe II	7.50	7.65	+0.06±0.19	20	7.13	+0.06±0.17	20	0.2	+0.01±0.14	9
Ni I	6.22	6.16	−0.15±0.15	4	5.63	−0.16±0.14	4	0.3	...	
Zn I	4.56	4.81	+0.16±0.30	2	4.28	+0.15±0.23	2	0.4	...	
Sr II	2.87	3.01	+0.05±0.07	2	2.38	−0.06±0.03	2	...	...	
Zr II	2.58	2.13	−0.54±0.08	2	1.65	−0.50±0.04	2	0.3	...	
Ba II	2.18	1.85	−0.42±0.15	2	1.30	−0.45±0.11	2	...	−0.35±0.00	1
Eu II	0.52	0.40	<−0.10±0.00	1	0.15	<+0.06±0.00	1	...	...	

[a]MOOG abundances computed using the He/H=0.1 model for the McDonald spectra.

[b]SPECTRUM abundances computed using the He/H=1.0 model for the McDonald spectra.

[c]SPECTRUM abundances computed using the He/H=1.0 model for the VBO spectra.

[d]$\triangle$ corresponds to the square root of the sum of the squares of the abundance errors due to uncertainties in the stellar parameters: $\triangle T_{\rm eff}$, $\triangle \log g$ and $\triangle \xi_t$

$=\log\epsilon(\mathrm{X})_* - \log\epsilon(\mathrm{X})_\odot$) versus the T_c computed by Lodders (2003) for a solar composition mixture.

Table 5.2: Comparision between abundances computed with SPECTRUM using the hydrogen-deficient He/H=0.4 model and our MOOG abundances using the He/H=0.1 model for HD 187885

		SPECTRUM[a]			MOOG[b]		
Species	$\log \epsilon_\odot$	$\log \epsilon$	[X/Fe]	n	$\log \epsilon$	[X/Fe]	n
H I	12.00	11.72	...	...	12.00	...	...
He I	10.98	11.35	...	...	10.98	...	...
C I	8.43	8.60	+1.05±0.20	22	8.93	+1.08±0.18	22
N I	7.83	7.89	+0.94±0.24	7	8.12	+0.87±0.26	7
O I	8.69	8.67	+0.86±0.09	6	8.91	+0.80±0.08	6
Mg I	7.60	7.02	+0.30±0.11	4	7.38	+0.36±0.05	4
Mg II	7.60	7.07	+0.35±0.07	3	7.31	+0.29±0.08	3
Al I	6.45	5.07	−0.50±0.05	2	5.43	−0.44±0.06	2
Si II	7.51	6.99	+0.36±0.02	3	7.21	+0.28±0.09	3
S I	7.12	6.82	+0.58±0.22	3	7.17	+0.63±0.21	3
Ca I	6.34	5.76	+0.30±0.03	4	6.13	+0.37±0.03	4
Sc II	3.15	2.76	+0.49±0.15	8	3.02	+0.45± 0.14	9
Ti II	4.95	4.43	+0.36±0.18	37	4.64	+0.27±0.18	37
V II	3.93	3.44	+0.39±0.00	1	3.70	+0.35±0.00	1
Cr I	5.64	4.90	+0.14±0.04	2	5.21	+0.15±0.04	2
Cr II	5.64	4.94	+0.18±0.14	30	5.17	+0.09±0.14	30
Fe I	7.50	6.61	−0.01±0.20	28	6.97	+0.05±0.11	28
Fe II	7.50	6.64	+0.02±0.12	59	6.88	−0.04±0.12	59
Y II	2.21	2.71	+1.38±0.22	17	2.99	+1.36±0.22	17
Zr II	2.58	3.04	+1.34±0.08	10	3.31	+1.31±0.07	10
Ba II	2.18	2.74	+1.44±0.09	2	3.04	+1.44±0.06	2
La II	1.10	1.51	+1.29±0.06	2	1.78	+1.26±0.05	2
Ce II	1.58	1.74	+1.04±0.13	4	2.04	+1.04±0.12	4

[a]SPECTRUM abundances computed using the He/H=0.4 model for HD 187885. The error bars on the derived abundances are same as those derived for SAO 40039.

[b]MOOG abundances computed using the He/H=0.1 model for HD 187885 .

The elements N and O depart from a general tendency for [X] to decrease with increasing T_c. In presenting Fig 5.6, the adopted reference has been that [X/Fe] $\simeq$ 0.0 for all elements in an unevolved star with [Fe/H] $\simeq -0.4$. This is essentially true for a thin disk star, although a dispersion in heavy elements at a given [Fe/H] was noted by Edvardsson et al. (1993). If SAO 40039 is a thick disk star, the α-elements in Fig 5.6 should be plotted with [X] about −0.2 dex less than shown in the figure but the overall trend and the scatter about that trend will be unaffected. The Na, S, and Zn abundances suggest that the initial metallicity of the star was $[Fe/H]_o \simeq -0.2$.

For an effective temperature of about 8000K, Venn (1995b) give non-LTE corrections

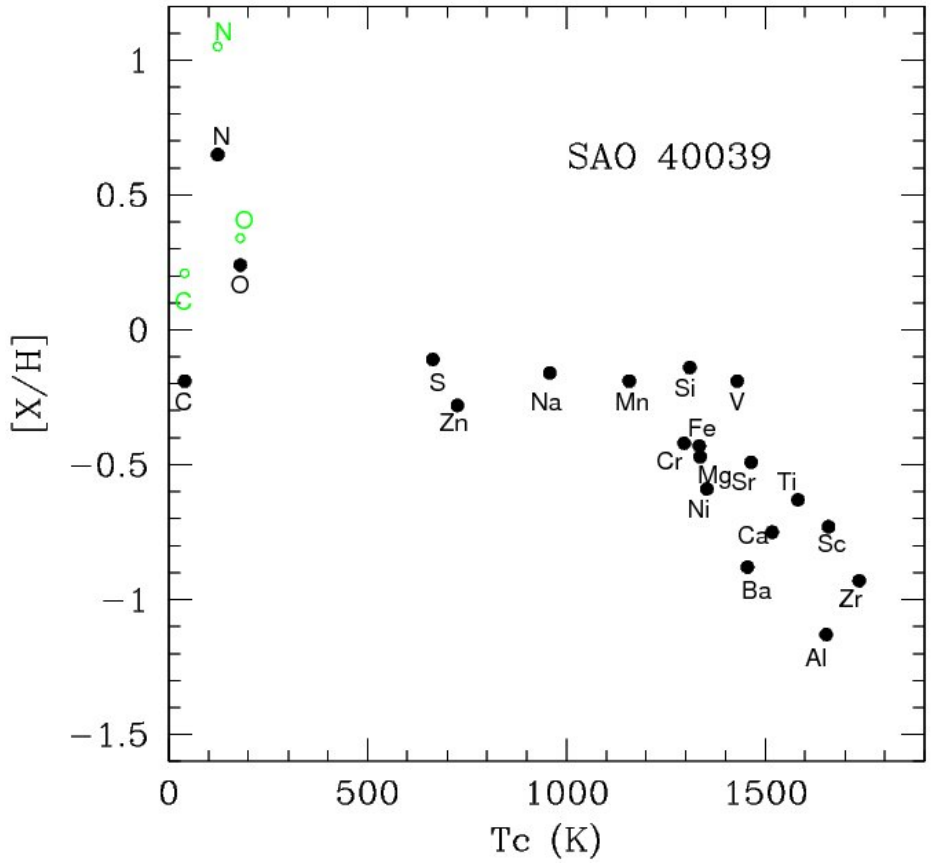

Figure 5.6: The [X] versus T_c plot for SAO 40039.

to C and N abundances from C I and N I lines of about −0.4 dex for normal supergiants. Takeda & Takada-Hidai (1998) have estimated non-LTE corrections for O I to be −0.1 dex at this effective temperature for supergiants. The C, N and O abundances after applying the non-LTE corrections have been marked in Fig 5.6 as open circles in green color for SAO 40039 and are given by $[C/Fe]_{NLTE}$ = -0.16 dex, $[N/Fe]_{NLTE}$ = +0.68 dex and $[O/Fe]_{NLTE}$ = +0.57 dex respectively. The C/O ratio is only 0.2 and it also exhibits mild effects of dust-gas winnowing. Since the star is affected by this process we have to compare the abundances of s-process elements with lighter elements of similar condensation temperatures to unmask the effects of dust-gas separation. But the s-process elements show no enrichment w.r.t the lighter elements of similar condensation temperatures. Thus the underabundance of s-process elements and a C/O ratio of 0.2 shows that the star did not suffer sufficient number of thermal pulses and would have pre-maturely evolved from the AGB phase (Fujii et al. (2002) have estimated that SAO 40039 has a low-mass progenitor. According to Herwig (2005), low-mass stars do not suffer sufficient amount of thermal pulses and dredge-ups and hence remain oxygen-rich.) The N and C abundances

after the non-LTE corrections are in agreement with the predictions of FDU. The O overabundance even after the non-LTE correction might be due to the incomplete operation of the CNO cycle during the late episode of H-burning further supporting the low mass nature of the star. The star is also overabundant in Helium (mildly hydrogen-deficient) and might be due to the partial removal of the hydrogen during a final Helium shell flash (Herwig 2001; Blöcker 2001). The abundances of SAO 40039 point towards efficient operation of only FDU whereas a final thermal pulse possibly has caused an overabundance of Helium. Possibly due to the low mass nature of the star, TDU and the thermal pulses have not been very efficient in producing C and s-process elements.

In our Table 5.2 we present the abundances derived with the SPECTRUM code using the He/H=0.4 model and the abundances generated with the code MOOG using the He/H=0.1 model for HD 187885. Our derived abundances relative to Fe, are in good agreement with the analysis of Van Winckel et al. (2000), except for Na relative to Fe. Note that the metallicity [Fe] derived by Van Winckel & Reyniers (2000) using solar He/H models is about −0.6. In our analysis, the surface material of HD 187885 shows nonsolar He/H ratio of about 0.4 i.e., He/H=30/70, hence, helium rich. For the adopted model with He/H=30/70, the derived metallicity [Fe] is about −0.9. Relative to Fe, the surface of HD 187885 is enriched in N and C than solar. This implies, the material is exposed to H- and He-burnt products. The abundances, relative to Fe, of α- and Fe-peak elements are like thick disk stars. No selective depletion of these elemental abundances is noticed as a function of their condensation temperature. Hence, the α- and the Fe-peak elements also represent the metallicity of the star. The *s*-process abundances (Y, Zr, Ba, La, and Ce), relative to Fe, are enriched when compared with solar.

By adopting the appropriate He/H models, we show that the atmosphere of HD 187885 is He-rich with a C/O ratio of about 1, and a remarkably high *s*-process elemental abundances satisfying the expected yields of a prototype post-AGB star with efficient TDU.

5.6 SUMMARY AND CONCLUSIONS

The origin of H-deficiency in post-AGB stars had been a long-standing problem. Earlier standard post-AGB evolution calculations predicted that appreciable amounts of H should remain present in the stellar envelopes (Schönberner 1979, 1983; Vassiliadis & Wood 1994; Blöcker & Schönberner 1997). But observationally many H-deficient stars have been discovered. H-deficient stars present a challenge to stellar evolution theory as it was unclear earlier how a star removes its H when evolving from AGB to PN stage.

According to current models only 20-25% of stars moving off the AGB are expected to be H-deficient (Blöcker 2001; Blöcker et al. 2001; Herwig 2005). This has also been confirmed observationally i.e. approximately 25% of the whole central star PN population appears to be H-deficient while the rest show Solar-like compositions (Herwig et al. 1999). H-deficiency has been explained in terms of late thermal pulses. If the last thermal pulse occurs well before the departure from AGB, the post-AGB stage will proceed undisturbed and will finally result in a H-rich white dwarf. However if the last thermal pulse occurs immediately before the departure from the AGB or during the early or late post-AGB phase then internal mixing as well as nuclear burning processes will lead to distinctive alterations of the surface abundances. The extent of H-deficiency depends on the amount of envelope mass at the last thermal pulse and the efficiency of dredge-up after this last thermal pulse.

Hydrogen deficient stars represent stars in the late stages of evolution with the hydrogen abundances in the range of $n_H \sim 10^{-5}$ to 10^{-1}. Thus the Balmer lines of hydrogen are weak or absent in these cases. Even though less extreme cases of hydrogen-deficient stars are known to exist like V854 Cen (Asplund et al. 1998), due to the lower effective temperature, the He/H ratio cannot be determined spectroscopically but has to be assumed.

Mild reductions of the hydrogen abundance results in reduction of the continuous opacity and hence strengthening of lines, a change that might be falsely attributed to an enrichment of metals or a change of surface gravity. Detecting mild-hydrogen deficiency and the He/H ratios spectroscopically is extremely difficult especially in the case of stars too cool to show He I lines (Lambert 1996). 'If mildly hydrogen-deficient stars exist, how are they to be detected?' When the Balmer lines of hydrogen together with He I lines are present in the stellar spectra it should be possible to extract the He/H ratio. The spectra of the post-AGB stars SAO 40039 and HD 187885 with surprisingly strong He I lines at an effective temperature of 8000 K seem to be responding to this call. The mild H-deficiency in these stars might have resulted from a partial removal of the H-rich convective envelope during its post-AGB evolution.

Though, the existence of extremely H-deficient stars with He/H ratio of about 10,000, showing He I lines in their absorption spectra, are known (Pandey et al. 2001; Pandey & Reddy 2006), SAO 40039 and HD 187885, from our estimated He/H ratios of about 1 and 0.4, appear to be the first detections of mildly H-deficient stars.

It is very likely that other post-AGB stars may belong to the mildly H-deficient class. Several examples like SAO 40039 and HD 187885 have detectable He I lines. The question then arises; are post-AGB stars of a temperature too low to provide He I lines also

He-rich and how can their H-deficiency be unmasked? Exploration of post-AGB stars showing He I lines need to be continued with models of appropriate H/He ratios. Additionally, non-LTE abundance analyses as described by Pandey & Lambert (2011) should be performed to further refine knowledge of the chemical compositions.

Studies of Mildly hydrogen-deficient stars are extremely important as they seem to provide an evolutionary link between a H-normal and a H-poor star and also they provide a unique opportunity to study directly the nuclear processing shells in AGB stars. Continued exploration of such rare post-AGB objects showing strong He I lines will help in better understanding of these exotic objects.

5.7 DETAILED LINE LISTS

Table 5.3: Detailed line list for SAO 40039

Line	χ (eV)	loggf	W_λ (mÅ)	$\log \epsilon$
He I λ4471.47	20.96	+0.053	Synth	11.40
He I λ4713.13	20.96	−0.975	Synth	11.40
He I λ4921.93	21.21	−0.435	Synth	11.45
He I λ5015.67	20.61	−0.819	Synth	11.50
He I λ5875.61	20.96	+0.739	Synth	11.45
C I λ4371.33	7.68	−1.960	52	8.43
C I λ4734.26	7.95	−2.370	9	8.14
C I λ4766.67	7.48	−2.400	26	8.34
C I λ4770.02	7.48	−2.437	30	8.45
C I λ4771.72	7.49	−1.870	81	8.44
C I λ4775.87	7.49	−2.304	35	8.41
C I λ4826.80	7.49	−2.140	24	8.04
C I λ4932.05	7.68	−1.775	49	8.18
C I λ5039.05	7.48	−2.100	33	8.15
C I λ5052.17	7.68	−1.303	75	7.95
C I λ6010.68	8.64	−1.940	16	8.46
C I λ6013.21	8.65	−1.673	27	8.44
C I λ6587.75	8.54	−1.000	53	8.08
C I λ7111.48	8.64	−1.090	42	8.13
C I λ7113.18	8.65	−0.773	59	8.01
C I λ7115.19	8.64	−0.934	52	8.10
C I λ7116.99	8.65	−0.907	72	8.27
C I λ7119.67	8.64	−1.150	59	8.38
C I λ7483.46	8.77	−1.440	23	8.30
C I λ7685.20	8.77	−1.520	15	8.19
C I λ7860.89	8.85	−1.155	33	8.24
Mean:				8.24±0.16
N I λ4109.94	10.69	−0.988	73	8.28
N I λ6644.96	11.76	−0.908	18	8.30

Table 5.3 – Continued

Line	χ (eV)	loggf	W_λ (mÅ)	$\log \epsilon$
N I λ7423.64	10.33	−0.706	150	8.66
N I λ7442.23	10.33	−0.385	200	8.74
N I λ8184.86	10.33	−0.286	190	8.63
N I λ8188.01	10.33	−0.292	200	8.72
N I λ8223.03	10.33	−0.267	240	8.33
N I λ8567.74	10.68	−0.664	145	8.35
N I λ8655.88	10.69	−0.627	140	8.29
Mean:				8.48±0.20
O I λ5329.69	10.74	−1.110	100	9.01
O I λ5330.74	10.74	−0.970	103	8.91
O I λ5435.78	10.74	−1.646	28	8.76
O I λ5436.86	10.74	−1.502	40	8.80
O I λ5554.94	10.94	−1.890	29	9.17
O I λ6156.78	10.74	−0.440	168	9.02
O I λ6158.18	10.74	−0.290	183	9.00
O I λ6453.60	10.74	−1.350	43	8.80
Mean:				8.93±0.14
Na I λ5682.65	2.10	−0.710	12	6.01
Na I λ5688.19	2.10	−0.400	31	6.14
Mean:				6.08±0.07
Mg I λ4703.00	4.34	−0.440	108	7.07
Mg I λ5167.32	2.70	−0.870	229	7.27
Mg I λ5172.68	2.70	−0.380	287	7.33
Mg I λ5528.42	4.34	−0.340	95	6.86
Mean:				7.13±0.18
Mg II λ4390.59	10.00	−0.523	108	7.11
Mg II λ4428.00	9.95	−1.210	64	7.31
Mg II λ4433.99	10.00	−0.907	56	6.95
Mg II λ7877.06	9.99	+0.390	160	7.11
Mean:				7.12± 0.15
Al I λ3944.02	0.00	−0.638	139	5.34

Table 5.3 – Continued

Line	χ (eV)	loggf	W_λ (mÅ)	$\log \epsilon$
Al I λ3961.53	0.01	−0.340	167	5.29
Mean:				5.32±0.03
Si II λ3853.66	6.83	−1.520	201	7.32
Si II λ4130.88	9.84	+0.552	235	7.23
Si II λ5978.93	10.07	+0.084	151	7.55
Mean:				7.37± 0.13
S I λ6748.79	7.83	−0.530	16	6.99
S I λ6757.19	7.87	−0.310	24	7.02
Mean:				7.01± 0.02
Ca I λ4226.73	0.00	+0.600	200	5.39
Ca I λ6162.18	1.90	−0.090	24	5.70
Mean:				5.55± 0.16
Ca II λ8248.80	7.51	+0.570	220	5.64
Mean:				5.64± 0.00
Sc II λ5239.82	1.45	−0.765	53	2.34
Sc II λ5526.82	1.77	+0.020	103	2.20
Sc II λ5657.90	1.51	−0.603	100	2.60
Sc II λ5667.15	1.51	−1.486	12	2.39
Sc II λ5669.04	1.50	−1.200	35	2.58
Mean:				2.42±0.15
Ti II λ3761.87	2.59	−0.620	166	4.44
Ti II λ3776.05	1.58	−1.348	106	3.91
Ti II λ4316.81	2.05	−1.420	85	4.09
Ti II λ4394.06	1.22	−1.590	153	4.15
Ti II λ4395.85	1.24	−2.170	118	4.49
Ti II λ4418.34	1.24	−2.450	89	4.55
Ti II λ4450.49	1.08	−1.450	222	4.52
Ti II λ4470.86	1.16	−2.280	130	4.61
Ti II λ4529.47	1.57	−1.650	148	4.41
Ti II λ4544.02	1.24	−2.530	55	4.31
Ti II λ4545.13	1.13	−2.460	77	4.36
Ti II λ4568.32	1.22	−2.650	24	3.98

Table 5.3 – Continued

Line	χ (eV)	loggf	W_λ (mÅ)	$\log \epsilon$
Ti II λ4708.66	1.24	−2.370	66	4.24
Ti II λ4779.98	2.05	−1.260	167	4.49
Ti II λ4874.01	3.09	−0.900	107	4.44
Ti II λ4911.19	3.12	−0.650	158	4.59
Ti II λ5129.18	1.89	−1.400	117	4.12
Ti II λ5154.07	1.57	−1.78	150	4.50
Ti II λ5188.68	1.58	−1.050	209	4.23
Ti II λ5211.54	2.59	−1.356	51	4.06
Mean:				4.32± 0.20
V II λ4564.58	2.27	−1.395	45	3.71
V II λ4600.17	2.27	−1.523	40	3.77
Mean:				3.74± 0.03
Cr I λ5204.51	0.94	−0.208	47	5.19
Cr I λ5206.04	0.94	+0.019	69	5.17
Cr I λ5208.40	0.94	+0.159	60	4.96
Mean:				5.11± 0.10
Cr II λ4252.62	3.86	−1.860	112	5.16
Cr II λ4269.28	3.86	−2.020	110	5.30
Cr II λ4539.60	4.04	−2.290	72	5.37
Cr II λ4565.74	4.04	−1.820	139	5.42
Cr II λ4812.35	3.86	−1.800	157	5.40
Cr II λ4836.23	3.86	−1.960	151	5.51
Cr II λ4884.61	3.86	−2.100	107	5.32
Cr II λ5249.44	3.76	−2.489	60	5.25
Cr II λ5308.41	4.07	−1.846	117	5.28
Mean:				5.33± 0.10
Mn II λ4755.73	5.39	−1.242	76	5.24
Mean:				5.24± 0.00
Fe I λ3724.35	2.28	−0.720	65	6.88
Fe I λ3756.94	3.57	−0.253	25	6.80
Fe I λ3760.05	2.40	−0.847	33	6.71
Fe I λ3781.124	2.20	−1.920	11	7.11

Table 5.3 – Continued

Line	χ (eV)	loggf	W_λ (mÅ)	$\log \epsilon$
Fe I λ4202.05	1.48	−0.708	182	7.20
Fe I λ4222.22	2.45	−0.967	66	7.20
Fe I λ4245.26	2.86	−1.170	10	6.77
Fe I λ4260.48	2.40	−0.020	172	7.09
Fe I λ4388.41	3.60	−0.580	27	7.15
Fe I λ4872.14	2.88	−0.590	55	6.97
Fe I λ4878.21	2.88	−0.888	42	7.12
Fe I λ4903.31	2.88	−0.926	30	6.97
Fe I λ4920.50	2.83	+0.068	170	7.20
Fe I λ4946.40	3.37	−1.180	13	7.17
Fe I λ5006.12	2.83	−0.638	55	6.97
Fe I λ5012.07	0.86	−2.642	24	7.11
Fe I λ5065.01	4.26	−0.134	36	7.26
Fe I λ5125.12	4.22	−0.140	29	7.13
Fe I λ5139.46	2.94	−0.509	80	7.14
Fe I λ5171.60	1.48	−1.793	59	7.18
Fe I λ5184.94	1.56	−2.090	14	6.84
Fe I λ5217.40	3.21	−1.100	9	6.87
Fe I λ5415.20	4.39	+0.510	52	6.92
Fe I λ5506.79	0.99	−2.800	14	7.11
Fe I λ5572.84	3.39	−0.275	43	6.88
Fe I λ5615.64	3.33	+0.050	64	6.73
Mean:				7.02± 0.17
Fe II λ4369.40	2.78	−3.660	182	7.43
Fe II λ4472.92	2.84	−3.430	175	7.17
Fe II λ4601.38	2.89	−4.428	56	7.20
Fe II λ4620.51	2.83	−3.290	200	7.22
Fe II λ4635.33	5.96	−1.650	110	7.00
Fe II λ4648.94	2.58	−4.389	72	7.10
Fe II λ4713.19	2.78	−4.932	34	7.36
Fe II λ4720.15	3.19	−4.750	27	7.34
Fe II λ4825.74	2.63	−4.829	35	7.15

Table 5.3 – Continued

Line	χ (eV)	loggf	W_λ (mÅ)		log ϵ
Fe II λ4893.82	2.83	−4.450	69		7.29
Fe II λ4993.36	2.81	−3.640	148		7.08
Fe II λ5000.74	2.78	−4.540	68		7.34
Fe II λ5120.35	2.83	−4.214	72		7.08
Fe II λ5127.87	5.57	−2.535	68		7.26
Fe II λ5132.67	2.81	−3.980	78		6.88
Fe II λ5254.93	3.23	−3.227	156		7.04
Fe II λ5264.81	3.23	−3.190	135		6.83
Fe II λ5408.84	5.96	−2.390	25		6.87
Fe II λ5425.26	3.19	−3.160	181		7.13
Fe II λ6147.74	3.89	−2.721	136		6.84
Mean:					7.13± 0.17
Ni I λ4714.43	3.38	+0.230	31	5.82	
Ni I λ4904.42	3.54	−0.170	8	5.64	
Ni I λ5080.54	3.65	+0.130	10	5.55	
Ni I λ5081.11	3.85	+0.300	9	5.49	
Mean:					5.63± 0.14
Zn I λ4722.16	4.03	−0.390	7		4.05
Zn I λ4810.53	4.08	−0.137	27		4.50
Mean:					4.28± 0.23
Sr II λ4077.72	0.00	+0.150	279		2.41
Sr II λ4215.54	0.00	−0.160	255		2.35
Mean:					2.38 ± 0.03
Zr II λ4149.22	0.80	+0.080	83		1.68
Zr II λ4359.74	1.23	−0.250	23		1.61
Mean:					1.65± 0.04
Ba II λ4554.04	0.00	+0.120	89		1.19
Ba II λ6141.71	0.70	−0.080	45		1.41
Mean:					1.30± 0.11

Table 5.4: Detailed line list for HD 187885

Line	χ (eV)	loggf	W_λ (mÅ)	$\log \epsilon$
He I λ4471.47	20.96	+0.053	Synth	11.35
He I λ4713.13	20.96	−0.975	Synth	11.35
He I λ4921.93	21.21	−0.435	Synth	11.35
He I λ5015.67	20.61	−0.819	Synth	11.35
He I λ5875.61	20.96	+0.739	Synth	11.35
C I λ4770.00	7.48	−2.437	42	8.81
C I λ4775.88	7.49	−2.304	54	8.82
C I λ4817.38	7.48	−3.039	13	8.83
C I λ5023.83	7.94	−2.210	32	8.75
C I λ5039.06	7.94	−1.790	41	8.14
C I λ5040.12	7.94	−2.302	23	8.69
C I λ5052.15	7.68	−1.303	97	8.31
C I λ5380.32	7.68	−1.616	59	8.32
C I λ6010.65	8.64	−1.938	15	8.62
C I λ6014.84	8.64	−1.584	27	8.56
C I λ6587.62	8.53	−1.003	78	8.50
C I λ6663.01	8.85	−2.127	15	8.98
C I λ6671.82	8.85	−1.651	15	8.51
C I λ6828.19	8.53	−1.461	28	8.41
C I λ7087.82	8.64	−1.442	41	8.67
C I λ7108.92	8.64	−1.594	32	8.69
C I λ7111.45	8.64	−1.085	52	8.44
C I λ7113.17	8.64	−0.773	93	8.50
C I λ7115.17	8.64	−0.900	95	8.65
C I λ7116.96	8.64	−0.907	99	8.68
C I λ7476.15	8.77	−1.574	25	8.66
C I λ7483.41	8.77	−1.372	37	8.66
Mean:				8.60±0.20
N I λ7423.64	10.33	−0.706	60	8.11
N I λ7442.23	10.33	−0.401	85	8.06
N I λ7468.27	10.33	−0.183	120	8.16

Table 5.4 – Continued

Line	χ (eV)	loggf	W_λ (mÅ)	$\log \epsilon$
N I λ8216.30	10.33	+0.138	162	7.64
N I λ8223.10	10.33	−0.275	86	7.53
N I λ8629.16	10.69	+0.077	162	7.97
N I λ8718.76	10.33	−0.349	108	7.79
Mean:				7.89±0.24
O I λ5329.69	10.74	−1.110	42	8.67
O I λ5330.74	10.74	−0.970	60	8.75
O I λ5435.78	10.74	−1.544	17	8.67
O I λ5436.86	10.74	−1.399	16	8.50
O I λ6156.80	10.74	−0.440	101	8.70
O I λ6158.17	10.74	−0.290	119	8.72
Mean:				8.67±0.09
Mg I λ4057.51	4.34	−0.900	31	7.02
Mg I λ4167.28	4.34	−0.745	40	7.00
Mg I λ4703.00	4.34	−0.440	90	7.16
Mg I λ5528.42	4.34	−0.498	71	6.89
Mean:				7.02±0.11
Mg II λ4390.59	10.00	−0.530	83	7.12
Mg II λ4428.00	10.00	−1.200	29	7.09
Mg II λ4433.99	10.00	−0.900	39	6.99
Mean:				7.07± 0.07
Al I λ3944.02	0.00	−0.638	85	5.10
Al I λ3961.53	0.01	−0.340	113	5.03
Mean:				5.07±0.05
Si II λ4128.05	9.79	+0.310	140	5.10
Si II λ5056.02	10.03	+0.440	118	5.10
Si II λ5978.93	10.07	+0.084	67	5.10
Mean:				5.07±0.05
S I λ4694.12	6.52	−1.400	5	5.10
S I λ6748.78	7.87	−0.530	10	5.10
S I λ6757.19	7.87	−0.240	16	5.10

Table 5.4 – Continued

Line	χ (eV)	loggf	W_λ (mÅ)	log ϵ
Mean:				5.07±0.05
Ca I λ4434.96	1.89	−0.010	17	5.72
Ca I λ5588.76	2.52	+0.210	12	5.77
Ca I λ6162.18	1.90	−0.090	20	5.80
Ca I λ6439.08	2.52	+0.470	22	5.75
Mean:				5.76± 0.03
Sc II λ4400.40	0.61	−0.780	153	2.78
Sc II λ4415.56	0.60	−0.890	122	2.65
Sc II λ4670.41	1.36	−0.576	128	2.91
Sc II λ5239.82	1.45	−0.765	55	2.57
Sc II λ5526.82	1.77	+0.020	134	2.62
Sc II λ5657.88	1.51	−0.603	84	2.69
Sc II λ5667.15	1.50	−1.485	26	2.95
Sc II λ5669.04	1.50	−1.200	45	2.92
Mean:				2.76±0.15
Ti II λ3932.02	1.13	−1.780	98	4.11
Ti II λ4028.35	1.89	−1.000	167	4.43
Ti II λ4163.64	2.58	−0.400	224	4.88
Ti II λ4171.90	2.59	−0.560	174	4.54
Ti II λ4287.88	1.08	−2.020	137	4.56
Ti II λ4290.22	1.16	−1.120	228	4.55
Ti II λ4301.93	1.16	−1.160	209	4.39
Ti II λ4307.90	1.16	−1.100	239	4.64
Ti II λ4312.86	1.18	−1.160	225	4.57
Ti II λ4314.98	1.16	−1.140	197	4.25
Ti II λ4330.24	2.05	−1.520	58	4.16
Ti II λ4344.29	1.08	−2.090	110	4.43
Ti II λ4350.84	2.06	−1.400	70	4.15
Ti II λ4386.85	2.60	−1.260	103	4.66
Ti II λ4395.85	1.24	−2.170	111	4.63
Ti II λ4399.77	1.23	−1.270	166	4.14
Ti II λ4417.72	1.16	−1.430	176	4.33

Table 5.4 – Continued

Line	χ (eV)	loggf	W_λ (mÅ)	$\log \epsilon$
Ti II λ4421.95	2.05	−1.770	73	4.53
Ti II λ4441.73	1.18	−2.410	63	4.44
Ti II λ4444.56	1.12	−2.030	80	4.16
Ti II λ4450.49	1.08	−1.450	180	4.32
Ti II λ4488.33	3.12	−0.820	107	4.62
Ti II λ4493.53	1.08	−2.740	36	4.39
Ti II λ4529.46	1.56	−2.030	99	4.63
Ti II λ4544.01	1.24	−2.400	50	4.34
Ti II λ4568.33	1.22	−2.650	26	4.22
Ti II λ4708.67	1.24	−2.210	67	4.45
Ti II λ4779.99	2.04	−1.370	129	4.51
Ti II λ4798.54	1.08	−2.670	55	4.52
Ti II λ4805.10	2.05	−1.100	158	4.46
Ti II λ4874.02	3.08	−0.790	102	4.49
Ti II λ5129.16	1.89	−1.400	116	4.31
Ti II λ5185.91	1.89	−1.350	109	4.22
Ti II λ5188.70	1.57	−1.210	159	4.20
Ti II λ5226.55	1.57	−1.290	178	4.43
Ti II λ5336.79	1.58	−1.700	118	4.40
Mean:				4.43± 0.18
Cr I λ5208.40	0.94	+0.170	42	4.93
Cr I λ5409.80	1.03	−0.670	6	4.87
Mean:				4.90± 0.04
Cr II λ4252.62	3.84	−2.020	64	5.11
Cr II λ4261.92	3.85	−1.530	105	4.97
Cr II λ4275.57	3.84	−1.710	108	5.16
Cr II λ4554.99	4.07	−1.370	105	4.94
Cr II λ4558.66	4.06	−0.660	159	4.65
Cr II λ4565.78	4.02	−2.110	44	5.10
Cr II λ4588.20	4.07	−0.640	203	5.03
Cr II λ4592.06	4.07	−1.220	107	4.80
Cr II λ4616.63	4.07	−1.290	88	4.72

Table 5.4 – Continued

Line	χ (eV)	loggf	W_λ (mÅ)	$\log \epsilon$
Cr II λ4618.83	4.06	−1.110	163	5.13
Cr II λ4634.11	4.05	−1.240	116	4.88
Cr II λ4812.35	3.86	−1.800	50	4.73
Cr II λ4824.13	3.85	−1.220	165	5.09
Cr II λ4848.25	3.86	−1.130	150	4.88
Cr II λ4876.41	3.84	−1.460	146	5.16
Cr II λ4884.60	3.86	−2.080	44	4.94
Cr II λ5237.32	4.07	−1.160	133	4.93
Cr II λ5246.78	3.71	−2.460	30	5.02
Cr II λ5249.43	3.76	−2.620	20	5.03
Cr II λ5274.99	4.05	−1.290	91	4.72
Cr II λ5305.87	3.83	−1.994	47	4.88
Cr II λ5308.43	4.07	−1.810	44	4.82
Cr II λ5310.70	4.07	−2.270	19	4.88
Cr II λ5313.59	4.06	−1.650	72	4.94
Cr II λ5334.88	4.05	−1.560	64	4.77
Cr II λ5369.36	3.87	−2.860	11	5.05
Cr II λ5420.93	3.76	−2.360	31	4.97
Cr II λ5478.35	4.16	−1.910	46	5.01
Cr II λ5502.09	4.17	−1.990	34	4.94
Cr II λ5508.63	4.15	−2.120	30	4.99
Mean:				4.94± 0.14
Fe I λ3949.96	2.18	−1.251	13	6.65
Fe I λ3956.69	2.69	−0.429	31	6.60
Fe I λ4157.79	3.42	−0.403	13	6.68
Fe I λ4181.76	2.83	−0.371	27	6.58
Fe I λ4199.10	3.05	+0.156	71	6.72
Fe I λ4202.04	1.48	−0.708	103	6.71
Fe I λ4227.44	3.33	+0.266	70	6.80
Fe I λ4260.49	2.40	+0.077	77	6.38
Fe I λ4531.16	1.48	−2.155	7	6.71
Fe I λ4872.14	2.88	−0.567	23	6.67

Table 5.4 – Continued

Line	χ (eV)	loggf	W_λ (mÅ)	$\log \epsilon$
Fe I λ4891.50	2.85	−0.112	55	6.34
Fe I λ4919.00	2.86	−0.342	33	6.61
Fe I λ5139.47	2.94	−0.509	29	6.76
Fe I λ5171.61	1.48	−1.793	17	6.74
Fe I λ5192.35	3.00	−0.421	22	6.58
Fe I λ5232.95	2.94	−0.057	38	6.45
Fe I λ5364.88	4.44	+0.228	12	6.71
Fe I λ5367.48	4.41	+0.443	18	6.65
Fe I λ5369.97	4.37	+0.536	20	6.58
Fe I λ5383.38	4.31	+0.645	24	6.51
Fe I λ5410.92	4.47	+0.398	21	6.82
Fe I λ5415.21	4.39	+0.642	20	6.49
Fe I λ5455.62	1.01	−2.091	23	6.82
Fe I λ5569.63	3.42	−0.486	12	6.66
Fe I λ5572.85	3.40	−0.275	17	6.60
Mean:				6.61± 0.20
Fe II λ4122.66	2.58	−3.260	131	6.68
Fe II λ4128.74	2.58	−3.630	82	6.66
Fe II λ4173.45	2.57	−2.180	247	6.72
Fe II λ4178.86	2.58	−2.510	207	6.62
Fe II λ4303.17	2.69	−2.490	220	6.79
Fe II λ4369.41	2.78	−3.650	56	6.58
Fe II λ4385.39	2.78	−2.660	187	6.68
Fe II λ4416.83	2.78	−2.650	175	6.55
Fe II λ4472.93	2.84	−3.360	85	6.58
Fe II λ4489.18	2.83	−2.960	152	6.70
Fe II λ4491.41	2.85	−2.710	158	6.51
Fe II λ4508.29	2.85	−2.440	211	6.70
Fe II λ4515.34	2.83	−2.480	186	6.50
Fe II λ4520.23	2.79	−2.600	153	6.31
Fe II λ4541.52	2.84	−3.050	144	6.72
Fe II λ4555.89	2.83	−2.400	213	6.68

Table 5.4 – Continued

Line	χ (eV)	loggf	W_λ (mÅ)	$\log \epsilon$
Fe II λ4576.34	2.84	−2.950	148	6.65
Fe II λ4580.06	2.57	−3.720	59	6.50
Fe II λ4582.83	2.84	−3.180	118	6.65
Fe II λ4620.52	2.83	−3.210	101	6.54
Fe II λ4629.34	2.79	−2.370	237	6.85
Fe II λ4635.31	5.95	−1.420	54	6.48
Fe II λ4666.75	2.83	−3.280	105	6.64
Fe II λ4731.44	2.88	−3.360	134	6.97
Fe II λ4871.27	2.69	−4.060	51	6.84
Fe II λ4893.82	2.83	−4.210	19	6.57
Fe II λ5136.80	2.84	−4.430	20	6.85
Fe II λ5146.12	2.83	−3.910	38	6.62
Fe II λ5197.58	3.23	−2.220	197	6.56
Fe II λ5234.63	3.22	−2.180	209	6.64
Fe II λ5275.99	3.19	−1.940	211	6.40
Fe II λ5284.11	2.89	−3.110	121	6.62
Fe II λ5325.56	3.22	−3.160	88	6.66
Fe II λ5362.86	3.19	−2.740	159	6.75
Fe II λ5414.07	3.22	−3.580	48	6.72
Fe II λ5425.26	3.20	−3.220	80	6.64
Fe II λ5534.85	3.24	−2.750	138	6.64
Fe II λ5813.67	5.57	−2.510	14	6.68
Fe II λ5991.38	3.15	−3.540	42	6.55
Fe II λ6084.10	3.20	−3.790	34	6.72
Fe II λ6113.33	3.22	−4.140	21	6.84
Fe II λ6147.73	3.87	−2.720	86	6.68
Fe II λ6149.25	3.89	−2.690	82	6.63
Fe II λ6179.40	5.57	−2.620	7	6.51
Fe II λ6239.95	3.89	−3.410	33	6.84
Fe II λ6247.56	3.89	−2.300	137	6.67
Fe II λ6369.46	2.89	−4.110	24	6.64
Fe II λ6383.72	5.55	−2.240	22	6.62

Table 5.4 – Continued

Line	χ (eV)	loggf	W_λ (mÅ)	$\log \epsilon$
Fe II λ6385.46	5.55	−2.590	13	6.71
Fe II λ6416.93	3.89	−2.640	75	6.54
Fe II λ6432.68	2.89	−3.570	57	6.57
Fe II λ6442.95	5.55	−2.440	11	6.52
Fe II λ6446.40	6.22	−1.970	14	6.62
Fe II λ6456.39	3.90	−2.050	153	6.56
Fe II λ6516.08	2.89	−3.310	94	6.63
Fe II λ7222.40	3.89	−3.260	21	6.50
Fe II λ7224.46	3.89	−3.200	47	6.84
Fe II λ7515.84	3.90	−3.390	24	6.70
Fe II λ7711.73	3.90	−2.500	78	6.48
Mean:				6.64± 0.12
Y II λ4124.91	0.41	−1.500	52	2.64
Y II λ4358.72	0.10	−1.324	92	2.55
Y II λ4398.02	0.13	−1.000	135	2.56
Y II λ4823.31	0.99	−1.125	81	2.89
Y II λ4883.65	1.08	−0.041	219	2.97
Y II λ4900.12	1.03	−0.090	191	2.72
Y II λ4982.14	1.03	−1.290	36	2.61
Y II λ5087.43	1.08	−0.170	140	2.41
Y II λ5119.12	0.99	−1.360	43	2.73
Y II λ5123.22	0.99	−0.824	110	2.78
Y II λ5200.41	0.99	−0.569	101	2.46
Y II λ5205.73	1.03	−0.340	140	2.54
Y II λ5289.82	1.03	−1.850	10	2.58
Y II λ5402.78	1.84	−0.630	76	2.96
Y II λ5509.91	0.99	−1.010	55	2.51
Y II λ5546.01	1.75	−1.097	49	3.11
Y II λ6613.73	1.74	−1.097	52	3.10
Mean:				2.71± 0.22
Zr II λ4018.39	0.96	−1.270	43	2.97
Zr II λ4034.09	0.80	−1.510	34	2.97

Table 5.4 – Continued

Line	χ (eV)	loggf	W_λ (mÅ)	$\log \epsilon$
Zr II λ4050.33	0.71	−1.060	91	3.02
Zr II λ4149.20	0.80	−0.040	204	3.02
Zr II λ4161.21	0.71	−0.590	148	2.97
Zr II λ4414.55	1.24	−1.080	65	3.18
Zr II λ4443.00	1.49	−0.420	118	3.11
Zr II λ4496.97	0.71	−0.890	116	2.99
Zr II λ4613.92	0.97	−1.540	39	3.14
Zr II λ5112.28	1.66	−0.590	72	3.00
Mean:				3.04± 0.08
Ba II λ5853.69	0.60	−1.016	63	2.67
Ba II λ6141.71	0.70	−0.069	191	2.80
Mean:				2.74± 0.09
La II λ4086.71	0.00	−0.070	37	1.46
La II λ4333.76	0.17	−0.060	37	1.55
Mean:				1.51± 0.06
Ce II λ4382.17	0.68	+0.130	6	1.62
Ce II λ4486.91	0.30	−0.180	10	1.84
Ce II λ4562.37	0.48	+0.210	12	1.64
Ce II λ5187.46	1.21	+0.170	6	1.86
Mean:				1.74± 0.13

CHAPTER 6

CONCLUSIONS

In our study of RV Tauri stars and other post-AGB candidates, we have conducted detailed abundance analysis using high resolution spectra of a sample of 12 RV Tauri stars and 10 post-AGB candidates.

• From the abundance analysis of RV Tauri stars we find indications of mild s-processing in V820 Cen and IRAS 06165+3158. This s-process enrichment is a rare-phenomenon in the galactic RV Tauri stars. Till now only one galactic RV Tauri star, V453 Oph has been known to show s-process enrichment. With the two out of three reported s-process enhanced objects belonging to RV Tau spectroscopic class C; these intrinsically metal-poor objects appear to be promising candidates to analyse the possible s-processing in RV Tau stars.

• A mild suggestion of dust-gas winnowing is seen in the RV Tauri stars SU Gem and BT Lac. A more extensive analysis of the heavily depleted RV Tau object HD 52961 has also been conducted which has resulted in a better definition of its depletion curve.

• From our analysis of post-AGB candidates for the first time we report moderate s-process enrichment ([s/Fe]~0.30) in three stars: IRAS 01259+6823, IRAS 05208-2035 and IRAS 08187-1905. All these objects are metal-poor and the moderate s-process enrichment may be caused by fewer thermal pulses experienced by relatively low mass stars but dredged up to the surface via efficient mixing of nucleosynthesis products in the metal-poor environment. We have also conducted a more extensive analysis of the two PAGB stars: IRAS 22223+4327 and IRAS 17279-1119 showing strong s-process enhancements.

• In our sample of PAGB candidates we also came across two exotic objects: SAO 40039 and HD 187885, two warm post-AGB stars showing strong He I lines. We determined spectroscopically the He/H ratio of 1.0 for SAO 40039 and He/H ratio of 0.4 for HD 187885 which is greater than the solar He/H value of 0.1. These are the first such de-

tections of stars showing mild hydrogen-deficiency. The mild hydrogen deficiency would have resulted from the partial removal of the hydrogen-rich convective envelope during a late thermal pulse. Detections of Mildly hydrogen-deficient stars are extremely important as they seem to provide an evolutionary link between a H-normal and a H-poor star. Continued exploration of such rare post-AGB objects showing strong He I lines will help in better understanding of these exotic objects.

• We have compiled the stellar parameters and abundances for RV Tau stars and post-AGB candidates with s-process enhancement, those showing the effects of dust-gas winnowing and those showing neither of these effects. The compilation shows that the s-process enhanced group contains very small number of binaries and probably represent AGB evolution of single stars. The depleted group contains large fraction of binaries and supports the hypothesis of dusty discs surrounding binary post-AGB stars via the shape of their SED and mid IR interferometry. The conditions for discernible depletion, minimum temperature of 5000K and initial metallicity larger than -1.0 dex found from the earlier work still serve as useful criterion. We also find that the orbital period range of 300-1300 days corresponding to asini of 0.3-1.6 AU appear to be the additional favourable conditions for strong dust-gas winnowing to operate in these stars.

• We have also attempted to explain the observed families of depletion plots in the framework of different star− circumstellar material geometries, the temperature and the composition of dust-gas reservoir, as well as the degree of mixing between the accreted clean gas with the atmosphere/envelope of the star.

6.1 Future perspectives:

• Optical-Infrared High-Resolution campaigns of selected RV Tauri stars over their pulsational and orbital periods may allow us to validate the recipes proposed here to explain various abundance patterns observed in these fascinating objects. Such a study may also unravel the possible role of pulsations/stellar wind in sustaining depletion. One cannot exaggerate the importance of photometric and radial velocity monitoring towards the increased detection of binary companions.

• Till now only 67 RV Tauri stars have been studied. But the GCVS lists 133 stars with the RV classification in our Galaxy and a large number of faint galactic RV Tauri stars remain unexplored. The exploration of RV Tau stars in external galaxies could be very rewarding as exemplified by the detection of few depleted RV Tauri stars in the LMC and also the heavily s-process enriched RV Tauri star in the LMC (MACHO 47.2496.8).

Appendix A

APPENDIX

A.1 LINES USED FOR DETERMINING THE STELLAR ABUNDANCES

The Appendix contains the list of all the lines measured in our program stars. For every line we list the atomic species, the rest wavelength (λ) in (Å), the lower excitation potential (χ) in eV, the oscillator strength (log *gf*) and the measured equivalent widths (W_λ) in mÅ.

Table A.1: Line identification for the stars: 1 = IRAS 01427+4633, 2 = TX Per, 3 = IRAS 06108+2743, 4 = IRAS 06165+3158, 5 = HD 52961, 6 = V820 Cen, 7 = V453 Oph

Line	χ	log(gf)	1	2	3	4	5	6	7
C I λ4228.31	7.68	−2.360					29		
C I λ4269.03	7.68	−2.359					62		
C I λ4770.00	7.48	−2.291	25				53		
C I λ4775.88	7.49	−2.304					90		
C I λ4932.07	7.68	−1.658					135		
C I λ5039.06	7.94	−1.791	44				74		
C I λ5052.15	7.68	−1.303					185		
C I λ5380.32	7.68	−1.570	67		82	20	110		
C I λ5545.05	8.64	−2.376					22		
C I λ6010.65	8.64	−1.938			12		11		
C I λ6013.20	8.64	−1.673					62		
C I λ6014.84	8.64	−1.584			22				
C I λ6587.62	8.53	−1.003	62		56		104		
C I λ6828.19	8.53	−1.461	34				37		
C I λ7087.82	8.64	−1.442					65		
C I λ7108.92	8.64	−1.594			21				
C I λ7111.45	8.64	−1.085					58		
C I λ7113.17	8.64	−0.773			58		83		
C I λ7115.17	8.64	−0.900			60		97		
C I λ7116.96	8.64	−0.907			62		112		
C I λ7119.70	8.64	−1.148					74		
N I λ7442.23	10.33	−0.385	34						
N I λ8188.02	10.33	−0.240	42						
N I λ8629.24	10.69	+0.090	70						
N I λ8683.65	10.33	+0.140					89		
O I λ6155.99	10.74	−0.660	22						
O I λ6156.78	10.74	−0.440	21						
O I λ6300.31	0.00	−9.752		97	110	61	36	40	
O I λ6363.79	0.02	−10.250		56	42		13		3
Na I λ4497.68	2.10	−1.520				66			

Table A.1 – Continued

Line	χ	log(gf)	1	2	3	4	5	6	7
Na I λ5682.65	2.10	−0.710		128	124		15		
Na I λ5688.22	2.10	−0.400					30		
Na I λ6154.23	2.10	−1.547		70	41	71			
Na I λ6160.75	2.10	−1.246		84	67	110			
Na I λ8194.84	2.10	+0.530						91	55
Mg I λ4057.51	4.34	−0.900							37
Mg I λ4571.10	0.00	−5.623	33						
Mg I λ4703.00	4.34	−0.377	168					86	68
Mg I λ4730.03	4.34	−2.347	17	112	68				
Mg I λ5167.33	2.71	−0.870					15		
Mg I λ5183.62	2.72	−0.158					59		
Mg I λ5528.42	4.34	−0.498						109	66
Mg I λ5711.10	4.34	−1.724	44	168	131	135			8
Mg I λ7657.61	5.11	−1.268				98			
Mg II λ4481.16	8.86	+0.973					5		
Al I λ3944.02	0.00	−0.620							140
Al I λ3961.53	0.00	−0.320							167
Al I λ5557.07	3.14	−2.104		13					
Al I λ6696.03	3.14	−1.342			24				
Al I λ6698.67	3.14	−1.643			13				
Al I λ7835.32	4.02	−0.470	8						
Al I λ8772.88	4.02	−0.170				37			
Al I λ8773.91	4.02	−0.030				59			
Si I λ5622.23	4.93	−1.640				46			
Si I λ5645.62	4.93	−1.630				53		11	
Si I λ5665.56	4.92	−1.730				52			
Si I λ5684.49	4.95	−1.420				68		27	
Si I λ5690.43	4.93	−1.760				51			
Si I λ5747.67	5.61	−0.780							9
Si I λ5753.65	5.61	−1.299			57				
Si I λ5772.15	5.08	−1.740		77	60				
Si I λ5793.08	4.93	−1.490				51			

Table A.1 – Continued

Line	χ	log(gf)	1	2	3	4	5	6	7
Si I λ5797.86	4.95	−2.050						7	
Si I λ5848.55	5.08	−1.230	44						
Si I λ6125.03	5.61	−1.513		52	29				
Si I λ6142.49	5.62	−1.540		51					
Si I λ6145.02	5.61	−1.479	15	53	39				
Si I λ6237.33	5.61	−1.138		76					
Si I λ6244.48	5.61	−0.690							9
Si I λ6414.99	5.87	−1.155			34				
Si I λ6527.22	5.87	−1.042			50				
Si I λ6721.84	5.86	−0.940	20						
Si I λ6741.63	5.98	−1.760			15				
Si I λ7034.91	5.87	−0.880		81	67				
Si I λ7275.29	5.61	−0.722				55			
Si I λ7680.27	5.86	−0.690				46		14	
Si I λ7849.98	6.19	−0.652			57				
Si II λ6347.10	8.12	+0.149					4		20
Si II λ6731.35	8.12	−0.082	147						12
S I λ4694.12	6.52	−1.810					12		
S I λ4695.45	6.52	−1.960					7		
S I λ4696.26	6.52	−2.190					4		
S I λ6046.02	7.87	−0.780	16						
S I λ6052.68	7.87	−0.630	25		43				
S I λ8694.64	7.87	+0.050					71		
Ca I λ4094.94	2.52	−0.400		142					
Ca I λ4302.54	1.90	+0.276	148						86
Ca I λ4425.44	1.88	−0.358							29
Ca I λ4434.97	1.89	−0.010	129						62
Ca I λ4456.63	1.90	−1.660	13						
Ca I λ4526.93	2.71	−0.420				120			
Ca I λ4578.56	2.52	−0.558			102	133			
Ca I λ4685.27	2.93	−0.880				65			
Ca I λ5260.39	2.52	−1.900		28					

Table A.1 – Continued

Line	χ	log(gf)	1	2	3	4	5	6	7
Ca I λ5261.71	2.52	−0.730		136		137		20	
Ca I λ5265.56	2.52	−0.260	66					33	
Ca I λ5349.47	2.71	−0.310						18	
Ca I λ5512.99	2.93	−0.300		134		109			
Ca I λ5581.98	2.52	−0.710			80	121			
Ca I λ5588.76	2.52	+0.210							33
Ca I λ5590.13	2.52	−0.710			89	117			
Ca I λ5598.49	2.52	−0.220						47	
Ca I λ5601.29	2.52	−0.690		152				19	
Ca I λ6102.73	1.88	−0.790						69	
Ca I λ6122.23	1.89	−0.315						93	
Ca I λ6161.30	2.52	−1.030			70				
Ca I λ6162.18	1.90	−0.089			199				
Ca I λ6166.44	2.52	−0.900				131			
Ca I λ6169.04	2.52	−0.540			107	141			
Ca I λ6169.56	2.52	−0.270			127	155			
Ca I λ6439.08	2.52	+0.470						100	
Ca I λ6471.67	2.52	−0.590	38	165	107	130			
Ca I λ6717.69	2.71	−0.610		140				26	
Ca I λ7202.21	2.71	−0.262		166					
Ca II λ8662.14	1.69	−0.770					408		
Sc II λ4354.61	0.61	−1.834			133				
Sc II λ4400.40	0.61	−0.480							96
Sc II λ5239.82	1.45	−0.942						29	
Sc II λ5318.36	1.36	−2.191	27		59				
Sc II λ5357.19	1.51	−2.287	18						
Sc II λ5526.82	1.77	−0.219						68	
Sc II λ5641.00	1.50	−0.990				93			14
Sc II λ5657.88	1.51	−0.825							36
Sc II λ5667.15	1.50	−1.485	74		105				
Sc I λ5669.04	1.50	−1.200			125				
Sc II λ5684.20	1.51	−1.250	115			77		27	

Table A.1 – Continued

Line	χ	log(gf)	1	2	3	4	5	6	7
Sc II λ6245.62	1.51	−0.935				109			10
Sc II λ6604.60	1.36	−1.310				79			
Ti I λ4287.41	0.84	−0.441		187	78				
Ti I λ4417.29	1.89	−0.020				107			
Ti I λ4453.71	1.87	−0.010				123			
Ti I λ4465.81	1.74	−0.163				124		9	
Ti I λ4512.74	0.84	−0.480				171			
Ti I λ4518.03	0.83	−0.324				198			
Ti I λ4548.77	0.83	−0.354				181			
Ti I λ4555.49	0.85	−0.488				182			
Ti I λ4623.10	1.74	+0.110				134			
Ti I λ4639.95	1.73	−0.192		122					
Ti I λ4645.19	1.73	−0.557		99					
Ti I λ4722.61	1.05	−1.330		116					
Ti I λ4758.12	2.25	+0.425			42				
Ti I λ4759.28	2.25	+0.514				118			
Ti I λ4778.26	2.24	−0.210		70		65			
Ti I λ4820.41	1.50	−0.439		134		134			
Ti I λ4913.62	1.87	+0.161				123			
Ti I λ4991.07	0.84	+0.380	89						
Ti I λ5007.27	0.82	+0.112	77						
Ti I λ5016.17	0.85	−0.547			76				
Ti I λ5022.87	0.83	−0.434							
Ti I λ5038.40	1.43	+0.013				163			
Ti I λ5043.59	0.84	−1.733		122					
Ti I λ5071.49	1.46	−1.063		105					
Ti I λ5224.31	2.13	+0.130						7	
Ti I λ5282.40	1.05	−1.300				130			
Ti I λ5338.33	0.83	−1.870				84			
Ti I λ5648.58	2.49	−0.250		50					
Ti I λ6258.11	1.44	−0.355							
Ti I λ6261.11	1.43	−0.479			41				

Table A.1 – Continued

Line	χ	log(gf)	1	2	3	4	5	6	7
Ti II λ4028.35	1.89	−1.000	187						
Ti II λ4184.31	1.08	−2.510			148				
Ti II λ4290.22	1.16	−1.118							134
Ti II λ4301.93	1.16	−1.160							139
Ti II λ4316.80	2.05	−1.420							31
Ti II λ4330.24	2.05	−1.729							
Ti II λ4386.85	2.60	−0.956						27	
Ti II λ4394.07	1.22	−1.890						80	78
Ti II λ4421.94	2.06	−1.630							16
Ti II λ4450.49	1.08	−1.450			213				103
Ti II λ4488.33	3.12	−0.820	134						
Ti II λ4493.53	1.08	−2.740							20
Ti II λ4549.64	1.58	−0.450					7		
Ti II λ4568.33	1.22	−2.650			115	69			15
Ti II λ4583.41	1.16	−2.720				70			
Ti II λ4589.96	1.24	−1.780		170					
Ti II λ4636.32	1.16	−3.230						11	
Ti II λ4657.20	1.24	−2.150				131			
Ti II λ4708.67	1.24	−2.210			170	119		46	37
Ti II λ4762.78	1.08	−2.710							16
Ti II λ4798.54	1.08	−2.679						38	
Ti II λ4865.62	1.12	−2.590				102		47	
Ti II λ5005.19	1.57	−2.540		85					
Ti II λ5129.16	1.89	−1.239						64	
Ti II λ5154.07	1.57	−1.920						73	
Ti II λ5185.91	1.89	−1.487						51	
Ti II λ5336.79	1.58	−1.700				113		73	
Cr I λ4230.48	3.01	−1.160				44			
Cr I λ4397.22	3.01	−1.060				47			
Cr I λ4511.90	3.09	−0.343				90			
Cr I λ4545.96	0.94	−1.380						21	
Cr I λ4569.62	3.12	−0.640		87					

Table A.1 – Continued

Line	χ	log(gf)	1	2	3	4	5	6	7
Cr I λ4651.28	0.98	−1.460	20					27	
Cr I λ4652.16	1.00	−1.030	32						
Cr I λ4697.06	2.71	−1.060		97					
Cr I λ4708.02	3.17	+0.070			87				
Cr I λ4801.03	3.12	−0.130				121			
Cr I λ4836.86	3.10	−1.137		47					
Cr I λ5204.51	0.94	−0.210							47
Cr I λ5206.04	0.94	+0.020							61
Cr I λ5208.40	0.94	+0.150							91
Cr I λ5287.18	3.44	−0.870				32			
Cr I λ5296.70	0.98	−1.360			145			25	
Cr I λ5298.28	0.98	−1.160						40	
Cr I λ5312.86	3.45	−0.562				49			
Cr I λ5344.76	3.45	−1.060				26			
Cr I λ5345.81	1.00	−0.980						51	
Cr I λ5348.33	1.00	−1.210			160			33	
Cr I λ5409.80	1.03	−0.670			199				13
Cr I λ5702.33	3.45	−0.666		61					
Cr I λ5712.78	3.01	−1.030				68			
Cr II λ4554.99	4.07	−1.370	123						
Cr II λ4558.65	4.07	−0.660							30
Cr II λ4592.06	4.07	−1.188	131						
Cr II λ4616.64	4.07	−1.290							7
Cr II λ4848.25	3.86	−1.000						18	
Cr II λ5237.32	4.07	−1.160		80				12	
Cr II λ5305.87	3.83	−2.080	77	40	111	33			
Cr II λ5310.70	4.07	−2.280	28		72				
Cr II λ5420.93	3.76	−2.360	62						
Cr II λ5508.63	4.15	−2.117	35						
Cr II λ6053.48	4.74	−2.150			31				
Mn I λ4026.44	3.13	−0.520		104					
Mn I λ4061.73	3.07	−0.550		111					

Table A.1 – Continued

Line	χ	log(gf)	1	2	3	4	5	6	7
Mn I λ4436.36	2.92	−0.287			102				
Mn I λ4457.55	3.07	−0.117	13	123					
Mn I λ4502.22	2.92	−0.344		161					
Mn I λ4671.69	2.89	−1.670		69					
Mn I λ4709.72	2.89	−0.339			97	121		6	
Mn I λ4739.11	2.94	−0.490				101			
Mn I λ4761.53	2.95	−0.138			112				
Mn I λ4765.86	2.94	−0.080		172					
Mn I λ4783.42	2.30	+0.042				206		47	
Mn I λ5117.94	3.13	−1.140				36			
Mn I λ6013.50	3.07	−0.252				125			
Mn I λ6021.80	3.07	+0.035	16						
Fe I λ4016.42	3.28	−1.600		148					
Fe I λ4049.34	2.59	−2.440		164					
Fe I λ4054.18	3.26	−2.020		122					
Fe I λ4088.56	3.64	−1.500		143					
Fe I λ4126.19	3.33	−0.920		185					
Fe I λ4153.91	3.40	−0.321							27
Fe I λ4154.81	3.37	−0.400							26
Fe I λ4156.81	2.83	−0.808							46
Fe I λ4195.63	3.02	−1.797				154			
Fe I λ4222.22	2.45	−0.967	127						
Fe I λ4233.61	2.48	−0.604							94
Fe I λ4235.94	2.43	−0.341							109
Fe I λ4238.82	3.40	−0.270							37
Fe I λ4260.49	2.40	+0.077							160
Fe I λ4266.97	2.73	−1.812		181					
Fe I λ4282.41	2.18	−0.779							104
Fe I λ4299.24	2.43	−0.405							99
Fe I λ4348.95	2.99	−2.140		134					
Fe I λ4383.56	1.48	+0.200					21		218
Fe I λ4404.76	1.56	−0.142							189

Table A.1 – Continued

Line	χ	log(gf)	1	2	3	4	5	6	7
Fe I λ4408.43	2.20	−1.780	63						
Fe I λ4430.20	3.02	−1.753						18	
Fe I λ4430.62	2.22	−1.659							28
Fe I λ4439.89	2.28	−3.002						8	
Fe I λ4442.84	2.18	−2.792				145			
Fe I λ4445.48	0.09	−5.441						12	
Fe I λ4478.02	2.20	−3.710		111					
Fe I λ4481.62	3.69	−1.390		149		130			
Fe I λ4484.23	3.60	−0.864	50	178		149			
Fe I λ4485.68	3.69	−0.990				132			
Fe I λ4487.75	3.24	−2.710		78					
Fe I λ4492.69	3.98	−1.630		107	55				
Fe I λ4502.60	3.57	−2.310		105					
Fe I λ4523.41	3.65	−1.990				96			
Fe I λ4531.16	1.48	−2.155	103						
Fe I λ4537.68	3.27	−2.980				32			
Fe I λ4551.65	3.94	−2.030		57		41			
Fe I λ4556.93	3.25	−2.660		78		53			
Fe I λ4561.42	2.76	−3.080		107					
Fe I λ4566.52	3.30	−2.380				84			
Fe I λ4574.23	3.21	−2.450		122					
Fe I λ4574.73	2.28	−2.890				140			
Fe I λ4592.66	1.56	−2.449						51	
Fe I λ4593.53	3.94	−2.030		63		45			
Fe I λ4596.07	3.60	−1.369				119			
Fe I λ4596.42	3.65	−2.280				70			
Fe I λ4598.12	3.28	−1.570				149			
Fe I λ4598.74	3.69	−2.660		52					
Fe I λ4602.01	1.61	−3.154						16	
Fe I λ4602.95	1.48	−2.220	102						
Fe I λ4603.95	2.99	−2.780		109		74			
Fe I λ4619.30	3.60	−1.080		166				13	
Fe I λ4625.05	3.24	−1.350		196		165		27	

Table A.1 – Continued

Line	χ	log(gf)	1	2	3	4	5	6	7
Fe I λ4630.13	2.28	−2.590		196		157			
Fe I λ4635.85	2.84	−2.358						9	
Fe I λ4637.51	3.28	−1.340	36			162			
Fe I λ4638.02	3.60	−1.119						8	
Fe I λ4643.47	3.65	−1.147		173	126				
Fe I λ4647.44	2.95	−1.351				198			
Fe I λ4657.59	2.84	−2.840		111		92			
Fe I λ4658.30	3.27	−3.040				55			
Fe I λ4661.54	4.56	−1.260				40			
Fe I λ4669.18	3.65	−1.211						7	
Fe I λ4673.17	3.65	−1.059						8	
Fe I λ4700.16	3.69	−1.680		127					
Fe I λ4704.95	3.69	−1.530		144	84	90			
Fe I λ4705.47	3.55	−2.270		109					
Fe I λ4726.15	3.00	−3.190		87					
Fe I λ4728.55	3.65	−1.172		181	136			12	
Fe I λ4729.68	3.40	−2.420		111					
Fe I λ4733.60	1.48	−2.987				198			
Fe I λ4733.85	4.07	−1.330				73			
Fe I λ4736.78	3.21	−0.752	94						
Fe I λ4741.53	2.83	−1.764						13	
Fe I λ4765.47	1.61	−4.010				128			
Fe I λ4786.81	3.02	−1.606				172			
Fe I λ4787.83	3.00	−2.600				110			
Fe I λ4788.77	3.24	−1.763		154	118			5	
Fe I λ4789.66	3.55	−0.958		196				18	
Fe I λ4794.36	2.42	−4.050				56			
Fe I λ4800.65	4.14	−1.029			96	95			
Fe I λ4804.52	3.57	−2.590		60					
Fe I λ4807.72	3.37	−2.150		137					
Fe I λ4834.52	2.42	−3.410		118		91			
Fe I λ4838.52	3.42	−1.900				120			
Fe I λ4849.66	3.57	−2.680		51					

Table A.1 – Continued

Line	χ	log(gf)	1	2	3	4	5	6	7
Fe I λ4859.75	2.87	−0.860	92						
Fe I λ4867.54	1.61	−4.700				95			
Fe I λ4869.47	3.55	−2.480				52			
Fe I λ4872.14	2.88	−0.567							
Fe I λ4874.36	3.07	−3.030		101					
Fe I λ4875.88	3.33	−2.020				119			
Fe I λ4891.50	2.85	−0.112						122	
Fe I λ4905.14	3.93	−2.020				56			
Fe I λ4917.23	4.19	−1.160				90			
Fe I λ4919.00	2.86	−0.342						91	
Fe I λ4924.78	2.28	−2.114				185		44	
Fe I λ4938.82	2.87	−1.077						53	
Fe I λ4962.58	4.18	−1.182		109					
Fe I λ4966.10	3.33	−0.871						32	14
Fe I λ4973.10	3.96	−0.920		174					
Fe I λ4985.26	3.93	−0.560						26	
Fe I λ4985.55	2.86	−1.331						43	
Fe I λ4994.14	0.91	−3.080							
Fe I λ5001.87	3.88	−0.010						44	
Fe I λ5014.95	3.94	−0.303				165		36	
Fe I λ5022.24	3.98	−0.560							
Fe I λ5029.62	3.41	−2.000				120			
Fe I λ5039.26	3.37	−1.573							
Fe I λ5054.65	3.64	−1.921		109		98			
Fe I λ5067.15	4.22	−0.970	16					7	
Fe I λ5068.77	2.94	−1.042						62	
Fe I λ5074.75	4.22	−0.230						32	
Fe I λ5083.35	0.96	−2.958	73						
Fe I λ5090.78	4.26	−0.440	39						
Fe I λ5121.65	4.28	−0.810				110		9	
Fe I λ5125.12	4.22	−0.144				151		29	12
Fe I λ5127.37	0.91	−3.306	51						
Fe I λ5131.48	2.22	−2.560				189		23	

Table A.1 – Continued

Line	χ	log(gf)	1	2	3	4	5	6	7
Fe I λ5141.75	2.42	−2.240	20					37	
Fe I λ5162.28	4.18	+0.020	81					49	
Fe I λ5187.92	4.14	−1.371			85				
Fe I λ5191.47	3.04	−0.551							
Fe I λ5194.95	1.56	−2.090	107						
Fe I λ5198.72	2.22	−2.135	39		165			48	
Fe I λ5215.19	3.26	−0.871	58						
Fe I λ5216.28	1.61	−2.150	76					94	27
Fe I λ5217.40	3.21	−1.162			168			31	
Fe I λ5228.38	4.22	−1.260			65				
Fe I λ5243.78	4.26	−1.120			84				
Fe I λ5250.65	2.20	−2.181						48	
Fe I λ5263.31	3.26	−0.879	73						
Fe I λ5288.53	3.69	−1.508		146		97			
Fe I λ5295.32	4.41	−1.670		56					
Fe I λ5302.31	3.28	−0.720						60	
Fe I λ5322.05	2.28	−3.040			97				
Fe I λ5330.00	4.07	−1.219			98				
Fe I λ5332.91	1.56	−2.776						53	
Fe I λ5339.94	3.26	−0.720						45	
Fe I λ5364.88	4.44	+0.228	95					34	
Fe I λ5367.48	4.41	+0.443	101					55	19
Fe I λ5369.97	4.37	+0.536	113					50	29
Fe I λ5373.71	4.47	−0.840		114		98			
Fe I λ5383.38	4.31	+0.645	135		184			81	35
Fe I λ5389.49	4.42	−0.400			113				
Fe I λ5393.18	3.24	−0.715	80					69	
Fe I λ5405.78	0.99	−1.844							
Fe I λ5406.78	4.37	−1.720		66					
Fe I λ5409.14	4.37	−1.270			61				
Fe I λ5410.92	4.47	+0.398						39	
Fe I λ5415.21	4.39	+0.510	113					44	
Fe I λ5434.53	1.01	−2.121	139						78

Table A.1 – Continued

Line	χ	log(gf)	1	2	3	4	5	6	7
Fe I λ5441.35	4.31	−1.700		71					
Fe I λ5445.05	4.39	−0.010	57						
Fe I λ5473.91	4.15	−0.790		159					
Fe I λ5491.85	4.19	−2.188		34					
Fe I λ5501.48	0.96	−2.960	74						
Fe I λ5506.79	0.99	−2.797							36
Fe I λ5543.94	4.22	−1.150				80			
Fe I λ5567.44	2.61	−2.810			94				
Fe I λ5569.63	3.42	−0.486							22
Fe I λ5572.85	3.40	−0.275	128						41
Fe I λ5576.10	3.43	−0.940	61						
Fe I λ5633.95	4.99	−0.320	18	102					
Fe I λ5638.27	4.22	−0.870	17					8	
Fe I λ5641.45	4.26	−1.150		117		85			
Fe I λ5650.69	5.08	−0.960			31				
Fe I λ5701.56	2.56	−2.216			141			25	
Fe I λ5705.47	4.30	−1.355				58			
Fe I λ5706.01	4.61	−0.530				117			
Fe I λ5709.39	3.37	−1.028	60						
Fe I λ5717.84	4.28	−1.100		102	73				
Fe I λ5731.77	4.26	−1.270		115					
Fe I λ5760.36	3.64	−2.440		68		68			
Fe I λ5809.25	3.88	−1.790			47				
Fe I λ5934.66	3.93	−1.120		154					
Fe I λ5952.73	3.98	−1.390		122					
Fe I λ6003.02	3.88	−1.120			116			10	
Fe I λ6020.19	4.61	−0.270						12	
Fe I λ6027.06	4.07	−1.089	14						
Fe I λ6065.49	2.61	−1.530						61	
Fe I λ6136.62	2.45	−1.400						83	
Fe I λ6137.70	2.59	−1.403	73					55	18
Fe I λ6151.62	2.18	−3.299			98				
Fe I λ6157.73	4.07	−1.220		124		92			

Table A.1 – Continued

Line	χ	log(gf)	1	2	3	4	5	6	7
Fe I λ6200.32	2.61	−2.437						19	
Fe I λ6213.43	2.22	−2.480			167				
Fe I λ6219.29	2.20	−2.433						46	
Fe I λ6232.65	3.65	−1.223							
Fe I λ6240.65	2.22	−3.390		168					
Fe I λ6246.33	3.60	−0.877						29	6
Fe I λ6252.56	2.40	−1.687	56						
Fe I λ6265.14	2.18	−2.550							6
Fe I λ6322.69	2.59	−2.426						24	
Fe I λ6335.34	2.20	−2.177						56	
Fe I λ6336.83	3.69	−0.856						24	
Fe I λ6344.15	2.43	−2.922		179	103				
Fe I λ6355.03	2.84	−2.291						10	
Fe I λ6358.69	0.86	−4.468							
Fe I λ6380.76	4.19	−1.376			61				
Fe I λ6393.61	2.43	−1.580	69						21
Fe I λ6400.01	3.60	−0.290						56	
Fe I λ6408.03	3.69	−1.018						24	
Fe I λ6411.66	3.65	−0.718						37	
Fe I λ6421.36	2.28	−2.027						71	
Fe I λ6430.86	2.18	−2.006						71	
Fe I λ6569.23	4.73	−0.450			102				
Fe I λ6593.88	2.43	−2.420			149				
Fe I λ6663.45	2.42	−2.479				178		31	
Fe I λ6678.00	2.69	−1.418						54	
Fe I λ6703.57	2.76	−3.060			52				
Fe I λ6750.15	2.42	−2.620			143				
Fe I λ6828.60	4.64	−0.890		85					
Fe I λ6855.17	4.56	−0.740		140		96			
Fe I λ6858.15	4.61	−0.930		86					
Fe I λ6988.53	2.40	−3.660		137					
Fe I λ7780.57	4.47	−0.091							12

Table A.1 – Continued

Line	χ	log(gf)	1	2	3	4	5	6	7
Fe II λ4385.39	2.78	−2.580						48	
Fe II λ4472.93	2.84	−3.360							16
Fe II λ4508.29	2.85	−2.440		161		112			
Fe II λ4555.89	2.83	−2.401							84
Fe II λ4576.34	2.84	−2.950		141					44
Fe II λ4582.83	2.84	−3.180						24	
Fe II λ4620.52	2.83	−3.210	139		166			24	16
Fe II λ4666.75	2.83	−3.290							21
Fe II λ4923.93	2.89	−1.260					14		
Fe II λ5018.44	2.89	−1.100					24		
Fe II λ5132.67	2.81	−4.170	77						
Fe II λ5136.80	2.84	−4.430			99	154			
Fe II λ5197.58	3.23	−2.054						51	
Fe II λ5234.63	3.22	−2.180							
Fe II λ5264.81	3.33	−3.130		85					
Fe II λ5284.11	2.89	−3.110			179				
Fe II λ5325.56	3.22	−3.160		95	150	41			
Fe II λ5414.07	3.22	−3.790	70	46	124	27			
Fe II λ5425.56	3.20	−3.220			161				
Fe II λ5534.85	3.24	−2.750			182	83			
Fe II λ5991.38	3.15	−3.650						8	
Fe II λ6149.25	3.89	−2.690			154				
Fe II λ6239.95	3.89	−3.410			101				
Fe II λ6247.56	3.89	−2.300		73					13
Fe II λ6248.91	5.51	−2.670			19				
Fe II λ6369.46	2.89	−4.110		42					
Fe II λ6383.72	5.55	−2.240			48				
Fe II λ6385.46	5.55	−2.590			32				
Fe II λ6416.93	3.89	−2.880						6	
Fe II λ6432.68	2.89	−3.500						17	
Fe II λ6442.95	5.55	−2.440			25				
Fe II λ6456.39	3.90	−2.050				76			27
Fe II λ6516.08	2.89	−3.310	133						

Table A.1 – Continued

Line	χ	log(gf)	1	2	3	4	5	6	7
Fe II λ7515.84	3.90	−3.390			87				
Ni I λ4401.54	3.19	+0.080							11
Ni I λ4410.52	3.31	−1.080		100					
Ni I λ4462.46	3.46	−0.600			120				
Ni I λ4470.48	3.40	−0.400		139					
Ni I λ4648.66	3.42	−0.150		165				19	
Ni I λ4686.22	3.60	−0.640		116					
Ni I λ4701.54	4.09	−0.380	13						
Ni I λ4715.77	3.54	−0.330				144			
Ni I λ4732.47	4.10	−0.550		68	49				
Ni I λ4752.43	3.66	−0.690			97	109			
Ni I λ4756.52	3.48	−0.340			125				
Ni I λ4852.56	3.54	−1.070		82	87				
Ni I λ4904.42	3.54	−0.170						15	
Ni I λ5000.35	3.63	−0.430		145	120				
Ni I λ5003.75	1.68	−2.800		156					
Ni I λ5035.37	3.63	+0.290							8
Ni I λ5080.52	3.67	+0.130						41	6
Ni I λ5081.12	3.85	+0.300						26	
Ni I λ5084.10	3.68	+0.097	70					23	
Ni I λ5137.08	1.68	−1.990						50	
Ni I λ5388.35	1.93	−3.550				79			
Ni I λ5435.87	1.99	−2.600		150					
Ni I λ5462.50	3.85	−0.930				78			
Ni I λ5476.91	1.83	−0.890						119	20
Ni I λ5592.27	1.95	−2.590						11	
Ni I λ5754.67	1.93	−2.340				171			
Ni I λ6108.12	1.68	−2.440		191	112			18	
Ni I λ6643.64	1.68	−2.300						30	
Ni I λ6767.78	1.83	−2.120	26						
Ni I λ7122.21	3.54	+0.040						34	
Zn I λ4680.14	4.00	−0.860					16		

Table A.1 – Continued

Line	χ	log(gf)	1	2	3	4	5	6	7
Zn I λ4722.16	4.03	−0.390	28	105		87	28	47	17
Zn I λ4810.54	4.08	−0.170		110	162	97	46	40	18
Zn I λ6362.35	5.79	+0.272	6		72				
Sr I λ4607.34	0.00	+0.300						27	
Sr II λ4215.54	0.00	−0.160					59		
Y I λ4128.31	0.07	+0.380		108					
Y II λ4358.73	0.10	−1.324							29
Y II λ4374.94	0.41	+0.155							126
Y II λ4398.02	0.13	−0.998							43
Y II λ4883.69	1.08	−0.041			167				51
Y II λ5200.41	0.99	−0.569				144			
Y II λ5402.78	1.84	−0.630	23			57			
Y II λ5509.91	0.99	−1.010			104				
Y II λ5546.03	1.75	−1.097			42				
Zr I λ5385.13	0.52	−0.710				68			
Zr I λ6127.48	0.15	−1.060				106			
Zr I λ6134.57	0.00	−1.280		16		112			
Zr I λ6140.46	0.52	−1.410				31			
Zr I λ6143.18	0.07	−1.100		17		105			
Zr II λ3714.79	0.53	−0.960							35
Zr II λ4161.21	0.71	−0.590							57
Zr II λ4208.98	0.71	−0.510							44
Zr II λ4443.00	1.49	−0.420						14	
Zr II λ4496.97	0.71	−0.890						49	27
Zr II λ5112.28	1.66	−0.850						7	
Ba II λ4934.10	0.00	−0.159					6		
Ba II λ5853.69	0.60	−1.016		163					55
Ba II λ6141.71	0.60	−0.030							155
La II λ3759.07	0.24	−0.030							30
La II λ4086.71	0.00	−0.070		131					47
La II λ4333.76	0.17	−0.060						50	
La II λ4804.04	0.23	−1.490				38			

Table A.1 – Continued

Line	χ	log(gf)	1	2	3	4	5	6	7
La II λ5303.53	0.32	−1.350				37		7	
Ce II λ4075.70	0.70	+0.230							11
Ce II λ4222.60	0.12	−0.150							13
Ce II λ4349.80	0.70	−0.320		14		52			
Ce II λ4364.66	0.50	−0.170	15	34	50				
Ce II λ4418.78	0.86	+0.270				75			
Ce II λ4486.91	0.30	−0.180	14		80	106	106		
Ce II λ4560.97	0.68	−0.260			49				
Ce II λ4562.37	0.48	+0.324	45						16
Ce II λ4628.16	0.52	+0.140		61					11
Ce II λ6043.37	1.21	−0.480				23			
Pr II λ5219.03	0.79	−0.053		17					
Pr II λ5322.82	0.48	−0.319		23					
Nd II λ4059.97	0.20	−0.520							7
Nd II λ4156.08	0.18	+0.160							19
Nd II λ4446.40	0.20	−0.590				96			
Nd II λ4462.99	0.56	+0.040						14	10
Nd II λ4811.35	0.06	−0.890						14	
Nd II λ4989.95	0.63	−0.500		48					
Nd II λ5092.80	0.38	−0.610		60					
Nd II λ5192.62	1.14	+0.270							7
Nd II λ5212.35	0.20	−0.960						8	
Nd II λ5255.52	0.20	−0.670			46				
Nd II λ5293.17	0.82	+0.100						8	
Nd II λ5319.82	0.55	−0.140			56	103			
Nd II λ5485.71	1.26	−0.120			18				
Sm II λ4467.34	0.66	+0.150		65	76			17	
Sm II λ4523.92	0.43	−0.390				78			
Sm II λ4566.18	0.33	−0.590				55			
Sm II λ4577.69	0.25	−0.650			53	66		7	
Sm II λ4642.24	0.38	−0.460		57	51				
Sm II λ4669.40	0.10	−0.600						9	

Table A.1 – Continued

Line	χ	log(gf)	1	2	3	4	5	6	7
Sm II λ4719.84	0.04	−1.240						5	
Eu II λ4129.72	0.00	+0.220							63
Eu II λ6645.13	1.38	+0.120							7
Dy II λ3996.70	0.59	−0.260							8
Dy II λ4073.12	0.54	−0.320							6

Table A.2: Line identification for the stars: 8 = IRAS 19135+3937, 9 = IRAS 22223+5556, 10 = IRAS 01259+6823, 11 = IRAS 04535+3747, 12 = IRAS 05208-2035, 13 = IRAS 07140-2321, 14 = IRAS 07331+0021

Line	χ	log(gf)	8	9	10	11	12	13	14
C I λ4770.00	7.48	−2.437	48					20	
C I λ4775.88	7.49	−2.304	62					30	
C I λ5052.15	7.69	−1.303				89		80	
C I λ5380.32	7.68	−1.616	92		24			43	17
C I λ6013.20	8.64	−1.314						22	
C I λ6014.84	8.64	−1.584						13	
C I λ6587.62	8.53	−1.003			17	50		42	8
C I λ7108.92	8.64	−1.594						13	
C I λ7111.45	8.64	−1.085				34		31	
C I λ7113.17	8.65	−0.773				52		41	
C I λ7115.17	8.65	−0.934				56		51	
C I λ7116.96	8.64	−0.907				58		48	
C I λ7848.20	8.85	−1.731	18						
N I λ7442.30	10.33	−0.385						31	
N I λ7468.27	10.33	−0.190				31		52	
N I λ8216.34	10.33	+0.132				56		94	
N I λ8223.10	10.33	−0.271						51	
N I λ8629.24	10.69	+0.075				45			
N I λ8747.37	10.34	−1.321				5			
O I λ6156.76	10.74	−0.898				14			
O I λ6158.19	10.74	−0.409				23		32	
O I λ6300.31	0.00	−9.752		150	45	44	55		170
O I λ6363.79	0.02	−10.250	15		20		42		103
Na I λ4751.82	2.10	−2.078					32		
Na I λ5682.65	2.10	−0.700			127		131	22	
Na I λ5688.22	2.10	−0.400				127	162		
Na I λ6154.23	2.10	−1.547		114	40	33	87	6	
Na I λ6160.75	2.10	−1.246		150	72	50	106	6	

Table A.2 – Continued

Line	χ	log(gf)	8	9	10	11	12	13	14
Na I λ8183.25	2.10	+0.237							
Mg I λ4057.51	4.34	−0.999	115						
Mg I λ4167.28	4.34	−0.946	121						
Mg I λ4703.00	4.34	−0.440			230		198	126	
Mg I λ4730.04	4.34	−2.347			68	39			92
Mg I λ5528.42	4.34	−0.340				193		145	
Mg I λ5711.09	4.34	−1.724		192	119	67	123	33	
Mg I λ8806.78	4.35	−0.134				272			
Mg I λ9255.79	5.75	−0.146				137			
Mg II λ7877.05	9.99	+0.391						57	
Al I λ3944.02	0.00	−0.638						169	
Al I λ5557.08	3.14	−2.104					30		
Al I λ6696.03	3.14	−1.320			42	32	85		
Al I λ6698.67	3.14	−1.620			14		57		
Al I λ7835.32	4.02	−0.500				18			
Al I λ7836.13	4.02	−0.290			36	27	70		
Al I λ8772.88	4.02	−0.170				38			
Al I λ8773.91	4.02	−0.030				54			
Si I λ5517.55	5.08	−2.027		51					
Si I λ5622.23	4.93	−1.640		100					
Si I λ5645.62	4.93	−1.630		142					
Si I λ5665.56	4.92	−1.730					48		46
Si I λ5690.43	4.93	−1.760				32	56		51
Si I λ5708.40	4.95	−1.470						20	
Si I λ5753.65	5.61	−1.299			63				
Si I λ5772.15	5.08	−1.740			52	46			65
Si I λ5793.08	4.93	−1.490	19				47		57
Si I λ5948.55	5.08	−1.230				80			
Si I λ6125.03	5.61	−1.513			36				
Si I λ6142.46	5.62	−1.540					24		
Si I λ6145.02	5.61	−1.479			43		22		
Si I λ6155.14	5.62	−0.966				64	59		

Table A.2 – Continued

Line	χ	log(gf)	8	9	10	11	12	13	14
Si I λ6237.33	5.61	−1.138			62	49		8	67
Si I λ6244.48	5.61	−1.363			45	30		5	
Si I λ6414.99	5.87	−1.155			47			7	
Si I λ6721.84	5.86	−1.062				28	47		
Si I λ7003.57	5.97	−0.910				46			
Si I λ7034.91	5.87	−0.880		112	52	45			
Si I λ7799.17	6.18	−1.110					16		
Si I λ7800.00	6.18	−0.712			46	42			
Si I λ7849.98	6.19	−0.652			63				
Si I λ8035.61	5.99	−1.340				28			
Si I λ8556.80	5.87	−0.195		185		114			
Si I λ8648.47	6.20	−0.100				122		36	
Si II λ6347.10	8.12	+0.149			64	142			
Si II λ6371.35	8.12	−0.082			57	102		115	
S I λ4695.45	6.52	−1.960	12						
S I λ4696.24	6.52	−2.191				16		7	
S I λ5278.95	6.86	−2.100				28			
S I λ6052.68	7.87	−0.630	15						
S I λ6748.78	7.87	−0.600						27	
S I λ6757.19	7.87	−0.310			24	69		43	
S I λ8874.48	8.42	+0.110				45			
S I λ8882.47	8.42	−0.630				32			
Ca I λ4094.94	2.52	−0.400							132
Ca I λ4302.54	1.90	+0.276				182			
Ca I λ4425.44	1.88	−0.360				139		29	
Ca I λ4434.97	1.89	−0.010						94	
Ca I λ4512.26	2.53	−1.890					44		
Ca I λ4526.93	2.71	−0.420		135					
Ca I λ4578.56	2.52	−0.558				54			
Ca I λ4685.37	2.93	−0.880					62		
Ca I λ5260.39	2.52	−1.900					46		
Ca I λ5261.71	2.52	−0.730			114				136

Table A.2 – Continued

Line	χ	log(gf)	8	9	10	11	12	13	14
Ca I λ5265.56	2.52	−0.260						37	
Ca I λ5349.47	2.71	−0.310			132				
Ca I λ5512.99	2.93	−0.300			101			6	110
Ca I λ5581.98	2.52	−0.710			112		135		
Ca I λ5588.76	2.52	+0.210	72		177			58	
Ca I λ5590.13	2.52	−0.710			106	72	123	15	
Ca I λ5598.49	2.52	−0.220	49					25	
Ca I λ5601.29	2.52	−0.690				85			
Ca I λ5857.46	2.93	+0.230				137			
Ca I λ6102.73	1.88	−0.790				131		27	
Ca I λ6122.23	1.89	−0.315	71					46	
Ca I λ6161.30	2.52	−1.030		116	96				
Ca I λ6162.18	1.90	−0.089						67	
Ca I λ6166.44	2.52	−0.900			93	38	119		
Ca I λ6169.04	2.52	−0.540			117	60		6	
Ca I λ6169.56	2.52	−0.270			150				
Ca I λ6439.08	2.52	+0.470				196		63	
Ca I λ6449.82	2.52	−0.550				81		14	
Ca I λ6462.57	2.52	+0.310				197			
Ca I λ6471.67	2.52	−0.590			131	80			
Ca I λ6493.79	2.52	+0.140				122		33	
Ca I λ6499.65	2.52	−0.590		150		64		9	
Ca I λ6717.69	2.71	−0.610	22			100			
Ca II λ8254.68	7.51	−0.390	23						
Sc II λ4294.78	0.61	−1.470				133		48	
Sc II λ4305.71	0.60	−1.523						57	
Sc II λ4354.61	0.61	−1.834	62						
Sc II λ4400.40	0.61	−0.780						128	
Sc II λ4415.56	0.60	−0.890						104	
Sc II λ5239.82	1.45	−0.942	79	133	130			52	
Sc II λ5318.36	1.36	−2.010			49			9	
Sc II λ5526.79	1.77	−0.219	134						137

Table A.2 – Continued

Line	χ	log(gf)	8	9	10	11	12	13	14
Sc II λ5640.99	1.50	−1.353		88					
Sc II λ5658.35	1.50	−1.384						20	
Sc II λ5667.15	1.50	−1.485			99	98		20	
Sc II λ5669.04	1.50	−1.200			119			42	
Sc II λ6604.60	1.36	−1.531			110	79			65
Ti I λ3998.64	0.05	−0.055			199				
Ti I λ4060.27	1.05	−0.530		90					
Ti I λ4480.60	1.74	+0.000					103		
Ti I λ4485.07	2.08	−1.628					19		
Ti I λ4512.74	0.84	−0.480				37			
Ti I λ4518.03	0.83	−0.324		169	128				
Ti I λ4548.77	0.83	−0.354		151					
Ti I λ4617.28	1.75	+0.389				26	135		181
Ti I λ4623.10	1.74	+0.110		110					
Ti I λ4656.47	0.00	−1.289			140				
Ti I λ4675.11	1.07	−1.372			29				
Ti I λ4747.67	2.25	−1.092					39		
Ti I λ4759.28	2.25	+0.514			65				
Ti I λ4778.26	2.24	−0.210					56		
Ti I λ4820.41	1.50	−0.439					101		
Ti I λ4840.88	0.90	−0.510		141	115	32			
Ti I λ4915.23	1.89	−1.019					38		
Ti I λ4981.74	0.85	+0.504				120			
Ti I λ5007.22	0.82	+0.112				132			
Ti I λ5016.17	0.85	−0.574		141		39			
Ti I λ5022.87	0.83	−0.434			125	41			
Ti I λ5024.85	0.82	−0.602		138		39			
Ti I λ5036.47	1.44	+0.130			127				
Ti I λ5038.40	1.43	+0.013			130				
Ti I λ5039.96	0.02	−1.130				50			
Ti I λ5043.59	0.84	−1.733		35					
Ti I λ5192.98	0.02	−1.005		183		60			

Table A.2 – Continued

Line	χ	log(gf)	8	9	10	11	12	13	14
Ti I λ5201.09	2.09	−0.749					87		
Ti I λ5210.39	0.05	−0.883				59			
Ti I λ5219.71	0.02	−2.292		43					
Ti I λ5223.63	2.09	−0.559					70		
Ti I λ5351.07	2.78	+0.010					53		
Ti I λ5438.31	1.43	−1.788					71		27
Ti I λ5471.20	1.44	−1.390					87		
Ti I λ5648.57	2.49	−0.250					73		
Ti I λ5965.84	1.88	−0.409			48				
Ti I λ5978.54	1.87	−0.496					99		
Ti I λ6121.01	1.88	−0.912					79		
Ti I λ6261.11	1.43	−0.479				22			
Ti I λ6258.11	1.44	−0.355			81				
Ti I λ6261.11	1.43	−0.479		103					
Ti II λ4316.80	2.05	−1.420		137		119			180
Ti II λ4386.85	2.60	−1.260						90	
Ti II λ4391.03	1.23	−2.760					64		
Ti II λ4395.85	1.24	−2.170				182		112	
Ti II λ4409.53	1.23	−2.570						49	
Ti II λ4418.34	1.24	−2.450						87	
Ti II λ4488.33	3.12	−0.820						72	
Ti II λ4493.53	1.08	−2.740			118			68	159
Ti II λ4568.33	1.22	−2.650	42		116				162
Ti II λ4589.96	1.24	−1.780					114		
Ti II λ4609.23	1.18	−3.260							88
Ti II λ4708.67	1.24	−2.370				139			
Ti II λ4719.52	1.24	−3.280					48		
Ti II λ4798.54	1.08	−2.430	83						
Ti II λ4806.33	1.08	−3.380				27			
Ti II λ4865.62	1.12	−2.592				124			
Ti II λ4911.20	3.12	−0.340				143			
Ti II λ5005.19	1.57	−2.540					68		

Table A.2 – Continued

Line	χ	log(gf)	8	9	10	11	12	13	14
Ti II λ5069.09	3.12	−1.400						26	
Ti II λ5185.91	1.89	−1.350	135	172	156				
Ti II λ5336.79	1.58	−1.700	102						
Ti II λ5492.86	1.58	−3.310					51		40
V I λ4379.24	0.30	+0.580			156				
V I λ4389.99	0.28	+0.200			144				
V I λ4406.65	0.30	−0.190			112				
V I λ4577.18	0.00	−1.048			72				
V I λ4864.74	0.02	−0.960			69				
V I λ4875.49	0.04	−0.810			76				
V I λ5670.86	1.08	−0.420			26				
V I λ6119.53	1.06	−0.320			53				
V I λ6243.11	0.30	−0.980			66				
V I λ6251.82	0.29	−1.340			27				
V I λ6274.66	0.27	−1.670			18				
Cr I λ4381.11	2.71	−1.060				6			
Cr I λ4496.86	0.94	−1.140	62						
Cr I λ4511.85	3.09	−0.343					72		
Cr I λ4545.96	0.94	−1.380				70		13	
Cr I λ4569.62	3.12	−0.640		65					
Cr I λ4580.06	0.94	−1.640			145				
Cr I λ4591.40	0.97	−1.760		190					
Cr I λ4651.29	0.98	−1.460	21						
Cr I λ4718.42	3.19	+0.100				49			
Cr I λ4801.03	3.12	−0.130					93		100
Cr I λ5208.43	0.94	+0.170	175					128	
Cr I λ5238.96	2.74	−1.305					54		
Cr I λ5247.57	0.96	−1.630				60			
Cr I λ5264.16	0.97	−1.288				151			
Cr I λ5296.70	0.99	−1.400				78			
Cr I λ5297.39	2.90	+0.167			117	63			
Cr I λ5298.28	0.98	−1.160						23	

Table A.2 – Continued

Line	χ	log(gf)	8	9	10	11	12	13	14
Cr I λ5300.75	0.98	−2.000			106	35			
Cr I λ5312.87	3.45	−0.562					44		
Cr I λ5329.15	2.91	−0.064			89	52	123	10	
Cr I λ5787.93	3.32	−0.083					79		56
Cr II λ4113.22	3.11	−2.740				54			
Cr II λ4588.20	4.07	−0.640	174						
Cr II λ4592.06	4.07	−1.220	108						
Cr II λ4616.63	4.07	−1.290	125						
Cr II λ4848.25	3.86	−1.130	132		152				
Cr II λ4884.60	3.86	−2.080				71			
Cr II λ5097.32	3.71	−2.630						27	
Cr II λ5237.32	4.07	−1.160	122	152	121		59		
Cr II λ5246.78	3.71	−2.460						35	
Cr II λ5305.87	3.83	−2.080	49				36		47
Cr II λ5308.43	4.07	−1.810							52
Cr II λ5310.70	4.07	−2.270			39	53		30	
Cr II λ5369.36	3.87	−2.860						16	
Cr II λ5502.09	4.17	−1.990			51				
Cr II λ5508.63	4.15	−2.120	43					40	
Cr II λ6053.48	4.75	−2.150				21			
Mn I λ4055.55	2.14	−0.070				119			
Mn I λ4061.73	3.08	−0.550				37			
Mn I λ4325.29	2.89	+0.170							180
Mn I λ4436.36	2.92	−0.287			99				
Mn I λ4470.14	2.94	−0.440				34			
Mn I λ4498.90	2.94	−0.343				26			
Mn I λ4709.72	2.89	−0.339			111			6	
Mn I λ4739.11	2.94	−0.490			95				74
Mn I λ4761.53	2.95	−0.138		174		54	118		
Mn I λ4766.42	2.92	+0.100			135	79		13	
Mn I λ4783.42	2.30	+0.042	93			147		27	
Mn I λ5377.61	3.84	−0.109							24

Table A.2 – Continued

Line	χ	log(gf)	8	9	10	11	12	13	14
Mn I λ5413.69	3.86	−0.589					50		
Mn I λ5432.55	0.00	−3.795			101				
Mn I λ6013.49	3.07	−0.252	15		103		143		
Mn I λ6021.80	3.07	+0.035		190	122	61			
Fe I λ3953.86	2.83	−2.030				52			
Fe I λ4001.67	2.18	−1.880				93			
Fe I λ4017.15	3.05	−0.920				128			
Fe I λ4031.97	3.27	−1.030		198					
Fe I λ4067.99	3.21	−0.420				94			
Fe I λ4072.51	3.43	−1.439							131
Fe I λ4082.11	3.42	−1.540				54			
Fe I λ4088.56	3.64	−1.500	17						
Fe I λ4091.56	2.83	−2.068							153
Fe I λ4109.06	3.29	−1.470				78			
Fe I λ4109.80	2.85	−1.470				105			
Fe I λ4114.94	3.37	−1.445		149					
Fe I λ4136.53	3.37	−1.520				40			
Fe I λ4137.01	3.41	−0.550	87						
Fe I λ4139.94	0.99	−3.628				55			
Fe I λ4147.68	1.48	−2.104	136			161			
Fe I λ4157.79	3.42	−0.403	128						
Fe I λ4158.80	3.43	−0.680				100			
Fe I λ4168.62	3.37	−1.940				42			
Fe I λ4175.64	2.85	−0.680				121			
Fe I λ4182.39	3.02	−1.190				96			
Fe I λ4187.05	2.45	−0.549						120	
Fe I λ4189.56	3.69	−1.300		137					
Fe I λ4195.34	3.33	−0.492						54	
Fe I λ4196.21	3.40	−0.696						41	
Fe I λ4199.10	3.05	+0.156						127	
Fe I λ4200.93	3.40	−0.827						17	
Fe I λ4213.65	2.84	−1.250						16	

Table A.2 – Continued

Line	χ	log(gf)	8	9	10	11	12	13	14
Fe I λ4224.18	3.37	−0.506						62	
Fe I λ4239.37	3.64	−1.540				35			
Fe I λ4264.22	3.37	−1.490				54			
Fe I λ4266.97	2.73	−1.812		200					
Fe I λ4298.04	3.05	−1.426	43						
Fe I λ4327.92	3.30	−1.700				46			
Fe I λ4352.74	2.22	−1.260				176			
Fe I λ4365.90	2.99	−2.250		144		22			
Fe I λ4375.94	0.00	−3.031						74	
Fe I λ4388.41	3.60	−0.682						35	
Fe I λ4401.30	3.60	−0.890						23	
Fe I λ4404.76	1.56	−0.142						196	
Fe I λ4423.85	3.65	−1.600							103
Fe I λ4430.62	2.22	−1.659						43	
Fe I λ4432.57	3.57	−1.560							96
Fe I λ4433.23	3.65	−0.690				76			182
Fe I λ4440.83	3.96	−1.600				22			
Fe I λ4461.66	0.09	−3.210						72	
Fe I λ4478.02	2.20	−3.620							56
Fe I λ4484.23	3.60	−0.864		182					
Fe I λ4485.68	3.69	−1.000							142
Fe I λ4489.75	0.12	−3.966				141			
Fe I λ4492.69	3.98	−1.630		84					
Fe I λ4523.41	3.65	−1.960		106					
Fe I λ4531.16	1.48	−2.154						55	
Fe I λ4531.63	3.63	−2.154				28			
Fe I λ4566.52	3.30	−2.380		96			73		
Fe I λ4574.23	3.21	−2.450		117			71		
Fe I λ4592.66	1.56	−2.448						37	
Fe I λ4593.53	3.94	−2.030					51		
Fe I λ4595.36	3.30	−1.758							164
Fe I λ4596.42	3.65	−2.280		71					
Fe I λ4598.12	3.28	−1.570	36						

Table A.2 – Continued

Line	χ	log(gf)	8	9	10	11	12	13	14
Fe I λ4602.01	1.61	−3.154		194					
Fe I λ4602.95	1.48	−2.220						38	
Fe I λ4614.20	3.30	−2.570					60		
Fe I λ4619.30	3.60	−1.120				72			190
Fe I λ4630.13	2.28	−2.610				67	133		191
Fe I λ4635.85	2.85	−2.420				32			
Fe I λ4661.98	2.99	−2.502							67
Fe I λ4669.18	3.65	−1.211	42						
Fe I λ4673.17	3.65	−1.060							181
Fe I λ4678.85	3.60	−0.833	61					26	
Fe I λ4683.57	2.83	−2.530	8			24	104		
Fe I λ4690.14	3.69	−1.682				33			
Fe I λ4705.46	3.55	−2.270					42		
Fe I λ4707.28	3.24	−1.080	77					26	
Fe I λ4728.55	3.65	−1.172		188				11	123
Fe I λ4729.68	3.40	−2.483				21			
Fe I λ4736.78	3.21	−0.752	101			159			
Fe I λ4741.53	2.83	−2.004				58			
Fe I λ4779.44	3.41	−2.020							77
Fe I λ4787.83	3.00	−2.600		89		17			
Fe I λ4788.77	3.24	−1.763		152		37			
Fe I λ4789.66	3.55	−0.958						16	
Fe I λ4791.26	3.27	−2.435							58
Fe I λ4799.41	3.64	−2.231				23			
Fe I λ4800.65	4.14	−1.029		135		37			83
Fe I λ4807.72	3.37	−2.150	6						
Fe I λ4809.94	3.57	−2.680					42		
Fe I λ4834.52	2.43	−3.330					92		64
Fe I λ4838.52	3.42	−1.900							73
Fe I λ4839.55	3.27	−1.820					90		
Fe I λ4842.79	4.11	−1.561				21			
Fe I λ4871.32	2.86	−0.410				204			
Fe I λ4872.14	2.88	−0.590				206		63	

Table A.2 – Continued

Line	χ	log(gf)	8	9	10	11	12	13	14
Fe I λ4882.15	3.42	−1.630				64			
Fe I λ4896.44	3.88	−2.020		65					
Fe I λ4905.14	3.93	−2.020		61					
Fe I λ4907.73	3.43	−1.840				32			
Fe I λ4924.78	2.28	−2.200				139			
Fe I λ4982.51	4.10	+0.144						63	
Fe I λ4983.26	4.15	−0.158						36	
Fe I λ4983.86	4.10	−0.068						52	
Fe I λ4988.95	4.15	−0.890				74			
Fe I λ4991.86	4.22	−1.900					56		
Fe I λ4994.14	0.91	−3.079						19	
Fe I λ5001.87	3.88	−0.010						54	
Fe I λ5002.80	3.40	−1.579				55			
Fe I λ5005.72	3.88	−0.009						44	
Fe I λ5012.07	0.86	−2.642				192			
Fe I λ5014.95	3.94	−0.303	69					26	
Fe I λ5022.24	3.98	−0.560						25	
Fe I λ5028.13	3.57	−1.123			130			13	
Fe I λ5029.62	3.41	−2.000			82	24			
Fe I λ5031.92	4.37	−1.650					40		
Fe I λ5039.26	3.37	−1.573			129				174
Fe I λ5044.22	2.85	−2.017		167			130		
Fe I λ5048.44	3.96	−1.256				45			104
Fe I λ5049.83	2.28	−1.430						41	
Fe I λ5051.64	0.91	−2.794						25	
Fe I λ5054.65	3.64	−1.921		94			75		
Fe I λ5067.15	4.22	−0.970				43			
Fe I λ5068.77	2.94	−1.042						34	
Fe I λ5074.75	4.22	−0.230			153		128		
Fe I λ5079.23	2.20	−2.067						21	
Fe I λ5090.78	4.26	−0.440			125	74	102		
Fe I λ5109.66	4.30	−0.980			86	50			
Fe I λ5121.65	4.28	−0.810			106				

Table A.2 – Continued

Line	χ	log(gf)	8	9	10	11	12	13	14
Fe I λ5125.13	4.22	−0.140						39	
Fe I λ5127.37	0.92	−3.306				131		19	
Fe I λ5139.47	2.94	−0.509	172					72	
Fe I λ5143.73	2.20	−3.690			42				
Fe I λ5145.10	2.20	−2.876		197	97	31			
Fe I λ5148.24	4.26	−0.274						27	
Fe I λ5159.06	4.28	−0.810			96	47			
Fe I λ5162.28	4.18	+0.020	75		168			44	
Fe I λ5164.55	4.44	−1.350				18			
Fe I λ5177.24	3.69	−2.380		72					
Fe I λ5184.27	4.29	−1.010				55			
Fe I λ5187.92	4.14	−1.371			73	36			
Fe I λ5191.47	3.04	−0.551						60	
Fe I λ5192.35	3.00	−0.421						63	
Fe I λ5194.95	1.56	−2.090						35	
Fe I λ5195.48	4.22	−0.002						35	
Fe I λ5198.72	2.22	−2.134				89		12	
Fe I λ5215.18	3.26	−0.871					169	32	
Fe I λ5216.28	1.61	−2.150						28	
Fe I λ5217.40	3.21	−1.162	56					22	
Fe I λ5223.19	3.64	−1.783					53		
Fe I λ5225.53	0.11	−4.790			169				
Fe I λ5228.38	4.22	−1.260		120		39	86		
Fe I λ5232.95	2.94	−0.057						110	
Fe I λ5242.50	3.63	−0.967						14	
Fe I λ5243.78	4.26	−1.120			82				
Fe I λ5250.22	0.12	−4.938			159				
Fe I λ5250.65	2.20	−2.180						21	
Fe I λ5253.47	3.28	−1.670				46	108		
Fe I λ5263.31	3.27	−0.969				104			
Fe I λ5273.17	3.29	−0.993	75					46	
Fe I λ5285.12	4.44	−1.620					43		
Fe I λ5288.53	3.69	−1.508							67

Table A.2 – Continued

Line	χ	log(gf)	8	9	10	11	12	13	14
Fe I λ5294.55	3.64	−2.810					44		
Fe I λ5295.32	4.41	−1.670			22		45		
Fe I λ5302.31	3.28	−0.720	84		187			31	
Fe I λ5307.37	1.61	−2.987	28						
Fe I λ5321.11	4.43	−1.090		120		27			
Fe I λ5322.05	2.28	−2.800		192					
Fe I λ5328.05	0.91	−1.465						138	
Fe I λ5328.54	1.56	−2.053						42	
Fe I λ5339.94	3.26	−0.720						50	
Fe I λ5364.88	4.45	+0.220					124	39	
Fe I λ5365.41	3.57	−1.020		193					
Fe I λ5367.48	4.41	+0.443						61	
Fe I λ5369.97	4.37	+0.536	111					74	
Fe I λ5373.71	4.47	−0.840		123	69	41	88		
Fe I λ5379.58	3.69	−1.514		134		30	88		
Fe I λ5383.38	4.31	+0.645						64	
Fe I λ5386.34	4.15	−1.740		78		10	43		
Fe I λ5398.29	4.44	−0.710		154		49			
Fe I λ5406.78	4.37	−1.720				15			
Fe I λ5410.92	4.47	+0.280						49	
Fe I λ5415.21	4.39	+0.642						63	
Fe I λ5417.03	4.41	−1.660					43		
Fe I λ5441.34	4.31	−1.730					50		
Fe I λ5445.05	4.39	−0.010	96					36	
Fe I λ5462.97	4.47	−0.156						29	
Fe I λ5463.29	4.43	+0.070						34	
Fe I λ5464.29	4.14	−1.400			73				
Fe I λ5473.91	4.15	−0.790			108			11	
Fe I λ5476.58	4.10	−0.453						38	
Fe I λ5493.51	4.10	−1.800							39
Fe I λ5501.48	0.96	−2.960	87						
Fe I λ5506.79	0.99	−2.797						44	
Fe I λ5522.45	4.21	−1.520			51		56		

Table A.2 – Continued

Line	χ	log(gf)	8	9	10	11	12	13	14
Fe I λ5525.56	4.23	−1.084					74		
Fe I λ5543.20	3.69	−1.570			85	42			
Fe I λ5553.59	4.44	−1.412				28			
Fe I λ5560.22	4.43	−1.160			58	31	56		
Fe I λ5567.40	2.61	−2.810			100	40			
Fe I λ5569.63	3.42	−0.540				151		39	
Fe I λ5572.85	3.40	−0.310				178		62	
Fe I λ5576.10	3.43	−0.940			157			29	
Fe I λ5584.77	3.57	−2.334				14			
Fe I λ5586.77	3.37	−0.210				198			
Fe I λ5618.64	4.21	−1.370				29			
Fe I λ5633.95	4.99	−0.320	21		64	45	83		
Fe I λ5638.27	4.22	−0.840		172					
Fe I λ5652.33	4.26	−1.950				11	45		
Fe I λ5653.89	4.39	−1.610					56		
Fe I λ5662.52	4.18	−0.573			132			20	
Fe I λ5679.03	4.65	−0.910				33			
Fe I λ5709.39	3.37	−1.240				139			
Fe I λ5731.77	4.26	−1.270			74	38			
Fe I λ5741.89	4.26	−1.670					58		
Fe I λ5753.13	4.26	−0.688		178					
Fe I λ5793.93	4.22	−1.660					54		29
Fe I λ5806.72	4.61	−1.030					69		
Fe I λ5809.22	3.88	−1.790			58		76		29
Fe I λ5814.81	4.28	−1.940			18				
Fe I λ5852.23	4.55	−1.340				16			
Fe I λ5856.10	4.30	−1.640				10			
Fe I λ5862.37	4.55	−0.058						21	
Fe I λ5927.80	4.65	−1.090				29			
Fe I λ5930.19	4.65	−0.230				69			
Fe I λ5934.66	3.93	−1.120			97				
Fe I λ5952.73	3.98	−1.390			86				
Fe I λ5956.71	0.86	−4.604			107				

Table A.2 – Continued

Line	χ	log(gf)	8	9	10	11	12	13	14
Fe I λ6003.02	3.88	−1.110			105				
Fe I λ6020.19	4.61	−0.270				95			
Fe I λ6027.06	4.07	−1.089			90	44	95	8	
Fe I λ6056.01	4.73	−0.460			84				
Fe I λ6078.50	4.79	−0.424						10	
Fe I λ6082.72	2.22	−3.573			65				
Fe I λ6096.67	3.98	−1.880					63		37
Fe I λ6136.62	2.45	−1.400	116			156		28	
Fe I λ6151.62	2.18	−3.299				31			
Fe I λ6157.73	4.07	−1.220		150	100				
Fe I λ6165.36	4.14	−1.474			55		78		
Fe I λ6173.34	2.22	−2.880			122				
Fe I λ6180.21	2.73	−2.780				29			
Fe I λ6187.99	3.94	−1.670		104	72		64		
Fe I λ6213.44	2.22	−2.650				75			
Fe I λ6219.29	2.20	−2.434				100		9	
Fe I λ6229.23	2.84	−2.810			65				
Fe I λ6240.65	2.22	−3.170		178					
Fe I λ6246.33	3.60	−0.877	80						
Fe I λ6252.56	2.40	−1.687				120			
Fe I λ6265.14	2.18	−2.550				73		8	
Fe I λ6297.80	2.22	−2.740				59			
Fe I λ6322.69	2.59	−2.426					125		
Fe I λ6336.84	3.69	−1.049				74			
Fe I λ6355.03	2.84	−2.291			132				
Fe I λ6380.75	4.19	−1.400				32			
Fe I λ6393.61	2.43	−1.610				143		20	
Fe I λ6411.66	3.65	−0.718	50				141	24	
Fe I λ6419.96	4.73	−0.250				53			
Fe I λ6421.36	2.28	−2.027				106			
Fe I λ6475.63	2.56	−2.940				27			
Fe I λ6533.94	4.56	−1.450				20			
Fe I λ6575.04	2.59	−2.820				27			

Table A.2 – Continued

Line	χ	log(gf)	8	9	10	11	12	13	14
Fe I λ6593.88	2.43	−2.422					152		
Fe I λ6609.12	2.56	−2.692				38	138		
Fe I λ6663.45	2.42	−2.478				87			
Fe I λ6703.58	2.76	−3.060		130			86		
Fe I λ6750.16	2.42	−2.620				53	140		
Fe I λ6752.72	4.64	−1.370				16			
Fe I λ6839.84	2.56	−3.350							61
Fe I λ6841.34	4.61	−0.750				40			
Fe I λ6843.65	4.55	−0.890			68				
Fe I λ6855.17	4.56	−0.740			97				
Fe I λ6999.89	4.11	−1.560				25			
Fe I λ7068.42	4.07	−1.330			88				
Fe I λ7418.67	4.14	−1.590				15			
Fe I λ7780.57	4.47	−0.091						28	
Fe I λ8804.63	2.28	−3.234				35			
Fe II λ4472.93	2.84	−3.360						77	
Fe II λ4491.41	2.85	−2.710	190	217					
Fe II λ4508.29	2.85	−2.440						182	
Fe II λ4576.34	2.84	−2.950							157
Fe II λ4582.83	2.84	−3.180							150
Fe II λ4620.52	2.83	−3.210		171		177			131
Fe II λ4635.31	5.95	−1.420						36	
Fe II λ4833.19	2.66	−4.783				54			
Fe II λ4893.82	2.83	−4.210		77		74			
Fe II λ4993.35	2.81	−3.620						86	
Fe II λ5000.73	2.78	−4.745				66			
Fe II λ5100.66	2.81	−4.170			60				
Fe II λ5132.67	2.81	−4.170	56			87			
Fe II λ5197.58	3.23	−2.220	208					170	
Fe II λ5234.62	3.21	−2.180							230
Fe II λ5264.81	3.33	−3.130			122			96	
Fe II λ5284.11	2.89	−3.110						120	

Table A.2 – Continued

Line	χ	log(gf)	8	9	10	11	12	13	14
Fe II λ5325.56	3.22	−3.160	130		106				
Fe II λ5414.07	3.22	−3.580			90		30	49	
Fe II λ5425.26	3.20	−3.220			110		48	74	
Fe II λ5534.85	3.24	−2.750			155			128	
Fe II λ5991.38	3.15	−3.740				115	46	56	
Fe II λ6084.10	3.20	−3.790			64				
Fe II λ6113.33	3.22	−4.140			50	61		26	
Fe II λ6149.25	3.89	−2.690	92		97	136	40	80	
Fe II λ6179.40	5.57	−2.810				15		11	
Fe II λ6239.95	3.89	−3.410						28	
Fe II λ6247.57	3.89	−2.300					53	128	
Fe II λ6248.91	5.51	−2.696						16	
Fe II λ6369.46	2.89	−4.110	68		71	76	24	26	
Fe II λ6383.72	5.55	−2.240	15					21	
Fe II λ6416.93	3.89	−2.460		152	87		40		
Fe II λ6456.39	3.90	−2.050						142	
Fe II λ6516.08	2.83	−3.440				180			
Co I λ4068.54	1.96	−1.170							136
Co I λ4749.66	3.05	−0.321							92
Co I λ4813.48	3.21	+0.050							92
Co I λ5230.20	1.74	−1.840					91		
Co I λ5331.45	1.79	−1.960					89		
Co I λ5342.71	4.02	+0.690							51
Co I λ5352.05	3.58	+0.060			31				
Co I λ5530.79	1.71	−2.060			31				
Co I λ5647.24	2.28	−1.560			16				41
Co I λ6117.00	1.78	−2.490							27
Ni I λ4027.67	3.90	−0.650		87					
Ni I λ4410.52	3.31	−1.080		117					93
Ni I λ4462.46	3.47	−0.600				59			
Ni I λ4605.00	3.48	−0.290		184					
Ni I λ4648.66	3.42	−0.150				77			

Table A.2 – Continued

Line	χ	log(gf)	8	9	10	11	12	13	14
Ni I λ4686.22	3.60	−0.640		147					
Ni I λ4701.36	3.48	−1.220	13						
Ni I λ4732.47	4.10	−0.550		94	40				
Ni I λ4752.43	3.66	−0.690		136					
Ni I λ4756.52	3.48	−0.340							143
Ni I λ4790.97	1.95	−3.400							30
Ni I λ4806.99	3.68	−0.640				33			
Ni I λ4829.03	3.54	−0.330			110	65			
Ni I λ4831.18	3.61	−0.410			110				
Ni I λ4852.56	3.54	−1.070		108	49		79		
Ni I λ4912.02	3.77	−0.788				37			
Ni I λ4913.98	3.74	−0.620		116					
Ni I λ4918.37	3.84	−0.230			93				
Ni I λ4953.21	3.74	−0.660					101		
Ni I λ4980.18	3.61	−0.110				81			
Ni I λ4984.12	3.80	+0.226						19	
Ni I λ4998.23	3.61	−0.780		132	64				
Ni I λ5000.35	3.63	−0.430		169	113	73			
Ni I λ5010.94	3.63	−0.870		114	72				
Ni I λ5017.58	3.54	−0.080	73			82			
Ni I λ5035.37	3.63	+0.290			145	94		37	
Ni I λ5042.19	3.66	−0.570			94				
Ni I λ5048.85	3.85	−0.370				51			
Ni I λ5080.54	3.65	+0.130						30	
Ni I λ5082.35	3.66	−0.540			73	35			
Ni I λ5084.10	3.68	+0.030		185				17	
Ni I λ5099.94	3.68	−0.100		185				16	
Ni I λ5102.97	1.68	−2.620			85		136		
Ni I λ5115.40	3.83	−0.110			103				
Ni I λ5155.77	3.90	−0.090	34			56			
Ni I λ5388.35	1.93	−3.550		56					21
Ni I λ5424.65	1.95	−2.770							112
Ni I λ5435.87	1.99	−2.600			88				109

Table A.2 – Continued

Line	χ	log(gf)	8	9	10	11	12	13	14
Ni I λ5476.92	1.83	−0.890						55	
Ni I λ5578.73	1.68	−2.640				29	128		
Ni I λ5589.36	3.90	−1.140					47		
Ni I λ5593.75	3.90	−0.840							39
Ni I λ5748.36	1.68	−3.260							92
Ni I λ5754.67	1.93	−2.340	13			47			158
Ni I λ5996.74	4.23	−1.060				10	52		
Ni I λ6007.32	1.68	−3.340					98		
Ni I λ6108.12	1.68	−2.440		186	111		148		
Ni I λ6111.08	4.09	−0.870				15			
Ni I λ6128.98	1.68	−3.320		82			109		
Ni I λ6175.37	4.09	−0.540		121			67		
Ni I λ6176.80	4.09	−0.530					71		
Ni I λ6327.60	1.68	−3.150			79				136
Ni I λ6586.30	1.95	−2.809					121		
Ni I λ6643.64	1.68	−2.300			143	72			
Ni I λ6772.32	3.66	−0.990		134		28			
Ni I λ7422.29	3.63	−0.130						19	
Ni I λ7525.12	3.63	−0.690	20						
Ni I λ7788.93	1.95	−2.420			134				
Ni I λ7797.59	3.90	−0.262					106		
Zn I λ4722.16	4.03	−0.390	45	180	123		50	12	
Zn I λ4810.54	4.08	−0.170	60	201	136	89	49	28	
Zn I λ6362.35	5.79	+0.272			40				
Sr I λ4607.34	0.00	+0.300			139	42			
Sr I λ4962.27	1.85	+0.190				41			
Y II λ4235.73	0.13	−1.502				141			
Y II λ4358.73	0.10	−1.324				134			
Y II λ4398.01	0.13	−0.998				175		44	
Y II λ4823.31	0.99	−1.115				213			
Y II λ4883.69	1.08	−0.041	136		171	203	132		
Y II λ4900.12	1.03	−0.090	126						

Table A.2 – Continued

Line	χ	log(gf)	8	9	10	11	12	13	14
Y II λ4982.14	1.03	−1.292				70			
Y II λ5087.43	1.08	−0.170		173		132		61	
Y II λ5119.12	0.99	−1.363			73	42			
Y II λ5123.22	0.99	−0.824				163		26	
Y II λ5200.41	0.99	−0.570		135	148	113			
Y II λ5205.73	1.03	−0.342						71	
Y II λ5289.82	1.04	−1.853				24	29		
Y II λ5402.78	1.84	−0.630			69	57	44		36
Y II λ5473.39	1.74	−1.018				52			
Y II λ5509.91	0.99	−1.015			112	82		14	
Y II λ5546.03	1.75	−1.100				51			
Y II λ6795.41	1.74	−1.190					30		
Y II λ7264.20	1.84	−1.502				29			
Zr I λ5385.15	0.52	−0.710					57		
Zr I λ5955.35	0.00	−2.330							120
Zr I λ6127.48	0.15	−1.060					91		
Zr I λ6134.57	0.00	−1.280					100		
Zr I λ6143.18	0.07	−1.100					99		
Zr II λ4034.09	0.80	−1.550				54			
Zr II λ4050.33	0.71	−1.060	44			72			
Zr II λ4071.09	1.00	−1.600				40			
Zr II λ4161.21	0.71	−0.590		140					
Zr II λ4312.22	1.76	−1.200			18				
Zr II λ4317.32	0.71	−1.379				55			
Zr II λ4496.97	0.71	−0.890				197			
Zr II λ5112.28	1.66	−0.850	21		52	44			
Mo I λ5533.04	1.33	−0.069							87
Mo I λ5570.40	1.33	−0.340					56		
Mo I λ6030.64	1.53	−0.523					40		
Ba II λ5853.69	0.60	−0.910					158	62	
Ba II λ6496.91	0.60	−0.369						108	
La II λ4086.71	0.00	−0.070				177			

Table A.2 – Continued

Line	χ	log(gf)	8	9	10	11	12	13	14
La II λ4322.51	0.17	−0.462				60			92
La II λ4333.76	0.17	+0.173	37			161			
La II λ4619.90	1.75	+0.145				13			
La II λ4748.74	0.93	−0.540				28			32
La II λ4804.04	0.23	−1.490			42		36		
La II λ5123.01	0.32	−0.850				83			
La II λ6390.49	0.32	−1.470			56		58		50
La II λ6774.33	0.13	−1.750				24	49		
Ce II λ3993.83	0.91	+0.290				62			
Ce II λ3999.24	0.30	+0.060				115			
Ce II λ4042.59	0.50	+0.007				60			
Ce II λ4073.49	0.48	+0.210				101			
Ce II λ4083.23	0.70	+0.270				77			
Ce II λ4120.84	0.32	−0.370		89	83				
Ce II λ4127.38	0.68	+0.312				131			
Ce II λ4361.67	0.53	−0.397			64	137			
Ce II λ4364.66	0.50	−0.170	7			53			61
Ce II λ4382.17	0.68	+0.130				49			
Ce II λ4418.78	0.86	+0.270		96		60			
Ce II λ4449.34	0.61	+0.040				46			
Ce II λ4486.91	0.30	−0.180		109	114	73			
Ce II λ4523.08	0.52	−0.080				78			
Ce II λ4560.28	0.91	+0.180				48			
Ce II λ4560.97	0.68	−0.260			72				
Ce II λ4562.37	0.48	+0.210				77			
Ce II λ4628.16	0.52	+0.140			119	84			
Ce II λ4773.96	0.92	+0.285			89	22			
Ce II λ5187.46	1.21	+0.170			50	36			
Ce II λ5274.24	1.04	+0.130				41			
Ce II λ5472.30	1.25	−0.177				12	34		
Ce II λ5512.06	1.01	+0.293				24			
Ce II λ6043.40	1.21	−0.480			20	10	21		

Table A.2 – Continued

Line	χ	log(gf)	8	9	10	11	12	13	14
Pr II λ4510.18	0.42	−0.007			49				
Pr II λ5219.03	0.79	−0.053				8			
Pr II λ5259.73	0.63	+0.114			39	31			
Pr II λ5322.82	0.48	−0.123			33	24	35		21
Nd II λ3851.76	0.18	−0.490			81				
Nd II λ3973.28	0.63	+0.360			113				
Nd II λ4133.36	0.32	−0.490			74				
Nd II λ4358.17	0.32	−0.160				66			
Nd II λ4446.40	0.20	−0.350							62
Nd II λ4811.35	0.06	−0.890			79	33			
Nd II λ4989.95	0.63	−0.500					59		
Nd II λ5092.80	0.38	−0.610				37	68		
Nd II λ5212.35	0.20	−0.960			63				
Nd II λ5249.58	0.98	+0.200			98				
Nd II λ5293.17	0.82	+0.100	17		104	58			
Nd II λ5306.46	0.86	−0.970					30		
Nd II λ5311.48	0.99	−0.420				22			
Nd II λ5319.82	0.55	−0.140			103				83
Nd II λ5431.54	1.12	−0.470			25				
Nd II λ5485.71	1.26	−0.120			45		33		
Nd II λ5740.86	1.16	−0.530					27		
Nd II λ5842.35	1.28	−0.600					19		
Sm II λ4329.04	0.18	−0.510				42			
Sm II λ4467.34	0.66	+0.150			89				99
Sm II λ4523.92	0.43	−0.390				30			75
Sm II λ4537.97	0.48	−0.480			49				36
Sm II λ4566.18	0.33	−0.590					61		
Sm II λ4577.69	0.25	−0.650			72		69		43
Sm II λ4642.24	0.38	−0.460			68	29			72
Sm II λ4719.86	0.04	−1.240		32			36		
Sm II λ4815.82	0.18	−0.820			75				
Sm II λ4913.27	0.66	−0.930		10					

Table A.2 – Continued

Line	χ	log(gf)	8	9	10	11	12	13	14
Eu II λ3971.99	0.21	+0.270				101			
Eu II λ6645.13	1.38	+0.120			46	52	37		53
Dy II λ3983.67	0.54	−0.310				28			
Dy II λ4073.12	0.54	−0.320				28			

Table A.3: Line identification for the stars: 15 = IRAS 08187-1905, 16 = HD 107369, 17 = IRAS 12538-2611, 18 = IRAS 17279-1119, 19 = IRAS 22223+4327, 20 = BD+39^o 4926

Line	χ	log(gf)	15	16	17	18	19	20
C I λ4228.33	7.69	−2.360						21
C I λ4269.03	7.68	−2.359				26		
C I λ4766.67	7.49	−2.617						17
C I λ4770.00	7.49	−2.437	97			39	100	20
C I λ4775.88	7.49	−2.304				55	118	36
C I λ5023.83	7.94	−2.210	42				67	17
C I λ5039.06	7.95	−1.791				91		26
C I λ5052.17	7.68	−1.240			24			88
C I λ5380.32	7.68	−1.615	166					55
C I λ5551.58	8.64	−1.900					32	
C I λ6001.12	8.64	−2.061					37	
C I λ6007.18	8.64	−2.062					30	
C I λ6010.65	8.64	−1.938				16	50	
C I λ6012.23	8.64	−2.004					52	
C I λ6013.20	8.65	−1.314				36		28
C I λ6014.83	8.64	−1.585					70	14
C I λ6016.44	8.64	−1.834					77	
C I λ6397.96	8.77	−1.778					26	
C I λ6587.62	8.53	−1.003	93		9		137	56
C I λ6655.52	8.54	−1.941					47	
C I λ6828.11	8.54	−1.461					116	
C I λ7108.94	8.64	−1.594	62			50		
C I λ7111.48	8.64	−1.085	95			60		59
C I λ7113.17	8.65	−0.773	94			94	137	72
C I λ7115.17	8.64	−0.900	97			69	140	71
C I λ7116.96	8.64	−0.907	146			85	141	68
C I λ7119.66	8.65	−1.148						40
C I λ7476.18	8.77	−1.574					66	
C I λ7483.44	8.77	−1.372						29

Table A.3 – Continued

Line	χ	log(gf)	15	16	17	18	19	20
C I λ7848.24	8.85	−1.731					49	
C I λ7852.86	8.85	−1.682					50	
C I λ9111.85	7.49	−0.297			160			
N I λ7423.63	10.33	−0.706		20				64
N I λ7442.29	10.33	−0.401	30	23		50	50	98
N I λ7468.27	10.33	−0.183	25	26		61	66	124
N I λ8184.87	10.33	−0.286				37		98
N I λ8187.95	10.32	−0.292		41				90
N I λ8210.72	10.33	−0.708						66
N I λ8216.34	10.34	+0.132						169
N I λ8223.10	10.33	−0.275	65					124
N I λ8567.74	10.68	−0.664						64
N I λ8629.24	10.69	+0.075	37	39		77		
O I λ4368.16	9.52	−1.709		13				63
O I λ5329.10	10.74	−1.330						27
O I λ5329.69	10.74	−1.110						35
O I λ5330.74	10.74	−0.970						53
O I λ5436.86	10.74	−1.399						26
O I λ6155.99	10.74	−0.660		9				56
O I λ6156.80	10.74	−0.440	15	19			49	78
O I λ6158.19	10.74	−0.290		25		38	65	88
O I λ6300.30	0.00	−9.752	42		96			
O I λ6363.77	0.02	−10.250	13		41			
O I λ6453.64	10.74	−1.353						14
O I λ6454.44	10.74	−1.138						34
Na I λ5682.65	2.10	−0.706	110				85	
Na I λ5688.22	2.10	−0.400			123			8
Na I λ6154.23	2.10	−1.547	19		16			
Na I λ6160.75	2.10	−1.246	30		30		41	
Na I λ8194.84	2.10	+0.530						64
Mg I λ4167.28	4.35	−0.745				160	199	
Mg I λ4571.10	0.00	−5.623					109	

Table A.3 – Continued

Line	χ	log(gf)	15	16	17	18	19	20
Mg I λ4703.00	4.34	−0.440	192			172		
Mg I λ5167.32	2.71	−0.856						22
Mg I λ5172.68	2.71	−0.381						56
Mg I λ5183.62	2.72	−0.158		141				69
Mg I λ5528.42	4.34	−0.340	205	54		157		
Mg I λ5711.10	4.34	−1.724	46		94			
Mg I λ8806.78	4.35	−0.137						28
Mg II λ4427.99	9.99	−1.208		6				
Mg II λ7877.13	10.00	+0.391		45				25
Al I λ3961.52	0.01	−0.340						9
Al I λ6696.03	3.14	−1.320			5		38	
Al I λ6698.67	3.14	−1.620			3		21	
Si I λ5645.62	4.93	−1.630			27			
Si I λ5665.56	4.92	−2.040	26		22			
Si I λ5701.11	4.93	−2.050	26					
Si I λ5708.40	4.95	−1.470			84	25		
Si I λ5772.15	5.08	−1.740					54	
Si I λ5793.08	4.93	−1.490					88	
Si I λ6125.03	5.61	−1.513			11	12		
Si I λ6145.02	5.61	−1.479				18		
Si I λ6237.33	5.61	−1.138	46					
Si I λ6244.48	5.61	−1.363					35	
Si I λ6721.85	5.86	−0.940			21	10		
Si I λ7849.98	6.19	−0.652			21		53	
Si II λ3853.66	6.86	−1.341						17
Si II λ3856.02	6.86	−0.406						67
Si II λ3862.59	6.86	−0.757						47
Si II λ4130.89	9.84	+0.463						25
Si II λ5041.02	10.07	+0.029		31				
Si II λ5055.98	10.07	+0.523		29				
Si II λ6347.10	8.12	+0.149		93		190		63
Si II λ6371.35	8.12	−0.082		68		153	195	44

Table A.3 – Continued

Line	χ	log(gf)	15	16	17	18	19	20
S I λ4694.12	6.52	−1.820			14		66	
S I λ4695.45	6.52	−1.960		4	10			
S I λ5278.96	6.86	−2.100					32	
S I λ6041.94	7.87	−1.000				24	49	
S I λ6052.67	7.87	−0.630	55			30		9
S I λ6743.53	7.87	−1.020				23	53	9
S I λ6748.84	7.87	−0.530				31	76	18
S I λ6757.17	7.87	−0.310	91	4		38		22
S I λ8880.69	8.42	−0.950	11					
S I λ8882.47	8.42	−0.800	25					
Ca I λ4526.93	2.71	−0.548				14		
Ca I λ5265.56	2.52	−0.260					124	
Ca I λ5349.47	2.71	−0.310					92	
Ca I λ5512.99	2.93	−0.300					85	
Ca I λ5581.98	2.52	−0.710			45			
Ca I λ5588.76	2.52	+0.210	147	12	147		172	
Ca I λ5590.13	2.52	−0.710	34					
Ca I λ5594.47	2.52	−0.050			108	78		
Ca I λ5598.49	2.52	−0.220			117	65		
Ca I λ5601.29	2.52	−0.690			43	31	87	
Ca I λ5857.46	2.93	+0.230			94			
Ca I λ6122.23	1.89	−0.315	162	14		69	169	
Ca I λ6161.30	2.52	−1.030					55	
Ca I λ6162.17	1.90	−0.089		16		95		
Ca I λ6169.56	2.52	−0.478			42			
Ca I λ6439.08	2.52	+0.470	172					
Ca I λ6449.82	2.52	−0.550	57					
Ca I λ6471.67	2.52	−0.590	47		41			
Ca I λ6493.79	2.52	+0.140	107		133			
Ca I λ6499.65	2.52	−0.590	47					
Ca I λ6717.79	2.71	−0.524			62	27	86	
Ca II λ5001.47	7.50	−0.520		7				

Table A.3 – Continued

Line	χ	log(gf)	15	16	17	18	19	20
Ca II λ5021.15	7.51	−1.230					34	
Ca II λ5339.22	8.44	−0.050					57	
Sc II λ4246.84	0.31	+0.020						15
Sc II λ4294.78	0.61	−1.634	148					
Sc II λ4320.75	0.61	−0.100						6
Sc II λ4415.56	0.60	−0.890				207		
Sc II λ4431.36	0.61	−2.191	68					
Sc II λ5031.02	1.36	−0.400		47				
Sc II λ5239.82	1.45	−0.942		18				
Sc II λ5526.82	1.77	−0.219	155	30	184	160		
Sc II λ5640.99	1.50	−1.353	80	6	94			
Sc II λ5657.90	1.51	−0.825		20				
Sc II λ5658.35	1.50	−1.384	100					
Sc II λ5667.15	1.50	−1.485			73	51	71	
Sc II λ5669.04	1.50	−1.200	119		71	81		
Sc II λ6245.62	1.51	−0.935			80			
Sc II λ6604.60	1.36	−1.531			34		92	
Ti I λ5210.39	0.05	−0.883			153			
Ti II λ3900.55	1.13	−0.440						32
Ti II λ3913.46	1.12	−0.530						32
Ti II λ4184.31	1.08	−2.510					183	
Ti II λ4312.88	1.18	−1.160						6
Ti II λ4394.07	1.22	−1.590	186					
Ti II λ4395.04	1.08	−0.660						29
Ti II λ4417.72	1.17	−1.430						6
Ti II λ4418.34	1.24	−1.820				175		
Ti II λ4421.95	2.06	−1.770		17		149		
Ti II λ4443.81	1.08	−0.710						16
Ti II λ4468.50	1.13	−0.620						21
Ti II λ4493.53	1.08	−2.740		11	149		149	
Ti II λ4501.27	1.12	−0.750						33
Ti II λ4524.69	1.23	−2.940				89		

Table A.3 – Continued

Line	χ	log(gf)	15	16	17	18	19	20
Ti II λ4533.97	1.24	−0.770						22
Ti II λ4563.76	1.22	−0.960						16
Ti II λ4568.33	1.22	−2.650			121	88		
Ti II λ4589.96	1.24	−1.780		52				
Ti II λ4636.32	1.16	−3.230				63	96	
Ti II λ4708.67	1.24	−2.210	125	25	185	124	194	
Ti II λ4779.98	2.05	−1.370		45				
Ti II λ4798.54	1.08	−2.430					191	
Ti II λ4805.09	2.06	−1.120		60				
Ti II λ4865.62	1.12	−2.610					181	
Ti II λ4911.19	3.12	−0.330		41				
Ti II λ5129.15	1.89	−1.400		46	221			
Ti II λ5154.06	1.57	−1.920		39				
Ti II λ5185.90	1.89	−1.350		39				
Ti II λ5188.68	1.58	−1.220		75				
Ti II λ5226.54	1.56	−1.290		69				
Ti II λ5336.79	1.58	−1.700		35				
Ti II λ5381.02	1.57	−2.080		26				
Cr I λ4651.29	0.98	−1.460			55			
Cr I λ5206.04	0.94	+0.020		17				
Cr I λ5208.40	0.94	+0.170		26				
Cr I λ5247.58	0.96	−1.640	52					
Cr I λ5296.69	0.98	−1.400	74		68			
Cr I λ5409.80	1.03	−0.720	114					
Cr II λ4555.02	4.07	−1.250				121		
Cr II λ4558.65	4.08	−0.660						29
Cr II λ4588.20	4.07	−0.640			143			22
Cr II λ4592.06	4.07	−1.220				122		
Cr II λ4616.63	4.07	−1.290		25			180	6
Cr II λ4634.10	4.07	−1.240						8
Cr II λ4812.35	3.86	−1.800	117					
Cr II λ4824.13	3.87	−1.230						18

Table A.3 – Continued

Line	χ	log(gf)	15	16	17	18	19	20
Cr II λ4848.25	3.86	−1.130	168	43	115			
Cr II λ4876.40	3.85	−1.470	169	27				
Cr II λ4884.60	3.86	−2.080		9				
Cr II λ5210.85	3.76	−2.788				61	61	
Cr II λ5237.32	4.07	−1.160			82			
Cr II λ5246.78	3.71	−2.460		7			88	
Cr II λ5305.87	3.83	−2.080					108	
Cr II λ5308.43	4.07	−1.810	91	9			98	
Cr II λ5310.70	4.07	−2.270	69		11			
Cr II λ5313.56	4.07	−1.650		13				
Cr II λ5407.62	3.83	−2.580	69					
Cr II λ5502.09	4.17	−1.990					121	
Cr II λ5508.63	4.15	−2.120	69					
Cr II λ6053.48	4.74	−2.150				10	31	
Mn I λ4451.58	2.89	+0.278				45		
Mn I λ4754.04	2.28	−0.085			97	27	101	
Mn I λ4765.86	2.94	−0.080					49	
Mn I λ4783.42	2.30	+0.042			121			
Mn II λ4755.73	5.40	−1.242		13				
Fe I λ3820.43	0.86	+0.119						58
Fe I λ3825.88	0.92	−0.037						37
Fe I λ3930.30	0.09	−1.590						11
Fe I λ4045.82	1.49	+0.280						27
Fe I λ4071.74	1.61	−0.022						18
Fe I λ4073.77	3.26	−0.902				51		
Fe I λ4114.45	2.83	−1.303	72					
Fe I λ4122.52	2.84	−1.386				35		
Fe I λ4225.46	3.42	−0.510				105		
Fe I λ4271.76	1.49	−0.163						13
Fe I λ4307.90	1.56	−0.070						27
Fe I λ4352.74	2.22	−1.287	157					
Fe I λ4383.55	1.49	+0.200						26

Table A.3 – Continued

Line	χ	log(gf)	15	16	17	18	19	20
Fe I λ4387.90	3.07	−1.523	50					
Fe I λ4404.76	1.56	−0.142						19
Fe I λ4408.43	2.20	−1.780				56		
Fe I λ4602.95	1.48	−2.220	153			57		
Fe I λ4625.05	3.24	−1.348				39		
Fe I λ4637.51	3.28	−1.340	65					
Fe I λ4643.47	3.65	−1.147					59	
Fe I λ4647.43	2.95	−1.351			132			
Fe I λ4678.85	3.60	−0.833					108	
Fe I λ4700.16	3.69	−1.680					25	
Fe I λ4707.28	3.24	−1.080					104	
Fe I λ4736.78	3.21	−0.752	125	12	180			
Fe I λ4800.65	4.14	−1.029					36	
Fe I λ4839.55	3.27	−1.822				14		
Fe I λ4872.14	2.88	−0.567			211			
Fe I λ4878.21	2.88	−1.010		9				
Fe I λ4920.50	2.83	+0.068		45				
Fe I λ4966.09	3.33	−0.871			164			
Fe I λ4983.86	4.10	−0.068				122		
Fe I λ4994.14	0.91	−3.079					121	
Fe I λ5002.80	3.40	−1.530				15	58	
Fe I λ5006.12	2.83	−0.615		18				
Fe I λ5014.95	3.94	−0.303	127					
Fe I λ5028.13	3.57	−1.123	48					
Fe I λ5048.44	3.96	−1.030					56	
Fe I λ5049.82	2.28	−1.355			208			
Fe I λ5051.64	0.91	−2.794				76		
Fe I λ5067.15	4.22	−0.970					48	
Fe I λ5068.77	2.94	−1.230					132	
Fe I λ5074.75	4.22	−0.230	96		109		115	
Fe I λ5083.35	0.96	−2.958	101					
Fe I λ5090.78	4.26	−0.440	73		58			
Fe I λ5121.67	4.28	−0.810			41			

Table A.3 – Continued

Line	χ	log(gf)	15	16	17	18	19	20
Fe I λ5126.19	4.26	−1.060			35			
Fe I λ5131.47	2.22	−2.520			108			
Fe I λ5133.69	4.18	+0.140			156			
Fe I λ5139.46	2.94	−0.509		28				
Fe I λ5141.75	2.42	−2.240	51		92		67	
Fe I λ5162.27	4.18	+0.020			142			
Fe I λ5171.60	1.48	−1.793		11				
Fe I λ5191.47	3.04	−0.551		18				
Fe I λ5192.35	3.00	−0.421		20				
Fe I λ5198.71	2.22	−2.135			144			
Fe I λ5215.19	3.26	−0.871	95					
Fe I λ5216.28	1.61	−2.150					141	
Fe I λ5217.40	3.21	−1.162	96					
Fe I λ5250.65	2.20	−2.180	106					
Fe I λ5253.47	3.28	−1.573			59			
Fe I λ5263.31	3.26	−0.879	105		134			
Fe I λ5266.56	2.99	−0.385		32				
Fe I λ5302.31	3.28	−0.720	154					
Fe I λ5324.18	3.21	−0.103		30				
Fe I λ5328.04	0.91	−1.466		47				
Fe I λ5364.88	4.44	+0.228	118		159			
Fe I λ5367.48	4.41	+0.443	139		157			
Fe I λ5369.97	4.37	+0.536	133	13				
Fe I λ5371.49	0.96	−1.645		32				
Fe I λ5383.38	4.31	+0.645	162	19	174			
Fe I λ5389.49	4.42	−0.400			61			
Fe I λ5393.18	3.24	−0.715	146					
Fe I λ5398.29	4.44	−0.710					51	
Fe I λ5404.11	4.31	+0.523		24				
Fe I λ5405.77	0.99	−1.844		27				
Fe I λ5410.92	4.47	+0.398		10	146			
Fe I λ5415.20	4.39	+0.510			189			
Fe I λ5434.53	1.01	−2.121					199	

Table A.3 – Continued

Line	χ	log(gf)	15	16	17	18	19	20
Fe I λ5445.04	4.39	−0.010			94			
Fe I λ5462.97	4.47	−0.156				49		
Fe I λ5473.91	4.15	−0.790	58					
Fe I λ5487.76	4.14	−0.710			53			
Fe I λ5497.53	1.01	−2.840				89		
Fe I λ5506.79	0.99	−2.797	126					
Fe I λ5543.20	3.69	−1.570					36	
Fe I λ5543.94	4.22	−1.110	34					
Fe I λ5560.22	4.43	−1.160	17					
Fe I λ5567.44	2.61	−2.810			31			
Fe I λ5569.62	3.42	−0.540				62		
Fe I λ5572.85	3.40	−0.275	160		215	80		
Fe I λ5576.09	3.43	−0.940			144	44	102	
Fe I λ5615.64	3.33	+0.050		28				
Fe I λ5633.95	4.99	−0.320					35	
Fe I λ5638.27	4.22	−0.870			37			
Fe I λ5658.82	3.40	−0.836			151			
Fe I λ5706.01	4.61	−0.530				22		
Fe I λ5709.39	3.37	−1.028	86				101	
Fe I λ5717.85	4.28	−1.100			29			
Fe I λ5731.77	4.26	−1.270	21					
Fe I λ5763.00	4.21	−0.470	50					
Fe I λ5809.25	3.88	−1.790			16			
Fe I λ6003.02	3.88	−1.120			65			
Fe I λ6020.19	4.61	−0.270			55			
Fe I λ6024.07	4.55	−0.060				30		
Fe I λ6065.48	2.61	−1.530			155			
Fe I λ6078.50	4.79	−0.424				27		
Fe I λ6102.18	4.83	−0.627				20		
Fe I λ6136.61	2.45	−1.400			219			
Fe I λ6137.70	2.59	−1.403	127		166			
Fe I λ6151.62	2.18	−3.299			34			
Fe I λ6170.49	4.79	−0.430			34			

Table A.3 – Continued

Line	χ	log(gf)	15	16	17	18	19	20
Fe I λ6173.34	2.22	−2.880			58			
Fe I λ6180.22	2.73	−2.650			24			
Fe I λ6213.43	2.22	−2.480			92			
Fe I λ6219.28	2.20	−2.433			119			
Fe I λ6229.24	2.85	−2.810			23			
Fe I λ6240.66	2.22	−3.170			35			
Fe I λ6252.55	2.40	−1.687			159			
Fe I λ6265.13	2.18	−2.550			103			
Fe I λ6301.51	3.65	−0.718				39		
Fe I λ6322.69	2.59	−2.430			65			
Fe I λ6335.34	2.20	−2.177			133			
Fe I λ6336.84	3.69	−0.856			81			
Fe I λ6344.15	2.43	−2.922			34			
Fe I λ6380.76	4.19	−1.376			11			
Fe I λ6400.00	3.60	−0.290		9				
Fe I λ6411.66	3.65	−0.718	68					
Fe I λ6419.96	4.73	−0.270	59		45		63	
Fe I λ6421.35	2.28	−2.027			147			
Fe I λ6569.23	4.73	−0.450			52			
Fe I λ6593.88	2.43	−2.420			83			
Fe I λ6663.45	2.42	−2.478			98			
Fe I λ6703.57	2.76	−3.060			12			
Fe I λ6750.15	2.42	−2.620			69			
Fe I λ6752.72	4.64	−1.204			11			
Fe I λ7807.92	4.99	−0.644				15		
Fe II λ4178.86	2.58	−2.510						20
Fe II λ4233.17	2.58	−1.970						84
Fe II λ4296.56	2.71	−2.920						17
Fe II λ4385.38	2.78	−2.660						22
Fe II λ4416.83	2.78	−2.650						26
Fe II λ4489.18	2.83	−2.960		45				10
Fe II λ4491.40	2.86	−2.710						12

Table A.3 – Continued

Line	χ	log(gf)	15	16	17	18	19	20
Fe II λ4508.29	2.86	−2.440		73				37
Fe II λ4515.34	2.85	−2.600		72				25
Fe II λ4520.22	2.81	−2.650		56				22
Fe II λ4522.63	2.85	−2.250		91				42
Fe II λ4555.89	2.83	−2.400						26
Fe II λ4576.34	2.84	−2.953				177		
Fe II λ4583.84	2.81	−1.930						74
Fe II λ4620.52	2.83	−3.210	185			145	211	
Fe II λ4629.34	2.81	−2.340		79				
Fe II λ4635.32	5.96	−1.420		15		57	108	
Fe II λ4666.76	2.83	−3.280		39				
Fe II λ4731.45	2.89	−3.100		41				
Fe II λ4893.82	2.83	−4.210					101	
Fe II λ4993.35	2.81	−3.620					171	
Fe II λ5018.44	2.89	−1.100						120
Fe II λ5100.66	2.81	−4.170			67		97	
Fe II λ5132.67	2.81	−4.080		11				
Fe II λ5146.12	2.83	−3.910		9				
Fe II λ5197.58	3.23	−2.220		73	216			21
Fe II λ5234.62	3.22	−2.180		79	226			26
Fe II λ5264.81	3.23	−3.130			138			
Fe II λ5272.40	5.95	−2.010	44					
Fe II λ5276.00	3.20	−2.010		90				31
Fe II λ5284.11	2.89	−3.110		42	156			6
Fe II λ5316.61	3.15	−1.870						60
Fe II λ5325.56	3.22	−3.220	133	25		120	184	
Fe II λ5337.71	3.23	−3.720		11				
Fe II λ5362.86	3.20	−2.570		52				
Fe II λ5414.07	3.22	−3.580		14	73	82	128	
Fe II λ5425.26	2.89	−3.110			117		167	
Fe II λ5534.85	3.25	−2.750						6
Fe II λ5813.67	5.57	−2.823	12				41	
Fe II λ6149.25	3.89	−2.690	164	23	83	82	152	6

Table A.3 – Continued

Line	χ	log(gf)	15	16	17	18	19	20
Fe II λ6179.40	5.57	−2.620				13	28	
Fe II λ6238.40	3.89	−2.600			103			
Fe II λ6239.95	3.89	−3.700	53					
Fe II λ6247.56	3.89	−2.300		38	122		223	
Fe II λ6248.91	5.51	−2.670					41	
Fe II λ6369.46	2.89	−4.110	86		56	55		
Fe II λ6383.72	5.55	−2.240	44	8		26	53	
Fe II λ6385.46	5.55	−2.590	26			10		
Fe II λ6416.92	3.89	−2.640		27	77			
Fe II λ6442.95	5.55	−2.440					49	
Fe II λ6456.39	3.90	−2.050		49		152		
Fe II λ6516.08	2.89	−3.610	135					
Fe II λ7449.34	3.89	−3.270		7		37	87	
Fe II λ7462.38	3.89	−2.740		29				
Fe II λ7515.84	3.90	−3.432	56					
Ni I λ4331.65	1.68	−2.100	54					
Ni I λ4686.22	3.60	−0.640					54	
Ni I λ4714.42	3.30	+0.230				45		
Ni I λ4756.52	3.48	−0.340			74		80	
Ni I λ4831.18	3.61	−0.410	45				52	
Ni I λ5017.57	3.54	−0.080		7				
Ni I λ5035.37	3.63	+0.290	86			89		
Ni I λ5080.54	3.65	+0.130	86					
Ni I λ5084.10	3.68	+0.030	70					
Ni I λ5099.94	3.68	−0.100			53		95	
Ni I λ5115.40	3.83	−0.110					92	
Ni I λ5155.77	3.90	−0.090			50			
Ni I λ5476.90	1.83	−0.890		17				
Ni I λ5754.67	1.93	−2.340			72		28	
Ni I λ6108.13	1.68	−2.440			43			
Ni I λ6176.81	4.09	−0.530			27		34	
Ni I λ6643.64	1.68	−2.300			103			

Table A.3 – Continued

Line	χ	log(gf)	15	16	17	18	19	20
Ni I λ6767.78	1.83	−2.170	32				37	
Ni I λ6772.32	3.66	−0.990			24		23	
Ni I λ7122.21	3.54	+0.050	98					
Ni I λ7422.29	3.63	−0.140					76	
Ni I λ7522.78	3.66	−0.330			48			
Ni I λ7525.12	3.63	−0.690			51		46	
Ni I λ7797.59	3.89	−0.230			60			
Zn I λ4680.13	4.01	−0.860				15		
Zn I λ4722.15	4.03	−0.390	87		119		117	4
Zn I λ4810.53	4.08	−0.170	74	10	130	70		5
Zn I λ6362.35	5.79	+0.272	16				41	
Sr I λ4607.33	0.00	+0.300				6	107	
Sr II λ4215.54	0.00	−0.560		65				
Y II λ4883.69	1.08	+0.070		11	163			
Y II λ5087.43	1.08	−0.170		6				
Y II λ5289.82	1.03	−1.850	33			14	162	
Y II λ5402.78	1.84	−0.630	125		28	105		
Y II λ5473.39	1.74	−1.018				60		
Y II λ5546.03	1.75	−1.100	53					
Y II λ5610.36	1.03	−2.910					73	
Y II λ6613.73	1.75	−1.110				47		
Y II λ6795.43	1.74	−1.190	57					
Y II λ6832.48	1.75	−1.940					88	
Y II λ7450.33	1.75	−1.590				13		
Zr II λ4208.98	0.71	−0.510	175					
Zr II λ4308.91	1.49	−0.800					199	
Zr II λ4312.22	1.76	−1.200					100	
Zr II λ4414.54	1.24	−1.200				60		
Zr II λ4445.90	1.67	−1.350					115	
Zr II λ5112.28	1.66	−0.850	58					
Zr II λ5418.02	1.76	−1.600					63	
Zr II λ6106.44	1.76	−1.500				14		

Table A.3 – Continued

Line	χ	log(gf)	15	16	17	18	19	20
Zr II λ6578.65	2.43	−1.500					34	
Ba II λ4554.04	0.00	+0.120		32				
Ba II λ5853.69	0.60	−1.016	164		176	133		
Ba II λ6141.71	0.70	−0.080		14		188		
Ba II λ6496.91	0.60	−0.410				221		
La II λ4230.94	1.96	−0.170					69	
La II λ4263.58	1.96	+0.030					104	
La II λ4333.76	0.17	−0.060				74		
La II λ4526.11	0.77	−0.770					145	
La II λ4559.28	0.77	−1.302					77	
La II λ4645.28	0.13	−1.790					70	
La II λ4692.49	1.75	−0.420					88	
La II λ4743.07	1.78	−0.135					70	
La II λ4804.04	0.23	−1.490					88	
La II λ4999.46	0.40	−0.890					170	
La II λ5303.53	0.32	−1.350					92	
La II λ5377.05	2.30	−0.430					40	
La II λ5482.27	0.00	−2.230					56	
La II λ5769.06	1.25	−0.950					90	
La II λ6262.25	0.40	−1.220			9			
La II λ6296.08	1.25	−0.950					74	
La II λ6390.49	0.32	−1.410			9	8		
La II λ6642.76	2.53	−0.960					11	
Ce II λ4042.59	0.49	+0.007				52		
Ce II λ4068.84	0.70	−0.170					110	
Ce II λ4120.84	0.32	−0.370					130	
Ce II λ4145.00	0.69	+0.010				44		
Ce II λ4349.79	0.70	−0.320				27		
Ce II λ4382.17	0.68	+0.130				51		
Ce II λ4437.61	0.82	−0.819					22	
Ce II λ4486.71	0.30	−0.180			34		150	
Ce II λ4560.28	0.91	+0.515					177	

Table A.3 – Continued

Line	χ	log(gf)	15	16	17	18	19	20
Ce II λ4560.97	0.68	−0.260			11	17	106	
Ce II λ4562.37	0.48	+0.210			60	65	178	
Ce II λ4628.16	0.52	+0.140				69		
Ce II λ5077.85	1.41	−0.576					16	
Ce II λ5117.17	1.40	+0.010					74	
Ce II λ5187.46	1.21	+0.300					88	
Ce II λ5472.30	1.25	−0.177					64	
Pr II λ5034.41	1.11	−0.141					23	
Pr II λ5259.73	0.63	+0.114				4		
Pr II λ5292.62	0.65	−0.411					47	
Pr II λ5322.77	0.48	−0.461					42	
Pr II λ6017.77	1.11	−0.358					17	
Pr II λ6025.73	1.44	−0.106					20	
Nd II λ4038.12	0.18	−0.870					81	
Nd II λ4098.17	0.47	−0.700					62	
Nd II λ4213.05	1.34	−0.300					49	
Nd II λ4228.23	0.47	−0.440					114	
Nd II λ4304.43	1.52	+0.440					112	
Nd II λ4366.39	0.32	−0.910					72	
Nd II λ4446.40	0.20	−0.500				21		
Nd II λ4724.36	0.74	−0.550					73	
Nd II λ4832.27	0.56	−0.920					61	
Nd II λ4959.15	0.06	−0.800			23			
Nd II λ4989.95	0.63	−0.500					99	
Nd II λ5063.72	0.98	−0.530					43	
Nd II λ5130.59	1.30	+0.570			19		128	
Nd II λ5181.17	0.86	−0.600					59	
Nd II λ5293.16	0.82	−0.060			22	17	142	
Nd II λ5361.47	0.68	−0.370					92	
Sm II λ4347.80	0.38	−0.761					66	
Sm II λ4424.34	0.48	−0.260					93	
Sm II λ4434.32	0.38	−0.576					84	

Table A.3 – Continued

Line	χ	log(gf)	15	16	17	18	19	20
Sm II λ4523.92	0.43	−0.390					94	
Sm II λ4745.71	0.10	−0.930					67	
Eu II λ4129.72	0.00	+0.220					186	
Eu II λ6645.13	1.38	+0.120					61	
Dy II λ4027.78	1.22	−0.520					97	
Dy II λ4328.90	0.54	−1.610					51	
Dy II λ4794.61	0.54	−2.170					29	

REFERENCES

Aikawa, T. & Bruegman, O. 1987, Ap&SS, 137, 115

Alcock, C., Allsman, R. A., Alves, D. R., et al. 1998, AJ, 115, 1921

Aldenius, M., Lundberg, H., & Blackwell-Whitehead, R. 2009, A&A, 502, 989

Allen, D. M. & Porto de Mello, G. F. 2011, A&A, 525, 63

Aller, L. H., Appenzeller, I., Baschek, B., et al., eds. 1982, Landolt-Börnstein: Numerical Data and Functional Relationships in Science and Technology - New Series ” Gruppe/Group 6 Astronomy and Astrophysics ” Volume 2 Schaifers/Voigt: Astronomy and Astrophysics / Astronomie und Astrophysik ” Stars and Star Clusters / Sterne und Sternhaufen, 455

Alonso, A., Arribas, S., & Martínez-Roger, C. 1999, A&AS, 139, 335

Arellano Ferro, A., Giridhar, S., & Mathias, P. 2001, A&A, 368, 250

Arkhipova, V. P., Noskova, R. I., Ikonnikova, N. P., & Komissarova, G. V. 2003, Astronomy Letters, 29, 480

Asplund, M., Grevesse, N., & Sauval, A. J. 2005, in Astronomical Society of the Pacific Conference Series, Vol. 336, Cosmic Abundances as Records of Stellar Evolution and Nucleosynthesis, ed. T. G. Barnes III & F. N. Bash, 25

Asplund, M., Grevesse, N., Sauval, A. J., & Scott, P. 2009, ARA&A, 47, 481

Asplund, M., Gustafsson, B., Kameswara Rao, N., & Lambert, D. L. 1998, A&A, 332, 651

Baird, S. R. 1981, ApJ, 245, 208

Belyakova, E. V. & Mashonkina, L. I. 1997, Astronomy Reports, 41, 530

Bensby, T., Feltzing, S., Lundström, I., & Ilyin, I. 2005, A&A, 433, 185

Bergemann, M. 2011, MNRAS, 413, 2184

Bergemann, M. & Cescutti, G. 2010, A&A, 522, A9

Biémont, E., Grevesse, N., Hannaford, P., & Lowe, R. M. 1981, ApJ, 248, 867

Blöcker, T. 2001, Ap&SS, 275, 1

Blöcker, T., Osterbart, R., Weigelt, G., Balega, Y., & Men'shchikov, A. 2001, in Astrophysics and Space Science Library, Vol. 265, Astrophysics and Space Science Library, ed. R. Szczerba & S. K. Górny, 241

Blöcker, T. & Schönberner, D. 1991, A&A, 244, L43

Blöcker, T. & Schönberner, D. 1997, A&A, 324, 991

Bogaert, E. 1994, PhD thesis, K. U. Leuven

Böhm-Vitense, E. 1989, Introduction to stellar astrophysics. Vol. 2. Stellar atmospheres., ed. Böhm-Vitense, E.

Bond, H. E. 1991, in IAU Symposium, Vol. 145, Evolution of Stars: the Photospheric Abundance Connection, ed. G. Michaud & A. V. Tutukov, 341

Bond, J. C., Lauretta, D. S., & O'Brien, D. P. 2010a, Icarus, 205, 321

Bond, J. C., O'Brien, D. P., & Lauretta, D. S. 2010b, ApJ, 715, 1050

Boyarchuk, A. A., Lyubimkov, L. S., & Sakhibullin, N. A. 1985, Astrophysics, 22, 203

Brown, J. A., Wallerstein, G., & Oke, J. B. 1990, AJ, 100, 1561

Buchler, J. & Kovács, G. 1987, ApJ, 320, L57

Bujarrabal, V., Bachiller, R., Alcolea, J., & Martin-Pintado, J. 1988, A&A, 206, L17

Buonanno, R., Corsi, C. E., & Fusi Pecci, F. 1981, MNRAS, 196, 435

Busso, M., Gallino, R., Lambert, D. L., Raiteri, C. M., & Smith, V. V. 1992, ApJ, 399, 218

Cameron, A. G. W. & Fowler, W. A. 1971, ApJ, 164, 111

Cami, J. & Yamamura, I. 2001, ARA&A, 367, L1

Cardelli, J. A. 1994, Science, 265, 209

Christlieb, N., Bessell, M. S., Beers, T. C., et al. 2002, Nature, 419, 904

Clube, K. L. & Gledhill, T. M. 2004, MNRAS, 355, L17

Collet, R., Asplund, M., & Thévenin, F. 2005, A&A, 442, 643

Conlon, E. S., Dufton, P. L., & Keenan, F. P. 1994, A&A, 290, 897

Conlon, E. S., Dufton, P. L., Keenan, F. P., & McCausland, R. J. H. 1991, MNRAS, 248, 820

Curry, J. J. 2004, J. Phys. Chemical Reference Data, 33, 725

Danks, A. C. & Lambert, D. L. 1985, A&A, 148, 293

De Ruyter, S., Van Winckel, H., Dominik, C., Waters, L. B. F. M., & Dejonghe, H. 2005, A&A, 435, 161

De Ruyter, S., Van Winckel, H., Maas, T., et al. 2006, A&A, 448, 641

De Smedt, K., Van Winckel, H., Karakas, A. I., et al. 2012, ArXiv e-prints

Demers, S. & Harris, W. E. 1974, AJ, 79, 627

Den Hartog, E. A., Lawler, J. E., Sneden, C., & Cowan, J. J. 2003, ApJS, 148, 543

Deroo, P. 2007, PhD thesis, K. U. Leuven

Deroo, P., Reyniers, M., Van Winckel, H., Goriely, S., & Siess, L. 2005, A&A, 438, 987

Deroo, P., Van Winckel, H., Min, M., et al. 2006, A&A, 450, 181

Deupree, R. G. & Hodson, S. W. 1976, ApJ, 208, 426

D'Odorico, S., Ghigo, M., & Ponz, D. 1987, An atlas of the thorium-argon spectrum for the ESO Echelle Spectrograph in the 3400-9000Å region, ed. D'Odorico, S., Ghigo, M., & Ponz, D.

Dominik, C., Dullemond, C. P., Cami, J., & Van Winckel, H. 2003, A&A, 397, 595

Edvardsson, B., Andersen, J., Gustafsson, B., et al. 1993, A&A, 275, 101

Eggen, O. J. 1986, AJ, 91, 890

El Eid, M. F. & Champagne, A. E. 1995, ApJ, 451, 298

Fleischer, A. J., Gauger, A., & Sedlmayr, E. 1992, A&A, 266, 321

Fokin, A. B. 1994, A&A, 292, 133

Forveille, T., Morris, M., Omont, A., & Likkel, L. 1987, A&A, 176, L13

Frankowski, A. 2003, A&A, 406, 265

Frebel, A., Aoki, W., Christlieb, N., et al. 2005, Nature, 434, 871

Fuhr, J. R., Martin, G. A., & Wiese, W. L. 1988, J. Phys. Chem. Ref. Data, 17, 493 pp.

Fuhr, J. R. & Wiese, W. L. 2005, NIST Atomic Transition Probabilities, 86th edn., ed. D. R. Lide (Boca Raton, FL: CRC Press)

Fuhr, J. R. & Wiese, W. L. 2006, J. Phys. Chem. Ref. Data, 35, 1669

Fujii, T., Nakada, Y., & Parthasarathy, M. 2002, A&A, 385, 884

Gallino, R., Arlandini, C., Busso, M., et al. 1998, ApJ, 497, 388

García-Hernández, D. A., García-Lario, P., Plez, B., et al. 2006, Science, 314, 1751

García-Hernández, D. A., García-Lario, P., Plez, B., et al. 2007, A&A, 462, 711

Garcia-Lario, P. 1992, PhD thesis, U. La Laguna, Spain

García-Lario, P. 2006, in IAU Symposium, Vol. 234, Planetary Nebulae in our Galaxy and Beyond, ed. M. J. Barlow & R. H. Méndez, 63–70

Garcia-Lario, P., Manchado, A., Pych, W., & Pottasch, S. R. 1997, A&AS, 126, 479

García-Lario, P. & Perea Calderón, J. V. 2003, in ESA Special Publication, Vol. 511, Exploiting the ISO Data Archive. Infrared Astronomy in the Internet Age, ed. C. Gry, S. Peschke, J. Matagne, P. Garcia-Lario, R. Lorente, & A. Salama, 97

Geballe, T. R., Noll, K. S., Whittet, D. C. B., & Waters, L. B. F. M. 1989, ApJ, 340, L29

Gehren, T., Liang, Y. C., Shi, J. R., Zhang, H. W., & Zhao, G. 2004, A&A, 413, 1045

Gehrz, R. D. 1971, PhD thesis, University of Minnesota

Gielen, C., Bouwman, J., van Winckel, H., et al. 2011a, A&A, 533, A99

Gielen, C., Cami, J., Bouwman, J., Peeters, E., & Min, M. 2011b, A&A, 536, A54

Gielen, C., Van Winckel, H., Matsuura, M., et al. 2009a, A&A, 503, 843

Gielen, C., Van Winckel, H., Min, M., Waters, L. B. F. M., & Lloyd Evans, T. 2008, A&A, 490, 725

Gielen, C., Van Winckel, H., Min, M., et al. 2011c, in Astronomical Society of the Pacific Conference Series, Vol. 445, Why Galaxies Care about AGB Stars II: Shining Examples and Common Inhabitants, ed. F. Kerschbaum, T. Lebzelter, & R. F. Wing, 281

Gielen, C., Van Winckel, H., Reyniers, M., et al. 2009b, A&A, 508, 1391

Gielen, C., Van Winckel, H., Waters, L. B. F. M., Min, M., & Dominik, C. 2007, A&A, 475, 629

Gillet, D., Duquennoy, A., Bouchet, P., & Gouiffes, C. 1989, A&A, 215, 316

Gingold, R. A. 1976, ApJ, 204, 116

Gingold, R. A. 1985, Mem. Soc. Astron. Italiana, 56, 169

Giridhar, S. 2000, in IAU Symposium, Vol. 177, The Carbon Star Phenomenon, ed. R. F. Wing, 117

Giridhar, S. & Arellano Ferro, A. 2005, A&A, 443, 297

Giridhar, S., Arellano Ferro, A., & Parrao, L. 1997, PASP, 109, 1077

Giridhar, S., Lambert, D. L., & Gonzalez, G. 1998, ApJ, 509, 366

Giridhar, S., Lambert, D. L., & Gonzalez, G. 2000, ApJ, 531, 521

Giridhar, S., Lambert, D. L., Reddy, B. E., Guillermo Gonzalez, & David Yong. 2005, ApJ, 627, 432

Giridhar, S., Molina, R., Arellano Ferro, A., & Selvakumar, G. 2010, MNRAS, 406, 290

Giridhar, S., Rao, N. K., & Lambert, D. L. 1994, ApJ, 437, 476

Goldsmith, M. J., Evans, A., Albinson, J. S., & Bode, M. F. 1987, MNRAS, 227, 143

Gonzalez, G. 1994, AJ, 108, 1312

Gonzalez, G., Lambert, D. L., & Giridhar, S. 1997a, ApJ, 479, 427

Gonzalez, G., Lambert, D. L., & Giridhar, S. 1997b, ApJ, 481, 452

Gonzalez, G. & Wallerstein, G. 1994, ApJ, 108, 1325

Gonzalez, G. & Wallerstein, G. 1996, MNRAS, 280, 515

Gorlova, N., Van Winckel, H., Gielen, C., et al. 2012a, A&A, 542, A27

Gorlova, N., Van Winckel, H., & Jorissen, A. 2012b, Baltic Astronomy, 21, 165

Grevesse, N., Noels, A., & Sauval, A. J. 1996, in Astronomical Society of the Pacific Conference Series, Vol. 99, Cosmic Abundances, ed. S. S. Holt & G. Sonneborn, 117

Gustafsson, B., Edvardsson, B., Eriksson, K., et al. 2003, in Astronomical Society of the Pacific Conference Series, Vol. 288, Stellar Atmosphere Modeling, ed. I. Hubeny, D. Mihalas, & K. Werner, 331

Habing, H. J. 1996, A&A Rev., 7, 97

Hannaford, P., Lowe, R. M., Grevesse, N., Biémont, E., & Whaling, W. 1982, ApJ, 261, 736

Hauschildt, P. H., Allard, F., Ferguson, J., Baron, E., & Alexander, D. R. 1999, ApJ, 525, 871

Heiter, U. & Eriksson, K. 2006, A&A, 452, 1039

Herwig, F. 2001, AP&SS, 275, 15

Herwig, F. 2005, ARA&A, 43, 435

Herwig, F., Blöcker, T., Langer, N., & Driebe, T. 1999, A&A, 349, L5

Hony, S., Tielens, A. G. G. M., Waters, L. B. F. M., & de Koter, A. 2003, A&A, 402, 211

Hony, S., Waters, L. B. F. M., & Tielens, A. G. G. M. 2002, A&A, 390, 533

Hoogzaad, S. N., Molster, F. J., Dominik, C., et al. 2002, A&A, 389, 547

Hrivnak, B. J. 1995, ApJ, 438, 341

Hrivnak, B. J., Van Winckel, H., Reyniers, M., et al. 2008, AJ, 136, 1557

Hrivnak, B. J., Volk, K., & Kwok, S. 2009, ApJ, 694, 1147

Jeffery, C. S., Woolf, V. M., & Pollacco, D. L. 2001, A&A, 376, 497

Jenkins, E. B. 2009, ApJ, 700, 1299

Joy, A. H. 1952, ApJ, 115, 25

Jura, M. 1986, ApJ, 309, 732

Justtanont, K., Barlow, M. J., Skinner, C. J., et al. 1996, A&A, 309, 612

Karakas, A. I. 2010, in Principles and Perspectives in Cosmochemistry, ed. A. Goswami & B. E. Reddy, 107

Karakas, A. I., Lattanzio, J. C., & Pols, O. R. 2002, PASA, 19, 515

Kelleher, D. E. & Podobedova, L. I. 2008a, J. Phys. Chem. Ref. Data, 37, 267

Kelleher, D. E. & Podobedova, L. I. 2008b, J. Phys. Chem. Ref. Data, 37, 709

Kelleher, D. E. & Podobedova, L. I. 2008c, J. Phys. Chem. Ref. Data, 37, 1285

Kiss, L. L., Derekas, A., Szabó, G. M., Bedding, T. R., & Szabados, L. 2007, MNRAS, 375, 1338

Klochkova, V. G. 1995, MNRAS, 272, 710

Klochkova, V. G., Chentsov, E. L., Tavolzhanskaya, N. S., & Panchuk, V. E. 2007, Astronomy Reports, 51, 642

Klochkova, V. G. & Panchuk, V. E. 1996, Bull.Spec.Astrophys.Obs, 41, 5

Klochkova, V. G. & Panchuk, V. E. 1998, Astronomy Letters, 24, 650

Klochkova, V. G., Panchuk, V. E., & Tavolzhanskaya, N. S. 2002, Astronomy Letters, 28, 49

Klochkova, V. G., Panchuk, V. E., & Tavolzhanskaya, N. S. 2010, Astronomy Reports, 54, 234

Kodaira, K., Greenstein, J. L., & Oke, J. B. 1970, ApJ, 159, 485

Kolláth, Z. 1990, MNRAS, 247, 377

Korotin, S. A. 2009, Astronomy Reports, 53, 651

Kovács, G. & Buchler, R. J. 1988, ApJ, 334, 971

Kubát, J. & Korcáková, D. 2004, in IAU Symposium, Vol. 224, The A-Star Puzzle, ed. J. Zverko, J. Ziznovsky, S. J. Adelman, & W. W. Weiss, 13–22

Kukarkin, B. V., Parenago, P. P., & Kholopov, P. N. 1958, General Catalogue of Variable Stars, 2nd edn. Academy of Sciences of USSR, Moscow

Kurucz, R. L. 1992, in IAU Symposium, Vol. 149, The Stellar Populations of Galaxies, ed. B. Barbuy & A. Renzini, 225

Kurucz, R. L., Furenlid, I., Brault, J., & Testerman, L. 1984, Solar flux atlas from 296 to 1300 nm, ed. Kurucz, R. L., Furenlid, I., Brault, J., & Testerman, L.

Kwok, S. 1993, ARA&A, 31, 63

Kwok, S., Volk, K. M., & Bernath, P. 2001, ApJ, 554, L87

Kwok, S., Volk, K. M., & Hrivnak, B. J. 1989, ApJ, 345, L51

Lambert, D. 1996, in Astronomical Society of the Pacific Conference Series, Vol. 96, Hydrogen Deficient Stars, ed. C. S. Jeffery & U. Heber, 443

Lattanzio, J. C. & Boothroyd, A. I. 1997, in American Institute of Physics Conference Series, Vol. 402, American Institute of Physics Conference Series, ed. T. J. Bernatowicz & E. Zinner, 85–114

Lawler, J. E., Bonvallet, G., & Sneden, C. 2001a, ApJ, 556, 452

Lawler, J. E., Den Hartog, E. A., Sneden, C., & Cowan, J. J. 2006, ApJS, 162, 227

Lawler, J. E., Sneden, C., Cowan, J. J., Ivans, I. I., & Den Hartog, E. A. 2009, ApJS, 182, 51

Lawler, J. E., Wickliffe, M. E., Den Hartog, E. A., & Sneden, C. 2001b, ApJ, 563, 1075

Lemke, M. 1997, A&AS, 122, 285

Lewis, B. M., Eder, J., & Terzian, Y. 1990, ApJ, 362, 634

Lind, K., Asplund, M., Barklem, P. S., & Belyaev, A. K. 2011, A&A, 528, 103

Lind, K., Bergemann, M., & Asplund, M. 2012, MNRAS, 427, 50

Lloyd Evans, T. 1985, MNRAS, 217, 493

Lloyd Evans, T. 1999, in IAU Symposium, Vol. 191, Asymptotic Giant Branch Stars, ed. T. Le Bertre, A. Lebre, & C. Waelkens, 453–457

Lodders, K. 2003, ApJ, 591, 1220

Loup, C., Forveille, T., Omont, A., & Paul, J. F. 1993, A&AS, 99, 291

Luck, R. E. & Bond, H. E. 1984, ApJ, 279, 729

Luck, R. E. & Bond, H. E. 1989, ApJ, 342, 476

Luck, R. E., Bond, H. E., & Lambert, D. L. 1990, ApJ, 357, 188

Luck, R. E., Lambert, D. L., & Bond, H. E. 1983, PASP, 98, 413

Lyubimkov, L. S., Lambert, D. L., Korotin, S. A., et al. 2011, MNRAS, 410

Maas, T., Giridhar, S., & Lambert, D. L. 2007, ApJ, 666, 378

Maas, T., Van Winckel, H., & Lloyd Evans, T. 2005, A&A, 429, 297

Maas, T., Van Winckel, H., Lloyd Evans, T., et al. 2003, A&A, 405, 271

Maas, T., Van Winckel, H., & Waelkens, C. 2002, A&A, 386, 504

Martin, G. A., Fuhr, J. R., & Wiese, W. L. 1988, Atomic transition probabilities. Scandium through Manganese, ed. Martin, G. A., Fuhr, J. R., & Wiese, W. L.

Mashonkina, L. 2011, in Magnetic Stars, 314–321

Mashonkina, L., Gehren, T., Shi, J.-R., Korn, A. J., & Grupp, F. 2011, A&A, 528, A87

Mashonkina, L., Korn, A. J., & Przybilla, N. 2007, A&A, 461, 261

Mathis, J. S. & Lamers, H. J. G. L. M. 1992, A&A, 259, L39

Mazzitelli, I., D'Antona, F., & Ventura, P. 1999, A&A, 348, 846

McCarthy, J. K., Sandiford, B. A., Boyd, D., & Booth, J. 1993, PASP, 105, 881

McCausland, R. J. H., Conlon, E. S., Dufton, P. L., & Keenan, F. P. 1992, ApJ, 394, 298

McWilliam, A. 1998, AJ, 115, 1640

Meléndez, J. & Barbuy, B. 2009, A&A, 497, 611

Miroshnichenko, A. S., Manset, N., Kusakin, A. V., et al. 2007, ApJ, 671, 828

Molster, F. J., Waters, L. B. F. M., Trams, N. R., et al. 1999, A&A, 350, 163

Moore, C. E. 1972, A multiplet table of astrophysical interest - Pt.1: Table of multiplets - Pt.2: Finding list of all lines in the table of multiplets, ed. Moore, C. E.

Moore, C. E., Minnaert, M. G. J., & Houtgast, J. 1966, The solar spectrum 2935 A to 8770 A, ed. Moore, C. E., Minnaert, M. G. J., & Houtgast, J.

Mowlavi, N. 1999, A&A, 350, 73

Mucciarelli, A., Caffau, E., Freytag, B., Hans-Günter Ludwig, & Bonifacio, P. 2008, A&A, 484, 841

Nook, M. A., Cardelli, J. A., & Nordsieck, K. H. 1990, ApJ, 100, 2004

Norris, J. E., Christlieb, N., Korn, A. J., et al. 2007, ApJ, 670, 774

Nozawa, T., Kozasa, T., Umeda, H., Maeda, K., & Nomoto, K. 2003, ApJ, 598, 785

O'Brien, G. T. J. & Lambert, D. L. 1986, ApJS, 62, 899

Pandey, G. 2006, ApJ, 648, L143

Pandey, G. & Lambert, D. L. 2011, ApJ, 727, 122

Pandey, G., Rao, N. K., Lambert, D. L., Jeffery, C. S., & Asplund, M. 2001, MNRAS, 324, 937

Pandey, G. & Reddy, B. E. 2006, MNRAS, 369, 1677

Parthasarathy, M. & Pottasch, S. R. 1986, A&A, 154, L16

Percy, J. R. 1999, New A Rev., 43, 449

Percy, J. R., Bezuhly, M., Milanowski, M., & Zsoldos, E. 1997, PASP, 109, 264

Percy, J. R. & Coffey, J. 2005, Journal of the American Association of Variable Star Observers (JAAVSO), 33, 193

Planesas, P., Bujarrabal, V., Le Squeren, A. M., & Mirabel, I. F. 1991, A&A, 251, 133

Plez, B., Smith, V. V., & Lambert, D. L. 1993, ApJ, 418, 812

Podobedova, L. I., Kelleher, D. E., & Wiese, W. L. 2009, J. Phys. Chemical Reference Data, 38, 171

Pollard, K. R., Cottrell, P. L., Kilmartin, P. M., & Gilmore, A. C. 1996, MNRAS, 279, 949

Preston, G. W., Krzeminski, W., Smak, J., & Williams, J. A. 1963, ApJ, 137, 401

Prochaska, J. X. & McWilliam, A. 2000, ApJ, 537, L57

Rao, N. K., Goswami, A., & Lambert, D. L. 2002, MNRAS, 334, 129

Rao, N. K. & Reddy, B. E. 2005, MNRAS, 357, 235

Rao, N. K., Sriram, S., Jayakumar, K., & Gabriel, F. 2005, J. Astrophys. Astr., 26, 331

Raveendran, A. V. 1989, MNRAS, 238, 945

Reddy, B. E., Bakker, E. J., & Hrivnak, B. J. 1999, ApJ, 524, 831

Reddy, B. E., Lambert, D. L., & Allende Prieto, C. 2006, MNRAS, 367, 1329

Reddy, B. E., Lambert, D. L., Gonzalez, G., & Yong, D. 2002, ApJ, 564, 482

Reddy, B. E. & Parthasarathy, M. 1996, AJ, 112, 2053

Relyea, L. J. & Kurucz, R. L. 1978, ApJS, 37, 45

Reyniers, M. 2002, PhD thesis, K. U. Leuven

Reyniers, M., Abia, C., Van Winckel, H., et al. 2007a, A&A, 461, 641

Reyniers, M., van de Steene, G. C., van Hoof, P. A. M., & Van Winckel, H. 2007b, A&A, 471, 247

Reyniers, M. & Van Winckel, H. 2001, A&A, 365, 465

Reyniers, M. & Van Winckel, H. 2007, A&A, 463, L1

Reyniers, M., Van Winckel, H., Gallino, R., & Straniero, O. 2004, A&A, 417, 269

Romano, D., Karakas, A. I., Tosi, M., & Matteucci, F. 2010, A&A, 522, A32

Sackmann, I. J. & Boothroyd, A. I. 1992, ApJ, 392, L71

Sansonetti, J. E. 2008, J. Phys. Chemical Reference Data, 37, 1659

Savage, B. D. & Sembach, K. R. 1996, ARA&A, 34, 279

Schaller, G., Schaerer, D., Mainer, G., & Maeder, A. 1992, A&AS, 96, 269

Schiller, F. & Pryzbilla, N. 2008, A&A, 479, 849

Schönberner, D. 1979, A&A, 79, 108

Schönberner, D. 1983, ApJ, 272, 708

Schönberner, D. 1993, in IAU Symposium, Vol. 155, Planetary Nebulae, ed. R. Weinberger & A. Acker, 415

Seeger, P. A., Fowler, W. A., & Clayton, D. D. 1965, ApJS, 11, 121

Shenton, M., Albinson, J. S., Barrett, P., et al. 1992, A&A, 262, 138

Shenton, M., Evans, A., Albinson, J. S., et al. 1994a, A&A, 292, 102

Shenton, M., Evans, A., Cardelli, J. A., et al. 1994b, A&A, 287, 852

Shenton, M., Monier, R., Evans, A., et al. 1994c, A&A, 287, 866

Siódmiak, N., Meixner, M., Ueta, T., et al. 2008, ApJ, 677, 382

Sloan, G. C., Kraemer, K. E., Wood, P. R., et al. 2008, ApJ, 686, 1056

Smith, V. V. & Lambert, D. L. 1986, ApJ, 311, 843

Smith, V. V., Plez, B., Lambert, D. L., & Lubowich, D. A. 1995, ApJ, 441, 735

Sneden, C. 1973, PhD thesis, AA(The University Of Texas at Austin.)

Sneden, C., Lawler, J. E., Cowan, J. J., Ivans, I. I., & Den Hartog, E. A. 2009, ApJS, 182, 80

Sobeck, J. S., Lawler, J. E., & Sneden, C. 2007, ApJ, 667, 1267

Stasińska, G., Szczerba, R., Schmidt, M., & Siódmiak, N. 2006, A&A, 450, 701

Straniero, O., Gallino, R., Busso, M., et al. 1995, ApJ, 440, L85

Suárez, O., García-Lario, P., Manchado, A., et al. 2006, A&A, 458, 173

Sumangala Rao, S., Giridhar, S., & Lambert, D. L. 2012, MNRAS, 419, 1254

Szczerba, R., Siódmiak, N., Stasińska, G., & Borkowski, J. 2007, A&A, 469, 799

Takeda, Y. 2003, A&A, 402, 343

Takeda, Y., Hashimoto, O., Taguchi, H., et al. 2005, PASJ, 57, 751

Takeda, Y., Sato, B., & Murata, D. 2008, PASJ, 60, 781

Takeda, Y. & Takada-Hidai, M. 1998, PASJ, 50, 629

Takeuti, M. & Petersen, J. O. 1983, A&A, 117, 352

Tempesti, P. 1955, Mem. Soc. Astron. Italiana, 26, 125

Thévenin, F. & Idiart, T. P. 1999, ApJ, 521

Tuchman, Y., Lebre, A., Mennessier, M. O., & Yarri, A. 1993, A&A, 271

Tull, R. G., MacQueen, P. J., Sneden, C., & Lambert, D. L. 1995, PASP, 107, 251

Valiante, R., Schneider, R., Bianchi, S., & Andersen, A. C. 2009, MNRAS, 397, 1661

van der Veen, W. E. C. J. & Habing, H. J. 1988, A&A, 194, 125

Van Kerckhoven, C., Tielens, A. G. G. M., & Waelkens, C. 2002, A&A, 384, 568

Van Winckel, H. 1995, PhD thesis, K. U. Leuven

Van Winckel, H. 1997, A&A, 319, 561

van Winckel, H. 1999, in IAU Symposium, Vol. 191, Asymptotic Giant Branch Stars, ed. T. Le Bertre, A. Lebre, & C. Waelkens, 465

Van Winckel, H. 2003, ARA&A, 41, 391

Van Winckel, H. 2007, Baltic Astronomy, 16, 112

Van Winckel, H., Hrivnak, B. J., Gorlova, N., Gielen, c., & Lu, W. 2012, ArXiv e-prints

Van Winckel, H., Lloyd Evans, T., Briquet, M., et al. 2009, A&A, 505, 1221

Van Winckel, H., Mathis, J. S., & Waelkens, C. 1992, Nature, 356, 500

Van Winckel, H. & Reyniers, M. 2000, A&A, 354, 135

Van Winckel, H., Waelkens, C., Fernie, J. D., & Waters, L. B. F. M. 1999, A&A, 343, 202

Van Winckel, H., Waelkens, C., & Waters, L. B. F. M. 1996, A&A, 306, L37

Van Winckel, H., Waelkens, C., & Waters, L. B. F. M. 2000, Proceedings of the IAU Symposium, Vol. 177, The Carbon Star Phenomenon, ed. R. F. Wing, 285

Van Winckel, H., Waelkens, C., Waters, L. B. F. M., et al. 1998, A&A, 336, L17

Vassiliadis, E. & Wood, P. R. 1993, ApJ, 413, 641

Vassiliadis, E. & Wood, P. R. 1994, ApJS, 92, 125

Velichko, A. B., Mashonkina, L. I., & Nilsson, H. 2010, Astronomy Letters, 36, 664

Venn, K. A. 1993, ApJ, 414, 316

Venn, K. A. 1995a, ApJS, 99, 659

Venn, K. A. 1995b, ApJ, 449, 839

Venn, K. A. & Lambert, D. L. 1990, ApJ, 363, 234

Venn, K. A. & Lambert, D. L. 2008, ApJ, 677, 572

Ventura, P. & D'Antona, F. 2009, A&A, 499, 835

Volk, K., Hrivnak, B. J., Matsuura, M., et al. 2011, ApJ, 735, 127

Waelkens, C., Van Winckel, H., Bogaert, E., & Trams, N. R. 1991, A&A, 251, 495

Waelkens, C., Waters, L. B. F. M., Cassatella, A., Le Bertre, T., & Lamers, H. J. G. L. M. 1987, A&A, 181, L5

Wahlgren, G. M. 1986, PhD thesis, Ohio State University, Columbus.

Wallerstein, G. 2002, PASP, 114, 689

Waters, L. B. F. M., Cami, J., de Jong, T., et al. 1998, Nature, 391, 868

Waters, L. B. F. M., Trams, N. R., & Waelkens, C. 1992, A&A, 262, L37

Wedemeyer, S. 2001, A&A, 373, 998

Whitelock, P. & Marang, F. 2001, MNRAS, 323, L13

Wiese, W. L. & Fuhr, J. R. 2007, J. Phys. Chem. Ref. Data, 36, 1287

Wiese, W. L., Fuhr, J. R., & Deters, T. M. 1996, Atomic transition probabilities of carbon, nitrogen, and oxygen : a critical data compilation, ed. Wiese, W. L., Fuhr, J. R., & Deters, T. M.

Wolff, S. C. & Heasley, J. N. 1984, PASP, 96, 231

Zhang, H. W., Gehren, T., & Zhao, G. 2008, in IAU Symposium, Vol. 252, IAU Symposium, ed. L. Deng & K. L. Chan, 127–128

Zsoldos, E. 1995, Journal of the British Astronomical Association, 105, 238